THE PREPARATION PENNING TRAP AND RECENT DEVELOPMENTS ON HIGH-PERFORMANCE ION DETECTION FOR THE PROJECT TRAPSENSOR

TESIS DOCTORAL

JUAN MANUEL CORNEJO GARCÍA

UNIVERSIDAD DE GRANADA
PROGRAMA DE
DOCTORADO DE FÍSICA Y CIENCIAS DEL ESPACIO

Granada, Enero de 2016

Editor: Universidad de Granada. Tesis Doctorales
Autor: Juan Manuel Cornejo García
ISBN: 978-84-9125-856-8
URI: http://hdl.handle.net/10481/43683

THE PREPARATION PENNING TRAP AND RECENT DEVELOPMENTS ON HIGH-PERFORMANCE ION DETECTION FOR THE PROJECT TRAPSENSOR

REALIZADO POR:

Juan Manuel Cornejo García

DIRIGIDO POR:

Daniel Rodríguez Rubiales[1]

DEPARTAMENTO:

[1]**Departamento de Física Atómica, Molecular y Nuclear**

UNIVERSIDAD DE GRANADA
PROGRAMA DE
DOCTORADO DE FÍSICA Y CIENCIAS DEL ESPACIO

Granada, Enero de 2016

A mis padres,
Juan y Luisa,
a mis hermanas,
Maria Paz, Vanesa y Alba,
y a mi esposa,
Sandra.

Resumen

El trabajo que se presenta en esta tesis doctoral se ha realizado en el marco del proyecto TRAPSENSOR que tiene como objetivo final implementar un método para la medida de masas de precisión basado en la detección de fotones de fluorescencia de un ion $^{40}Ca^{+}$. Uno de los elementos principales de la instalación es la línea de trampas magnéticas (Penning traps), construida a lo largo de este trabajo, que está compuesta por una fuente de producción de iones por ablación láser, una sección de transferencia, para transporte y primera identificación de los iones producidos, y el sistema de trampas magnéticas, fijadas en el interior de un imán superconductor de 7 T, al que sigue una sección de tiempo de vuelo para llevar a cabo las medidas. La parte más destacable de la línea de trampas magnéticas es la que comprende el diseño, construcción, puesta en funcionamiento y caracterización de la trampa de preparación, demostrando que dicho dispositivo cumple los requisitos necesarios para su utilización con iones estables y/o radioactivos. En paralelo a la línea de trampas magnéticas, también se ha construido otra línea formada por una trampa de radiofrecuencia, con su fuente de iones y elementos de vacío, y un sistema de láseres con su mecanismo de regulación, que ha permitido realizar experimentos de enfriamiento Doppler con un ion $^{40}Ca^{+}$, primer paso para la utilización de este ion con el método propuesto en el proyecto. La otra parte relevante presentada en este trabajo engloba los desarrollos de las dos técnicas de detección no destructiva de iones atrapados que se han llevado a cabo en la universidad para las medidas de masas de precisión a partir de la señal de fluorescencia (proyecto TRAPSENSOR) y por el método de amplificación de la señal electrónica inducida por el ion atrapado en los electrodos de la trampa (proyecto FPA2012-32076). Los sistemas construidos cumplen las especificaciones electrónicas y se probarán con iones a finales de 2016.

Palabras clave: Trampas de iones, espectrometría de masas, enfriamiento con gas, enfriamiento con láser, detección electrónica, fluorescencia.

Abstract

The work presented in this manuscript has been carried out in the framework of the project TRAPSENSOR. The final goal of the project is to implement a novel method for mass spectrometry based on the detection of fluorescence photons from a single laser-cooled $^{40}Ca^{+}$ ion in a Penning trap. One of the main elements is the Penning-traps beamline, which has been designed and built in the course of this thesis work. It is comprised of a laser-desorption ion source, a transfer section for transport and rough identification by time of flight of the ions, the Penning-traps system, built in a vacuum tube inside the bore of a 7-T superconducting solenoid, and another transfer section for measurements. The most remarkable part has been the design, construction, commissioning and characterization of the preparation Penning trap in this beamline. The results show that the system meets the requirements for its use with stable and/or radioactive isotopes. In parallel to the Penning-traps beamline, another setup comprising a radiofrequency trap with an ion source and vacuum components, and eight diode lasers with a regulation system was built. With this setup, Doppler cooling of a single laser-cooled ion was accomplished, which is the first step needed to use the proposed method in the project. Another remarkable work within this thesis was devoted to developments on high-performance detection for high-precision mass spectrometry, i.e. building up the system for the detection of fluorescence photons (project TRAPSENSOR) and the electronics to perform a measurement based on the amplification of the current induced by a single ion stored in the trap (project FPA2012-32076). Both systems have been successfully tested; and will be implemented in the traps to test them with ions by the end of 2016.

Key words: Ion traps, mass spectrometry, buffer-mas cooling, laser cooling, electronics detection, fluorescence detection.

Contents

1 Introduction **1**

2 Fundamentals of ions traps **7**
2.1 Trapping potential 7
2.2 Penning trap principles 9
2.3 Ion manipulation techniques 11

3 Accuracy and sensitivity in Penning-trap mass spectrometry: Different techniques **19**
3.1 Systematic uncertainties in a Penning trap 19
3.2 Destructive detection techniques 21
3.2.1 Time-of-flight Ion-Cyclotron-Resonance 21
3.2.2 Phase-Imaging Ion-Cyclotron-Resonance 23
3.3 Non-destructive detection techniques 25
3.3.1 Induced Image Current (IIC) detection 25
3.3.2 The Quamtum Sensor (QS) technique 28
3.3.3 Applications of mass values 31

4 The TRAPSENSOR facility **33**
4.1 The Penning-traps beamline 33
4.1.1 The laser-desorption ion source 36
4.1.2 The transfer section 40
4.1.3 The superconducting magnet and the Penning trap system 43
4.1.4 The time-of-flight section and the detector 45
4.1.5 Vacuum system and electronic connections 46
4.2 The laser system 48
4.2.1 Frequency stabilization 49
4.2.2 Power regulation 51
4.3 The open-ring Paul trap test bench 51
4.3.1 The open-ring trap 52
4.3.2 Doppler cooling of a single $^{40}Ca^{+}$ ion 54
4.3.3 Geometry for the QS system 55

5 The preparation Penning trap **57**
5.1 Mechanical design 57

5.2 Magnetic-field alignment 61
5.3 Pumping barrier 64
5.4 Control system and cycles 66
5.5 Electronics 69

6 Characterization of the preparation Penning trap 73
6.1 Potential shape along the z-axis 73
6.2 Determination of the characteristic frequencies 74
6.3 Cooling resonances for different ion species 77
6.4 Ion energy distribution 82
6.5 Injection into the measurement trap 87
6.5.1 The open-ring Penning trap 87
6.5.2 The double Penning-(micro)-trap system 90

7 Developments for high-performance detection 93
7.1 Mass spectrometry based on optical detection 93
7.1.1 Micro-trap construction 93
7.1.2 Electronics for ion-ion coupling 96
7.2 Mass spectrometry based on electronic detection 100
7.2.1 Circuit description 101
7.2.2 Quartz crystal resonator 104
7.2.3 Performance 108

8 Summary and outlook 117

A Beyond the project TRAPSENSOR: MATS at FAIR 121

B Resumen en Castellano 125
B.1 Motivación y objetivos 125
B.2 Estructura y contenido 127
B.2.1 Principios y técnicas utilizadas en trampas de iones . . . 127
B.2.2 La instalación TRAPSENSOR 128
B.2.3 La trampa magnética de preparación 129
B.2.4 Recientes desarrollos en detección no destructiva 130
B.3 Resultados y conclusiones 131

Bibliography 133

List of Figures

1.1 Penning-trap facilities worldwide 2

2.1 Electrostatic potential in an ion trap 8
2.2 Sketch of a Paul and a Penning trap 9
2.3 Ion trayectory in a Penning trap 10
2.4 Penning trap configurations 11
2.5 Dipole and quadrupole electric field in the radial direction 12
2.6 Trajectory of an excited ion in a Penning trap 13
2.7 Trajectory of an ion in a Penning trap filled with buffer gas . . . 15
2.8 Trajectory of an excited ion in a Penning trap filled with buffer gas 16
2.9 Longitudinal view of the equipotential lines resulting from the field applied for axial-radial coupling 17

3.1 Sketch of the TOF-ICR detection setup 22
3.2 Energy and time of flight in TOF-ICR measurements 23
3.3 Sketch of the PI-ICR detection setup 24
3.4 Variation of the charge induced by a trapped ion 25
3.5 Amplification stages for IIC detection 26
3.6 Equivalent circuits for IIC and QS detection 29
3.7 Measurement sequence using the QS technique 30

4.1 Technical drawing of the Penning-traps beamline 34
4.2 Three-dimensional technical drawing of the Penning-traps beamline 35
4.3 Three-dimensional technical drawing of the different sections inside the Penning-traps beamline 36
4.4 Top view of the laser-desorption ion source 37
4.5 Time-of-flight signal of Re^+ ions produced with the laser-desorption ion source 39
4.6 Kinetic energy of the ions versus the inverse of the square of the time-of-flight. 40
4.7 Technical drawing of the transfer section 40
4.8 Transmission through the Penning-traps beamline 41
4.9 Distribution of Ca^+ ions as a function of the ion-beam energy . . 42
4.10 Energy levels for $^{40}Ca^+$ in a 7-T magnetic field and sketch of the open-ring trap with the optical system 44

4.11 Diagram of the vacuum system in the Penning-traps beamline . . 46
4.12 Diagram of the electrical connections in the Penning-traps beamline 47
4.13 Sketch of the TRAPSENSOR facility at the University of Granada 48
4.14 Lasers system to perform Doppler cooling on $^{40}Ca^{+}$ 49
4.15 Stability of the laser frequencies 50
4.16 Regulation of the laser powers 51
4.17 Different views of the setup to perform Doppler cooling 52
4.18 Sketch of the optical system to collect the fluorescence photons and different views of the open-ring trap 53
4.19 Image of a single laser-cooled $^{40}Ca^{+}$ ion 54

5.1 Three-dimensional CAD drawing of the preparation Penning trap (PPT) inside the vacuum tube 58
5.2 Photograph of one electrode taken with an electron microscope . 59
5.3 Photograph of the PPT components 60
5.4 Three-dimensional drawing of the connection system 61
5.5 Sketch of the setup for the alignment of the PPT with the magnetic field 62
5.6 Different views showing the alignment and misalignment of the PPT with the magnetic field 63
5.7 Measurements to align of the Penning-traps system with the magnetic field 64
5.8 Elements taken into account to design the pumping barrier . . . 65
5.9 Conductance versus temperature for several diameters of the pumping barrier 66
5.10 Diagram of the control system for the Penning-traps beamline . . 67
5.11 Operation schemes for the PPT 68
5.12 Electrical connections and devices to run the PPT 69
5.13 Diagram detailing the voltages applied to the central ring electrode 70
5.14 Elements for data acquisition 71

6.1 Potential shape along the z-axis in the PPT 74
6.2 Dipole excitation of the magnetron motion in the PPT 76
6.3 Magnetron and reduced-cyclotron frequency in the PPT as a function of the helium-gas pressure 77
6.4 Timing sequence for a cooling resonance in the PPT 78
6.5 Cooling resonance for $^{40}Ca^{+}$ 79
6.6 Cooling resonances for $^{185}Re^{+}$ and $^{187}Re^{+}$ 80
6.7 Measurement of the magnetic field stability 81
6.8 Potential shapes utilized for stepwise extraction of the ions from the PPT 83
6.9 Time-of-flight spectrum resulting from a stepwise extraction . . . 84
6.10 $^{40}Ca^{+}$ and $^{187}Re^{+}$ ions as a function of the axial energy 85
6.11 Evolution of the axial energy of rhenium and calcium ions in the PPT with time 86

6.12 Spatial and energy distributions of ions in the PPT 87
6.13 Potential shape along the z-axis to capture the ions in the open-ring trap 88
6.14 Trapping efficiency in the open-ring trap 89
6.15 Potential shape along the z-axis to trap the ions in the QS system 90
6.16 Trapping efficiency in a micro trap 91

7.1 Construction details of the double Penning-(micro)-trap system . 94
7.2 Measurement of gaps and aperture in the double Penning-(micro)-trap system 95
7.3 Variation of the coupling strength with the aperture in the trap electrodes. 96
7.4 Allan deviation of the voltage to be applied to the micro-trap electrodes for ion-ion coupling 97
7.5 Sketch showing the electronic circuit wired to electrodes of one trap of the double Penning-(micro)-trap system 98
7.6 Photograph of the electronic boards housing the electronics for the operation of the double Penning-(micro)-trap system 99
7.7 Output signal V_{R} of the transistor used as switch (ON state) versus the V_{GS} 100
7.8 Main parameters of an electronic circuit used for IIC detection (I) 101
7.9 Main parameters of an electronic circuit used for IIC detection (II) 102
7.10 Circuit diagram of a preamplifier built at the University of Granada 103
7.11 Main parameters of an electronic circuit used for IIC detection (III) 104
7.12 Butterworth Van-Dyke equivalent model for a quartz crystal . . . 105
7.13 Crystallographic axes and overtones in a quartz crystal 105
7.14 Simplified diagram of the circuit for narrow-band detection . . . 106
7.15 Photograph of the quartz crystal integrated in the Printed Circuit Board 107
7.16 Connections diagram between the PCB cards and the PPT central electrodes 109
7.17 Technical drawing of the experimental setup built to test electronics at cryogenic temperature 110
7.18 Diagrams of the setups built to measure the gain factor and density noise of the amplifier 111
7.19 BODE plot (broad-band) 112
7.20 Input voltage and current noise density versus frequency 113
7.21 BODE plot (narrow-band) in V/V 114
7.22 BODE plot (narrow-band) in dB 115

A.1 MATS at FAIR 122

List of Tables

3.1 Performance of Penning-trap techniques for mass spectrometry . 28
3.2 Time for energy exchange in the QS for different ion pairs 31
3.3 Applications of mass values 32

4.1 Laser energy and counts per second for several delay values of the Q-switch 38
4.2 Typical voltages used for the operation of the Penning-traps beamline 45
4.3 The 397-nm radial laser beam and the fluorescence image 55
4.4 Comparison between different trap geometries (I) 56
4.5 Comparison between different trap geometries (II) 56

5.1 Dimensions of the PPT electrodes 60

6.1 Voltages applied to the PPT electrodes 75
6.2 Cyclotron frequencies for $^{187}Re^{+}$, $^{185}Re^{+}$ and $^{40}Ca^{+}$ 82
6.3 Distribution of $^{40}Ca^{+}$ and $^{187}Re^{+}$ ions as a function of energy . . 84
6.4 Voltages applied to the electrodes of the open-ring trap used as Penning trap 89
6.5 Voltages applied to the electrodes of the double Penning-(micro)-trap system (I) 91

7.1 Voltages applied to the electrodes of the double Penning-(micro)-trap system (II) 97
7.2 Values of the parameters of the equivalent circuit for a quartz crystal 106
7.3 Resonator, resonance frequency and Q-value in LC circuits used in different experiments 108
7.4 Characteristic parameters for several amplifiers 112
7.5 Bandwidth and Q-value provided by the narrow-band circuit . . 114

Chapter 1

Introduction

High-precision mass measurements are especially important in fundamental physics. For an elementary particle, this is a fundamental property, and for a quantum mechanical system such as an atom, the mass yields directly the binding energy, which reflects all interactions present among its constituents. Up to date, the most suitable device for precise mass measurements on exotic and stable charged particles is the Penning trap [1].

In a Penning trap, the mass of any charged particle confined between the electrodes, can be measured from its motional frequencies, which can be in turn determined even to a sub-Hz level in the radiofrequency regime (see e.g. [2]). The requested relative mass uncertainty will depend on the application, being for example, the hardly attainable level of 10^{-11}, needed for contributions in neutrino physics.

There are currently several Penning traps devoted to perform high-precision mass measurements, either on exotic nuclei at Radioactive Ion Beam (RIB) facilities, or on naturally abundant isotopes. Figure 1.1 shows these facilities, including also facilities under construction, in the planning stage and Penning traps at accelerators utilized for other experiments like beta-neutrino correlation measurements (WITCH experiment [3] at ISOLDE/CERN), precision laser spectroscopy (SPECTRAP experiment [4] at GSI) or matter-antimatter comparison tests (ATRAP [5] or BASE [6, 7] experiments at CERN).

Opposite to Penning traps using stable ions, those at RIB facilities have to be built together with complex systems to match the high energy of the RIB with the eV regime requested for trapping. Furthermore, the exoticism of the nuclei is also a constraint for preparation and observation. This is the situation of the SHIPTRAP experiment at GSI (Helmholtzzentrum für Schwerionenforschung) in Darmstadt (Germany), where mass measurements of transuranium elements [8, 9] have been carried out, requesting strong developments in ion-gas catcher technology, accelerators and sensitivity to proceed with nuclei closer to the theoretically predicted Island of Stability [10]. Other developments are important to get larger values of the oscillation frequencies and therefore higher resolving

powers for the ions to be studied; higher magnetic fields (LEBIT project at MSU [11]), which would slightly contribute to this improvement, or the charge breeding of the ions (HITRAP experiment at GSI [12]). All these issues have been considered for the future (planned) facility MATS (Precision Measurements on very short-lived nuclei using an Advanced Trapping System) at FAIR (Facility for Antiproton and Ion Research) [13].

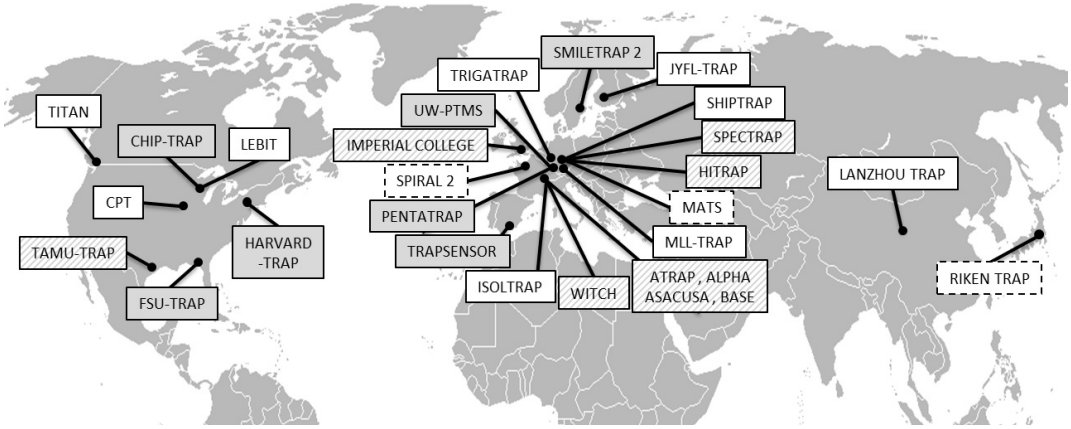

Figure 1.1: Penning-trap facilities for fundamental physics studies. The boxes filled in white contain the names of Penning-trap facilities where high-accuracy mass measurements with RIBs are carried out. Off-line Penning trap facilities at universities or research institutes are delimited by boxes filled in grey. The boxes filled with an incline-lines pattern contain the names of Penning traps for laser spectroscopy, experiments with antiprotons, test of the standard model, or production of highly charged ion for reacceleration. The boxes delimited with dashed lines stand for the planned facilities. The MLLTRAP setup at the Maier-Leibnitz Laboratory (MLL) in Garching (Germany) [14] will be operated at DESIR (SPIRAL2) [15].

Besides the developments around the Penning-trap system or facility, the detection method of the ion in the trap has to be further developed in order to improve sensitivity. The technique which has been currently used at RIB facilities for mass measurements, i.e., the Time-of-Flight Ion-Cyclotron-Resonance (TOF-ICR) [16] technique needs of a few tens of ions for a mass measurement, which is not possible when dealing with elements with very low cross sections as it is the case of superheavy elements (SHEs) ($Z \geq 104$) [10]. A novel technique referred to as Phase-Imaging Ion-Cyclotron-Resonance (PI-ICR) [17], needs only about ten detected ions to measure the mass with a fivefold gain in precision, and will be used in the next measurement campaign at GSI [18]. However, for heavier elements produced in fusion-evaporation reactions, the expected rates are very low; being in some cases of one atom per day or even one atom per week, and thus, single-ion sensitivity is needed.

There are several experiments where single-ion sensitivity has been reached allowing for ultra-precise mass measurements; the UW-PTMS experiment at the

University of Washington in Seattle, installed at the Max-Planck-Institute for Nuclear Physics in Heidelberg since 2008, the MIT-TRAP experiment, since 2008 FSU-TRAP, at Florida State University in Tallahassee (United States) and the Mainz experiment. These spectrometers have delivered relative uncertainties in the order of 10^{-11} for stable nuclides [2, 19, 20]. Measurements with such relative mass uncertainty on some specific nuclides, allow using the Penning trap data, in combination with other experiments, for neutrino mass measurements.

Although, at the beginning the neutrino [21] was postulated massless, the results with solar neutrinos in the SNO (Sudbury Neutrino Observatory) in 2001, established that they have mass [22]. Several international collaborations are building up complex experiments to measure directly the neutrino mass. This is the case of the KArlsruhe TRitium Neutrino experiment (KATRIN), which aims to reach a sensitivity on the neutrino mass of 0.2 eV (90% C.L.) [23]. There are several experiments based on the bolometer principle. The Micro-calorimeter Array for a Rhenium Experiment (MARE) [24], which was initially aiming at determining the mass of the electron antineutrino from the β-decay spectrum of rhenium ($T_{1/2} = 43.2 \times 10^9$ years)

$$^{187}\mathrm{Re} \rightarrow {}^{187}\mathrm{Os} + e^- + \overline{\nu}_e + 2.4653(17)\mathrm{keV}, \tag{1.1}$$

where the total energy $E_\mathrm{Q} = 2.4653(17)$ keV [25] is shared between the electron (e^-), and the antineutrino ($\overline{\nu}_\mathrm{e}$). E_Q has been measured recently with a Penning trap [26]. The absolute mass can be determined by analyzing the end of the electron energy spectrum near the endpoint and comparing with the energy-value obtained from the difference between the masses of the mother and the daughter nuclides [27]. A second experiment, the Electron Capture Holmiun experiment (ECHo), studies the electron-capture (EC) process, from holmium ($T_{1/2} = 4.5 \times 10^3$ years) [28]

$$^{163}\mathrm{Ho} + e^- \rightarrow {}^{163}\mathrm{Dy} + \nu_e + 2.80(5)\mathrm{keV} \tag{1.2}$$

(see also [29]). There are two recent experiments HOLMES (The Electron Capture Decay of ^{163}Ho to Measure the Electron Neutrino Mass) [30] and NuMECS (Neutrino Mass via Electron Capture Spectroscopy) [31]. The measurement of the neutrino mass, considering CPT symmetry and thus that the masses of particles and antiparticles are equal, is based on the X-ray spectra following the EC-decay. Therefore, Penning trap with ultra-precise mass value (below $\delta m/m = 10^{-11}$) for the mother and daughter nucleus of the β or EC-decay, with low E_Q energy ($\ll 100$ keV), and micro-calorimeters experiments with about 1 eV resolution in the energy region can provide a new upper limit for the electron neutrino mass [32]. Very recently the masses of ^{163}Ho and ^{163}Dy has been determined with the SHIPTRAP facility at GSI [33].

These topics have motivated the construction of the TRAPSENSOR facility at the University of Granada, and the so-called *Quantum-Sensor*, which will permit overcoming limitations with respect to accuracy and sensitivity in Penning trap mass spectrometry [34]. The device consists of a double Penning-(micro)-trap

system, where a laser-cooled $^{40}Ca^{+}$ ion (*Quantum-Sensor*) is stored in one trap while the ion of interest, which is under investigation, is stored in a second trap. The two ions are coupled through the charges they induce in a common electrode. Any motional frequency of the ion of interest can be probed and monitored by the fluorescence photons of the *Quantum-Sensor* (laser-cooled ion). This technique lies on a former idea by Heinzen and Wineland in 1990 [35], and might be applied, only to stable or long-lived nuclides.

TRAPSENSOR will be the first facility where Penning traps and laser cooling are combined to reach ultra-high sensitivity for mass spectrometry, with applications in SHE research and neutrino physics [10, 34, 36]. There is a similar experiment under completion at the University of Hannover [37], within the BASE collaboration aiming at coupling the motions of a laser cooled $^{9}Be^{+}$ ion and a proton (latter an antiproton when coupled to the facility at CERN) confined in different potential wells of the same Penning trap. Coupling between two ions in different potential wells, has been demonstrated already in a radiofrequency trap [38]. The TRAPSENSOR facility is unique in Spain with respect to ion traps and laser cooling. This is the only ion traps laboratory in Spain where these kinds of experiments can be performed.

The work carried out in this thesis has various goals. The first goal was to build up and commission a full beamline to work with the double Penning-(micro)-trap system under similar experimental conditions as with SHIPTRAP. For that purpose, a laser-desorption ion source was installed, to produce stable and long-lived nuclides, coupled to a transfer section comprising many electrostatic lenses and deflectors, and, this section to a preparation Penning trap designed and built following specifications for the future MATS experiments. This trap is located in the first homogeneous region of a 7-T superconducting solenoid, identical to the SHIPTRAP magnet. The second homogeneous region coincides at present with the center of a novel Penning trap based on an open-ring trap, initially operated as a Paul trap, to perform for the first time, laser cooling on $^{40}Ca^{+}$ in a 7-T magnetic field. The full beamline will be called Penning-traps beamline in this work. A second objective, where most of the effort was devoted, was to build up, commission and fully characterize the preparation Penning trap in the mass range from 40 to 190 amu. The final aim of this trap is to deliver cooled and isobarically-pure samples to the double Penning-(micro)-trap system to replace the existing trap in the second homogeneous region of the 7-T magnet. It has been shown that the system meets the requirements for TRAPSENSOR. The third and final objective pertains to developments on non-destructive single-ion detection yielding two important outcomes: 1) the first tests at cryogenic temperature of an electronic circuit developed within this work for broad-band and narrow-band (single-ion) detection, and 2) the first prototype of the double Penning-(micro)-trap system with the associated electronics.

This thesis consists of eight chapters. Chapter 2 is devoted to the fundamentals of ion traps, and to describe the techniques to manipulate and prepare ions in a Penning trap. The current state-of-the-art in Penning-trap detection techniques

focuses on sensitivity and accuracy and will be described in Chapter 3. The TRAPSENSOR facility comprising the Penning-traps beamline and a complex laser system to perform laser cooling on $^{40}Ca^{+}$ in the 7-T magnetic field of the superconducting solenoid will be presented for the first time in Chapter 4, where the open-ring trap built up for Doppler cooling studies will be also shown. This trap has been the seed for all the developments carried out for the coupling of the two ions. Chapter 5 is devoted to the design and construction of the preparation Penning trap, while in Chapter 6, the characterization and results are presented. The performance of the electronics for ion-ion coupling with the double Penning-(micro)-trap system will be described in the first part of Chapter 7, while the developments for single-ion electronic detection, at cryogenic temperature are presented in the second part. Chapter 8 is devoted to the conclusions and outlook.

Chapter 2

Fundamentals of ions traps

There are basically two kinds of ion traps: radiofrequency, or Paul traps, and magnetic or Penning traps. In both cases the geometry is such to perform a quadrupole electric potential in a small region of the space [39, 40]. In the Paul trap, the electric potential is oscillating as a function of time, while in a Penning trap, the electric potential is constant allowing only for the axial confinement of the ions. Trapping in the radial direction is possible due to the high magnetic field provided by a superconducting solenoid. Ion traps together with manipulation techniques, allow for a long storage time and precise observation of atomic properties [41, 42]. This chapter is devoted to explain the fundamental of ions traps and ion manipulation techniques, which are important for the work presented later.

2.1 Trapping potential

Confinement in three dimensions needs a restoring force, and the simplest way would be to have one of the form

$$\vec{F} = -k\vec{r}, \tag{2.1}$$

which can be originated by an electric field like

$$\vec{E} \propto x\hat{e}_{\mathrm{x}} + y\hat{e}_{\mathrm{y}} + z\hat{e}_{\mathrm{z}}, \tag{2.2}$$

where $\hat{e}_{\mathrm{u}}$ with $u = x, y, z$, is the unit vector in the direction of u-axis. Since $\vec{E}$ is the result of applying the nabla operator to the electric potential, this potential can be expressed as [39]

$$\phi = \frac{\phi_0}{2r_0}(\alpha x^2 + \beta y^2 + \gamma z^2), \tag{2.3}$$

where ϕ_0 is the maximum amplitude of the electric potential, r_0 depends on the structure of the field, and α, β and γ are constants. In the absence of charge, this potential follows the Laplace´s equation

$$\nabla^2\phi = 0 \longrightarrow \alpha + \beta + \gamma = 0, \tag{2.4}$$

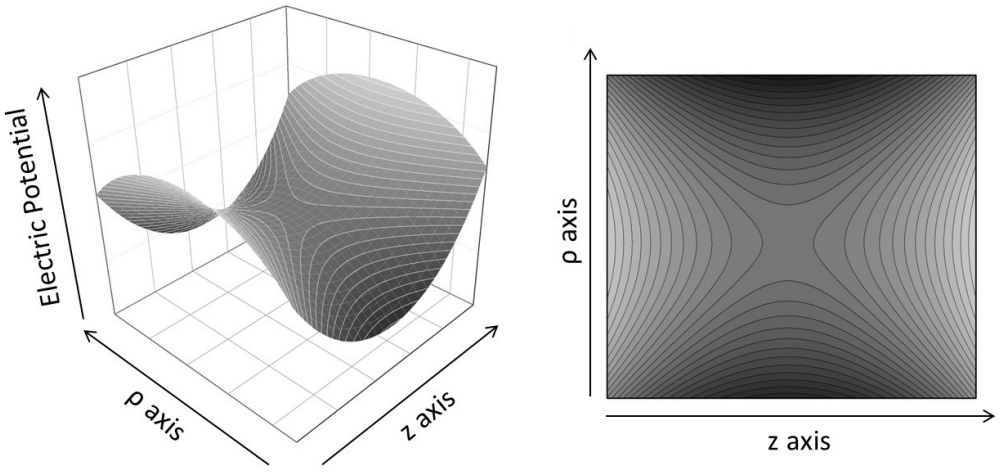

Figure 2.1: Equipotential lines in an ion trap with cylindrical geometry. Right: Three-dimensional view of the equipotential lines at a fixed time. Left: Projection in the ρ-z plane of the electric potential.

with several possible solutions. For $\alpha = \beta = 1$ and γ = -2, an electric quadrupole potential, which can be written in cylindrical coordinates as

$$\phi = \frac{\phi_0}{4d_0^2}(\rho_0^2 - 2z_0^2), \tag{2.5}$$

is obtained, where $2d_0^2 = z_0^2 + \rho_0^2/2$, with z_0 and ρ_0 the axial and radial sizes of the trap, respectively. Figure 2.1 shows a three-dimensional view of the equipotential lines at a fixed time and a projection in the ρ-z plane of an electrostatic potential given by Eq. (2.5). Electrodes following infinite hyperboloids of revolution are needed to generate such potential. However, in a real case, the electrodes are not infinite and the hyperbolic trap comprises a ring electrode and two endcaps with finite sizes, as shown in Fig. 2.2. The electric trapping potential can be generated using others geometries (see Fig. 2.4). Such geometries would facilitate the injection of the ions into the trap or cool them, using lasers, although they have the disadvantage of introducing higher-order electric multipoles [43].

Figure 2.2 shows the two configurations used to solve the problem of not having a restoring force in the three dimensions. Figure 2.2.a shows the Paul-trap configuration, where the ion is stored by means of a radiofrequency field created between the ring electrode and the endcaps. The ion moves to the center of the trap in the radial or axial directions as a function of the time and the electric potential changes the polarity due to the radiofrequency. The ion will be trapped when the range of frequencies and amplitudes of the signal is within a certain range [39, 40]. The second configuration is shown in Fig. 2.2.b, where the ions are stored in the radial direction using a magnetic field. This kind of trap is called Penning trap [44, 45].

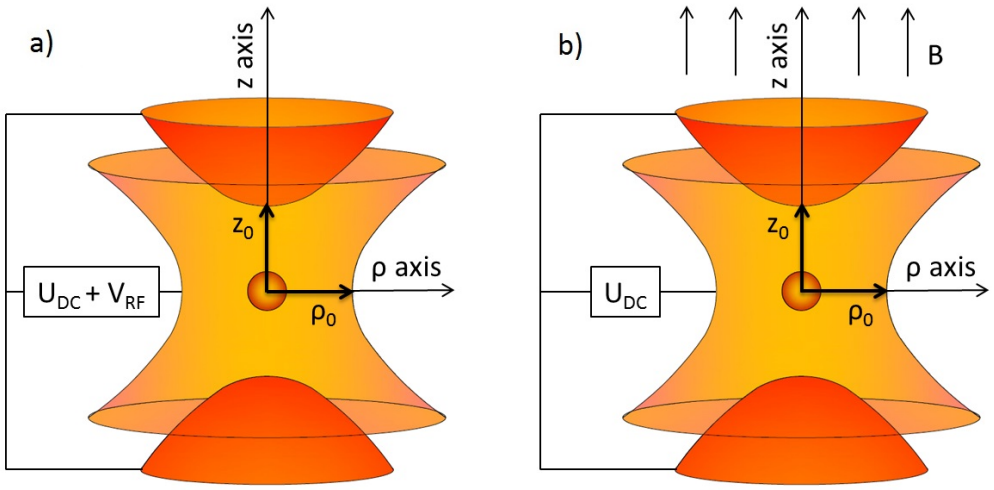

Figure 2.2: Sketch of the real hyperbolic trap to be operated as a Paul (a) or as a Penning trap (b). The hyperbolic trap is comprised of a ring electrode (clear orange) and two endcaps (dark orange). U_{DC} is a constant voltage while $\pm\ V_{\mathrm{RF}}$ is a voltage varying with a radiofrequency (RF).

2.2 Penning trap principles

In a Penning trap the ions are confined in three dimensions due to the superposition of an electric field $\vec{E}$ and a strong homogeneous magnetic field $\vec{B}$. A particle of mass m and charge q, moving with a velocity $\vec{v}$, experiences the Lorentz force

$$\vec{F} = q(\vec{E} + \vec{v} \times \vec{B}). \tag{2.6}$$

The equation of motion can be written in a matrix form as

$$m \begin{pmatrix} \ddot{x} \\ \ddot{y} \\ \ddot{z} \end{pmatrix} = q \begin{pmatrix} E_{\mathrm{x}} \\ E_{\mathrm{y}} \\ E_{\mathrm{z}} \end{pmatrix} + q \begin{vmatrix} \hat{e}_{\mathrm{x}} & \hat{e}_{\mathrm{y}} & \hat{e}_{\mathrm{z}} \\ \dot{x} & \dot{y} & \dot{z} \\ B_{\mathrm{x}} & B_{\mathrm{y}} & B_{\mathrm{z}} \end{vmatrix}. \tag{2.7}$$

Assuming $B_{\mathrm{x}} = B_{\mathrm{y}} = 0$, the motion of the ion in a Penning trap is described in Cartesian coordinates by

$$\ddot{x} - \omega_{\mathrm{c}}\dot{y} + \frac{1}{2}\omega_{\mathrm{z}}^2 x = 0 \tag{2.8}$$

$$\ddot{y} + \omega_{\mathrm{c}}\dot{x} + \frac{1}{2}\omega_{\mathrm{z}}^2 y = 0 \tag{2.9}$$

$$\ddot{z} + \omega_{\mathrm{z}}^2 z = 0 \tag{2.10}$$

where

$$\omega_z = \sqrt{\frac{qU_{\mathrm{DC}}}{md_0^2}} \tag{2.11}$$

is the axial frequency, U_{DC} is the voltage indicated in Fig. 2.2, and

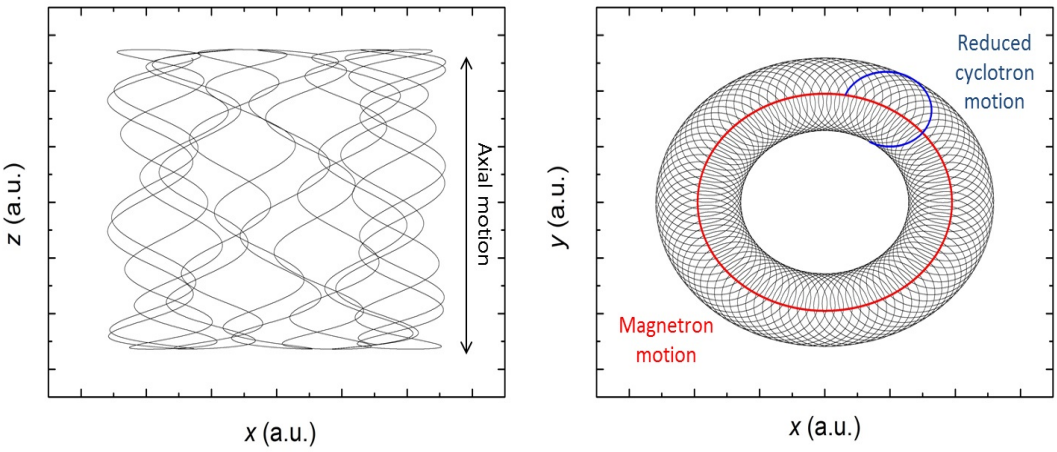

Figure 2.3: Simulation of the trajectory of an ion in a Penning trap. The magnetic field is along the z-axis. Left: Projection of the ion motion in the x-z plane. Right: Projection of the ion motion in the radial plane. The magnetron motion is shown in red, and the so-called reduced-cyclotron motion in blue.

$$\omega_c = \frac{q}{m} B \tag{2.12}$$

is the cyclotron frequency, directly related to the mass and charge of the ion. Multiplying Eq. (2.9) by the imaginary unit j, and defining the complex variable $u = x + jy$, one obtains

$$\ddot{u} + j\omega_c \dot{u} - \frac{1}{2}\omega_z^2 u = 0. \tag{2.13}$$

Using $u = e^{-j\omega t}$, ω can be expressed as

$$\omega_\pm = \frac{1}{2}\omega_c \pm \sqrt{\frac{\omega_c^2}{4} - \frac{\omega_z^2}{2}}, \tag{2.14}$$

where ω_+ and ω_- are called reduced-cyclotron frequency and magnetron frequency, respectively. Figure 2.3 shows two projections of the motion of an ion in a Penning trap. The slow magnetron motion is depicted as a large circular orbit, while the fast reduced-cyclotron motion is shown as a small one. From Eq. (2.14), the following relationships can be obtained:

$$\omega_c = \omega_+ + \omega_- \quad \text{and} \tag{2.15}$$

$$2\omega_+\omega_- = \omega_z^2. \tag{2.16}$$

In addition, the inequality $\omega_c^2 - 2\omega_z^2 > 0$ is required to obtain real solutions from Eq. (2.14). Another relationship, very important in high-precision mass spectrometry, is known as invariance theorem [46], and is given by

$$\omega_c^2 = \omega_+^2 + \omega_z^2 + \omega_-^2. \tag{2.17}$$

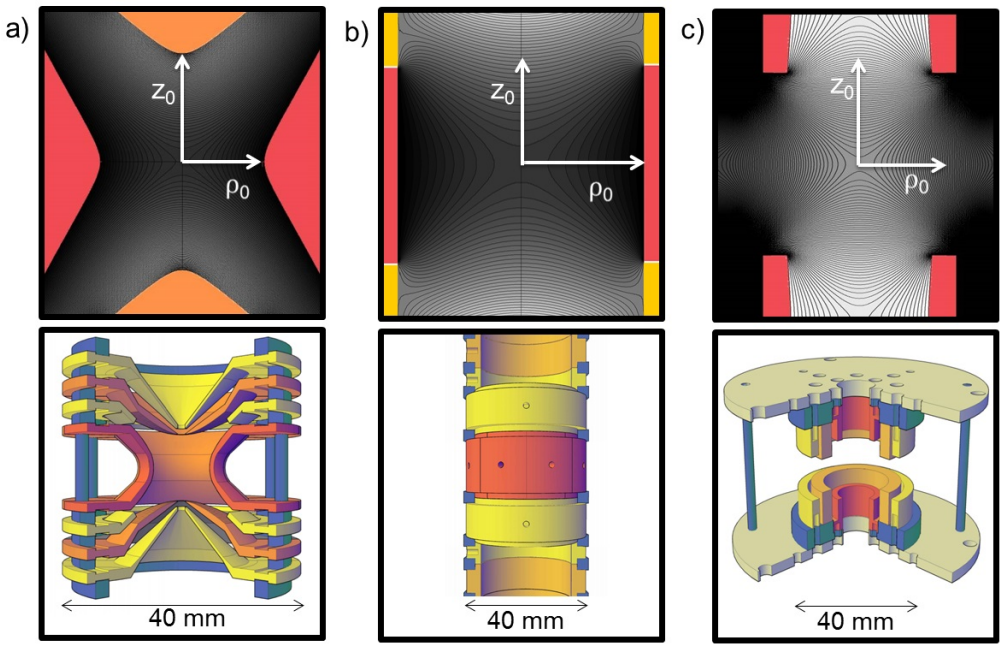

Figure 2.4: Penning trap configurations. The upper panels show the equipotential lines obtained from a longitudinal cut. The lower panels show cuts from 3D-CAD drawings. a) Hyperbolic trap at the TRIGA reactor in Mainz [47], b) cylindrical trap, and c) open ring-trap. Although operated as a Paul trap, this trap can be used as Penning trap. It is similar to the trap built for the LPCTrap facility at GANIL in Caen [48].

Figure 2.4 shows several geometries for Penning traps. The ions are injected parallel to the magnetic field in the axial direction. Insulators are drawn in blue. Ring electrodes, endcaps and corrections electrodes are colored in red, orange and yellow, respectively. The cylindrical trap shown in Fig. 2.4.b, is the central part of the preparation Penning trap used in the TRAPSENSOR project and subject to detail studies within this thesis work. The open ring-trap (Fig. 2.4.c) is identical to the one installed at the LPCTrap facility at GANIL (France) for β-ν correlation measurements, and has been built up at the University of Granada to study Doppler cooling of $^{40}Ca^{+}$. This trap will be described in Sec. 4.3.1.

2.3 Ion manipulation techniques

The electrodes around the trapping region of a Penning trap are usually segmented to apply external radiofrequency fields in order to excite, and thus manipulate the ion motions. These techniques are described in the following.

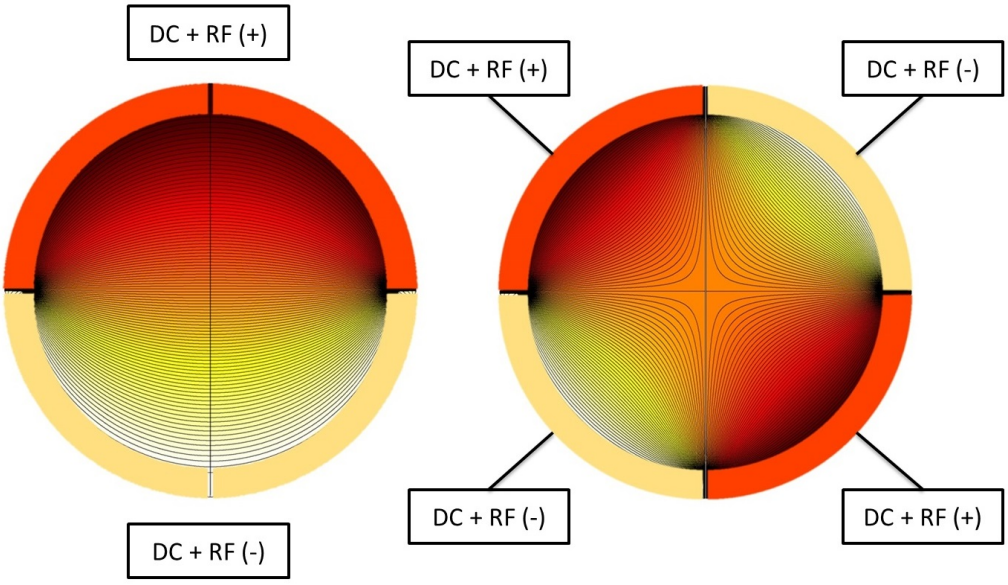

Figure 2.5: Transversal cut of a four-fold segmented ring electrode in a cylindrical trap. The electric field gradient is shown in clear yellow (negative polarity) to dark red (positive polarity). Left: Configuration to perform dipole excitation. Right: Configuration to perform quadrupole excitation.

Dipole excitation

Figure 2.5 shows a transverse cut of a four-fold segmented ring electrode in a cylindrical Penning trap. The left side of the figure shows the field gradient for a dipole configuration. For radial excitation, a radiofrequency signal is delivered with a phase shift of 180° to opposite segments of the ring electrode. The electric field can be written as

$$\vec{E} = (d_{\mathrm{x}}\hat{e}_{\mathrm{x}} + d_{\mathrm{y}}\hat{e}_{\mathrm{y}})\cos(\omega_{\mathrm{d}}t + \phi_{\mathrm{d}}), \tag{2.18}$$

where d_{x} and d_{y} are related to the voltage applied to the ring electrodes, ω_{d} is the radiofrequency and ϕ_{d} is the phase of the excitation. This electric field is acting in the x-y plane. Excitation in the axial direction can be performed by applying such radiofrequency field to the endcaps electrodes.

The application of a dipole electric field originates an increase of the radius of the ion motion when the radiofrequency is equal to an eigenfrequeny of the ion in the trap. Although, the radius of the ion motion will be increased linearly, for small time ($< 2/\nu$), the effect of the excitation depends on the phase ϕ_{d} of the radiofrequency and on the initial position and velocity of the ion in the trap [49]. The dependence of the oscillation frequencies on the mass of the ion, allows using dipole excitation for several features:

- $\omega_d = \omega_-$: the orbits of all ion species will be increased, since ω_- does not depend on the mass in first approximation.

- $\omega_d = \omega_+$: this is used to remove unwanted ions from the trap due to the strong dependence between ω_+ and the ion mass.

- $\omega_d = \omega_z$: this is used to increase the axial energy in order to detect the electric signal induced by the ions on the endcap electrodes.

Quadrupole excitation

Quadrupole excitation in the radial plane is used to couple the eigenmotions in this plane, provided the radiofrequency of the external field $\nu_{RF} = \nu_+ + \nu_-$. The electric field lines are shown in the right panel of Fig. 2.5. The electric field in the radial plane for a quadrupole configuration with frequency ω_q and phase ϕ_q is given by

$$\vec{E} = (y\hat{e}_x + x\hat{e}_y)A_q \cos(\omega_q t + \phi_q), \tag{2.19}$$

where the amplitude A_q is proportional to the voltage applied. The equation of the radial motion $\ddot{\vec{\rho}} = q/m(\vec{E_\rho} + \dot{\vec{\rho}} \times \vec{B})$ in cylindrical coordinates leads to the amplitude of the radial motions [16]:

$$\rho^{\pm}(t) = \left\{ \rho^{\pm}(0)\cos(\omega_B t) \mp \frac{1}{2} \frac{\rho^{\pm}(0)\,[j(\omega_q - \omega_c)] + \rho^{\mp}(0)k^{\pm}}{\omega_B} \times \sin(\omega_B t) \right\} e^{j(\omega_q - \omega_c)t/2}, \tag{2.20}$$

where $\rho^{\pm}(0)$ are the amplitudes of the radial eigenmotions at $t = 0$,

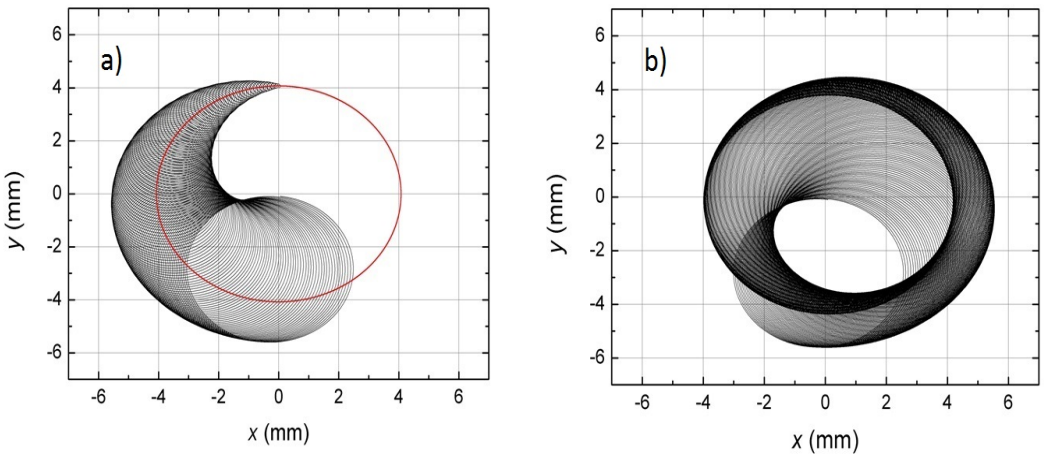

Figure 2.6: Simulation of an ion trajectory in a Penning trap where $B = 7$ T, when applying an external quadrupole field with a radiofrequency $\omega_q = \omega_c$. a) The motion of the ion is pure magnetron (red line) before excitation, and there is a gradual conversion to pure cyclotron (b).

$$\omega_{\mathrm{B}} = \frac{1}{2}\sqrt{(\omega_{\mathrm{q}} - \omega_{\mathrm{c}})^2 + k^2} \quad \text{and} \tag{2.21}$$

$$k^{\pm} = k e^{\pm j\Delta\phi}, \tag{2.22}$$

with $k = q\ A_{\mathrm{q}}\ /\ m\ (\omega_+ - \omega_-)$ and $\Delta\phi = \phi_{\mathrm{q}} - (\varphi_+ + \varphi_-)$. φ_+ and φ_- are the phases of the two radial motions. Since $\omega_+ \gg \omega_-$, the radial kinetic energy of a stored ion is given by

$$E_{\mathrm{r}}(t) = \frac{1}{2}m\left(\omega_+^2\rho^+(t)^2 + \omega_-^2\rho^-(t)^2\right) \approx \frac{1}{2}m\omega_+^2\rho^+(t)^2. \tag{2.23}$$

From Eqs. (2.20) and (2.23), and considering $\rho^+(0) = 0$, the radial kinetic energy reads

$$E_{\mathrm{r}} \propto \frac{\sin^2(\omega_{\mathrm{B}}\tau_{\mathrm{q}})}{\omega_{\mathrm{B}}^2}, \tag{2.24}$$

where τ_{q} is the excitation time. If $\omega_{\mathrm{q}} = \omega_{\mathrm{c}}$, the radius of the magnetron motion decreases while the one of the reduced-cyclotron motion increases. This conversion is shown in Fig. 2.6. From Eq. (2.20), one can obtain the time for a full conversion of the radial motion, which is given by [16]

$$\tau_{\mathrm{conv}} = \frac{\pi}{k} = \frac{\pi}{A_{\mathrm{q}}}\frac{m}{q}(\omega_+ - \omega_-). \tag{2.25}$$

This conversion is periodic, and therefore the ion motion is back to a pure magnetron motion when $\tau_{\mathrm{q}} = 2\tau_{\mathrm{conv}}$.

Quadrupole excitation with buffer gas

Buffer-gas cooling is a technique widely used to decrease the ion energy by collisions with atoms of an inert gas [50]. The interaction between any ion with the buffer-gas atoms can be described using a viscous-drag model. The ion experiences a force counteracting its motion, given by

$$\vec{F} = -\delta m\vec{v}. \tag{2.26}$$

The damping coefficient δ is given by

$$\delta = \frac{q}{m\mu_0}\frac{p/p_{\mathrm{N}}}{T/T_{\mathrm{N}}}, \tag{2.27}$$

where μ_0 is the ion mobility, p is the pressure, T is the temperature and, p_{N} and T_{N} are pressure and temperature in normal conditions, respectively. Incorporating this force to Eq (2.7), the amplitude of the eigenmotions can be expressed as

$$\rho^z(t) = \rho^z(0)e^{-\alpha_z t} \tag{2.28}$$

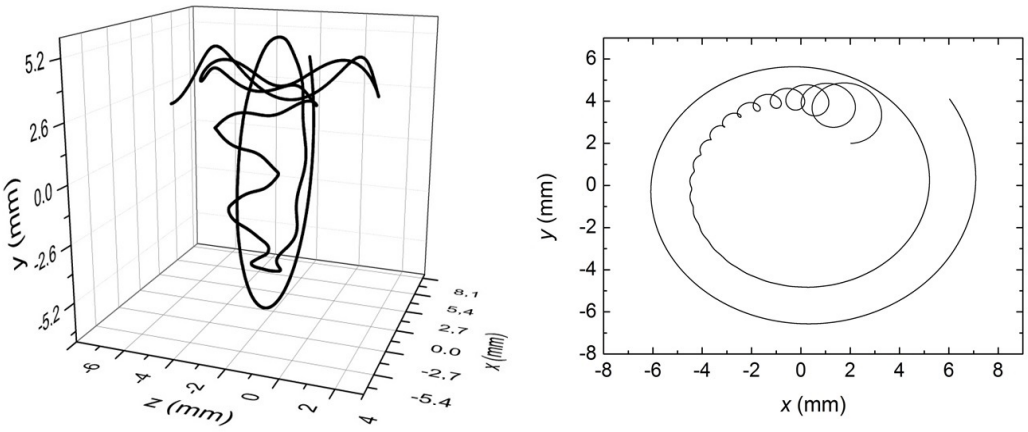

Figure 2.7: Simulation of the trajectory of a $^{40}Ca^{+}$ ion in a Penning trap (B = 7 T), filled with helium gas at a pressure of 10^{-6} mbar and a temperature of 298 K. Left: Ion trajectory in three dimensions. Right: Projection of the ion trajectory in the x-y plane. The radius of the magnetron motion increases.

$$\rho^{+}(t) = \rho^{+}(0)e^{-\alpha_{+}t} \tag{2.29}$$

$$\rho^{-}(t) = \rho^{-}(0)e^{+\alpha_{-}t} \tag{2.30}$$

where $\alpha_{\pm} = \delta\,\omega_{\pm}\,/\,(\omega_{+} - \omega_{-})$ and $\alpha_{z} = \delta\,/\,2$. From Eqs. (2.28), (2.29) and (2.30), it is possible to infer that the amplitudes of the axial and reduced-cyclotron motions of the ion decreases exponentially due to the buffer gas atoms, while, the amplitude of the magnetron motion increases. This effect is shown in Fig. 2.7.

Radiofrequency quadrupole excitation at $\omega_{q} = \omega_{c}$ allows coupling the radial motions of the ion, which originates a decrease in the amplitude of the radial eigenmotion in the presence of buffer gas, and, the ions are concentrated in the geometrical center. Figure 2.8 shows a simulation of the trajectory of a $^{40}Ca^{+}$ ion in a Penning trap filled with helium buffer gas, and applying a quadrupole field at $\omega_{q} = 2.689$ MHz with $V_{q} = 1$ V. The ions are not ejected from the trap if the radius of the radial motion is larger than the diaphragm behind the trap. Therefore, only one ion species will be ejected from the trap for a fixed value of the excitation frequency

$$\nu_{q} = \nu_{c} = \frac{B}{2\pi}\left(\frac{q}{m}\right)_{\text{Ion of interest}} \tag{2.31}$$

This method is known as mass-selective buffer-gas cooling [50], and it is used for high resolution for mass separation. Cooling results from experiments with several ions of interest for the project TRAPSENSOR will be shown in Chapter 6.

Collisions with electrons instead of neutral atoms have also been used as cooling mechanism for ions, protons or antiprotons in Penning traps [51]. Trapped

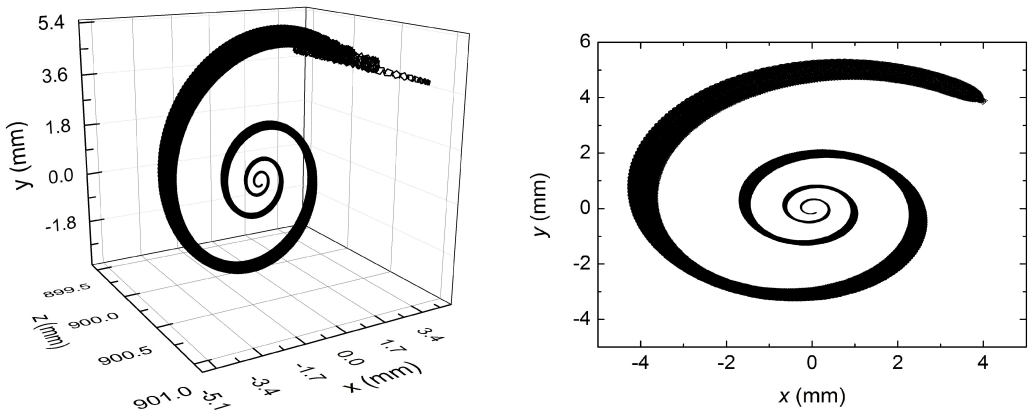

Figure 2.8: Simulation of the trajectory of a $^{40}Ca^{+}$ ion in a Penning trap (B = 7 T) filled with helium gas at 10^{-6} mbar at temperature of 298 K when applying a radiofrequency quadrupole field with $\omega_q = \omega_c$. Left: Ion trajectory in three dimensions. Right: Ion trajectory in the x-y plane.

electrons in a high magnetic field are self-cooled due to the radiation. The cyclotron energy of an electron in a Penning trap decreases as [43]

$$E_c = E_c(0)e^{-\alpha_c t}, \tag{2.32}$$

where

$$\alpha_c^{-1} = \frac{3\pi\epsilon_0 m_e^3 c^3}{e^4 B^2}, \tag{2.33}$$

and ϵ_0 is the permittivity in vacuum given by 8.854×10^{-12} C^2/N·m^2, and m_e and e are the mass and charge of the electron, respectively. Trapped ions are cooled via Coulomb interaction with the cold electrons.

Cooling via Coulomb interaction of ions with other ions, laser-cooled previously in the Penning trap, has also been studied [52]. Ions with an appropriate level structure can be laser cooled and used to cool other ions with a level structure not practicable with lasers. This mechanism allows reaching temperatures below 1 K for the ion of interest.

Axial-radial coupling by π pulse

Quadrupole excitation applied to the correction electrodes of the trap can also provide coupling between the radial and the axial motion of the ion. Coupling between the cyclotron and axial motion requires applying a pulsed excitation with a frequency equal to the sum of the eigenfrequencies, thus $\omega_p = \omega_+ + \omega_z$. The coupling strength is defined as [53],

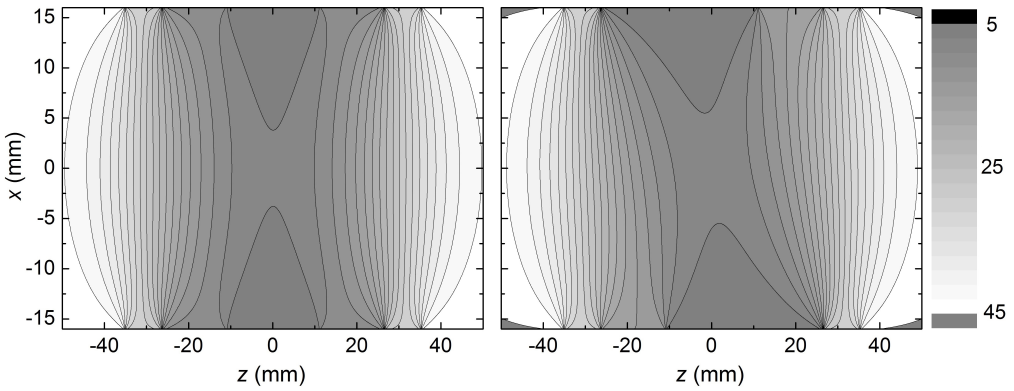

Figure 2.9: Longitudinal cut along the z-axis of a cylindrical trap with the equipotential lines in a harmonic potential (left) and a quadrupole field for axial-radial coupling (right). The potential is given in Volts.

$$V = \frac{q}{2m} \frac{j\zeta}{\sqrt{\omega_+ \omega_z}}, \tag{2.34}$$

where ζ is a complex amplitude of the coupling-field gradients arising from the coupling field, which, near the center of the trap, results in an oscillating quadrupole field tilted with respect to the static field

$$E_p = \mathrm{Re}\left(\zeta e^{i\omega_p t}\right)(x\hat{e}_z + z\hat{e}_x) \tag{2.35}$$

Figure 2.9 shows the equipotential lines resulting from a quadrupole field for axial-radial coupling along the z-axis in a cylindrical trap. The correction ring electrodes are split in two segments to apply the quadrupole excitation. The maximum amplitude of the ions in the axial direction will be obtained when the strength (V) and duration (τ) of the pulse are such that $\tau\ |V| = \pi$ and $\rho_z(0) \ll \rho_r(0)$.

Chapter 3

Accuracy and sensitivity in Penning-trap mass spectrometry: Different techniques

In a Penning trap, the mass of any ion is obtained by measuring the ions eigenfrequencies. Several methods can be used, depending on the accuracy to be reached. This chapter is devoted to describe systematic uncertainties and detection techniques in Penning traps. The maximum accuracy will be obtained with the highest sensitivity, i.e., using a single ion. Besides the well-known techniques, a novel method based on optical detection will be presented.

3.1 Systematic uncertainties in a Penning trap

The real Penning trap is subject to imperfections from the ideal configuration and deviations from a perfect superposition of the electrostatic and magnetic fields. This originates shifts in the eigenfrequencies of the ions in the trap and thus, systematic uncertainties, which must be quantified in order to perform accurate mass measurements. The most important sources for these uncertainties, which must be taken into account regardless the technique in use, are listed in the following [54].

Electric field imperfections

Electric field imperfections are originated from deviations from the ideal quadrupole field due to the holes in the trap electrodes for injection and extraction of the ions, or to the finite size of the electrodes with hyperbolical shapes. The shift in the cyclotron frequency is given by:

$$\Delta\omega_c^e = \frac{\omega_-}{1-\frac{\omega_-}{\omega_+}}\left[\frac{3}{2}\frac{C_4}{d_0^2}\left(\rho_-^2-\rho_+^2\right)+\frac{15}{4}\frac{C_6}{d_0^4}\left(\rho_-^2\left(\rho_z^2-\rho_-^2\right)+\rho_+^2\left(\rho_z^2+\rho_+^2\right)\right)\right], \quad (3.1)$$

where C_4 and C_6 are the coefficients of the octupole and dodecapole components of the electrostatic field. This kind of effect can be counteracted by building up a trap with a large d_0, by applying small U_{DC}, or by minimizing the higher multipoles of the electrostatic field.

The electric field imperfections introduce a relative mass uncertainty, which is mass independent if $\omega_+ \gg \omega_-$, and can be reduced by using, for the magnetic field determination, a reference ion with a mass close to that of the ion of interest. Another observable effect originated from imperfections of the electric field, important if one aims at reaching high precision, is the shift arising from the charge induced by the ions in the trap electrodes, which scales with d_0^3.

Misalignment of the trap with the magnetic field

Misalignment between the axis of the electrostatic quadrupole field and the magnetic field (see Fig. 2.2) originates a shift in the cyclotron frequency, which is related to the angle θ between $\vec{B}$ and $\vec{E}$, resulting in

$$\Delta\omega_{\mathrm{c}}^{d} = \frac{9}{4}\omega_{-}\sin^2\theta \tag{3.2}$$

Magnetic field imperfections

The Penning trap needs a high-homogeneity magnetic field, which should present high stability with time (higher if one aims at reaching better accuracy). Nowadays, a commercial superconducting magnet can reach an homogeneity of about 0.1 ppm in a volume of 1 cm^3. The frequency shift arising from the different magnetic field a stored ion experiences depending on the motional amplitude, is a function of the even power of the distance of the ion from the trap center. The lowest inhomogeneity is quantified by the magnetic hexapole, which leads to a frequency shift

$$\Delta\omega_{\mathrm{c}}^{m} = \beta_2\omega_{\mathrm{c}}\left(\rho_{\mathrm{z}}^2 - \rho_{-}^2\right), \tag{3.3}$$

proportional to the cyclotron frequency. This shift is mass dependent. β_2 is the relative strength of the hexapole component.

Space charge due to the storage of more than one ion

An external field has to be applied in order to determination the mass. This field will act on the center of mass of an ion distribution if several ions with the same mass-to-charge ratio are stored. Thus, the frequency obtained after excitation will be the center-of-mass frequency. Having more than one ion in the trap with different mass-to-charge ratios will also originates a frequency shift due to the

Coulomb interaction between the ions. This is an important reason for using a single ion to carry out ultra-accurate mass measurements. The use of a single ion is not always possible depend on the mass-to-charge ratio.

Other uncertainties

There are systematic uncertainties, originating from the specific detection technique. A detailed review for one Penning trap mass spectrometer can be found in Ref. [2]. It is important also to note that some effects can be counteracted by storing two ions simultaneously in the same trap and placing them in the same magnetron orbit [55].

3.2 Destructive detection techniques

The techniques included in this section are the so-called Time-of-flight Ion-Cyclotron-Resonance (TOF-ICR) and the Phase-Imaging Ion-Cyclotron-Resonance (PI-ICR). Using these methods one needs to extract the ions from the trap every measurement cycle.

3.2.1 Time-of-flight Ion-Cyclotron-Resonance

This method makes use of an external radiofrequency quadrupole field to modify the radial energy of the ions in the trap [16, 56]. This energy can be expressed as a function of the radiofrequency of the field (see Eq. (2.24)). In a magnetic field $\vec{B} = B\ \hat{e_z}$, the ion experiences a force in the axial direction due to its magnetic moment $\vec{\mu}(\omega_\mathrm{q})$, which reads

$$\vec{F}(\omega_\mathrm{q}, z) = -\nabla \left[\vec{\mu}(\omega_\mathrm{q}) \cdot \vec{B}(z)\right] = \mu(\omega_\mathrm{q}) \frac{\partial B}{\partial z} \hat{e}_\mathrm{z}. \tag{3.4}$$

Figure 3.1 shows schematically the configuration for the TOF-ICR method, where the trap is located in the high-homogeneous magnetic field region, and the detector in the region of vanishing magnetic field. The force given in Eq. (3.4) accelerates the ions, yielding a minimum time-of-flight when the magnetic moment is maximum. The time of flight as a function of the excitation frequency is given by

$$TOF(\omega_\mathrm{q}) = \int_{z_0}^{z_1} \sqrt{\frac{m}{2\left[E_0 - qV(z) - \mu(\omega_\mathrm{q})B(z)\right]}}\, dz, \tag{3.5}$$

where E_0 is the initial energy of the ions in the trap, $V(z)$ is the electric potential along the flight path, z_0 and z_1 are the position of the center of the trap and the detector, respectively. The determination of the cyclotron frequency of an ion, and thus its mass, is achieved by measuring the time of flight of the ion as a function of the excitation frequency. Figure 3.2 shows the theoretical line shape

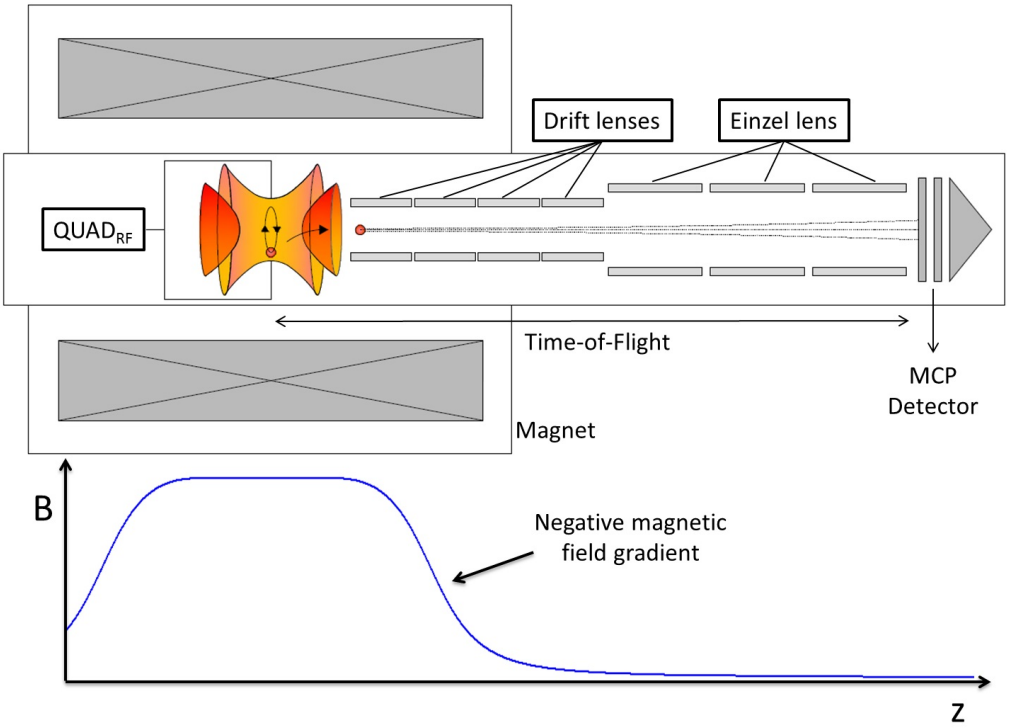

Figure 3.1: Sketch of the TOF-ICR detection setup and magnetic field strength along the z axis. The center of the trap is located in the high-homogeneity magnetic-field region provided by the magnet. The ions are ejected out of the trap towards the detector, and the amount of radial energy gained by the ions after they are probed with an external quadrupole field will be observed by measuring their time of flight.

of a time-of-flight cyclotron resonance. The line width $\Delta\nu_{\mathrm{FWHM}}$ of the deep in the center, defines the resolving power

$$\Re = \frac{\omega_c}{\Delta\omega_c} = \frac{\nu_c}{\Delta\nu_{\mathrm{FWHM}}} = \frac{m}{\Delta m}, \tag{3.6}$$

where $\nu_c = \omega_c \ / \ 2\pi$. The uncertainty in the determination of the frequency is given by [16]

$$\delta\nu \propto \frac{\nu_c}{\Re\sqrt{N_{\mathrm{ion}}}}, \tag{3.7}$$

where N_{ion} is the number of detected ions.

A variant of this technique utilizes the Ramsey scheme [57]. Two pulses with a duration τ_1 are used for the quadrupole excitation. These pulses are separated by a waiting time τ_0. The standard TOF-ICR technique corresponds to $\tau_0 = 0$. The theoretical line shape of a cyclotron resonance obtained using the Ramsey scheme for TOF-ICR is shown in Fig. 3.2. The radial energy is given by [58]

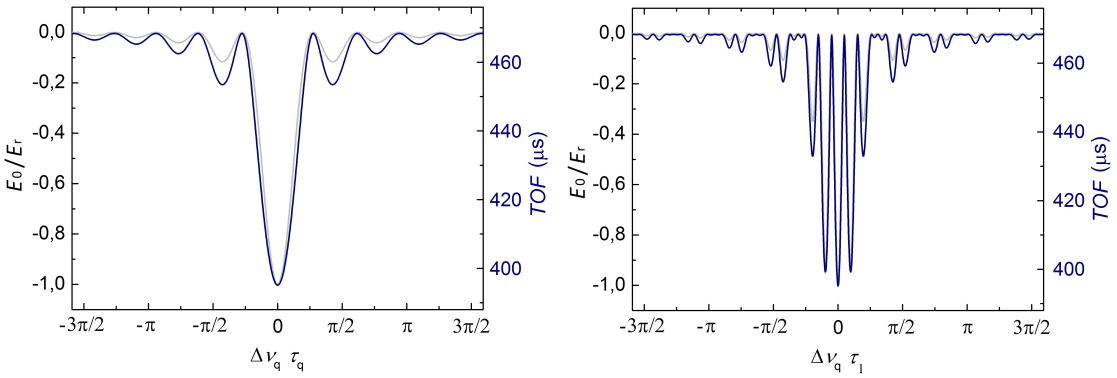

Figure 3.2: Radial energy gained by the ion and Time-of-Flight (right vertical axis) as a function of the detuning $\Delta\nu_\mathrm{q} = (\omega_\mathrm{q} - \omega_\mathrm{c})/2\pi$. Left panel: the theoretical line shape of a cyclotron resonance obtained by applying the TOF-ICR technique is shown blue, and the grey line depicts the radial energy when applying a pulse with duration τ_q and with $k = \pi/\tau_\mathrm{q}$. The radial energy is given by Eq. (2.24). Right panel: theoretical line shape of a cyclotron resonance in blue, obtained applying the Ramsey scheme with the TOF-ICR, i.e., using two pulses of duration τ_1 separated in time by τ_0, with $\tau_0 = 2\tau_1$. The grey line represents the radial energy gained by the ion for $k = \pi/2\tau_1$. The radial energy is given by Eq. (3.8).

$$E_\mathrm{r} \propto \frac{\sin^2(\omega_\mathrm{B}\tau_1)}{\omega_\mathrm{B}^2}\left[\cos\left(\frac{\delta\,\tau_0}{2}\right)\cos(\omega_\mathrm{B}\tau_1) - \frac{\delta}{2\omega_\mathrm{B}}\sin\left(\frac{\delta\,\tau_0}{2}\right)\sin(\omega_\mathrm{B}\tau_1)\right]^2, \quad (3.8)$$

where ω_B was defined in Eq. (2.21) and $\delta = (\omega_\mathrm{c} - \omega_\mathrm{q})$. Mass measurements using this technique has reported a threefold-gain in precision with respect to the TOF-ICR method [59].

The standard TOF-ICR method and its variant, the Ramsey TOF-ICR technique, are widely used in high-precision Penning-trap mass spectrometry, and mass measurements with a relative mass uncertainty ($\delta m/m$) in the order of 10^{-9} have been reported. Several tens of ions are needed to measure the mass of an isotope, thus it is not possible the application of this technique to nuclides produced with a very low rate. The limit of the technique was obtained for ^{256}Lr with a detection rate of 0.5 ions per hour [9].

3.2.2 Phase-Imaging Ion-Cyclotron-Resonance

The radial eigenfrequencies are determined from the phases of the ion motions, by registering the impact position of the ion in a position-sensitive detector, after they are extracted from the trap [60]. An external radiofrequency dipole field is used to excite the magnetron and reduced-cyclotron frequencies (see Sec. 2.3). Figure 3.3 depicts the radial positions of the ions in the trap. The green and blue circles represent the position of the ions before and after the excitation,

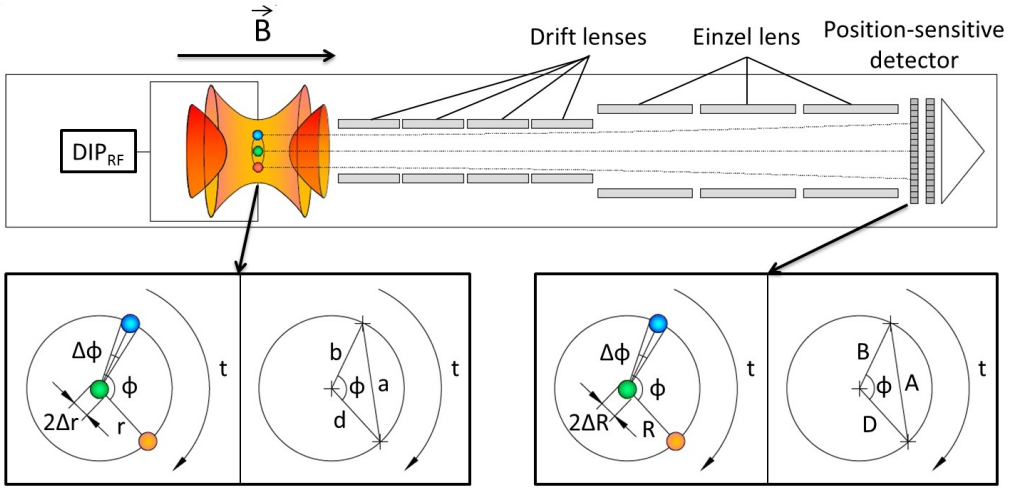

Figure 3.3: Top: Sketch of the experimental setup for phase-imaging ion-cyclotron-resonance detection. The ions are ejected out of the trap to a high-resolution position-sensitive detector. Bottom: The radius and two phases of the ions radial motion are shown, in the trap and how they are observed with the detector.

respectively. The radial position (phase) of the ion after a time t is represented by the orange circle. For the reduced-cyclotron excitation, a π-pulse at ν_c is required to exchange this motion to a pure magnetron one. The frequency of any radial motion is given by

$$\nu = \frac{v_r}{2\pi r} = \frac{\phi + 2\pi n}{2\pi t}, \tag{3.9}$$

where v_r is the radial velocity, r is the radius of the ion orbit, ϕ is the phase of the ion motion and n is the number of full revolutions. Taking the cosines law for the sides of the triangle a, b and d of Fig. 3.3, one obtains the relationship $a^2 = b^2 + d^2 - 2bd\cos\phi$. Defining $\phi = \arccos(\varphi)$ for $0 \leq \phi \leq \pi$ and $\phi = 2\pi$ - $\arccos(\varphi)$ for $\pi \leq \phi \leq 2\pi$, the uncertainty in the frequency results in

$$\delta\nu = \frac{\delta\varphi}{2\pi t\sqrt{1-\varphi^2}}. \tag{3.10}$$

The radial position (phase) of the ions in the trap, can be measured by ejecting the ions out, and registering them with a position-sensitive detector. In the ideal case, the angle ϕ will be preserved. Assuming $B = D = R$, when $R = R_-$ and $R = R_+$, and $\Delta R = \Delta R_-$ or ΔR_+, the uncertainty for each radial frequency can be expressed as

$$\delta\nu \approx \frac{1}{\pi t\sqrt{N_{\text{ion}}}} \times \frac{\Delta R}{R}. \tag{3.11}$$

Considering $\omega_+ \gg \omega_-$, the resolving power is

$$\Re = \frac{\omega_c}{\Delta\omega_c} \approx \frac{\pi\nu_+ t R_+}{\Delta R_+}. \tag{3.12}$$

Mass measurements with a 40-fold increase in resolving power, compared with the TOF-ICR technique using the Ramsey scheme, have been reported, and this would allow to decrease the time needed for the measurement by a factor of 25 [17]. This is an excellent option for the determination of masses of very short-lived nuclides, provided that a few tens of ions are detected.

3.3 Non-destructive detection techniques

The techniques included in this section are the so-called Induced Image Current (IIC) and the novel Quantum Sensor (QS) method. In both cases, the ions remain in the trap. The mass of the ion, is obtained directly from the frequency ν_c, which is determined after measuring the three eigenfrequencies and applying the invariance theorem (Eq. (2.17)).

3.3.1 Induced Image Current (IIC) detection

The charge induced by an ion with electronic charge q is given, as a function of the position x by [61]

$$Q_i(x) = -q\frac{\Delta\psi(x)}{\Delta U}, \tag{3.13}$$

where $\Delta\psi(x)$ is the change of potential in x due to a voltage change ΔU at the electrodes. In the case of two infinitely extended parallel flat electrodes separated by d, with voltages $-V_0$ and V_0, the induced charge is

$$Q_i(x) = -q\frac{x}{d}, \tag{3.14}$$

and the current flowing through an external circuit attached to the electrodes is given by [62],

$$i = \frac{dQ_i(x,t)}{dt} = -\frac{q}{d}\frac{dx}{dt} = 2\pi q\frac{x(t)\nu}{d}, \tag{3.15}$$

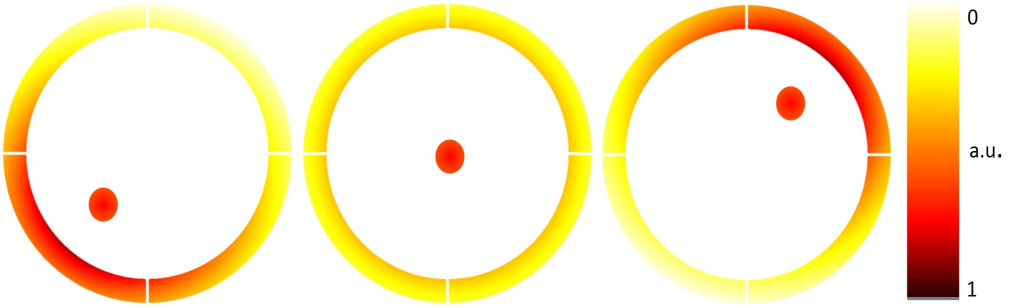

Figure 3.4: Transversal cut in a cylindrical trap showing a stored ion at different positions. The charge density in the trap electrodes as a function of the position of the ion is shown on the color palette on the right. The charge becomes an oscillating current due to the motion of the ion.

where ν is the frequency of the ion motion. Figure 3.4 shows the charge-density distribution of an ion at different positions in the radial plane of a cylindrical trap. The current induced is very small, so that several amplification stages are needed, depending on the mass-to-charge ratio (m/q) and on the number of ions with the same m/q available in the trap. If several hundred of ions from different species are stored, the so-called broad-band detection will be used. For ultra-accurate mass measurements, only one ion must be used at a time in the trap. In this case, the amplification needs to be larger but this will be only possible in a narrower band. Figure 3.5 shows the IIC detection scheme, particularly to measure the reduced-cyclotron frequency for broad and narrow band. This variant of the IIC technique is known as Fourier-Transform Ion-Cyclotron-Resonance (FT-ICR) [63].

Broad-band IIC detection

In broad-band, ions with different mass-to-charge ratios are excited by applying an external dipole field varying the radiofrequency such that it matches ν_+ for the different ion species during the time the field is applied [64]. The current I induced by the ions in the trap electrodes is amplified and a Fourier analysis is applied, yielding a frequency spectrum with maximums at the ν_+ frequencies of the different ions stored in the trap. The current induced regardless the geometry of the trap, is given by

$$I_{\text{eff}} = \frac{i}{\sqrt{2}} = \frac{\sqrt{2}\,\pi\,q\,\nu\,\rho}{D_{\text{eff}}}, \tag{3.16}$$

where ρ is the amplitude of the ion motion, and $D_{\text{eff}} = \epsilon z_0$ is the so-called effective distance in the trap, where z_0 is the distance between the center of the trap and one endcap, and ϵ is a geometrical factor to account for the deviation of the geometry of the trap from the consideration of two parallel plates [65]. The limit

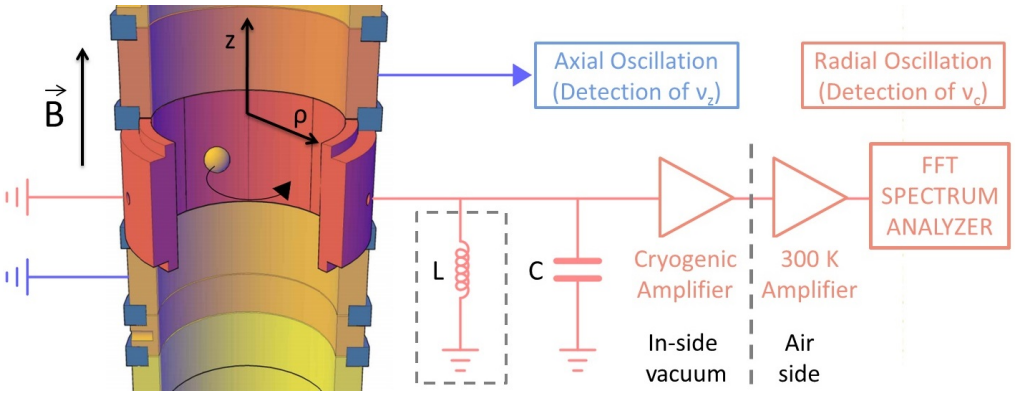

Figure 3.5: Amplification stages for IIC detection. This scheme is particularly used for FT-ICR. For the detection of the axial motion in the cylindrical trap, an electronic circuit should be attached to the corrections electrodes (orange electrodes). For narrow-band detection, a resonant circuit has to be added, which is inside the grey box. For further details see text.

in sensitivity when the trap is operated at room temperature, is around 1000 ions, but this depends on the mass-to-charge ratio [66]. The resolving power for high mass-to-charge ratios is around 10^6.

Narrow-band IIC detection

The frequency, and thus the mass of a single ion can be measured accurately by introducing an inductive circuit in resonance with any of the ion motions, as it is shown in Fig. 3.5 particularly for FT-ICR. This circuit should have a high quality factor Q to increase the voltage signal originated by the current induced ($\approx$ 10 fA). The circuit is generally made of an inductance L, coupled to the parasite capacity C of the trap electrodes in order to obtain a parallel resonance LC circuit, providing an impedance

$$Z_{\mathrm{LC}}(\omega) = \frac{1}{\frac{1}{R} - j\left(\omega C - \frac{1}{\omega L}\right)}, \tag{3.17}$$

where R is the resistance. The impedance $|Z_{\mathrm{LC}}(\omega)|$ has a maximum for a frequency ω_{LC}, which is given by

$$\omega_{\mathrm{LC}} = \frac{1}{\sqrt{LC}}. \tag{3.18}$$

The width $\Delta\omega$ defines an important parameter of the circuit called the quality factor

$$Q = \frac{\omega_{LC}}{\Delta\omega}. \tag{3.19}$$

From the relationship $|Z(\omega)/Z(\omega_{\mathrm{LC}})| = 1/\sqrt{2}$, the quality factor can be expressed as

$$Q = \frac{R}{\omega_{\mathrm{LC}} L} = R\omega_{\mathrm{LC}} C. \tag{3.20}$$

The voltage signal of the circuit in resonance, i.e., when $Z(\omega_{\mathrm{LC}}) = R$, is given by

$$S = RI_{\mathrm{LC}} = \frac{1}{\sqrt{2}} \frac{\rho}{D} \frac{q}{C} Q, \tag{3.21}$$

and the thermal noise of the circuit by [67]

$$N = \sqrt{4k_{\mathrm{B}} T R \Delta\nu}, \tag{3.22}$$

where k_{B} is the Boltzmann´s constant and T the temperature. Finally, the signal-to-noise ratio is given by

$$\frac{S}{N} = \frac{\sqrt{\pi}}{2} \frac{\rho}{D} q \sqrt{\frac{\nu}{\Delta\nu}} \sqrt{\frac{Q}{k_{\mathrm{B}} T C}}. \tag{3.23}$$

Reducing the temperature of the circuit allow decreasing the thermal noise and thus improving the sensitivity [68]. The dependence of S/N on the motional frequency makes difficult measurements on ions with high mass-to-charge ratios. Using this technique, the relative frequency uncertainty results in

$$\frac{\delta\nu}{\nu} \approx \frac{1.1}{\nu\tau_{\mathrm{m}}}, \tag{3.24}$$

where τ_{m} is the sampling time. The application of the narrow-band IIC technique using a cryogenically-cooled (at 4.2 K) high-Q inductor, has yielded precise mass values for ions with low and medium mass-to-charge ratios, reaching relative mass uncertainties in the order of 10^{-11} [2, 19, 20].

The performance of the different techniques is summarized in Tab. 3.1.

Table 3.1: Performance of Penning-trap techniques for mass spectrometry. (1) The uncertainty in the determination of the mass depends of the number of ions and the measurement time (see Eq. (3.7) and (3.11)). (2) The signal-to-noise ratio increases with the number of ions.

Technique	$\delta m/m$	Sensitivity	m/q	Measurement time
TOF-ICR	$10^{-9}/10^{-8}$	$\approx$ 50 ions (1)	–	$\approx$ 200 ms (1)
PI-ICR	$10^{-10}/10^{-9}$	$\approx$ 20 ions (1)	–	$\approx$ 10 ms (1)
Broad-band IIC	10^{-6}	$\approx$ 1000 ions (2)	low/medium	$\approx$ 10 ms
Narrow-band IIC	10^{-11}	1 ion	low/medium	$\approx$ 5 min

3.3.2 The Quamtum Sensor (QS) technique

The QS technique was conceived to overcome the current limitations in single-ion Penning-trap mass spectrometry, aiming at extending the applicability to the detection of ions with medium and high mass-to-charge ratios. A detailed study of this technique and the application to mass spectrometry is shown in Ref. [34]. The method is based on a previous idea presented in 1990 by Heinzen and Wineland [35]. A laser-cooled (sensor) ion is used as detector, instead of a resonant LC circuit. The sensor ion is stored in a trap and connected to the ion of interest through the charges the two ions induce in a common endcap electrode. Figure 3.6 shows equivalent citcuits to compare the IIC and the QS methods.

The measurement sequence using the QS technique is shown in Fig. 3.7. There are four important steps. (1) The sensor ion is laser-cooled to mK temperatures. The oscillation frequencies of the two ions are tuned to be equal, the ions are coupled, and thus, the axial motion of the ion of interest is damped through the sensor ion. (2) The radial motion of the ion of interest is excited, by means an

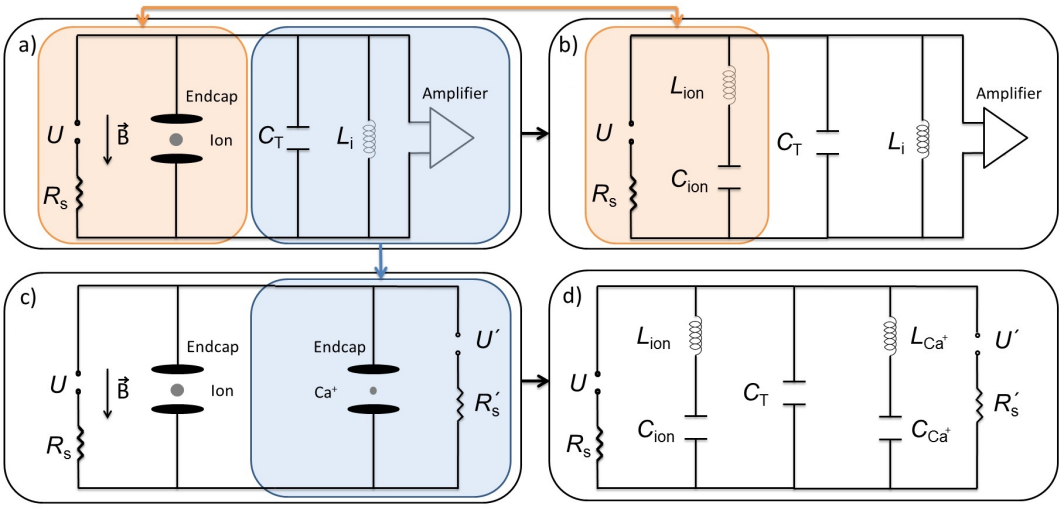

Figure 3.6: Equivalent circuits for IIC and QS detection. (a) Sketch of a Penning trap attached to the DC voltage source and to a parallel LC circuit. Two parallel discs represent the Penning trap. C_T is the parasite capacitance of the trap. (b) Electronic-circuit equivalent of a trapped ion in a Penning trap. The ion is represented by an inductance L and a capacitance C in series (inside the orange square box). (c) The resonance circuit in (a) is exchanged with a $^{40}Ca^+$ ion stored in another Penning trap (inside the blue square box). The two traps have a common endcap electrode. (d) Equivalent circuit for two ions coupled but stored in different traps.

external radiofrequency field, to measure a motional frequency. The conversion of the radial motion to axial after excitation is accomplished by applying a π-pulse (see Sec. 2.3). During this time, the switch is closed so that the endcaps are grounded. (3) The ion of interest transfers its axial energy, gained in the excitation and conversion process, to the sensor ion. The laser beams are blocked and the switch is opened. (4) After energy exchange, the laser beams interact with the sensor ion and the amount of energy gained in (3) is observed by monitoring the fluorescence light. This energy can be quantified as a function of the time needed to reach the maximum fluorescence after energy exchange. The most critical aspect of this technique is the interaction between the two ions in different traps (Fig. 3.6.c), something that it has not been accomplished yet. The axial oscillation of the ions in the traps due to the potential induced in the common electrode can be modeled as a forced oscillator, i.e., following the equation

$$\frac{d^2z}{dt^2} + \omega_z^2 z = \frac{F_0}{m}\sin(\omega_z t)\,, \tag{3.25}$$

which has the solution

$$z(t) = bt\cos(\omega_z t + \phi_z)\,, \tag{3.26}$$

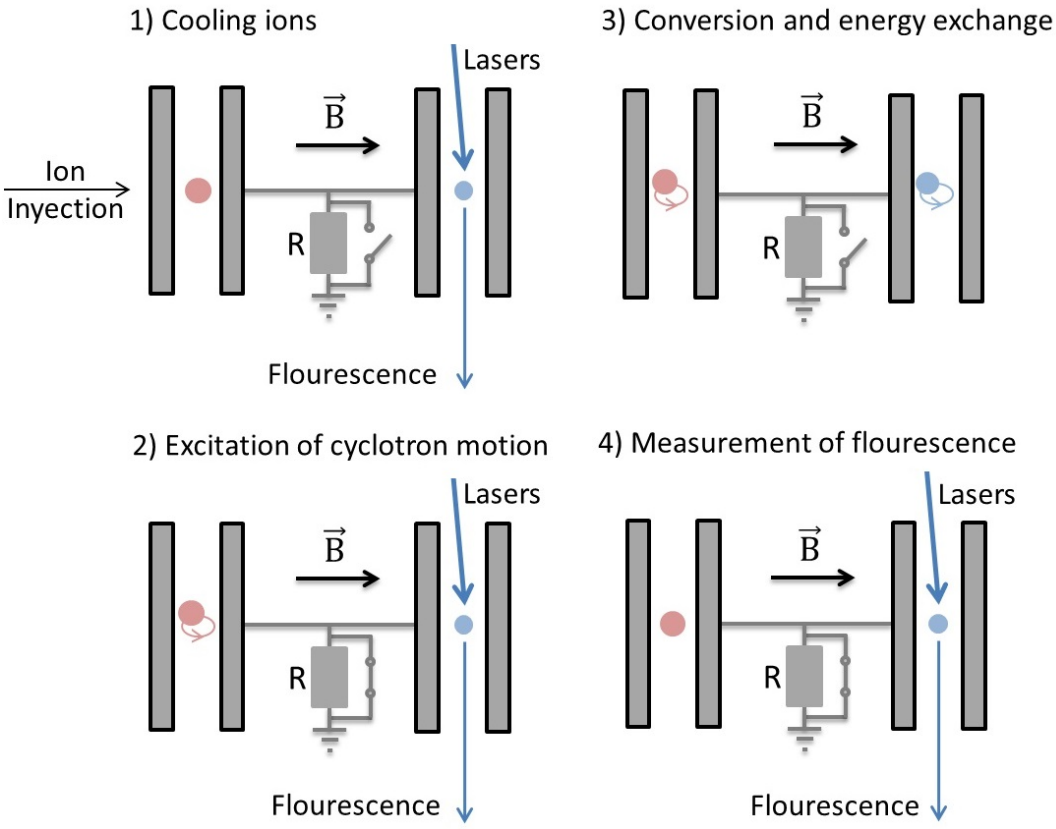

Figure 3.7: Measurement sequence using the QS technique. The ion of interest is represented by a red circle while the sensor ion is depicted by a blue one. Both traps are connected to ground via a large resistance R when a switch, in parallel with R, is opened. When the switch is closed, the two endcaps are connected to ground. Red and blue lines depict the laser beams and another blue line represents the fluorescence light from the sensor ion. Further details are given in the text.

where $b{=}F_0/(2m\omega)$. Since electric field imperfections originates axial frequency shifts, a good harmonic potential and a small amplitude of the axial motion are requested for better precision. The axial frequency shift is given by (see e.g. [69])

$$\Delta\nu_z = \frac{3qC_4k_BT}{16\pi^4m^2\nu_z^3}. \tag{3.27}$$

An important parameter in this respect is the time needed for the energy exchange between the $^{40}Ca^+$ ion and the ion of interest. Considering $U = U' = 0$ (Fig. 3.6), this time is given by [35]

$$t_{ex} = 2\pi^2\nu_z C\sqrt{L_{ion_1}L_{ion_2}}, \tag{3.28}$$

where C is the total capacitance, ν_z is the axial frequency and L_{ion} is defined as

Table 3.2: Time for energy exchange for different ion pairs. The axial frequency has been fixed to 100 kHz in order to reduce the time for energy exchange. $D_{\text{eff}} = 1.25$ mm, and $C = 0.5$ pF.

Ion-pair	Exchange time
$^{1}\text{He}^{+}$ - $^{40}\text{Ca}^{+}$	0.6 s
$^{40}\text{Ca}^{+}$ - $^{40}\text{Ca}^{+}$	4.0 s
$^{187}\text{Re}^{+}$ - $^{40}\text{Ca}^{+}$	8.7 s
$^{187}\text{Re}^{++}$ - $^{40}\text{Ca}^{+}$	4.3 s

$$L_{\text{ion}} = m \left(\frac{D_{\text{eff}}}{q} \right)^2 . \tag{3.29}$$

Smaller values of L_{ion}, or trap size, result in smaller values of t_{ex}. Values of this parameter for different ion pairs is shown in Tab. 3.2.

A successful completion of the QS technique will allow single-ion detection and high-performance mass spectrometry on ions with any mass-to-charge ratio. Since the $^{40}\text{Ca}^{+}$ ion is laser-cooled to mK temperature, small oscillations amplitudes can be observed already without moving the ion into large orbits. Such a system, however, needed a complex infrastructure including lasers, ion production and beam preparation, if later one applied the technique for exotic ions.

3.3.3 Applications of mass values

Table 3.3 shows the relative mass uncertainty required to use mass values for several applications and the most appropriate technique in each case. The relative mass uncertainty requested can vary from 10^{-6}, for molecules or isotope identification, to below 10^{-11}, for neutrino mass measurements (see e.g. [13, 32, 70]). For exotic nuclides the half-live will limit the observation time and this also restricts the technique to be used.

Table 3.3: Applications of mass values with the techniques to be used. The relative mass uncertainties required are also shown. (1) Highly-charged ions.

Field	Sub-field	Mass Uncertainty	Appropriate technique
Chemistry	Identification of molecules	10^{-5} - 10^{-6}	Broad IIC
Nuclear structure physics	Shell and Sub-shells, deformations, halos, δV_{pn}, S_{2p}, S_{2n}, SHEs	10^{-6} - 10^{-8}	TOF/PI-ICR
Nuclear models and mass formulas	IMME	10^{-6} - 10^{-8}	TOF/PI-ICR
Astrophysics	(r)-process, (rp)-process, waiting point nuclides	10^{-7}	TOF/PI-ICR
Weak interactions studies	CVC hypothesis, CKM matrix unitary	10^{-8}	TOF/PI-ICR
Fundamental constants	Fine-structure constant	10^{-9}	IIC/QS
Metrology	Silicon mass	$< 10^{-9}$	IIC/QS
Neutrino physics	$0\nu\beta\beta$, 0ν2EC Neutrino mass	10^{-8} - 10^{-9} $< 10^{-11}$	PI-ICR/IIC/QS IIC(1)/QS
CPT Test	m_p and $m_{\bar{p}}$	$< 10^{-11}$	IIC/QS

Chapter 4

The TRAPSENSOR facility

The TRAPSENSOR facility has been built within this thesis work at the University of Granada. The project is funded by the European Research Council (ERC) and by the Spanish Ministry of Economy and Competitiveness. The facility comprises a Penning-traps beamline, a complex laser system and a Paul trap test bench to study the Doppler cooling of the $^{40}Ca^{+}$ (sensor) ion.

4.1 The Penning-traps beamline

A two dimensional technical drawing of the Penning-traps beamline is shown in Fig. 4.1. The ions are produced by means of a commercial MALDI-TOF apparatus adapted for this experiment. The acronyms MALDI-TOF stands for Matrix-Assisted-Laser-Desorption-and-Ionization Time-Of-Flight. A pulsed laser is used for desorption and ionization. This technique is widely utilized in mass identification of ions from chemical compounds [71, 72]. This device will be referred in this manuscript as laser-desorption ion source. The laser-desorption/ionization method allows producing ions of alkaline earth and transition metals with positive [73] or negative polarity [74].

After production, the ions are transported towards the Penning-traps system through a first time-of-flight (tof) and a transfer section comprised of an electrostatic quadrupole, two beam steerers and fifteen electrostatic lenses. The ion beam can be monitored at the entrance of the transfer section with a micro-channel plate detector. The Penning-traps system is housed in the bore of a 7-T superconducting magnet. The system consists of a preparation Penning trap with cylindrical geometry and a novel Penning-trap made of rings with an open geometry [75] for first experiments. This trap will be replaced later by a double Penning-(micro)-trap system [76, 77]. A Time-Of-Flight (TOF) section for identification and measurements made of nine electrostatic lenses to accelerate and focus the ions into a micro-channel plate detector is located downstream from the second Penning trap. Figure 4.2 shows three dimensional technical drawings of the different parts of the beamline, and Fig. 4.3 shows the beamline indicating the trajectory on an ion [78].

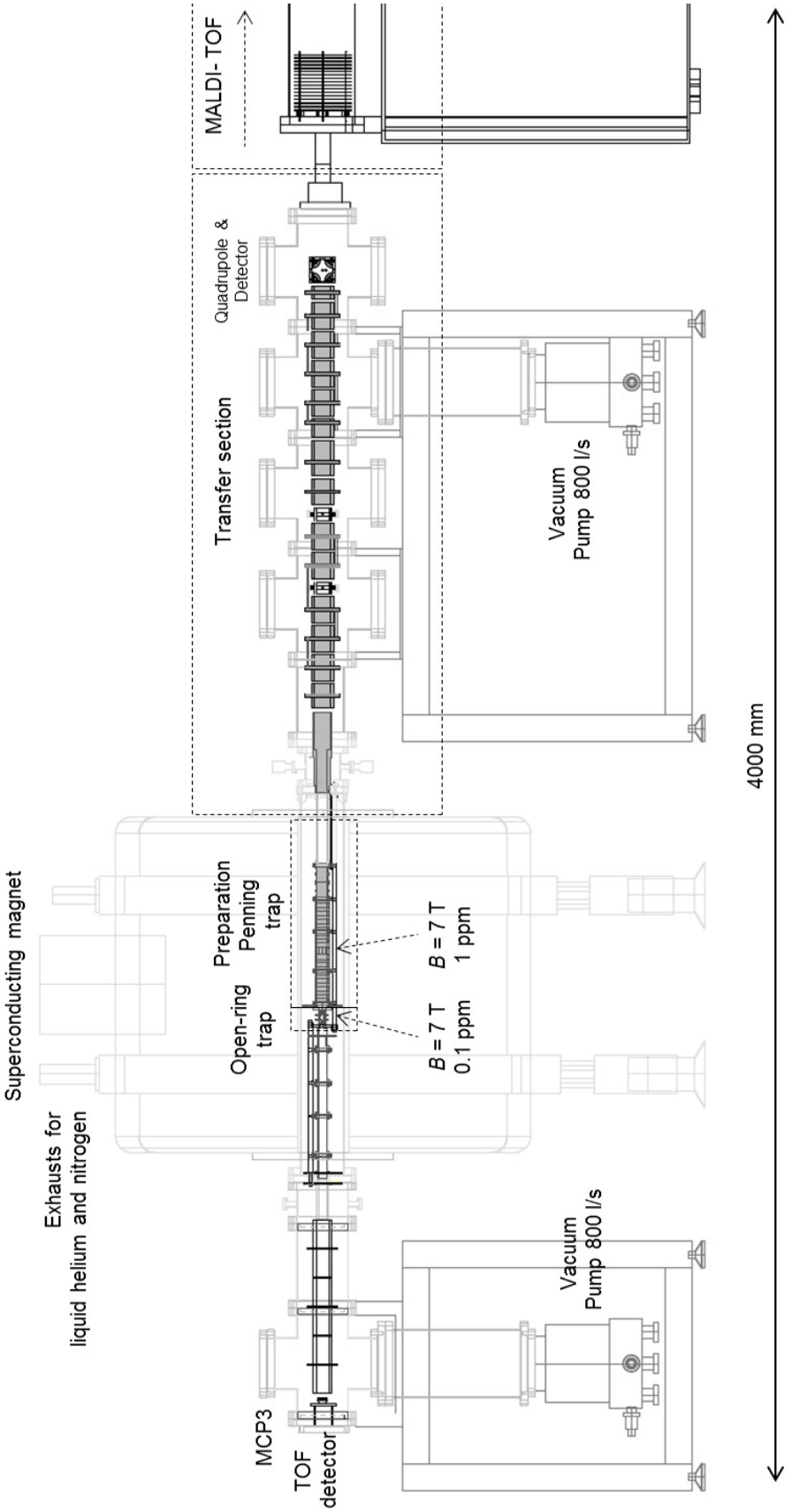

Figure 4.1: Technical drawing of the Penning-traps beamline of the TRAPSENSOR facility. See text for details.

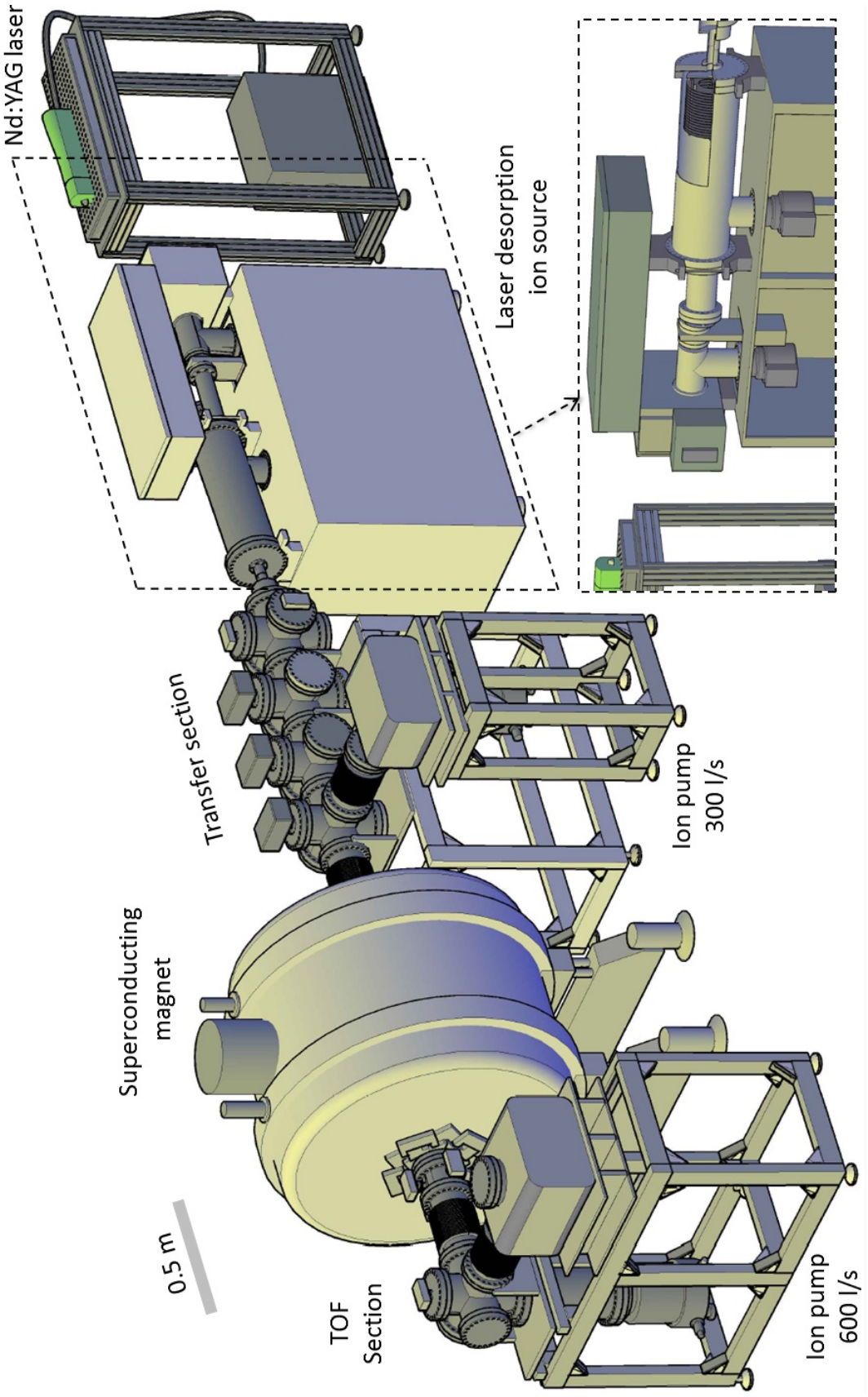

Figure 4.2: Three-dimensional technical drawing of the Penning-traps beamline of the TRAPSENSOR facility. See text for details.

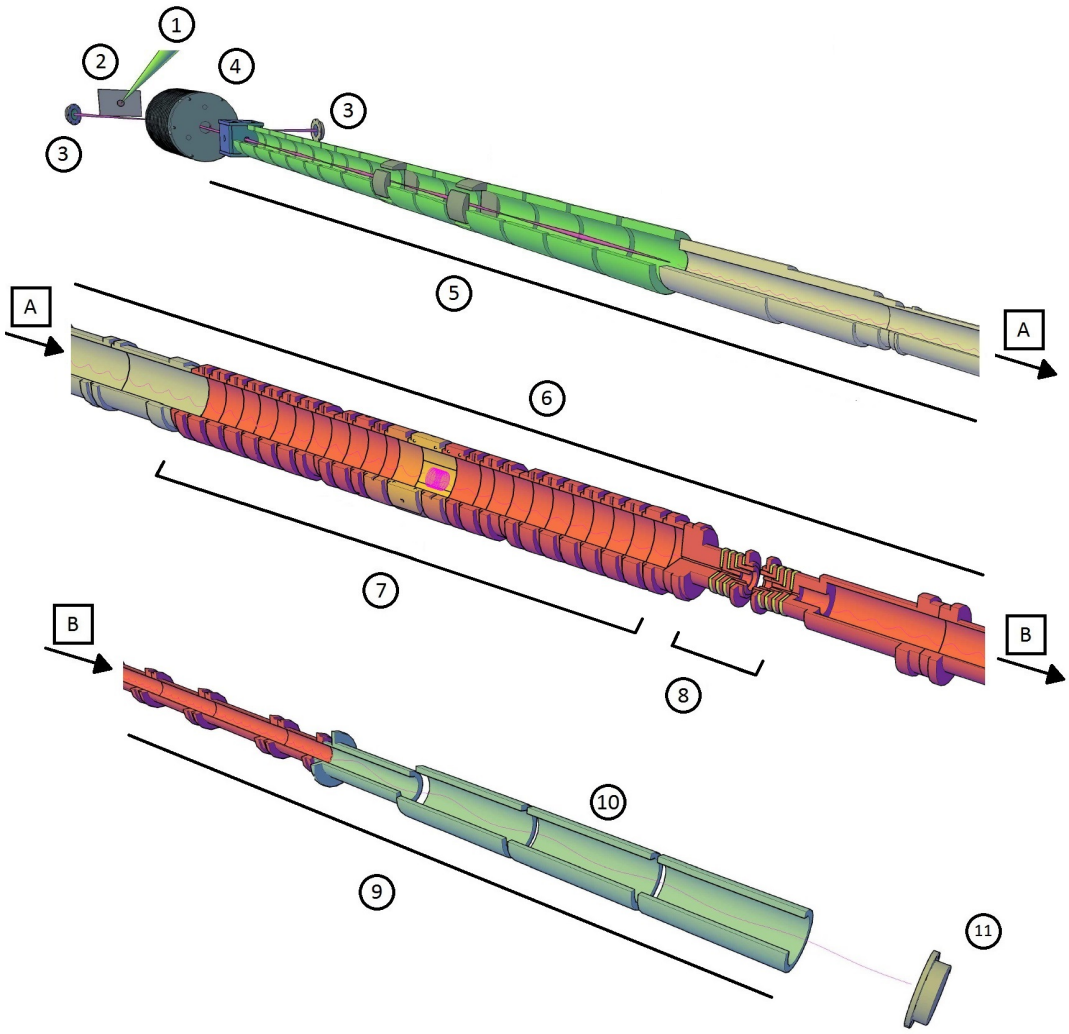

Figure 4.3: Three dimensional drawing showing the different parts of the Penning-traps beamline built up in the framework of the project TRAPSENSOR. A possible trajectory for the ions has been drawn in magenta. The beamline has a total length of 5.6 m. Note that some parts are not to scale. The main elements are: 1) pulsed laser beam for desorption, 2) holder plate with the target, 3) micro-channel plate detectors for *tof* analysis of the ion beam from the source, 4) electrostatic lenses in the time-of-flight region of the laser-desorption ion source, 5) transfer section, including deflectors and electrostatic lenses, 6) elements in the superconducting-magnet bore, 7) preparation Penning trap, 8) Open-ring trap 9) TOF section for identification, 10) electrostatic lenses of the TOF section and 11) micro-channel plate detector for the measurements presented in this thesis. The figure has been adapted from Fig. 1 in Ref. [78].

4.1.1 The laser-desorption ion source

The laser desorption ion source is shown in Fig. 4.4. The laser system is a Nd:YAG (Neodymium: Yttrium Aluminum Garnet) *Q-switch* laser (see e.g. [79])

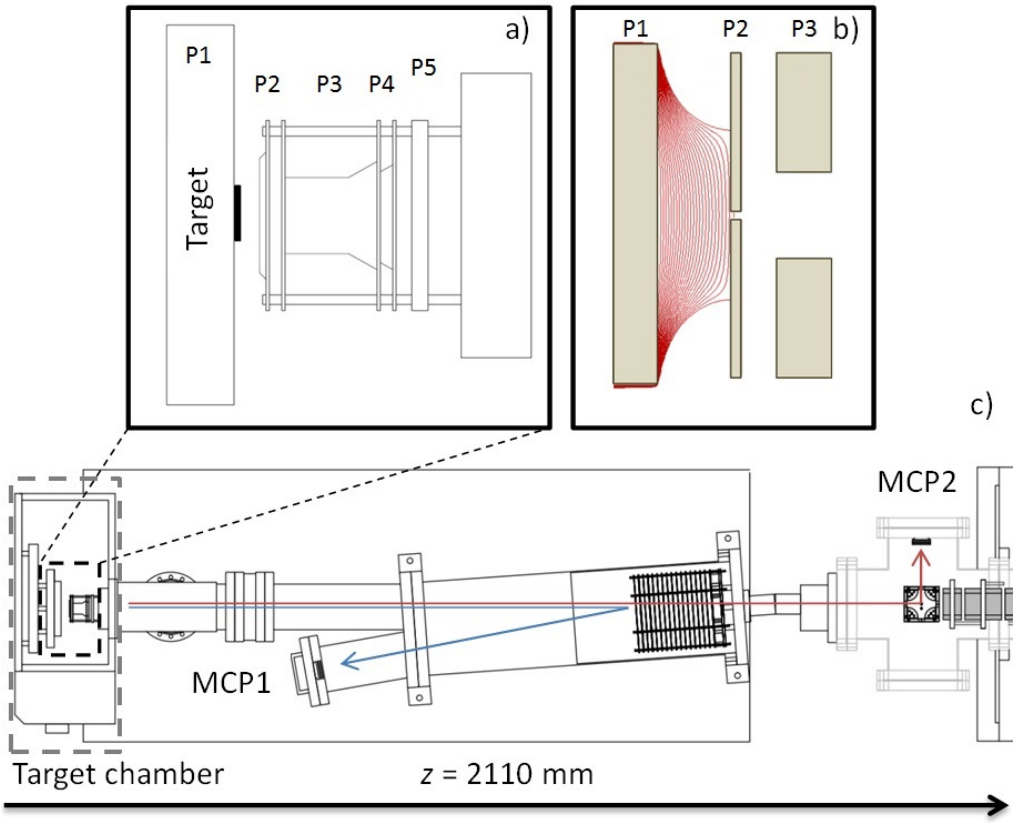

Figure 4.4: Bottom: Top view of the laser-desorption ion source and *tof* identification system, coupled to the first CF160 vacuum cross in the transfer section. The blue and red lines indicate the ions trajectory in the so-called reflectron and linear mode, respectively. The electrostatic quadrupole in the CF160 chamber deflects the ion beam onto a micro-channel plate detector MCP2. Top: magnification of the ion creation and extraction regions a) CAD drawing and b) Equipotential lines between electrodes P1 and P2 simulated with SIMION® version 8.0.

(Quantel model Brillant) which emits at a wavelength of 1064 nm, which is frequency doubled to $\lambda = 532$ nm. The repetition rate of the laser beam is 20 Hz with a pulse width of 4 ns. The maximum average power of the laser is 4 W with a maximum energy per pulse of 200 mJ. Table 4.1 shows the energy of the laser beam for several values of the Q-switch delay. A telescopic system composed of two optical lenses is used to focus the laser beam on the target. One lens of the telescopic system is mounted on a lineal motor with remote control to vary the size of the laser spot on the sample, normally having a diameter of about 1 mm. A small fraction of the beam is directed into a photodiode to generate the signal to trigger the measurement process.

The chamber housing the target is a customized vacuum vessel made of stainless steel with rectangular shape and dimensions 400 mm × 220 mm × 320 mm. The target is fixed in a plate (see Fig. 4.4), and a CF16 viewport allows entering

Table 4.1: Laser energy and counts per second for several Q-switch delay values. A power meter was located at the viewport in front of the target. The count rate is for rhenium ions.

Q-Switch delay (μs)	Energy (mJ)	Count rate
320	0.30 ± 0.03	0
310	0.81 ± 0.05	4
300	1.47 ± 0.07	118
290	1.75 ± 0.07	34
280	2.10 ± 0.10	139
270	3.90 ± 0.30	586
260	6.50 ± 0.30	1187

the laser beam into the vacuum vessel. This rectangular chamber can be vented separately from the rest of the system using a high-vacuum valve (VAT F10) enabling the exchange of the target without disturbing the rest of the system. The holder plate can be moved with a motor in X and Y directions allowing for the use of different targets. This motor is controlled in step sizes of 400 μm using a program made in the course of this work with LabVIEW™.

The ions are transported from the target chamber to the transfer section trough the *tof* tube (see Fig. 4.4.c). This is a CF40 to CF200 tube made of 304L stainless steel, 1600 mm long. A set of 19 lenses is placed inside of this tube. These lenses are plates of 2 mm thickness, with a hole of 90 mm diameter. In reflectron mode, the ion beam is reflected towards MCP1, by applying the proper DC-voltages to the lenses. In linear mode, the lenses are grounded and the ion beam continues towards the transfer section.

Figure 4.4.a shows the electrodes of the laser-desorption ion source in the region where the ions are created. The electrode P1 (holder plate) defines the kinetic energy of the ions, the electrodes P3 and P5 are grounded and the electrode P4 is biased to a DC potential. Extraction is accomplished by switching the electrode P2. This technique is known as Pulse Ion Extraction [80] and the voltage applied to P2 is switched between the voltage applied to P1 and ground. An electric-field is generated between P1 and P2. This kinetic energy reads

$$K = \frac{mv^2}{2} = zeV \approx eV_{\mathrm{P1}}, \tag{4.1}$$

where m is the mass of the ion, v is the velocity, ze the electronic charge in Coulombs, and V_{P1} is the voltage applied to P1.

The resulting time-of-flight is given by

$$tof = s\sqrt{\frac{m}{2zeV}} \approx s\sqrt{\frac{m}{2eV_{\mathrm{P1}}}}, \tag{4.2}$$

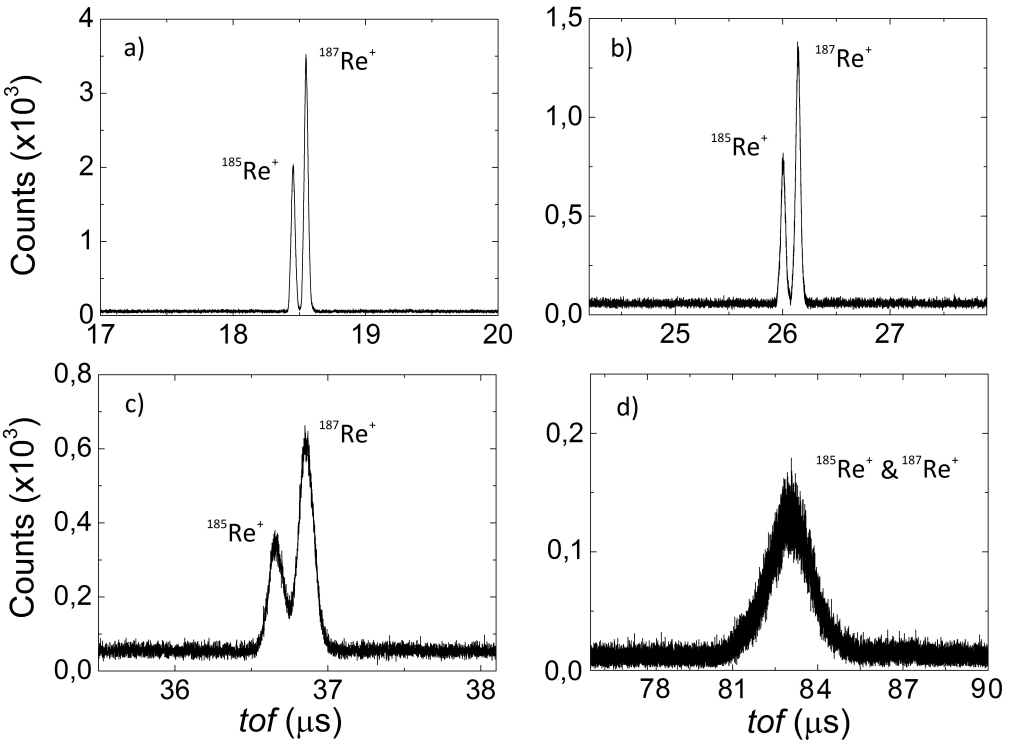

Figure 4.5: Time-of-flight (tof) signal of Re^+ ions produced with the laser-desorption ion source at four different kinetic energies: a) 20 keV, b) 10 keV, c) 5 keV and d) 1 keV.

which is obtained after substituting v in Eq. (4.1) by s/t, where s is the length of the ion´s fly path.

Figure 4.5 shows tof signals of rhenium ions produced using a target with natural isotopic composition. Figure 4.6 shows the inverse of the square of the time-of-flight for different kinetic energies of calcium and osmium ions in linear mode, and calcium and rhenium ions in reflectron mode [73]. High kinetic energy provides

- an increase of the ion detection rate,
- smaller full width at half maximum FWHM in the time-of-flight distributions of the ions, and
- lower energy spread of the ion beam.

However, it requests

- high-voltages power supplies, switches and insulators,
- larger cooling powers in the preparation Penning trap to deliver cooled samples at room temperature (≈ 0.025 eV), and
- better resolution of the time sequencer due to the smaller tofs.

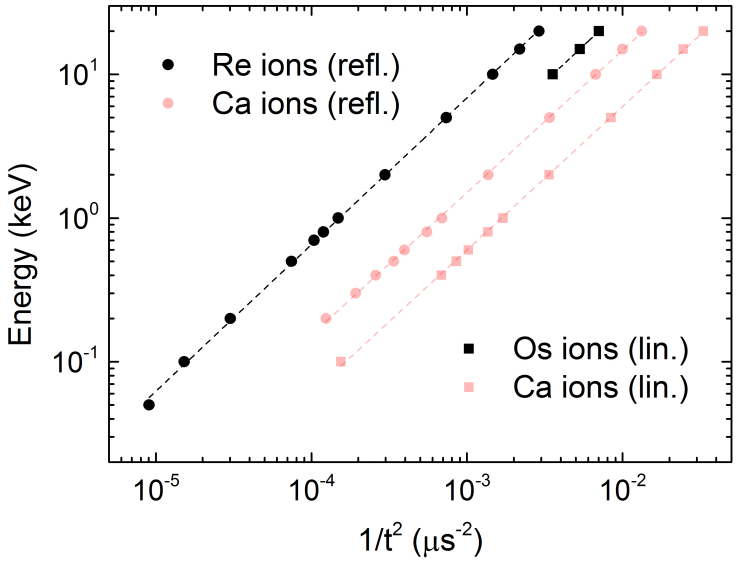

Figure 4.6: Kinetic energy of the ions versus the inverse of the square of the time-of-flight. Calcium ions are shown in red, while osmium and rhenium ions are depicted in black. The dashed lines are linear fits to the data

4.1.2 The transfer section

The transfer section shown in Fig. 4.7 allows the transport and injection of the ion beam from the laser-desorption ion source to the Penning-traps system. It has been taken from the one existing at the SHIPTRAP facility [81, 82]. The

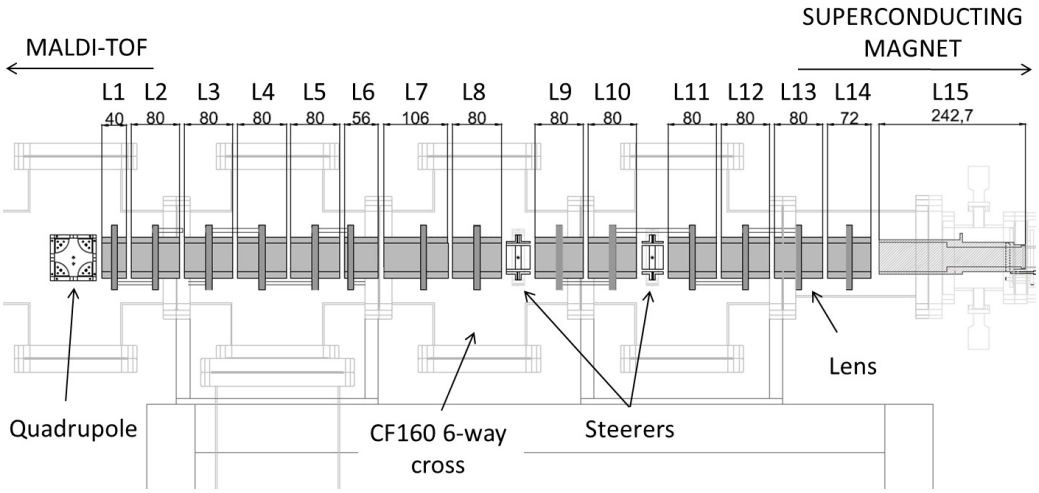

Figure 4.7: Technical drawing of the transfer section, comprising an electrostatic quadrupole, steerers and fifteen lenses. The transfer section is housed in four CF160 six-way vacuum crosses and a spring bellow. The lengths of the lenses are shown in mm. They are separated by gaps of 8 mm.

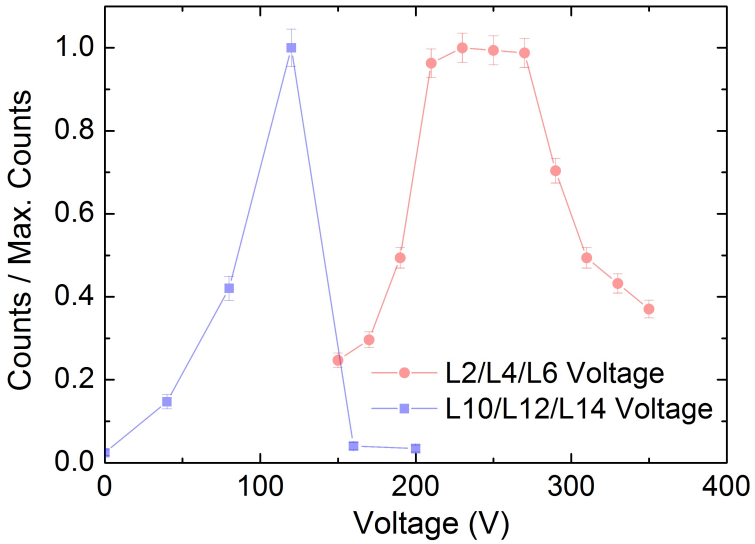

Figure 4.8: Normalized number of counts in the MCP3 detector (see Fig. 4.1) versus voltage applied to L2, L4 and L6 (in red), and L10, L12 and L14 (in blue). The lenses are numbered in Fig. 4.7.

quadrupole located in the first cross, can be used in two configurations, one to deflect the ion beam by 90° for diagnostics with a micro-channel plate detector, and the other for transmission. The lenses are hollow cylinders made of aluminum with an inner diameter of 48 mm and are biased to several hundred volts (see Tab. 4.2). The lengths are shown in Fig. 4.7. The steerers are made of four rectangular segments made of aluminum with a length of 48 mm in the directions perpendicular to the beam axis and 40 mm in the direction of the beam. Potentials in the order of a few volts are utilized to handle the ion beam. Insulating rings, made of PEEK (PolyEther Ether Ketone), screwed to the lenses, serve to fix those into the CF160 crosses. The lenses are used as Einzel lenses to focus ions in flight without changing their energies. The software package SIMION® version 8.0 has been used to study the trajectories of charged particles in the electric and magnetic fields of the beamline.

A voltage of -240 V has been applied to L2, L4 and L6 in order to focus the ions in the position of L8. Another three Einzel lenses after L8 allows performing a strong focusing of the ion beam, important to reduce the magnetron radius of the ion orbit when they enter into the strong magnetic field. A potential of -120 V is applied to L10, L12 and L14. Figure 4.8 shows the normalized count rate detected with the MCP3 detector (see Fig. 4.1) as a function of the voltage applied to lenses in the transfer section shown in Fig. 4.7.

The voltage applied to L2, L4 and L6 is larger than the voltage applied to L10, L12 and L14, since an electric pulse with 0-V low-level and 340-V high-level is

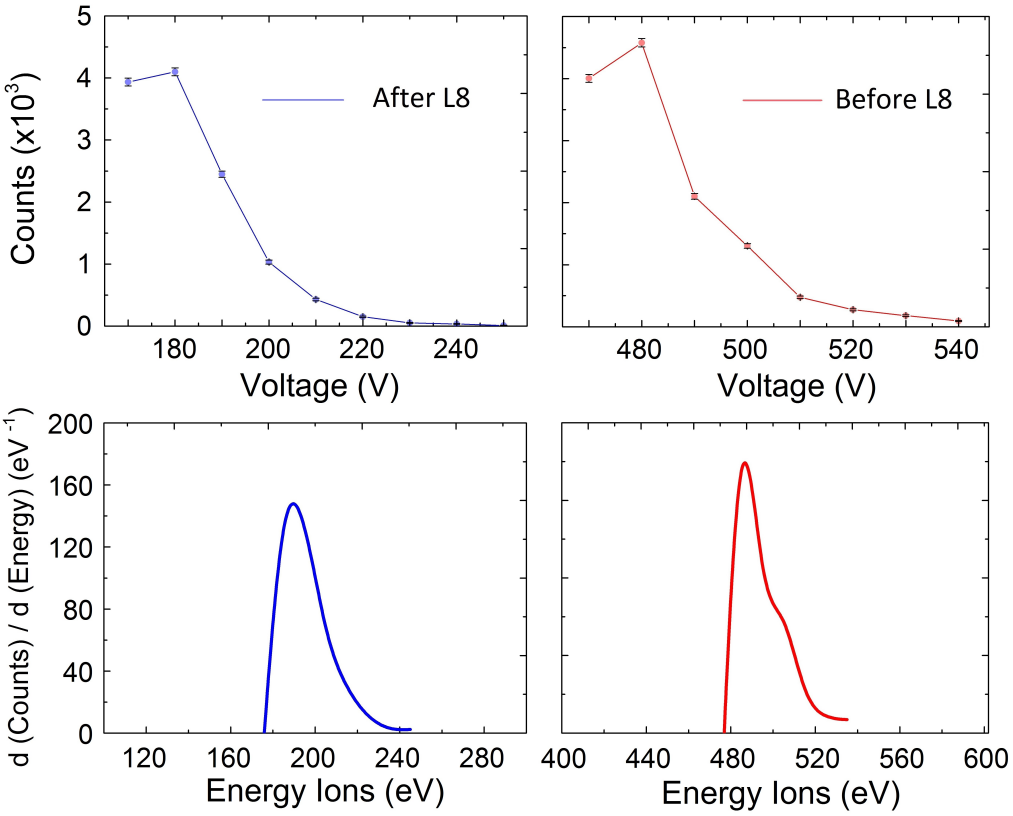

Figure 4.9: Distribution of Ca^+ ions as a function of the ion-beam energy before and after L8 (Fig. 4.7). Top: Ca^+ ions as a function of the voltage applied to an electrode of the Penning-traps beamline. Bottom: Energy distributions of the ion beam obtained after applying the derivative to the distributions shown in the upper panels.

applied to L8 to decrease the ions´ kinetic energy. After L8, this energy can be expressed, for ions with charge $ze = e$ as

$$K_F = K - eV_{\mathrm{L8}}(P) \approx e(V_{\mathrm{P1}} - V_{\mathrm{L8}}(P)), \tag{4.3}$$

where $V_{\mathrm{L8}}(P)$ is the electrical potential at a point P, where the ions are located when switching.

The width of the pulse, its delay with respect to the ion production, and the low and high levels, are optimized for each element in order to increase the transport efficiency for ions with a final kinetic energy of 200 eV. This is the maximum voltage applied to the electrodes in the preparation Penning trap. The target plate in the laser-desorption ion source is biased to about 500 V. Figure 4.9 shows the energy profile of the ion beam, before and after applying the pulse, thus when the mean kinetic energy is around 500 eV and 200 eV, respectively.

4.1.3 The superconducting magnet and the Penning trap system

The Penning-traps system is located in a CF100 to CF160 vacuum tube made of 316LN stainless steel with an inner diameter of 125 mm and a length of 1150 mm. This tube is inside the bore of the 7 Tesla superconducting magnet (Agilent™ 7T/160MM AS). The magnetic field is generated by a coil made of multi-filament NbTi conductor wire. The coils are positioned in a liquid-helium reservoir surrounded by a gas-cooled radiation shielding structure made of aluminum, which is surrounded in turn by a liquid-nitrogen reservoir. The magnet provides two regions with high-homogeneity within 1 cm^3, separated by 200 mm along the axial axis of the magnet.

Passive shims have been installed around the magnet bore in an aluminum tube, which has a diameter of 155 mm. A CF100 cross and a CF160 cross are coupled to the tube, each of them with four ports for the electrical connections to the Penning-traps system. Two ConFlat® spacer flanges align the Penning traps system with the beamline.

The Penning-traps system is shown in Fig. 4.3. It comprises a Preparation Penning Trap (PPT) and the open-ring trap. The PPT and the open-ring trap are placed in the first ($\Delta B \leq 1$ ppm) and second ($\Delta B \leq 0.1$ ppm) high-homogeneity regions of the solenoid, respectively. A diaphragm between the traps allows working with different pressures in each device [83], and serves to transport the ions from the PPT to the open-ring trap. This diaphragm has a length of 23 mm and an inner diameter of 2 mm.

The PPT, has been built to deliver pure and cooled samples, following the specifications of the PPT envisaged for the MATS experiment [13]. It is a cylindrical Penning trap with a total length of 312 mm, and an inner diameter of 32 mm. The radial and axial motions of the ions are cooled by applying the mass-selective buffer-gas cooling technique [50]. After cooling within typical times of 450 ms, the ions are extracted with an energy spread of a few meV.

The open-ring trap is an adapted version of the transparent Paul trap used in the project TRAPSENSOR to study Doppler cooling on the $^{40}Ca^{+}$ ion [75]. The open-ring trap used as Paul trap will be shown in Sec. 4.3.1. This trap has been scaled down by a factor of 2 and modified to be placed in the Penning-traps beamline. It is comprised of two set of four concentric rings along the z axis. The electrodes are made of oxygen-free high conductivity (OFHC) copper. A magnified view of this trap will be shown in Fig. 6.13 (top). The screws fixing electrodes and insulators are attached to a couple of support disks. The open-ring trap has a length of 40 mm and an outer diameter of 38 mm. An inner diameter of 2 mm in the electrode behind the diaphragm allows the injection and extraction of the ions. The ring electrodes are four-fold segmented to apply ion-excitation techniques. The inner electrode was added later to the original design and can be used for the detection of the axial motion. A similar electrode

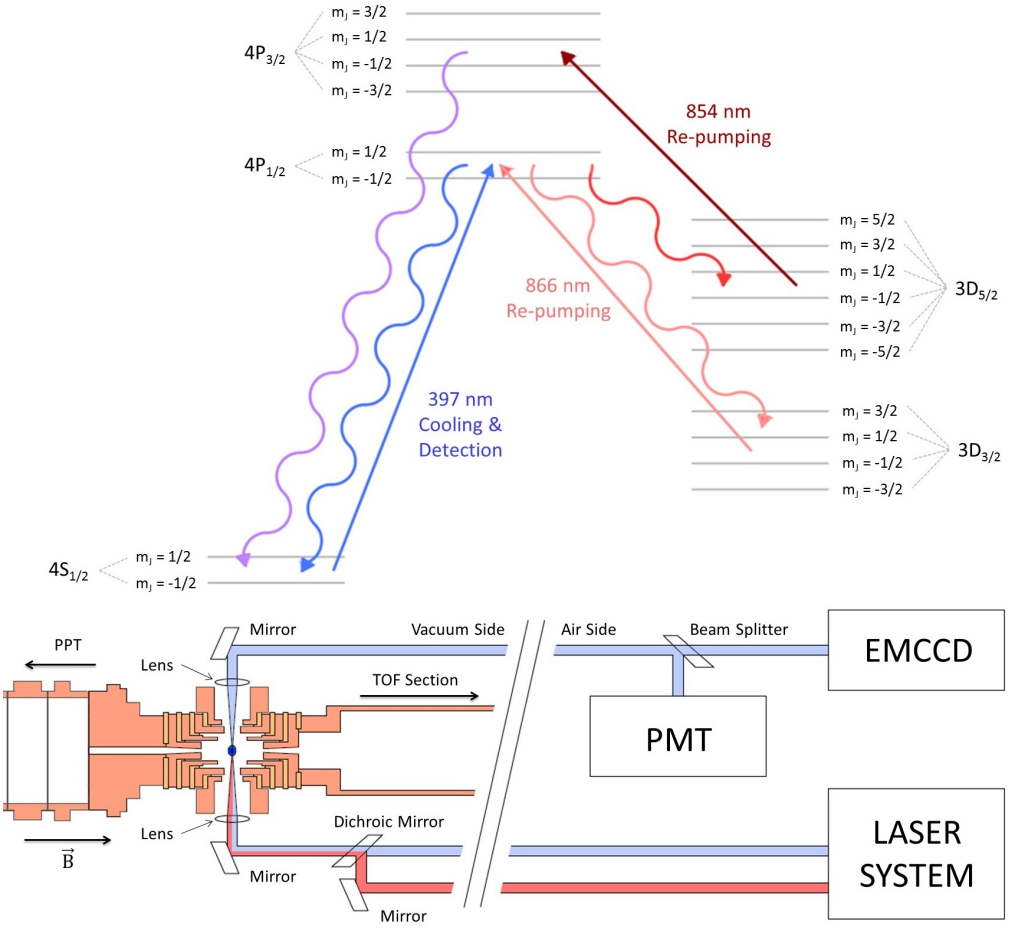

Figure 4.10: Top: Energy levels for $^{40}Ca^{+}$ in a 7-T magnetic field. The transitions addressed with lasers are represented by the red and blue straight arrows. The sinusoidal arrows represent the emission between the transitions. The probabilities for these decays are different. Bottom: Sketch of the open-ring trap developed to perform single-trapped-ion mass-spectrometry with the optical elements to apply laser cooling and detect fluorescence photons. The trap electrodes are shown in orange. The fluorescence photons are represented by a blue line. They are collimated by a series of lenses. The blue and red laser beams, represented by a blue and a red line, respectively, are brought inside vacuum by special vacuum feedthroughs and fibers. They are combined inside using a dichroic mirror.

will be used as coupling electrode in the QS device.

In the open-ring trap, a single $^{40}Ca^{+}$ ion will be cooled to the Doppler limit using 12 laser beams. Doppler cooling is widely described in Ref. [84, 85]. Since the ion is sitting in a 7-T magnetic field, there is a large splitting of the energy levels due to the Zeeman effect (see Fig. 4.10), and a complex laser system is needed (see Sec. 4.2). Figure 4.10 (bottom) shows a sketch of the open-ring trap with the optical system to perform fluorescence detection and laser cooling. The

fluorescence image will be observed using an Electron Multiplier Charge Coupled Device (EMCCD) Camera (iXon 397) and/or a photomultiplier tube (PMT).

The open-ring trap used as Penning trap will be replaced by the QS device (under construction), which it is a double Penning-(micro)-trap. This system comprises two identical traps, where each trap is a modified version (scaled down by a factor 5) of the open-ring trap used as Penning trap. The geometry of this system and the associated electronics will be shown in Sec. 4.3.3 and Sec. 7.1, respectively.

4.1.4 The time-of-flight section and the detector

The ions from the Penning-traps system are ejected out towards a micro-channel plate detector through the TOF section. Along this section a negative-ramp potential is applied using nine lenses, five of them made of OFHC copper with gold and silver plating, and four made of aluminum. The copper lenses with 24 mm inner diameter are located inside the magnet bore. The aluminum lenses with 38 mm inner diameter are placed in a CF160 cross and a CF160 bellow behind the magnet. Several micro-channel plate detectors are placed in the Penning-

Table 4.2: Typical voltages used for the operation of the laser-desorption ion source, transfer and TOF sections in the Penning-traps beamline. The elements are shown in Fig. 4.1, 4.4 and 4.7.

Element / Section	Value
Laser-desorption ion source	
P1 electrode	500 V
Lenses Set	0 V (linear mode) / 500 V (reflectron mode)
Transfer section	
Quadrupole electrode 1	0 V (linear mode) / 500 V (diagnosis mode)
Quadrupole electrode 2	0 V (linear mode) / 500 V (diagnosis mode)
Quadrupole electrode 3	0 V (linear mode) / 500 V (diagnosis mode)
Quadrupole electrode 4	0 V (linear mode) / -250 V (diagnosis mode)
Lenses 1,3,5,7,9,11,13,15	0 V
Lenses 2,4,6	-240 V
Lens 8	Switched between 0 V and 340 V
Lenses 10,12,14	-120 V
Deflector 1	0 V
Deflector 2 Up	0 V
Deflector 2 Down	0 V
Deflector 2 Left	-5 V
Deflector 2 Rigth	0 V
TOF section	
Lenses set	-400 V
Detector	-2300 V

traps beamline (see Fig. 4.1 and Fig. 4.4).

The detector for the TOF signal (TOPAG MCP 25-10) is comprised of two micro-channel plates in chevron configuration and a metallic anode. The active area is a circle with 25 mm diameter and a gain factor of 10^8 can be reached by applying a voltage of 2600 V. The electrons are collected in the anode. A potential difference of 2300 V is applied between the first and last plate and a capacitor $C = 1$ nF is used to decouple the electronic signal and the DC potential applied to the anode. The voltages applied along the whole beamline are shown in Tab. 4.2.

4.1.5 Vacuum system and electronic connections

The vacuum system is shown in Fig. 4.11. In the laser-desorption ion source area, two turbomolecular pumps (Pfeiffer vacuum TMU 260 DN100 CF-F) with

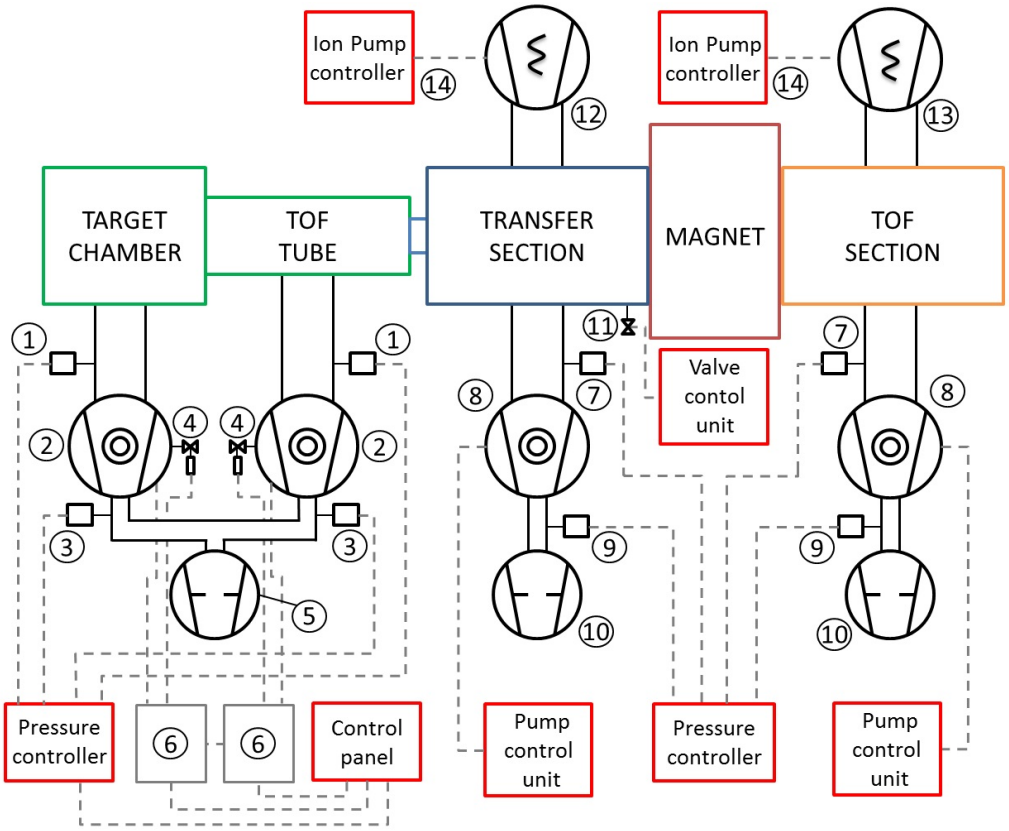

Figure 4.11: Sketch of the vacuum system in the Penning-traps beamline. 1) Cold-cathode ionization vacuum gauge. 2) Turbomolecular pump (260 l/s). 3) Pirani vacuum gauge. 4) Valve. 5) Oil-free dry scroll vacuum pump (10 m^3/h). 6) Turbomolecular pump control unit. 7) Active ion vacuum gauge. 8) Turbomolecular pump (800 l/s). 9) Pirani vacuum gauge. 10) Oil-free dry scroll vacuum pump (35 m^3/h). 11) Gas regulating valve. 12) Ion pump (300 l/s). 13) Ion pump (600 l/s). 14) Ion pump control unit.

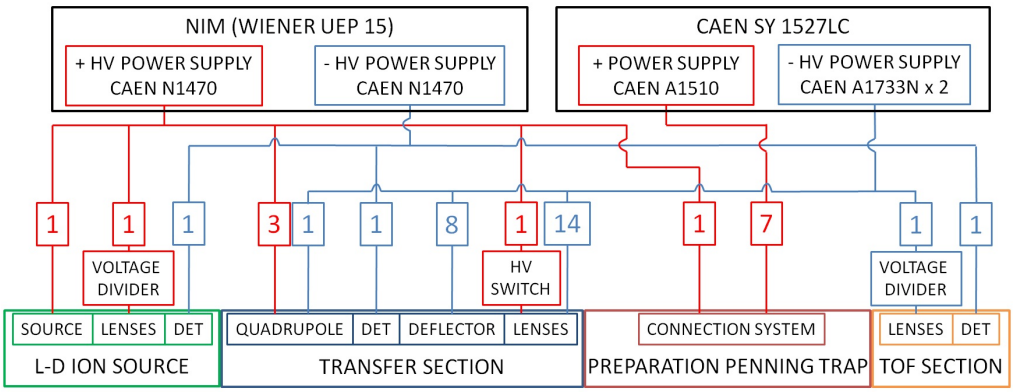

Figure 4.12: Sketch of the electrical connections in the Penning-traps beamline. The number of channels in use is shown for each power supply. Negative and positive polarities are depicted in blue and in red, respectively.

a pumping speed of 260 l/s are connected to the target chamber and the *tof* tube. An oil-free dry scroll vacuum pump (Edwards XDS-10) with a pumping speed of 10 m^3/h is attached to the turbomolecular pumps. Two cold-cathode ionization high-vacuum gauges (Balzers IKR-050) and two Pirani vacuum gauges (Pfeiffer vacuum TPR010) are placed to monitor the pressure at different stages. Two automatic venting valves (Pfeiffer vacuum TSF012) are connected to the turbomolecular pumps.

A turbomolecular pump (Edwards TSTP-0803C DN160CF) with a pumping speed of 800 l/s is located in the transfer and TOF sections. Each turbomolecular pump is attached to an oil-free dry scroll vacuum pump (Edwards XDS-35i) with a pumping speed of 35 m^3/h. Two active ion gauges (Edwards AGX-S) and two Pirani vacuum gauges (Edwards APG100-XLS) are placed in the transfer and TOF sections. In addition, ion pumps are located in the transfer section (Gamma vacuum 300TV) and in the TOF section (Gamma vacuum 600TV). All pressure values are displayed in a controller from Edwards (model TIC 6HD). A gas regulating valve (Pfeiffer vacuum EVR 116) allows the injection of the helium with high purity ($> 99.999\%$) into the PPT. A DN 16 ISO-KF to 6 mm tube Swagelok® adapter, located in the transfer section, is used for this. The gas flow is regulated using a control unit (Pfeiffer vacuum RVC 300) with a resolution of 0.01 mbar l/s. The average pressure without any gas inlet is about 1×10^{-7} mbar in the target chamber, about 5×10^{-8} mbar in the *tof* tube, in the order of 1×10^{-8} mbar in the transfer section (with the ion pump turned off), and about 5×10^{-9} mbar in the TOF section.

The DC-Voltages applied to the electrodes along the full beamline are delivered by two positive/negative high-voltage power supplies (CAEN N1470), two negative high-voltage power supplies (CAEN A1733N) and one floating power supply (CAEN A1510) with 20 mV voltage resolution. Figure 4.12 shows a sketch of the power supplies indicating channels number, polarity and electrode. The voltages of the CAEN N1470 power supplies, located in a NIM crate, are controlled

by a LabVIEW™ software program realized in the course of this work. The CAEN A1510 and CAEN A1733N power supplies are housed in a CAEN SY 1527LC crate, which is controlled by the Control System (see Sec. 5.4). Inside vacuum, the DC-voltages are delivered to the elements through Kapton® wires with 0.9 mm diameter.

The lens L8 in the transfer section is switched from 340 V to ground in order to reduce the kinetic energy of the ion beam from 500 eV to 200 eV as described earlier in Sec. 4.1.2. A fast high-voltage switch (BEHLKE HTS 151-01) with 5-ns turn-on rise time and 10 ns turn-off fall time is used. The TTL signal to define the pulse width and time location with respect to the full measurement cycle is delivered by a Pulse Pattern Generator created using an FPGA card (see Sec. 5.4).

4.2 The laser system

Figure 4.13 shows a sketch of main elements in the laboratory, not to scale. Many lasers will be needed in such experiment due the strength of the magnetic field (see Fig. 4.10). Since the geometry is also new, Doppler cooling has been tested operating the open-ring trap as a Paul trap. The laser beams are transported with optical fibers to the Penning-traps beamline.

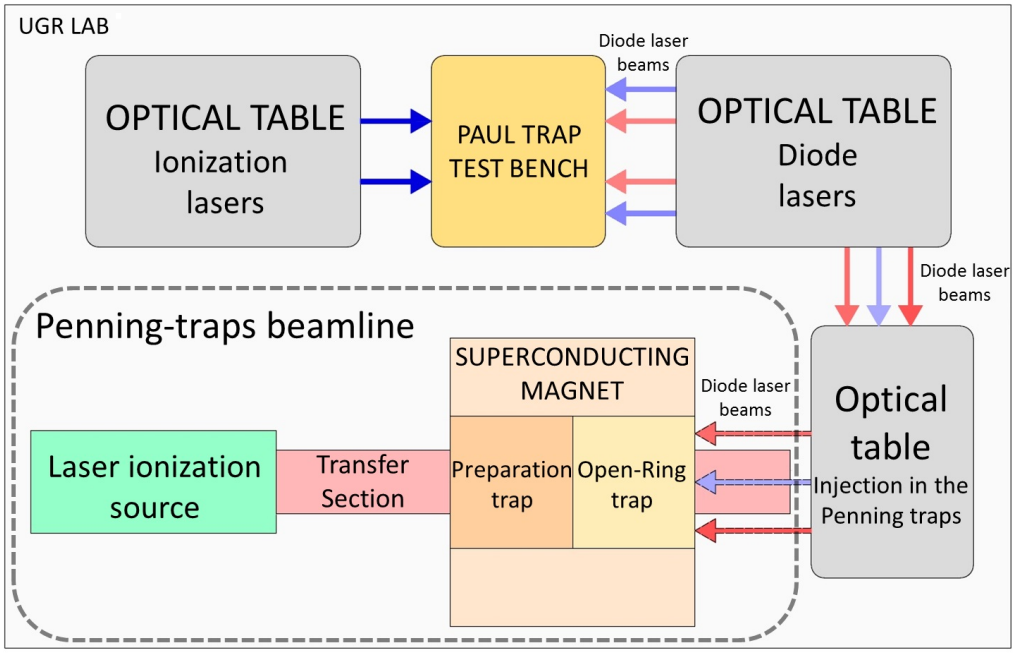

Figure 4.13: Systems of the TRAPSENSOR facility at the University of Granada: optical tables, Paul trap test bench and Penning-traps beamline. The drawing is not to scale.

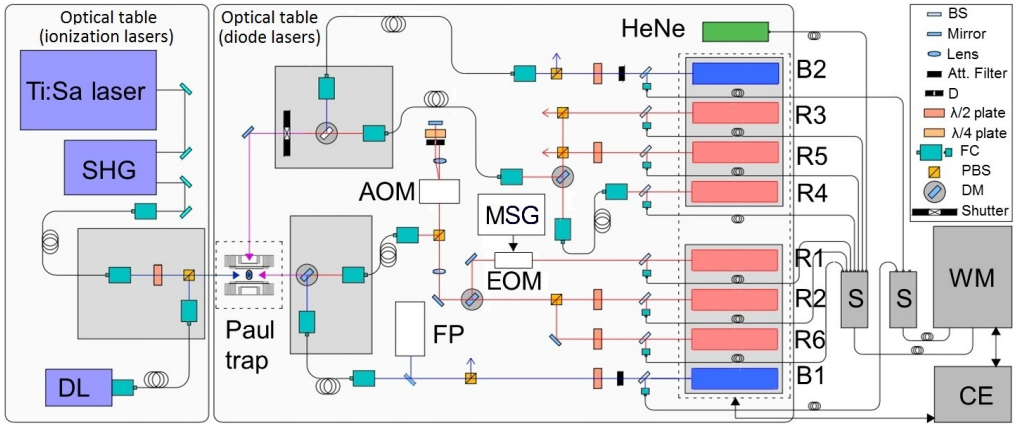

Figure 4.14: Sketch of the optical table with the lasers system and the Paul trap with optical elements to perform Doppler cooling on the $^{40}Ca^{+}$ ion. The drawing is not to scale. Figure adapted from Ref. [75].

4.2.1 Frequency stabilization

The lasers system is shown in Fig. 4.14. It is placed on an optical table with dimensions 2.5 m × 1.5 m. and it comprises eight tunable diode lasers (DL Pro TOPTICA Photonics) with external-cavity resonator in Littrow configuration. Two lasers (B1 and B2) are used for cooling through the electric-dipole transition at $\lambda = 397$ nm from the ground state $4^2S_{1/2}$ to the excited state $4^2P_{1/2}$ of the $^{40}Ca^{+}$ ion. This is the most critical laser and a Fabry-Perot interferometer (FP) is used in order to monitor the laser beam modes so as to adjust the regulation to provide a single one. Four lasers (R2, R3, R5 and R6) at $\lambda = 866$ nm are required to restore the cooling when it is interrupted via the decay from $4^2P_{1/2}$ to the dark state $3^2D_{3/2}$, which can occur with a probability of 7%. Another two lasers (R1 and R4) emitting at $\lambda = 854$ nm, will be used to drive the transition $3^2D_{5/2} \rightarrow 4^2P_{3/2}$, since the state can be populated from $4^2P_{1/2}$ with a probability that increases with the strength of the magnetic field with a branching ratio relative to the main decay of $4.2 \times 10^{-7}\ B^2$ (B given in Tesla) [86]. The maximum energy of the lasers in the laboratory is 15, 50, and 170 mW for $\lambda = 397$, 866, and 854 nm, respectively.

Following Fig. 4.10, four more laser beams with $\lambda \approx 854$ nm have to be used to pump from the state $3^2D_{5/2}$ to $4^2P_{3/2}$ in the 7-T magnetic field. Such laser beams will be generated by means of an electro-optical modulator (EOSPACE model PM-AV5-40-PFA-PFA-900) from the two beams provided by the diode lasers [87]. A microwave signal generator (RS®SMB100A RF) with a frequency range from 9 kHz to 40 GHz is used to drive the EOM.

The wavelength of the lasers is measured and stabilized using a Fizeau-based wavelength meter (HighFinesse WSU-10) with 10 MHz absolute accuracy (3 σ). A stabilized HeNe laser ($\lambda = 632.9909463$ nm) with very high frequency stability ($\pm\ 2 \times 10^{-9}$ h^{-1}) provides the reference value to calibrate the wavemeter.

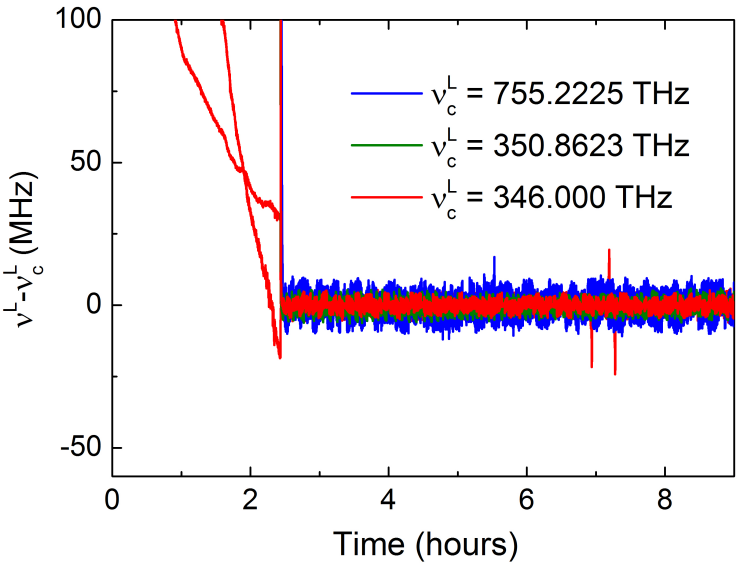

Figure 4.15: Deviation of the frequencies of the lasers used to perform Doppler cooling on a single $^{40}Ca^+$ ion, with respect to a fixed value (ν_c^L) as a function of the time. PID regulation allows locking the frequency of the lasers with standard deviations of 3-4 MHz around the fixed value. The figure has been adapted from Ref. [88].

Figure 4.14 shows beam splitters located in the optical table behind the laser heads to obtain about 10% of the laser light for the measurement and the stabilization. The light is transported using single-mode optical fibers to two fast micro-mechanical switches (HighFinesse), one for the HeNe and infrared lasers and another for the 397-nm lasers. The first multichannel switch delivers sequentially the 397-nm laser beams into the front port of the wavemeter and the second one, the IR (infrared) laser beams and the HeNe laser light into the rear port of the wavemeter.

Each diode laser has an electronic module comprising a DC 110 monitor unit to display the operating parameters, an operator control module DCC 110 to modulate the current to the diode of the laser, a temperature control module DTC 110, and a scan control module SC 110. A voltage signal from the module SC 110 to the piezo allows an external control of the grating to select the wavelength of the lasers. Proportional-Integrative-Derivative (PID) regulation is used to lock the frequency of all the lasers. The electronic control loop uses a card installed in the computer (CE). The software integrated in the computer sends the voltage signal to the scan control module SC 110 and this to the piezo on the laser head, which acts on the grating and makes wavelength tuning. Figure 4.15 shows the frequencies of the diode lasers over several hours. The frequencies for this measurement are locked to the values displayed in the NIST data base,

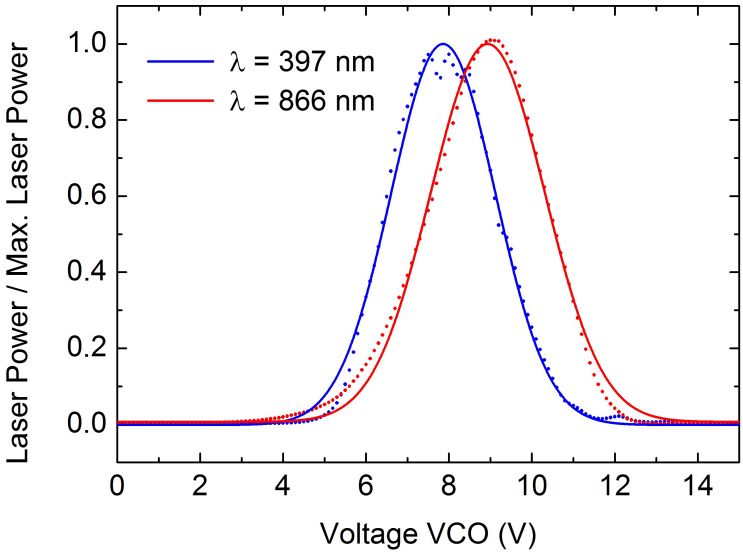

Figure 4.16: Relative laser power as a function of the voltage applied to the VCO driving the AOM for one of the laser beams emitting at $\lambda = 397$ nm and another at $\lambda = 866$ nm. Blue ($\lambda = 397$ nm) and red ($\lambda = 866$ nm) dots represent the laser-power values. The laser powers have been fitted using Gaussian functions. The figure has been adapted from Ref. [89].

755.2225, 350.8623 and 346.000 THz [90].

4.2.2 Power regulation

Acoustic-Optical Modulators (AOM) are used to regulate power and to fine tuning the laser frequency. AOMs from Crystal Technology (models 3200-125 and 3110-120) with first-order frequencies around 200 and 110 MHz, respectively and bandwidths in the range 50-24 MHz are used in double-pass configuration. The RF signal for the AOM is generated by an electronic system comprising a Voltage Controlled Oscillator (VCO), a Voltage Variable Attenuator (VVA) and a fixed-gain amplifier. Figure 4.16 shows the relative laser power as a function of the voltage applied to the VCO [89]. The AOM can be used also as a fast shutter for the laser light.

4.3 The open-ring Paul trap test bench

The laser system described above has been used to study laser cooling on the $^{40}Ca^{+}$ ions in an open-ring Paul trap, as this geometry has been chosen for the final design of the QS system. It has only a point where the electric field is equal to zero, opposite to a linear RF trap [91], which have $\vec{E} = 0$ along the z-axis. However, the geometry of the open-ring trap, allows utilizing such a device as a

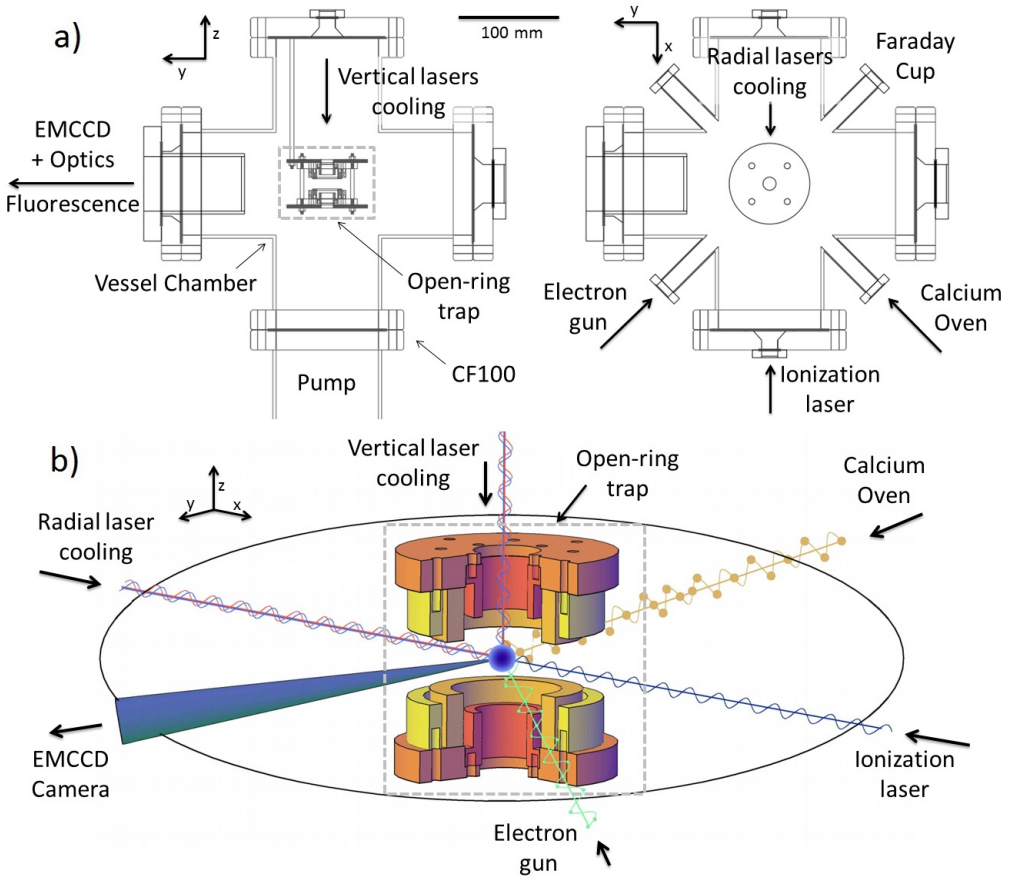

Figure 4.17: Different views of the Paul trap set up to perform Doppler cooling. a) Technical (simplified) two-dimensional drawing of the Paul trap housed in a customized 6-way CF100 vacuum chamber: left, side view and right, top view. b) Cut from a 3D-CAD drawing of the open-ring Paul trap. The Paul trap is inside the square box delimited by the dashed line in the side view of the chamber. The blue/red line represents the UV/IR diode lasers for Doppler cooling. The laser beams for ionization are also represented by a blue line. The fluorescence photons emitted within a certain solid angle are depicted by a cone. The electron beam and the calcium atomic beam are represented by a green and a yellow line, respectively.

Penning trap later. The vacuum chamber is fixed at the end of the optical table where the lasers and optics are installed.

4.3.1 The open-ring trap

The open-ring trap Paul trap is made of two sets of three concentric rings made of 304L stainless steel centered on the z axis and mounted in sapphire substrates. The Paul trap, based on a previous device built at GANIL (France) to perform high-precision β-decay experiments [48], is mounted in a CF100 flange on top of a 6-way vacuum chamber with 4 additional CF16 ports (see Fig. 4.17). The vacuum pressure in the chamber, for the measurements presented here is in the

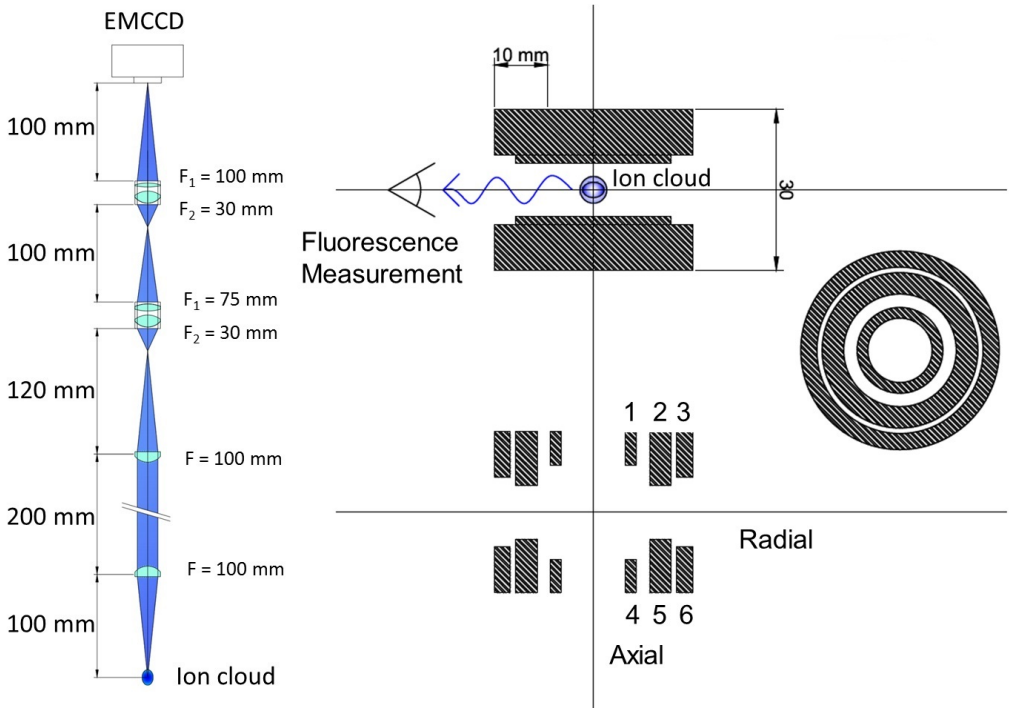

Figure 4.18: Left: Optical system to collect the fluorescence photons. Right: Different views of the open-ring trap. Figure adapted from Ref. [92].

order of 10^{-10} mbar, which is reached by means of an ion pump (Gamma Vacuum Titan™ 300TV) with a pumping speed of 300 l/s. Figure 4.18 shows the electrodes of the open-ring trap. A radiofrequency (RF) quadrupole field is performed by applying the potential to the inner electrodes (numbered 1 and 4 in Fig. 4.18). The middle (numbered 2 and 5) and the most outer rings (numbered 3 and 6) are normally at ground. They can be used however, to compensate possible deviations from the ideal quadrupole field by applying small DC potentials.

In this setup, the ions are created by electron bombardment or by photoionization of an atomic beam evaporated from an oven (Alvatec type C). Figure 4.17 shows also schematically the atomic, electron and laser beams. In the case of electron impact, ionization is achieved by crossing the atomic beam with a 500 eV electron beam generated with an electron gun (Omicron EKF 300). The efficiency of the process is about a factor of 7 below the maximum, when the electron kinetic energy is around 20 eV [93]. Nevertheless this will also help to reduce the ionization of atoms and/or molecules from the remaining background gas in the chamber. The electron beam current is maximized using a miniaturized Faraday cup detector developed within this work.

Photoionization is accomplished using two laser beams. One laser beam at $\lambda = 422.79$ nm is used to excite the transition from the ground state 4^1S_0 to the first excited state 4^1P_1 in the calcium atom. A second laser beam at $\lambda = 375$ nm is

superimposed to drive the electron from the 4^1S_0 state to the continuum. The beam at $\lambda = 422.79$ nm was generated using a Ti:Sa laser (Matisse Sirah TX) stabilized at $\lambda = 845.5820$ nm, and later doubled in frequency using a module from Toptica photonics TA/DL-SHG pro. The light at 375 nm is delivered by a diode laser (Toptica photonics iBeam smart). The two lasers are sketched in Fig. 4.14. Note that the dimensions of the optical table are the same as the optical table for the diode lasers. The advantages of using photoionization with respect to electron bombardment were already shown in Ref. [94].

4.3.2 Doppler cooling of a single $^{40}Ca^+$ ion

In the setup at the University of Granada, vertical and radial laser beams are used for Doppler cooling as shown in Fig. 4.14. A radiofrequency (RF) quadrupole field at $\nu_{RF} = 650$ kHz with an amplitude of $V_{RF} = 223$ V_{pp} is used to trap the ion. The Mathieu parameters for these values [95] are $q_r = 0.205$ and $q_z = 0.410$.

The fluorescence photons from the $^{40}Ca^+$ ion are collimated using an optical system and detected with an EMCCD camera (Andor Ixon3). The optical elements are shown schematically in Fig. 4.18. The optical system provides a magnification factor of about 8. A planar-convex lens with focal distance $f = 100$ mm and a diameter $2r_1 = 24.5$ mm is located at a distance $R = 100$ mm from the trap center so that the solid angle is given by

$$\Omega = \frac{\pi r_1^2}{R^2} = \frac{4\pi}{248}. \tag{4.4}$$

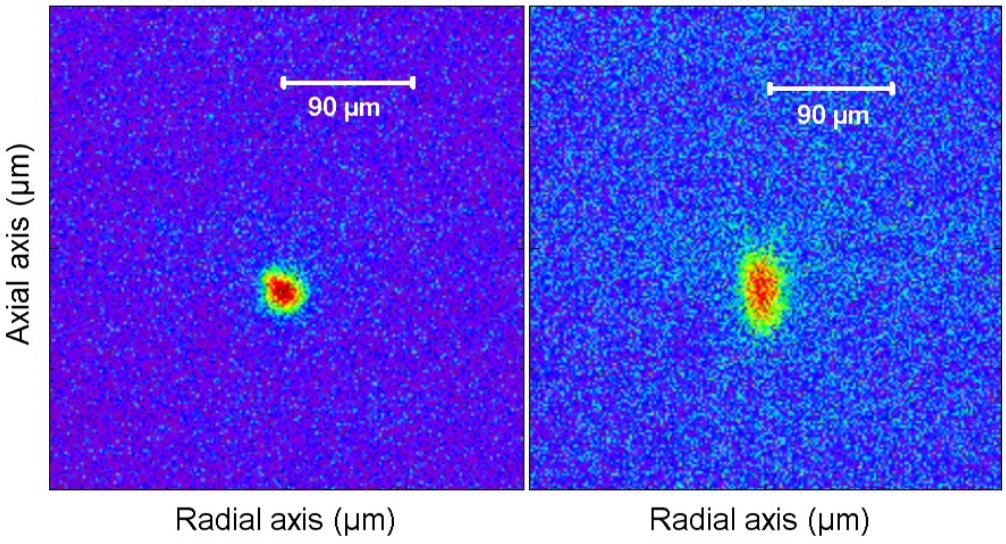

Figure 4.19: Left: Image of a single laser-cooled $^{40}Ca^+$ ion. The photon count rate per second registered with the EMCCD camera was 2.5×10^4. Right: the same when applying an RF dipole field in resonance with the axial motion. See text for further details.

Table 4.3: Intensity of the 397-nm laser in the radial direction to perform the single laser-cooled $^{40}Ca^{+}$ ion measurements and its effect on the fluorescence image. Ratio (axial) and ratio (radial) are the normalized areas resulting from Gaussian fits to the projections of the image in the axial and radial directions, respectively. σ (axial) and σ (radial) are also extracted from the Gaussian fits.

I(radial) (μW/mm^2)	Ratio (axial)	Ratio (radial)	σ (axial) (μm)	σ (radial) (μm)
570	0.21	0.22	10.6(3)	11.7(4)
2000	0.40	0.41	10.1(2)	11.5(2)
2700	0.48	0.48	10.0(2)	11.1(2)
7200	1	1	10.1(1)	11.6(1)

The EMCCD camera has a sensor with 512 × 512 active pixels with a pixel size of 16 μm and a quantum efficiency for $\lambda = 397$ nm of $\approx 55\%$. The left side of Fig. 4.19 shows the image of a single laser-cooled $^{40}Ca^{+}$ ion with the UV-laser frequencies fixed about 10 MHz below resonance. The right side of the figure shows the same but applying a dipole field in the axial direction in resonance with the axial motion. The dipole excitation was applied to the electrodes numbered 1 and 4 in Fig. 4.18. The amplitude was 0.5 mV_{pp} and the frequency 93.88 kHz. The kinetic energy of the ion in the trap can be related to its temperature, following the equation:

$$\frac{1}{2}k_{\mathrm{B}}T = \frac{1}{2}m\left(\omega_{\mathrm{z}}^{\mathrm{sec}}u_{\mathrm{z}}^{\mathrm{sec}}\right)^2, \tag{4.5}$$

where $u_{\mathrm{z}}^{\mathrm{sec}}$ is the oscillation amplitude of the ion in the trap. As it can be inferred from Fig. 4.19, the amplitude of the axial motion increases by a factor of ≈ 2, which increases the temperature by a factor of ≈ 4.

Table 4.3 shows results for several intensities of the 397-nm laser in radial direction (B2 in Fig. 4.14). The 397-nm laser in the axial direction (B2 in Fig. 4.14) and all the 866-nm laser beams were fixed to 1700 μW/mm^2 and 400 μW/mm^2, respectively. The saturation intensity for $^{40}Ca^{+}$ is 466 μW/mm^2. Thus, taking into account the overall efficiency of the optical and detection system, the detected count rate corresponds to a scattering rate of $\approx \Gamma/4 = 3.5 \times 10^7$ photons/s.

The temperature of the Doppler-cooled $^{40}Ca^{+}$ ion was measured, to be in the interval $T_{limit}^{upper} = 3.9$ mK to $T_{limit}^{lower} = 1.5$ mK [75]. These limits correspond to average values of the occupational quantum number of $\langle n_z\rangle = \frac{\langle k_B T\rangle}{\hbar\omega_z^{sec}} \approx 864$, and 332, where $\hbar$ is the reduced Plancks constant and $\omega_z^{sec} = \pi q_z \nu_{\mathrm{RF}}/\sqrt{2}$.

4.3.3 Geometry for the QS system

The studies carried out using the Paul-trap test setup have provided useful information about the production of calcium ions, the image-collection system,

Table 4.4: Comparison between different trap geometries (I). Axial oscillation amplitude (A), induced charge (ΔU) and transfer constant (b in Eq. (3.26)) for the system $^{187}Re^{+}$-$^{40}Ca^{+}$ for different trap geometries. The energy of 0.025 eV corresponds to a temperature of 300 K.

	Planar trap	Circular trap	Cylindrical trap	Ring trap
E (eV)	0.025	0.025	0.025	0.025
A (mm)	0.08	0.22	0.25	0.25
ΔU (V)	2.48×10^{-23}	1.18×10^{-9}	7.34×10^{-12}	2.95×10^{-10}
b (m/s)	9.41×10^{-13}	2.30×10^{-7}	2.77×10^{-24}	4.00×10^{-8}

vacuum conditions and laser cooling. Several trap geometries were investigated in order to decide the optimal one for a double Penning-(micro)-trap [76, 77]. Table 4.4 shows the values of the most important parameter obtained in Ref. [76], where the magnetic field strength is $B = 7$ T and the parasitic capacitance of the trap 10 pF. Table 4.5 shows other characteristics of the different geometries, which are relevant for the proposed experiment. The final design adopted for the trap is based on the open-ring trap, which allows for:

- revolution symmetry around the magnetic axis,
- possibility to access with the lasers in the radial and axial directions,
- ion beam injection from outside the trap, and
- strong ion-ion coupling through the induced image charges in the common endcap electrode.

Table 4.5: Comparison between different trap geometries (II). (1) Two planar traps are needed to capture the ions.

Trap Geometry	Revolution symmetry around the magnetic axis	Radial laser access	Ion injection from outside	Ion-ion coupling
Planar	No	Yes	Yes(1)	Weak
Circular	Yes	Yes	No	Strong
Cylindrical	Yes	No	Yes	Weak
Ring	Yes	Yes	Yes	Strong

Further details about electronic for ion-ion coupling and the micro-trap construction will be shown in Sec. 7.1.

Chapter 5

The preparation Penning trap

This chapter describes the relevant elements of the preparation Penning trap (PPT) to feed the second Penning trap in the project TRAPSENSOR. The PPT has been built following the specifications of the PPT envisaged for the MATS (Precision Measurements of very short-lived nuclei using an Advanced Trapping System) experiment at FAIR (Facility for Antiproton and Ion Research).

5.1 Mechanical design

The PPT of the TRAPSENSOR project is a cylindrical Penning trap made of a stack of 25 electrodes. The center of the trap is placed in the first high-homogeneous region of the superconducting magnet. Figure 5.1 shows the PPT inside the vacuum tube fixed inside the magnet bore. The trap is fixed to three rods made of OFHC copper with a diameter of 12.7 mm and a length of 740 mm. These rods serve to align the Penning-traps system inside the vacuum tube, which is connected to the transfer and TOF sections of the Penning-traps beamline. The vacuum tube has to be aligned with the magnetic field of the superconducting solenoid. Insulating pieces made of fiberglass impregnated and cured with a non-brominated epoxy resin, known as G10, are used to fix the Penning trap and isolate thermally the system, if this has to be operated at cryogenic temperature, from the electrical connections to the power supplies. The material G10 has very low thermal conductivity at low temperature (0.3 W/(m·K) at 45 K is given in Ref. [96]).

The mechanical design of the PPT for the TRAPSENSOR project is based on the conceptual design of the PPT for the MATS experiment [13], thus taking into account the following issues:

- It has to be operated to cryogenic temperature, and thus the insulators between segments must be machined using materials with good thermal conductivity.

- The materials must be also compatible with ultra-high vacuum.

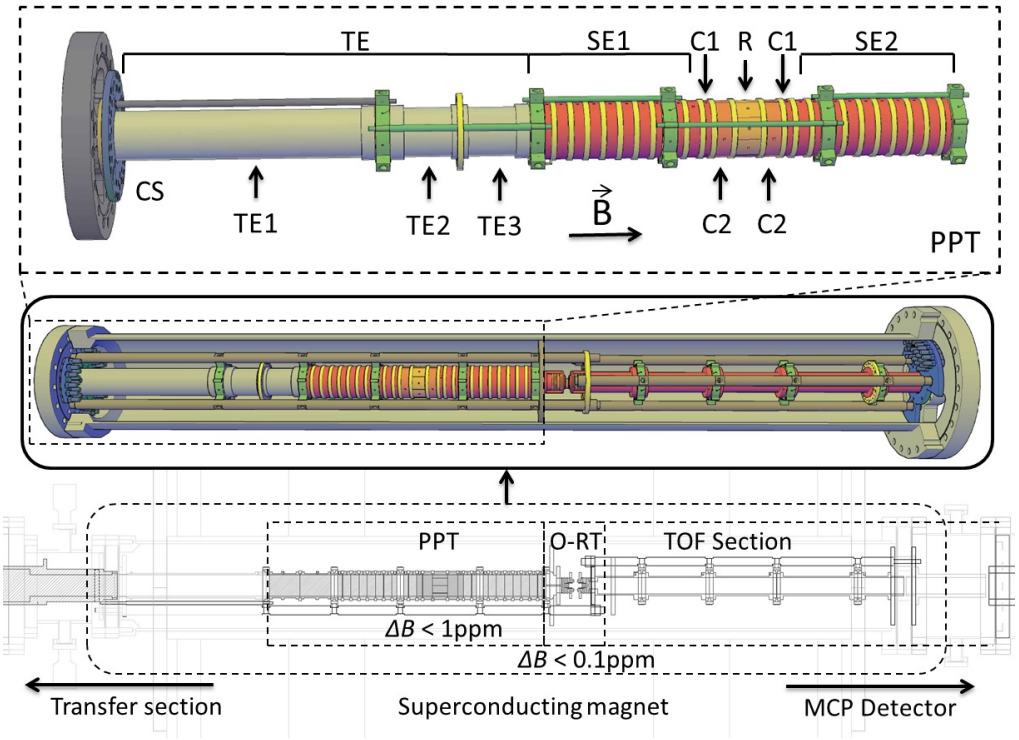

Figure 5.1: Top: Three-dimensional CAD drawing of the PPT, connection system (CS) built in a CF100 flange, transfer electrodes (TE). The segmented electrodes are gathered in two sections (SE1 and SE2). The correction electrodes in the trapping region are marked with C1 and C2, and the central ring is named R. Middle: Three-dimensional CAD drawing of the Preparation Penning Trap (PPT), the Open-Ring Trap (O-RT) and lenses for injection and extraction of the ions into the trap. The segmented electrodes of the PPT, diaphragm, and lenses in the time-of-flight section behind the trap, are shown in red, while the central ring and the correction electrodes are shown in clear and dark orange, respectively. The system for the electrical connections is shown in blue and the insulators in yellow. The rods used to support and fix the structure are shown in brown. They are screwed to the trap tower through the pieces in green. The system is housed in a customized vacuum tube with a CF 100 flange on the side entering the ions and a CF160 one on the side close to the detector. Bottom: Longitudinal view of the trap shown in the middle part of the figure.

- The mechanical accuracy has to provide a good alignment of the electrodes and avoid discharges between them.

- The trap tower, alignment rods, connections system and electronics for IIC detection, have to be fixed within the radial limitation of 125 mm due to the magnet bore, identical to the one at the SHIPTRAP facility.

- All materials should have lower magnetic susceptibility due to the high strength of the field.

- The electrodes should be segmented in such a way to allow applying buffer gas cooling in the central region, for the project TRAPSENSOR, but also electron or even laser cooling, if needed later.

- It must be a system which can be easily integrated in the SHIPTRAP beamline.

The electrode stack

Figure 5.1 (top) shows the PPT sections. The PPT has an overall outer diameter of 87 mm and a length of 638 mm. All the electrodes have cylindrical symmetry with an inner diameter of 32 mm. The electrodes are made of OFHC copper, and they are gold-plated to prevent oxidation. Silver is deposited between the copper and the gold to avoid diffusion of the gold into the copper [97]. The electrodes have been machined in a local company (INMACO SL[1]) and the plating has been done at GSI-Darmstadt. The electrodes were polished with dolomite powder ($CaMg(CO_3)_2$) to increase the flatness. This reduces the grooves of the inner surfaces and avoid discharges when switching the electrodes between different voltages if the system is running with a gas load. Figure 5.2 shows a photograph of an electrode taken with a high-resolution scanning electron microscope of variable pressure (Zeiss SUPRA40VP) located at the Centro de Instrumentación Científica (CIC) at the University of Granada. The size of the grooves is about 1 μm.

[1]INMACO SL Calle Albuñol parc. 252-B 18220-Albolote, Granada (Spain).

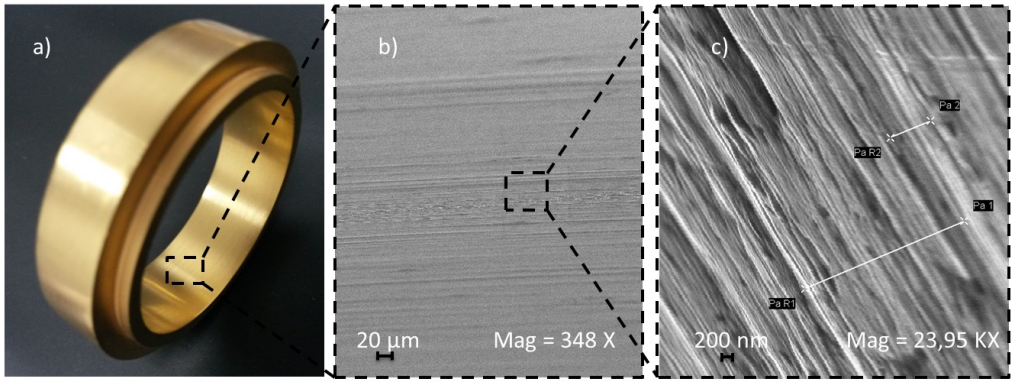

Figure 5.2: a) Photograph of one electrode of the PPT made of OFHC copper and gold-plated. b) A section of the same electrode photographed with a high-resolution scanning electron microscope. The magnification for this picture was set to 348. c) Photograph of a smaller section of the electrode with the same instrument but using a magnification of 23950. The distance between Pa1 and Pa2 is 919.6 nm, and the distance between Pb1 and Pb2 is 3651 nm. The photograph was taken with an angle of 36.9º.

Table 5.1: Outer diameter and length of the PPT electrodes. All electrodes have an inner diameter of 32 mm.

Electrode	Outer diameter (mm)	Length (mm)
Transfer electrode 1	40	224.4
Transfer electrode 2,3	40	50.1
Segmented electrodes	42	12.0
Corrections electrodes 1	42	8.25
Corrections electrodes 2	42	15.0
Central ring	42	21.5

The electrodes are staked and electrically insulated with rings made of sapphire (Al_2O_3) with a purity higher than 99.9%. High-purity sapphire presents high thermal conductivity at room temperature (41.9 W/(m·K) at 300 K) and cryogenic temperature (5000 W/(m·K) at 50 K) [98], high electrical resistivity (10^{16} m·Ohm at 298 K) and low magnetic susceptibility (-0.25 $\times 10^{-6}$) [99]. These rings, with 36 mm inner diameter, 44 mm outer one and 4 mm long, are placed between electrodes leaving a gap between two adjacent electrodes of 0.2 mm. The central ring of the PPT is eight-fold segmented in order to apply excitation techniques to the stored ions. The two correction electrodes marked as C2 in Fig. 5.1 are also two-fold segmented to allow for axial excitation, detection and coupling between the axial and radial motion. The different sections of these electrodes are separated by sapphire rods with a length of 12 mm and a diameter of 1 mm. A groove is machined in each sector to place these rods. The radial gap between the sectors is 0.2 mm. The dimensions of the electrodes of the PPT are summarized in Tab. 5.1. The green pieces in Fig. 5.1 are also made of OFHC

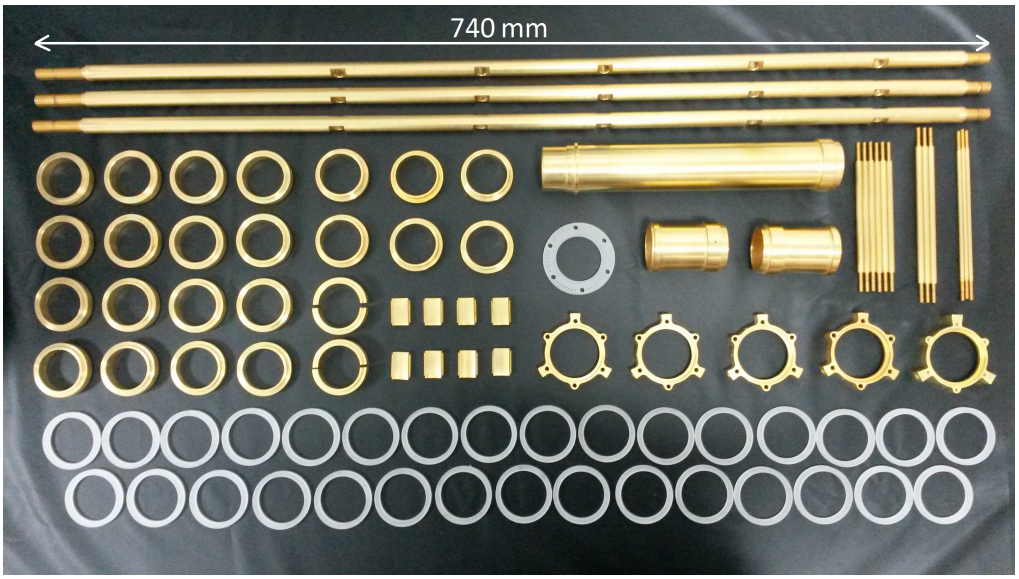

Figure 5.3: Photograph of the components of the PPT. Electrodes, insulating rings, rods and support plates are shown.

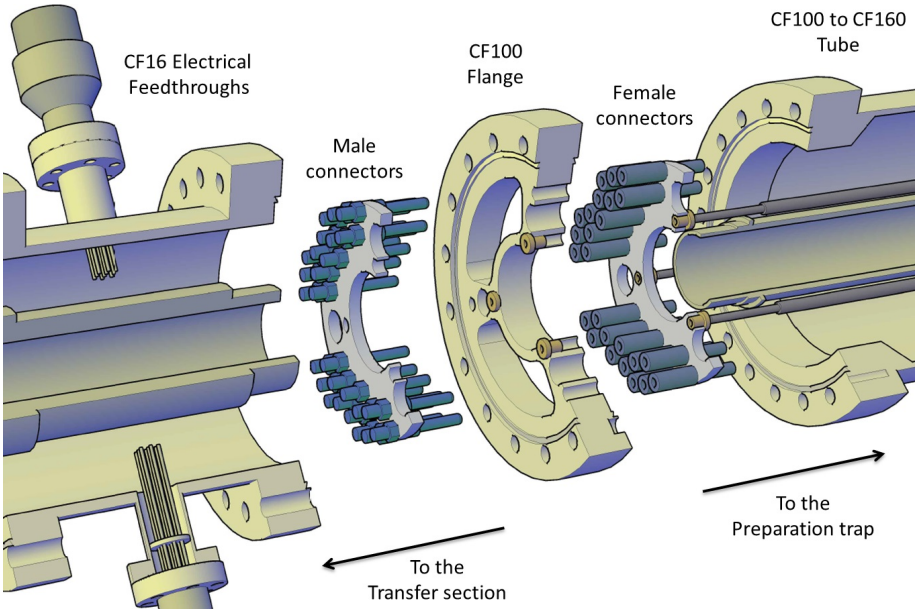

Figure 5.4: Three-dimensional drawing of a cut of the connection system in the PPT side. The male and female electrical connectors are drawn in blue.

copper and gold-plated. These plates support a stack of several electrodes. At the same time, the plates are screwed to the large rod for good alignment and stability of the full trap tower and lenses downstream and upstream of the trap. A photograph of all components of the PPT is shown in Fig. 5.3.

Connection system

The Penning trap system needs 39 electrical connections in the PPT side and 19 electrical connections in the TOF side, 5 for the TOF lenses and 14 for the open-ring trap located in the second core of the magnet. Due to the large number of connectors it was necessary to build up a mechanical push-pull connection system. Figure 5.4 shows a 3D cut of the connection system in the PPT side. This system is comprised of two plates, one with female and the other with male connectors. The connectors (Allectra 360-PPO-4) are made of beryllium copper and they are silver-plated. They are screwed to the G10 disks. The connection system on the other side of the Penning-traps system is similar (see Fig. 5.1). The disks with the female connectors are attached to the Penning trap system, and those with male connectors to the CF100 and CF160 crosses located on both sides of the tube (see Fig. 4.1). The wires are made of manganin with 0.25 mm diameter, insulated with Kapton®.

5.2 Magnetic-field alignment

The alignment of the Penning-traps system with respect to the magnetic field is important to avoid shifts in the cyclotron frequency of the stored ions [54, 100].

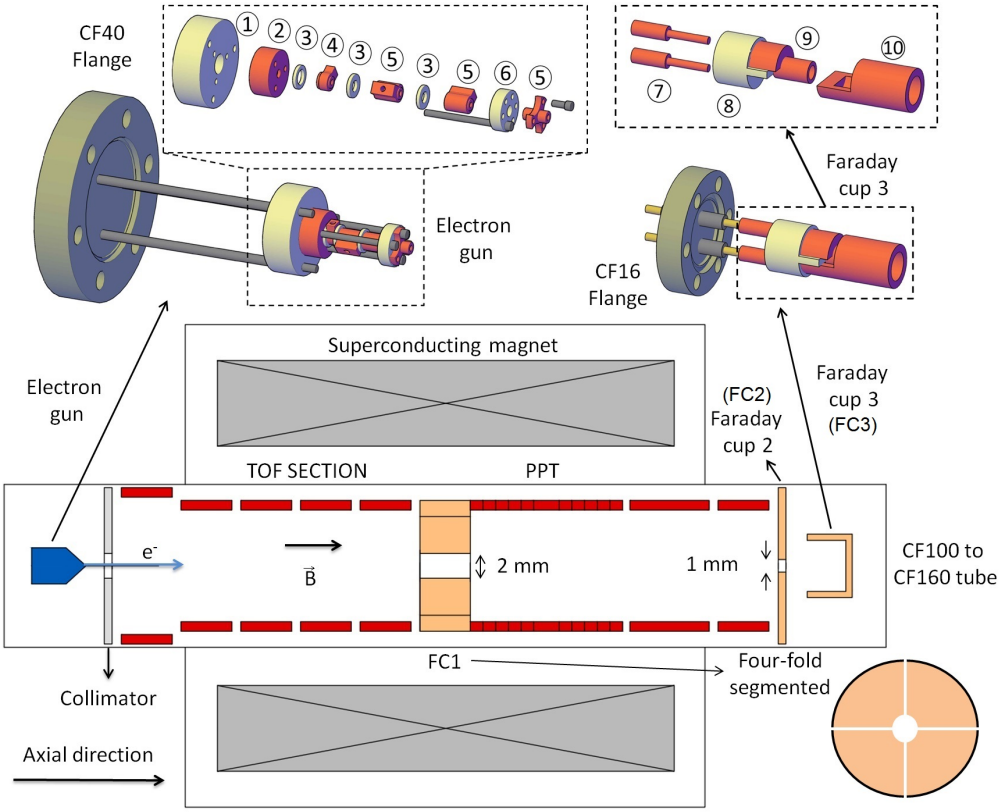

Figure 5.5: Sketch of the setup for the alignment of the PPT with the magnetic field. The electron gun (left) and miniaturized Faraday cup (right) developed within the course of this work are also shown. The electrodes and insulating pieces are shown in red and white, respectively. Insulating pieces are made of alumina (Al_2O_3) and the electrodes are made of OFHC copper. The main elements are: 1) Support 2) Grid 3) Electrical insulating rings 4) Accelerator 5) Einzel lens 6) Support and electrical insulating ring 7) Connectors 8) Support 9) Electrode to pick up the electrons 10) Grid.

A schematic layout of the setup for the alignment, with a description of the different components is shown in Fig. 5.5. An electron beam is used to align the system. Figure 5.5 shows a homemade electron gun which produces an electron beam with up to 1500 eV. The maximum electron current is ≈ 1 μA. A four-fold segmented diaphragm with 28 mm length and 2 mm inner diameter, coupled to the Penning-traps system was used as Faraday cup detector (FC1 in Fig. 5.5). A plate made of aluminum with a hole of 1 mm was used as Faraday cup detector (FC2). FC3 is a homemade Faraday cup detector with 4 mm diameter. A picoammeter (Keithley 6285) was used to read the current from the different detectors. The orientation of the vacuum tube housing the traps with respect to the magnet bore can be varied using a special support structure fixed to the bore (see Fig. 5.6). This system allows horizontal and vertical displacements of the tube with an accuracy of 0.35 mm.

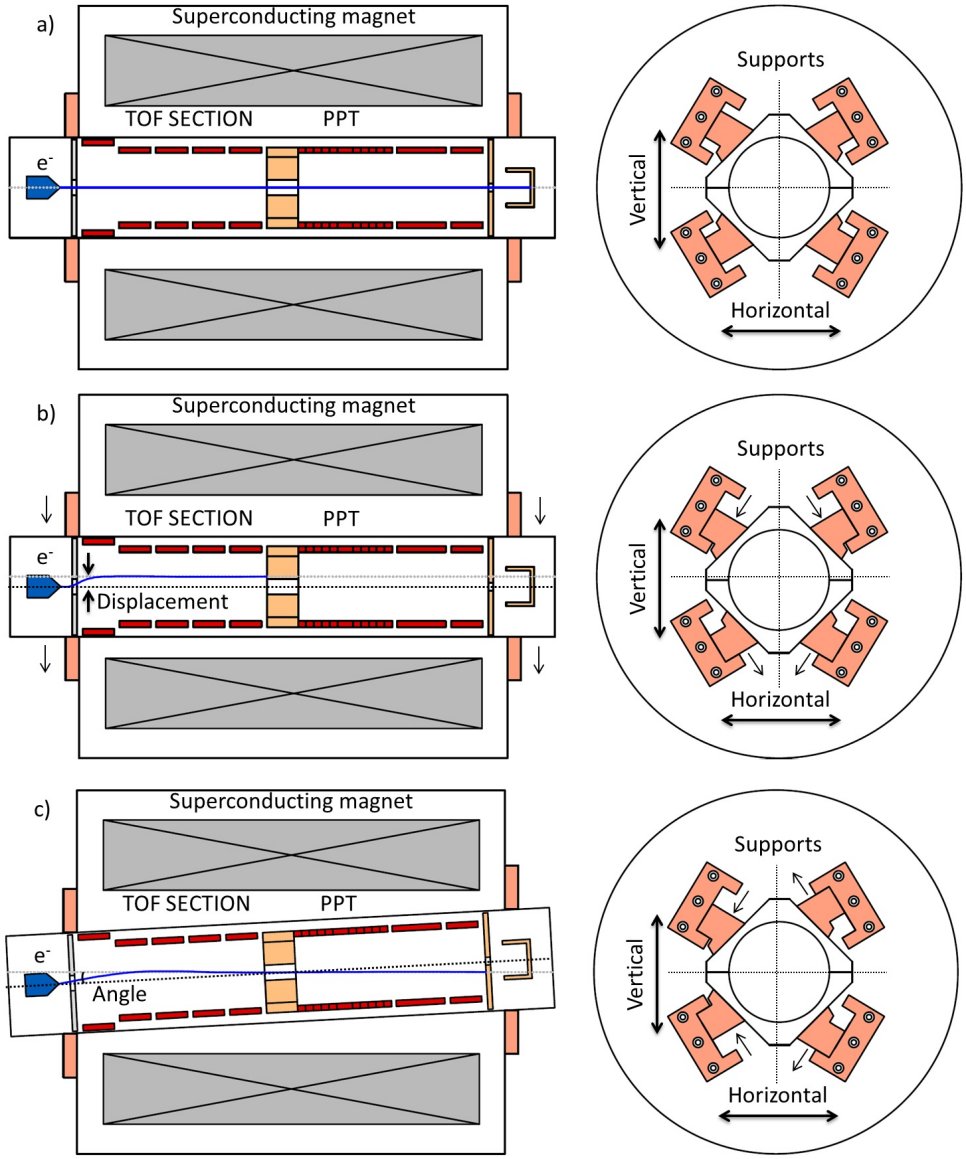

Figure 5.6: Different views showing the alignment and misalignment of the PPT with the magnetic field. The dotted black line and dottted-grey line represent the center in the radial plane along the axial direction of the PPT, and the magnetic field, respectively. The blue line shows the trajectory of the electrons. Displacements of the supports (red squares) allow the alignment of the PPT with the magnetic field. a) The PPT and the magnetic field are aligned. b) The PPT and the magnetic field are shifted in vertical position. c) The PPT an the magnetic field are misaligned with an angle.

Figure 5.7 shows the electron currents detected with the Faraday cup detectors for several positions and orientations of the tube with respect to the superconducting magnet. The electron current detected for different displacements in the horizontal and vertical directions are shown in Fig. 5.7 (top panel). After maxi-

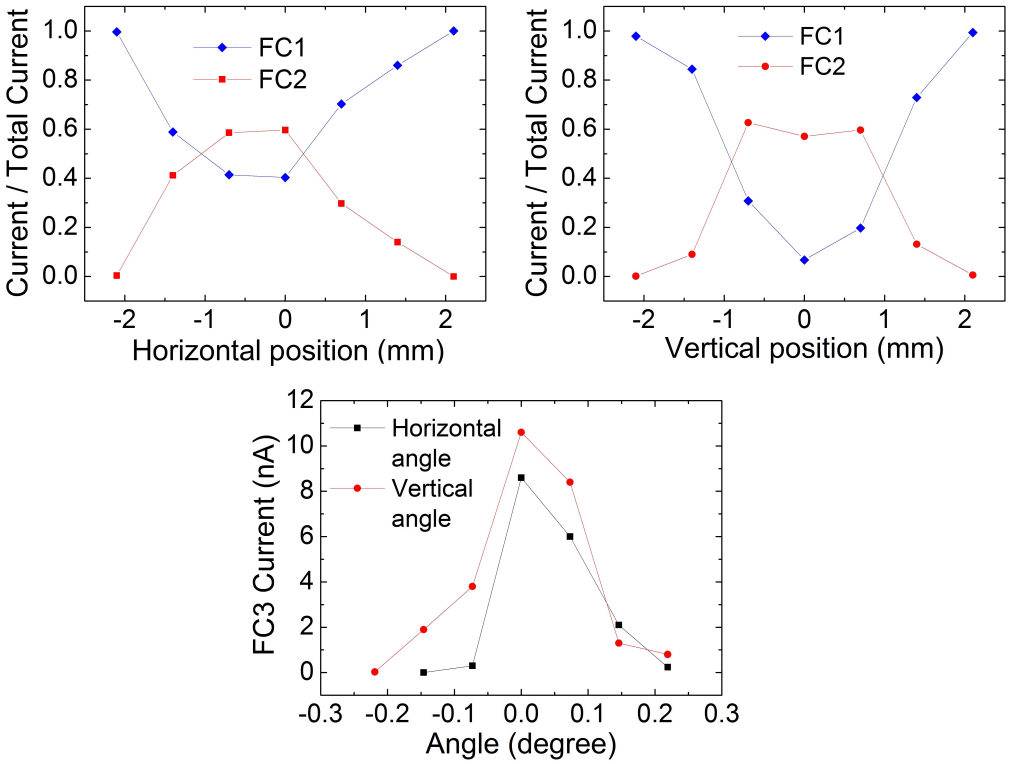

Figure 5.7: Top: Electron current detected with FC1 and FC2 for several horizontal and vertical positions of the Penning-traps system with respect to the magnetic field. The reference for the horizontal plane was taken arbitrarily parallel to the floor. The zero position has been chosen as the one for which the current detected with FC2 was a maximum or a minimum with FC1. Bottom: Electron current detected with FC3 for several orientation angles of the trap with respect to the magnetic field. The angle is defined from the center of the vacuum tube housing the trap to FC3. Zero was assigned to the angle yielding the maximum current detected with FC3.

mizing the current, the angles in horizontal and vertical directions are modified in order to further increase the electron current detected with FC3 (see Fig. 5.7 bottom panel). The center of the tube was fixed in the same position. A fine alignment allows for an angle resolution of 0.04° and a horizontal and a vertical resolution of 0.35 mm.

5.3 Pumping barrier

The main function of the PPT in the project TRAPSENSOR is to perform mass-selective buffer-gas cooling. This is done using helium as buffer gas. The gas is injected via a tube made of Teflon® with an inner diameter of 6 mm, which is connected to an aperture in the radial directions in electrode E8 in section SE1 (see Fig. 5.1). An L-shaped connector, made of G10, is screwed to the electrode

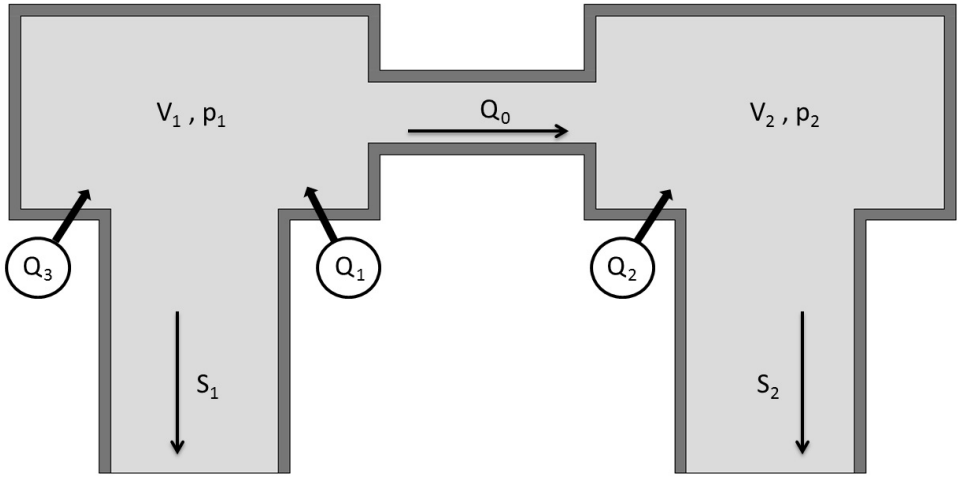

Figure 5.8: Elements taken into account to design the pumping barrier. The details are given in the text.

and connected to the tube. The other end of the tube is connected to a DN 16 ISO-KF (to outside) to 6 mm tube Swagelok® adapter in the transfer section. A bottle of helium gas with high purity ($> 99.999\%$) is connected to a gas regulating valve through a cooling coil. This is a wound of copper tube with an inner diameter of 8 mm, which is located inside a dewar with liquid nitrogen.

The pumping barrier located between the PPT and the measurement trap is an electrode with a length of 23 mm and an inner diameter of 2 mm. Figure 5.8 shows a sketch of the pumping barrier indicating the most important parameters to calculate the pressure at both sides. V_1 and V_2 are the volumes, p_1 and p_2 are the pressures, and S_1 and S_2 are the pumping speed in the PPT (1) and in the measurement trap (2), respectively. Q_1 and Q_2 are the outgassing rates. The helium gas flow through the pumping barrier is Q_0. The helium flow from the gas bottle to the PPT is represented by Q_3. The pressures in sections 1 and 2, can be expressed as a function of the time, in differential form [83]

$$V_1 \frac{dp_1}{dt} + S_1 p_1 + l(p_1 - p_2) = Q_1 + Q_3, \tag{5.1}$$

$$V_2 \frac{dp_2}{dt} + S_2 p_2 + l(p_1 - p_2) = Q_0 + Q_2, \tag{5.2}$$

$$l(p_1 - p_2) = Q_0, \tag{5.3}$$

where l is the conductance. From Eqs. (5.1), (5.2) and (5.3), the relation between the pressure p_1 and p_2 can be expressed as

$$\frac{p_1}{p_2} = \left(\frac{S_2}{l} + 1\right) + \frac{1}{p_2}\left(p_1^0 - p_2^0 - \frac{S_2}{l} p_2^0\right), \tag{5.4}$$

where p_1^0 and p_2^0 are the residual pressure in the PPT and the measurement trap due to the outgassing rates Q_1 and Q_2, respectively. The first term in Eq. (5.4)

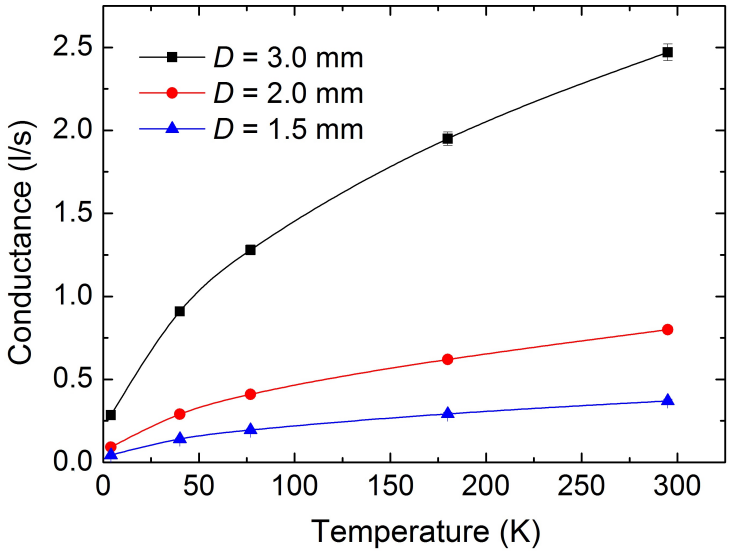

Figure 5.9: Conductance versus temperature for several diameters of the pumping barrier: 1.5, 2.0, and 3.0 mm. The length is always 23 mm and it is defined by the distance between the two homogeneous regions provided by the superconducting magnet, and the size of the traps. The conductance is calculated using a software package based on the MonteCarlo technique. The gas was helium, and temperatures of 4.2, 45, 77, 180 and 298 K were taken. 20000 events were considered in the simulations.

implies that a lower conductance appears due to an increase of the ratio p_1/p_2. The second term becomes important if the pressure in (2) is $\approx 10^{-7}$ mbar or below [101].

The conductance can be calculated using a software package based on the MonteCarlo technique, developed by Prof. Dr. E. Lux. With this software one can calculate the probability of a particle to go through an orifice with a diameter D and a length L. The input parameters are the temperature and the mass of the gas molecules. Figure 5.9 shows the conductance obtained with the software as a function of the temperature for different diameters of the pumping barrier. These results have been combined with numerical simulations using the software package SIMION® version 8.0 to optimize also the transport of the ions between the traps through the barrier.

5.4 Control system and cycles

The control system (CS) was firstly developed for the ISOLTRAP and SHIPTRAP experiments [102]. CS is an object-oriented, multi-threaded, event-driven framework with Supervisory Control and Data Acquisition (SCADA) functionality. This system allows the control on the HV power supplies, signal gener-

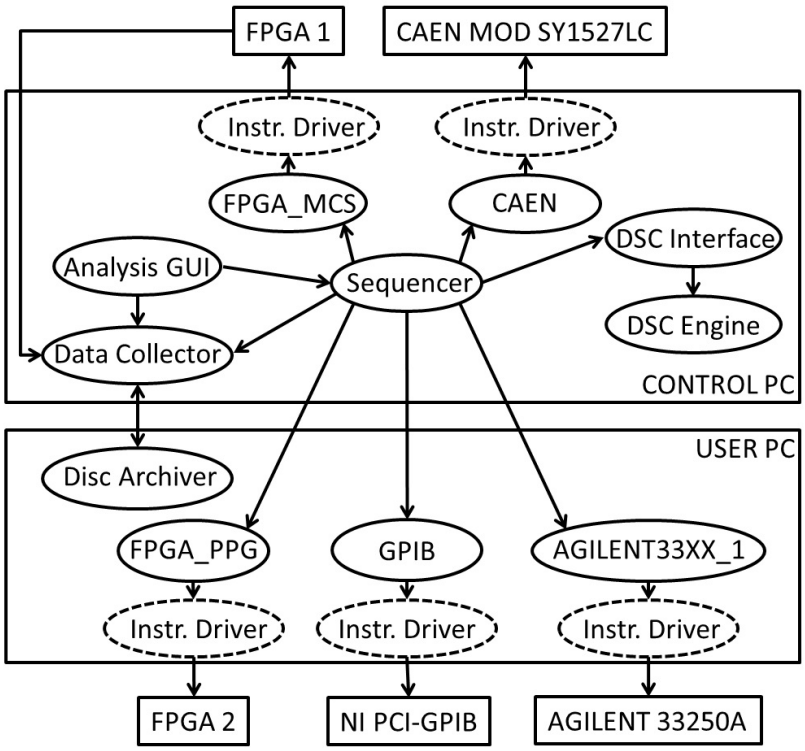

Figure 5.10: Diagram of the control system used in the TRAPSENSOR project for the Penning-traps beamline. PCs and devices are depicted by boxes with rectangular shapes, delimited by solid lines. Windows of the control system representing software are shown inside oval boxes delimited by solid lines. Oval boxes delimited by dashed lines contain the names of instrument drivers. All is running in two PCs, named CONTROL and USER PC

ators, field programmable gate array (FPGA) cards and other devices used in the TRAPSENSOR project. At the same time, the data from the experiment are analyzed and stored in disc. The system is distributed over two PCs. Figure 5.10 shows a diagram of the CS used in the TRAPSENSOR project with the CONTROL and USER PC. The *Sequencer* is the most important part of the CS. The sequencer calls to the different devices and software, configure and initialize the hardware devices and stop the measurement if encounters problems. The graphical user interface (GUI) is used to analyze the data from the *Data Collector*, and send the initial values to the *Sequencer*. The *Data Collector* picks up the data from the FPGA 1 (see Fig. 5.14), and the streaming data are sent to the *Disc Archiver*, which writes it in the 1 TB hard disk of the USER PC. The *DSC Engine* (Datalogging Supervisory Control) serves for trending and alarming of the status of the software and devices. The *DSC Interface* is the interface with the *DSC Engine*. The FPGA 2 is used as pulse pattern generator, i.e., to generate the TTL signals of the measurement cycles. The DC voltages for the PPT electrodes and the elements in the whole beamline are delivered by a CAEN SY1527LC power supply. The RF voltages for excitation of the ions motion are delivered by signal generators from Agilent (33250A). Finally, a

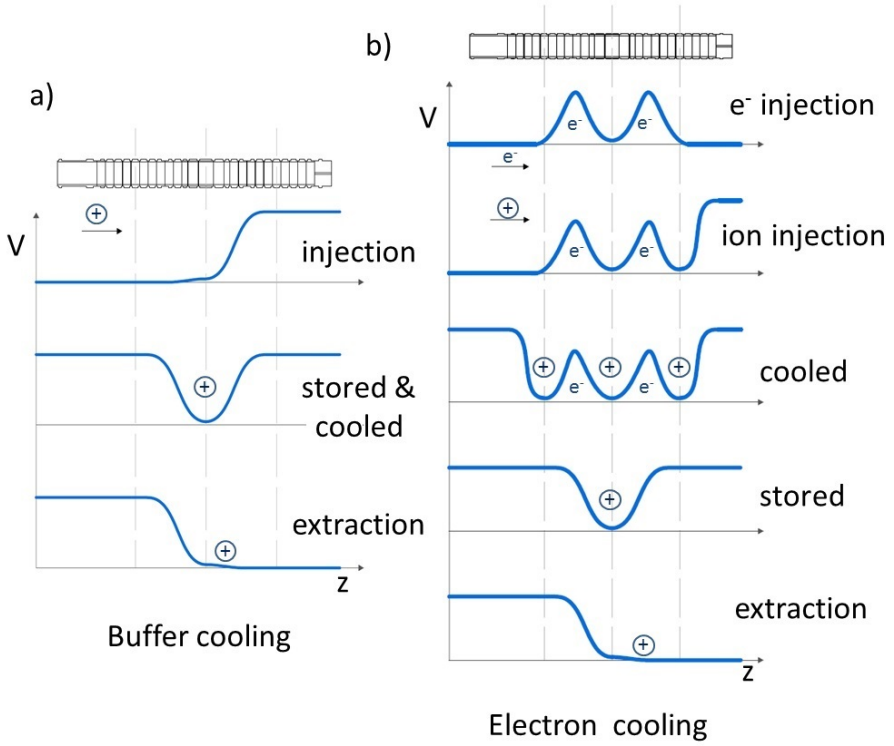

Figure 5.11: a) Simplified time sequence to apply the buffer-gas cooling technique in the PPT. b) Simplified time sequence to apply the electron cooling in the PPT. A drawing of the trap is shown on top.

high-performance peripheral component interconnect (PCI) to general purpose instrumentation bus (GPIB) from national instrument (NI) can be used to control up to 14 devices with GPIB interface.

The parameters for the measurement cycles are controlled by the *Analysis GUI* of the CS. This *Analysis GUI* allows performing scans of different parameters and any kind of timing sequence. Time, voltage or frequency can be scanned during a measurement. A measurement cycle can be repeated as many times as necessary. Figure 5.11 shows the working cycles used to inject, store, cool and eject out the ions from the PPT for mass-selective buffer-gas cooling and for electron cooling. Currently, only mass-selective buffer-gas cooling is performed, although the system has been built considering later the possibility to apply electron cooling. The homemade electron source used for the magnetic-field alignment can be located in the quadrupole deflector in the transfer section (see Sec. 4.7) and will allow the injection of the electrons in the PPT. Electrons at ≈ 50 eV will be stored in the negative potential wells of the PPT. The electrons are self-cooled in a Penning trap due to the the radiation damping of the cyclotron motion. A time constant $\alpha_c^{-1} \approx 50$ ms (see Eq. (2.33)) is obtained for a magnetic field $B = 7$ T.

5.5 Electronics

The power supplies and electrical connection for the whole Penning-traps beamline were shown in Fig. 4.12. Figure 5.12 shows the devices for the electrical signals and how they are applied to the PPT electrodes. The TTL signals from

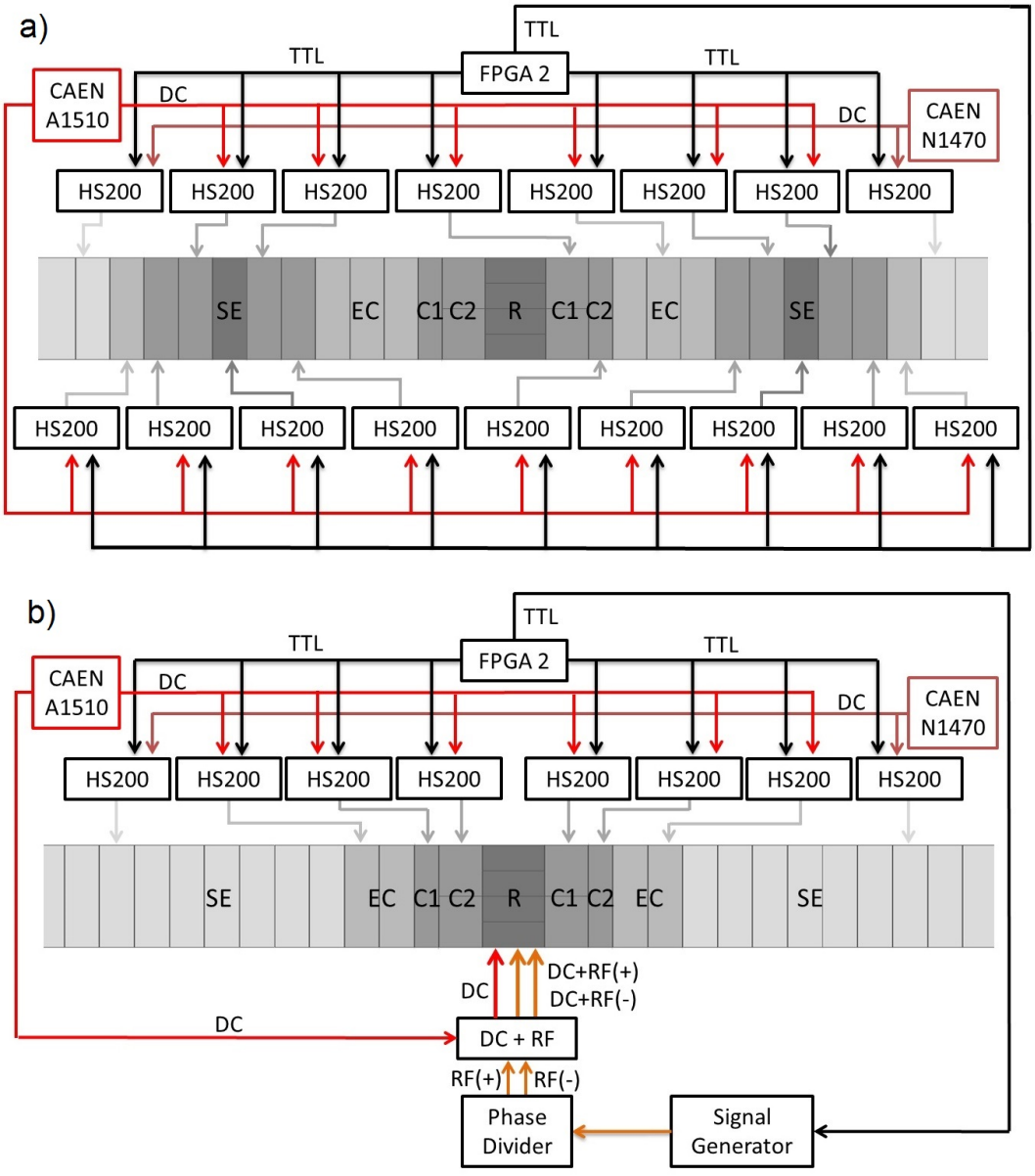

Figure 5.12: Electrical connections and the devices to run the PPT. HS200 stands for high-voltage switch. The TTL signals to drive the switches to inject and extract the ions, are represented by black arrows. The DC voltages applied to the electrodes are depicted by red and brown arrows. The voltages to the electrodes are drawn in grey. a) Diagram for electron cooling. b) Diagram for buffer gas cooling. Dark orange arrows represent the RF voltage connections.

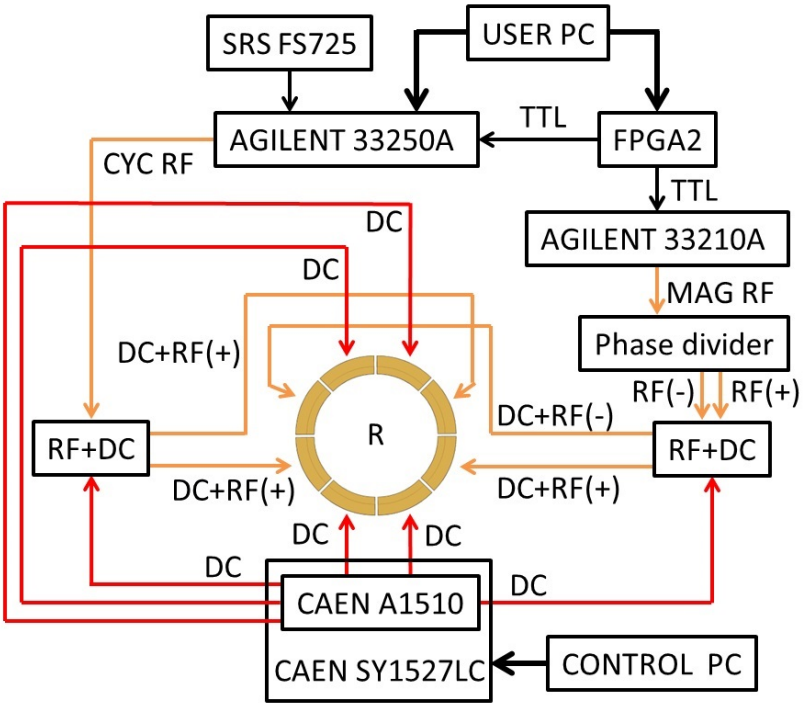

Figure 5.13: Diagram detailing the voltages applied to the central ring electrode.

FPGA2 are connected to the low noise high-voltage switches acting as the control input, to define the on time. HV switches (model HS200 from Stahl electronics) provide voltage differences between the two levels of the switch of up to 200 V, with a rise time of 25 ns. The DC voltages applied to the endcaps, correction and central ring electrodes are delivered by the CAEN A1510 power supply. These voltages are used to perform the trapping potential along the z-axis. The DC potential to capture the ions is given by the CAEN N1470 power supply.

The RF voltages are applied to the central ring electrode for magnetron and cyclotron excitation. Two signal generators are used. Figure 5.12 shows a sketch of the voltages and devices, and Fig. 5.13 a detailed one for the central ring. TTL signals from FPGA2 are connected to the signal generators to provide external trigger. Agilent 33210A and 33280A function generators with up to 10 MHz and 80 MHz maximum frequencies are used in burst mode to generate the magnetron and cyclotron excitation fields, respectively. A 10 MHz rubidium frequency standard (SRS FS725) is connected to the Agilent 33280A function generator to provide a stable and accurate cyclotron frequency determination. The magnetron excitation signal is split using a circuit with two operational amplifiers AD811AN with high bandwidth (140 MHz, 3 dB at gain equal one) and low voltage noise (1.9 nV/$\sqrt{\text{Hz}}$). This circuit has been assembled following the design presented in Ref. [103]. All segments of the central ring are connected at the same DC voltage source. Two opposite segments of the central ring are used for magnetron excitation. The DC voltage for trapping is coupled to two radiofrequency signals, which have a phase difference of 180° between each other

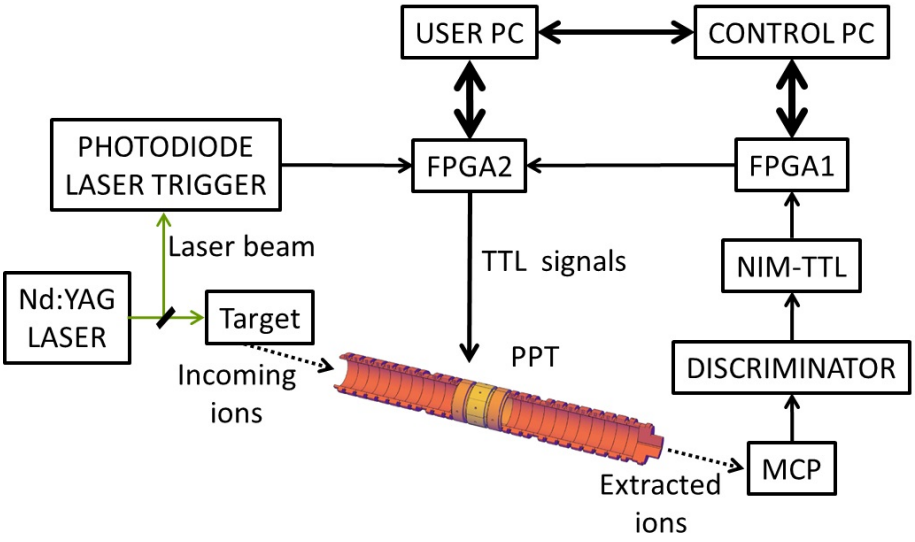

Figure 5.14: Elements utilized for data acquisition.

to perform a dipole field. Another two opposite segments are used to perform cyclotron excitation. The DC voltage is coupled to two radiofrequency signals identical, and applied to opposite segments to perform the quadrupole field. The coupling between the DC and the radiofrequency voltages is accomplished by means of a capacitor (C) in parallel with a resistor (R). For magnetron excitation, $C = 10$ nF and $R = 33$ kΩ, and for cyclotron excitation, $C = 4.7$ nF and $R = 20$ kΩ.

Figure 5.14 shows the elements for the ion detection and signal processing. The ion signal from the MCP detector is attached to a CAEN N840 discriminator. The output NIM logic signal from the discriminator is fed into a CAEN N89 NIM-TTL-NIM adapter and the output TTL signal is delivered to the FPGA1 and recorded with the CS. At the same time, the trigger signal from a photodiode located in the laser-desorption ion source is connected to the FPGA2 and it is used as the trigger for the Analysis GUI of the CS. A delay of the trigger signal can be performed with the Analysis GUI for measurements with stored ions.

Chapter 6

Characterization of the preparation Penning trap

Following the construction and commissioning of the Penning-traps beamline, a full characterization of the Preparation Penning trap (PPT) for the TRAPSENSOR facility was performed, using targets with natural isotopic compositions from calcium and rhenium so as to cover a huge mass spectrum. Mass-selective buffer-gas cooling was applied providing cooled ion samples from the trap. The full characterization of the PPT will be presented in this chapter showing that the device meets the requirements for its use at the TRAPSENSOR facility.

6.1 Potential shape along the z-axis

The potential to trap the ions along the trap axis is shown in Fig. 6.1. The electrodes shown in clear grey in Fig. 6.1 are used to catch the ions in the first high-homogeneous region of the superconducting magnet. A voltage between 200 and 220 V is applied to these electrodes to capture the ions produced with the laser-desorption ion source. The initial kinetic energy of 500 eV, is reduced to about 200 eV before entering the trap (see Fig. 4.9). This potential allows for axial confinement between z = -75 and z = 75 mm. The minimum of the potential is about 7.3 V with respect to ground. This potential was kept as small as possible in order to apply smaller DC voltages to the endcaps electrodes of the QS system to trap the ions.

The electrodes on the left side of the central electrode in Fig. 6.1 (labeled as A) were connected to ground for injection. Using several HV switches (see Fig. 5.12), the voltages on the electrodes were applied when the ions were inside the trap. For the extraction of the ions, the electrodes on the right side of the central electrode in Fig. 6.1 (labeled as B) were connected to ground. The kinetic energy of the extracted ions is defined from the potential of about 5.4 V with respect to ground in the center of the trap in extraction mode.

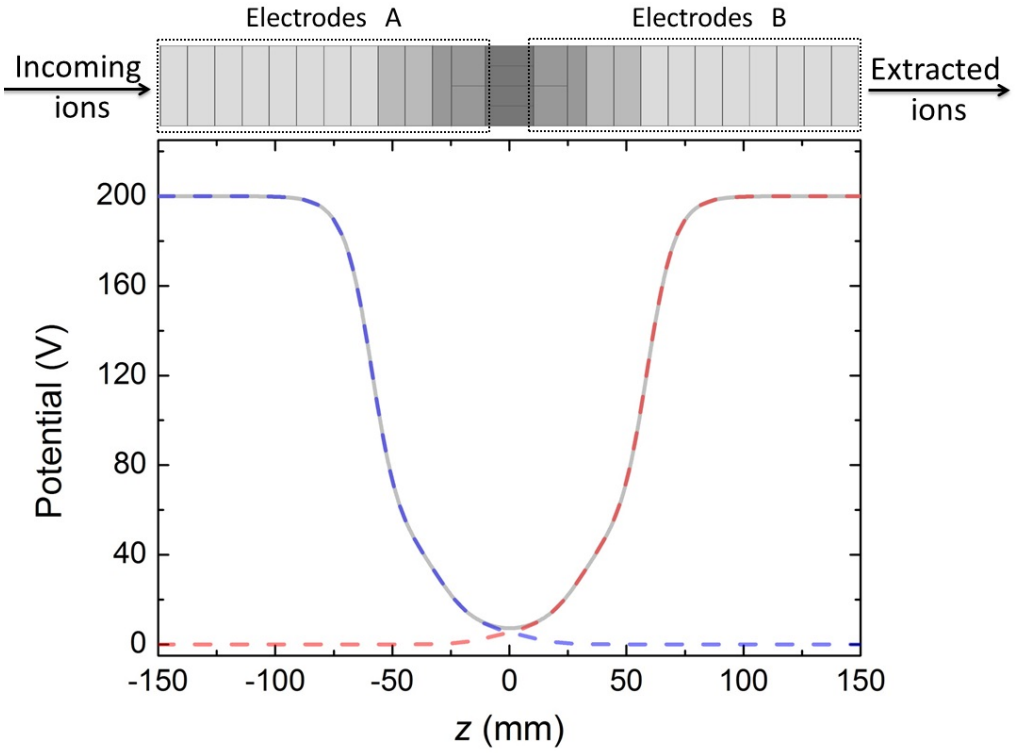

Figure 6.1: Top: Longitudinal view of the PPT. The central ring, correction electrodes 2, correction electrodes 1, endcaps and segmented electrodes are shown in grey. The electrodes on the left and right side of the central electrode are labeled as electrodes A and B, respectively. Bottom: Potential shape along the z-axis obtained using SIMION® version 8.0, for injection (dashed-red line), capture (solid-grey line) and ejection (dashed-blue line). The voltages are listed in Tab. 6.1.

The voltages applied to the electrodes of the trap are listed in Tab. 6.1. They are chosen to provide a good harmonic potential [104, 105] along the trap axis, which follows, close to the trap center, the equation

$$V(z) \approx C_0 + C_2 z^2 + C_4 z^4 + \ldots, \tag{6.1}$$

with C_0 = 7.26 V, C_2 = 0.021 V/mm^2 and C_4 = -1.74 $\times$ 10^{-6} V/mm^4. The odd coefficients are zero due to the symmetry of the trap. The characteristic trap dimension is $d_0 \approx 26$ mm and the trap depth is $U_{\mathrm{DC}} \approx 28$ V. The ions are confined in this region when their energy is reduced due to collisions with buffer-gas atoms.

6.2 Determination of the characteristic frequencies

A calcium target was used firstly for the determination of the eigenfrequencies of the stored ions, due to the importance of the $^{40}Ca^+$ isotope for the TRAPSENSOR project. After the ions are stored in the PPT, they are cooled in the axial

Table 6.1: Voltages applied to the PPT electrodes for injection, trapping and extraction of the ions. Electrodes are labeled according to Fig. 5.1 and 6.1.

	Voltage		
Electrode	Injection	Trapping	Extraction
Segmented electrodes A	0 V	200 V	200 V
Endcap electrodes A	0 V	45 V	45 V
Correction electrode 1 A	0 V	29.58 V	29.58 V
Correction electrode 2 A	0 V	9.78 V	9.78 V
Central Ring	5 V	5 V	5 V
Correction electrode 2 B	9.78 V	9.78 V	0 V
Correction electrode 1 B	29.58 V	29.58 V	0 V
Endcap electrodes B	45 V	45 V	0 V
Segmented electrodes B	200 V	200 V	0 V

direction due to collisions with helium atoms. The diameter of the reduced-cyclotron orbit also decreases during this time, while the diameter of the magnetron orbit becomes larger (see Sec. 2.3). After this waiting time, referred to as axial cooling, a varying dipole field in resonance with the magnetron motion is applied in the radial direction, resulting in an orbit for the magnetron motion of the stored ions larger than the diameter of the diaphragm. This will prevent the extraction of the unwanted ions out of the trap.

The upper panel in Fig. 6.2 shows the number of detected counts as a function of the frequency of the radial dipole field applied to the ions in the PPT. The measurement is the accumulation of 21 scans. The calcium ion beam was injected into the PPT with a kinetic energy of 200 eV. Prior to the radial field, an axial cooling time of 100 ms and a helium gas pressure of 8×10^{-8} mbar were used. The pressure was measured using a vacuum gauge located in the transfer section indicated in Fig. 4.11. Due to the gas load, the total number of detected counts decreases and the dispersion in the number is high. In addition, when the external field is in resonance with the magnetron frequency, the amplitude of the magnetron orbit increases and the number of extracted ions decreases. The field was applied for 50 ms (excitation time) and the amplitude was 70 $\mathrm{mV_{pp}}$. The Gaussian fit in Fig. 6.2 yields a magnetron frequency of $\nu_- = 452(1)$ Hz with a $FWHM = 20(3)$ Hz. The lower panel of Fig. 6.2 shows the number of counts as a function of the amplitude of the dipole field when the frequency was fixed to 452 Hz. The number of counts drop almost to zero for a excitation amplitude of 70 $\mathrm{mV_{pp}}$.

The maximum energy of the ions in the potential well (see Fig. 6.1) decreases due to the collisions with the helium atoms, and thus the axial frequency will be smaller according to Eq. (2.11). This will originate an increase of the reduced-cyclotron frequency and a decrease of the magnetron one. Both frequencies are related to the potential well and between them by

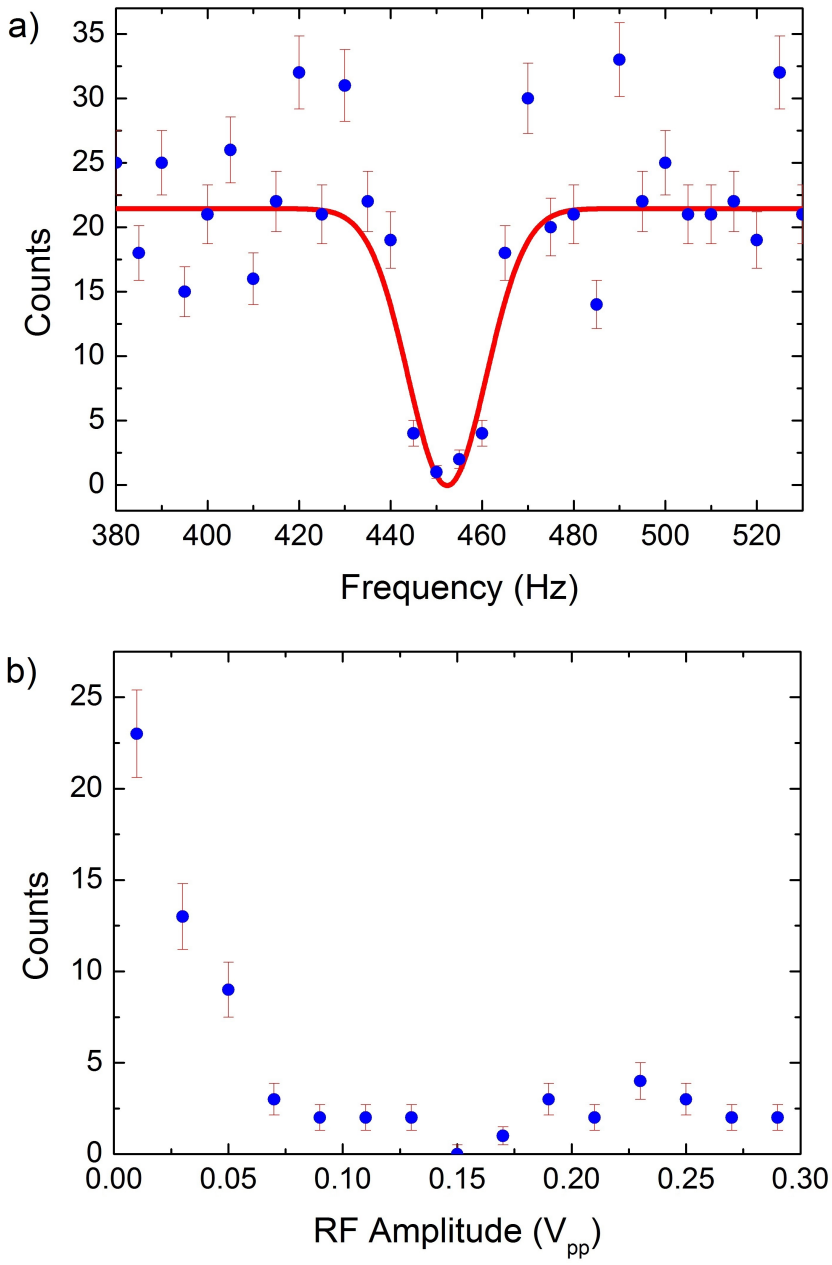

Figure 6.2: a) Detected counts as a function of the frequency of the dipole field applied radially in the center of the PPT. The red line represents a Gaussian fit to the data ($\nu_- = 452(1)$ Hz and $FWHM = 20(3)$ Hz). b) Counts as a function of the amplitude of the dipole field for a frequency of $\nu = 452$ Hz.

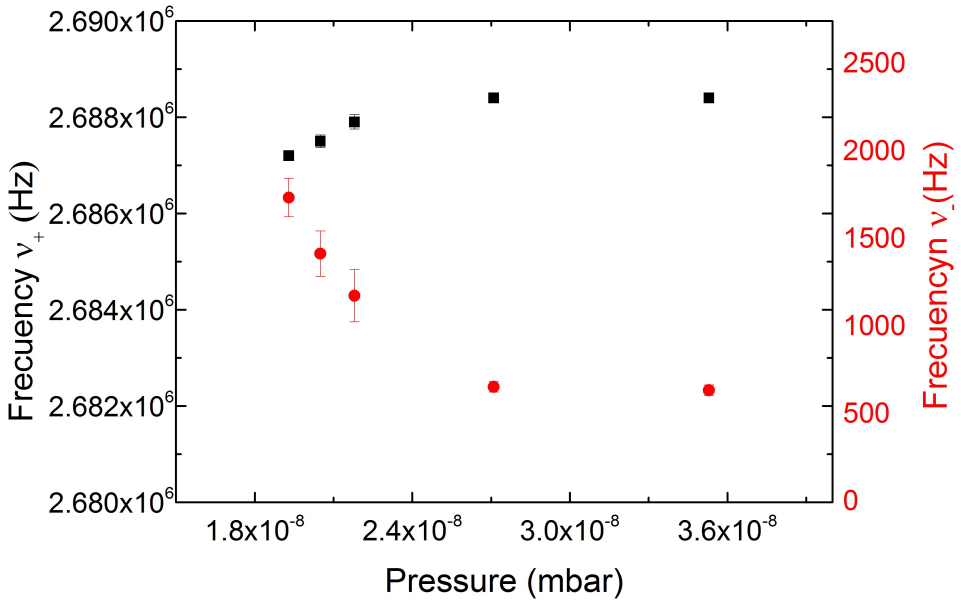

Figure 6.3: Reduced-cyclotron frequency (black squares) and magnetron frequency (red circles), for calcium ions stored in the PPT, as a function of the helium-gas pressure. The axial cooling and excitation times were 100 and 50 ms, respectively, as in Fig. 6.2. Without helium-gas, the background pressure was 1.9×10^{-8} mbar.

$$\omega_+ = \frac{qU}{md_0^2}\frac{1}{2\omega_-},$$

obtained from Eqs. (2.11) and (2.16). The cyclotron frequency is constant. In an ideal Penning trap, $\omega_c = \omega_+ + \omega_-$, which holds also if the relative uncertainty in the cyclotron frequency is above $\approx 10^{-9}$. One can observe this in Fig. 6.3 for several helium-gas pressures.

6.3 Cooling resonances for different ion species

Figure 6.4 shows the time sequence used for mass selective buffer gas cooling in the PPT. The axial cooling time required for rhenium ions was 150 ms, while for calcium ions, due to its lower mass, was only 100 ms as mentioned above. After axial cooling, dipole excitation at the magnetron frequency is performed with an amplitude of 70 mV_{pp} for calcium ions. An amplitude of 150 mV_{pp} has been determined for rhenium ions in the same way as for calcium ones (see section above). The magnetron frequency for rhenium ions was 470 Hz with a $FWHM = 15(4)$ Hz. Once the magnetron orbit has been increased for all the ions stored in the trap, a quadrupole field at the cyclotron frequency of an specific ion species is applied, and will allow centering these ions in the trap (see

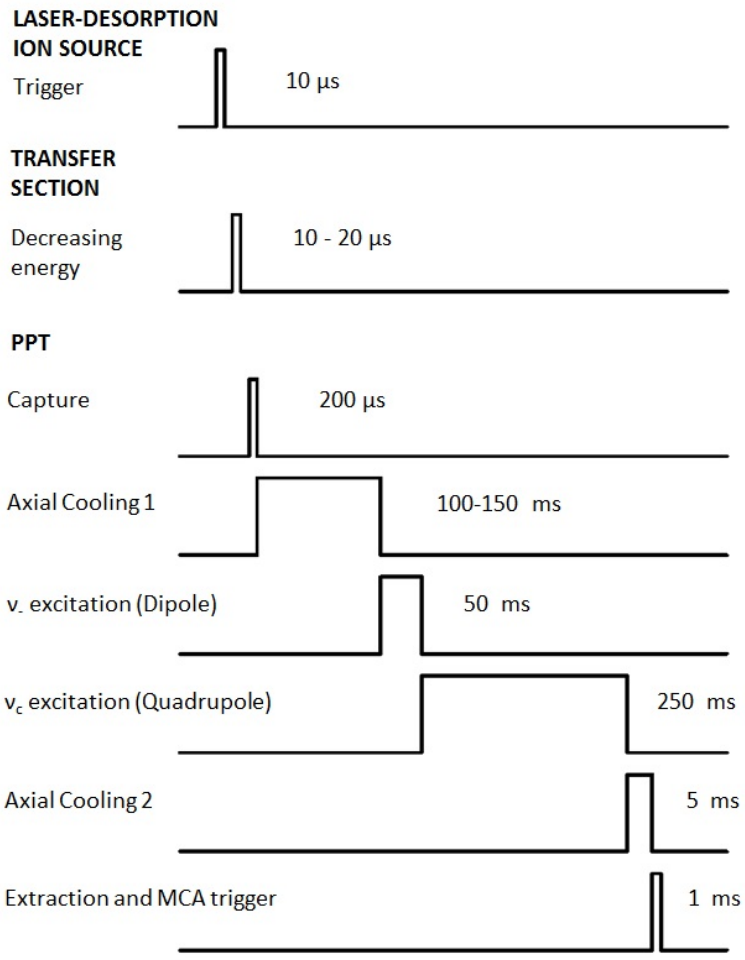

Figure 6.4: Timing sequence for a cooling resonance in the PPT.

Sec. 2.3), while leaving unaltered the other ion species. After this, further axial cooling takes place before the ions are extracted from the trap. The helium-gas pressure was varied between 2.7×10^{-8} and 1×10^{-7} mbar. Outside this range, cyclotron resonances were not obtained, within it, measurements of the cyclotron frequency were constant ($\pm$ 3 Hz). A helium pressure of about 9×10^{-8} mbar was used for the measurements following the time sequence shown in Fig. 6.4.

Figure 6.5.a shows the number of detected $^{40}Ca^{+}$ ions as a function of the frequency of the quadrupole field when this frequency is varied around the cyclotron one for $^{40}Ca^{+}$. The measurement is the accumulation of 20 scans. The amplitude of the quadrupole field was 200 mV_{pp} and the excitation time 250 ms. The Gaussian fit of the data yields a cyclotron frequency ν_c = 2689067.5(3) Hz and a $FWHM$ = 10.1(5) Hz, which corresponds to a resolving power $m/\Delta m$ = 2.7 $\times$ 10^5. The centering time depends on the amplitude of the quadrupole excitation (see Eq. (2.25)), and the excitation time and the detuning (see Fig. 3.2). For a lower excitation amplitude, a shorter detuning is required, if the excitation

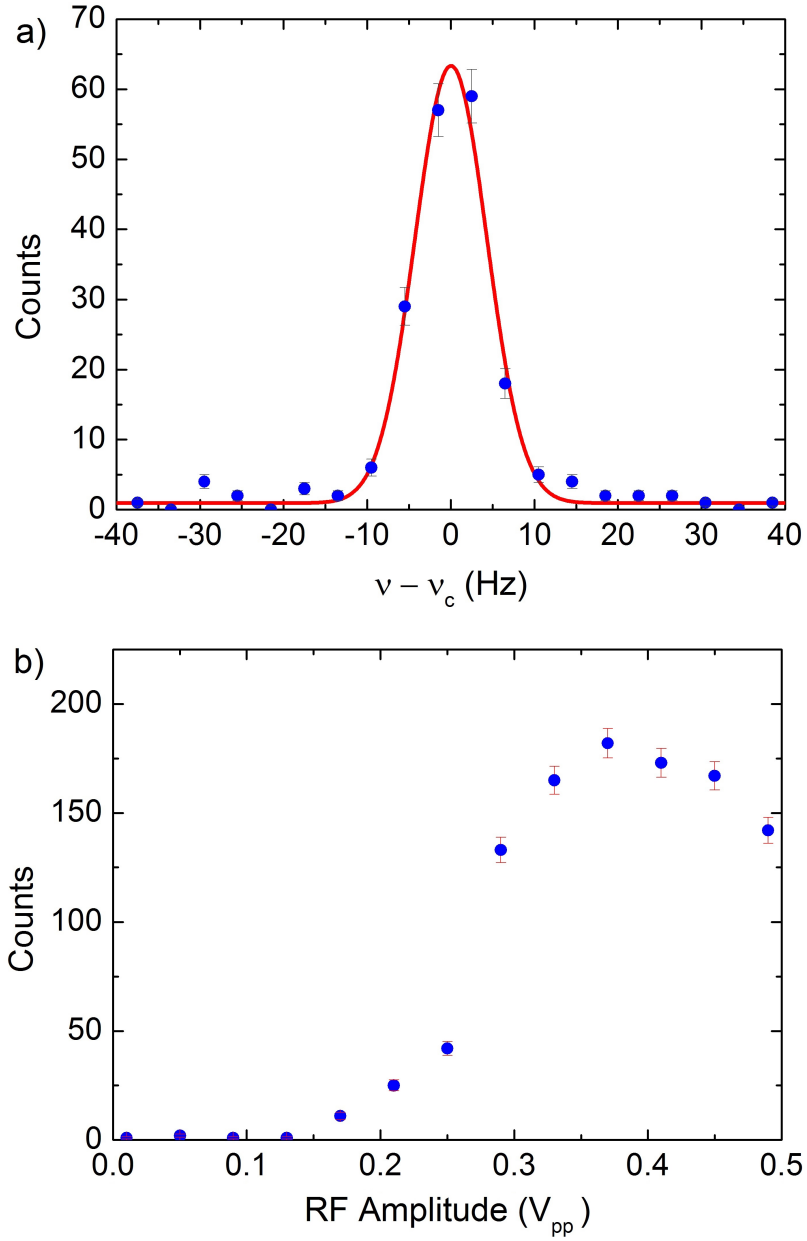

Figure 6.5: a) Cooling resonance for $^{40}Ca^{+}$. Counts as a function of the quadrupole excitation applied to the central ring of the PPT. The red line is a Gaussian fit to the data yielding $m/\Delta m = 2.7 \times 10^5$. b) $^{40}Ca^{+}$ counts as a function of the amplitude of the quadrupole field for the central frequency. Further details are given in the text.

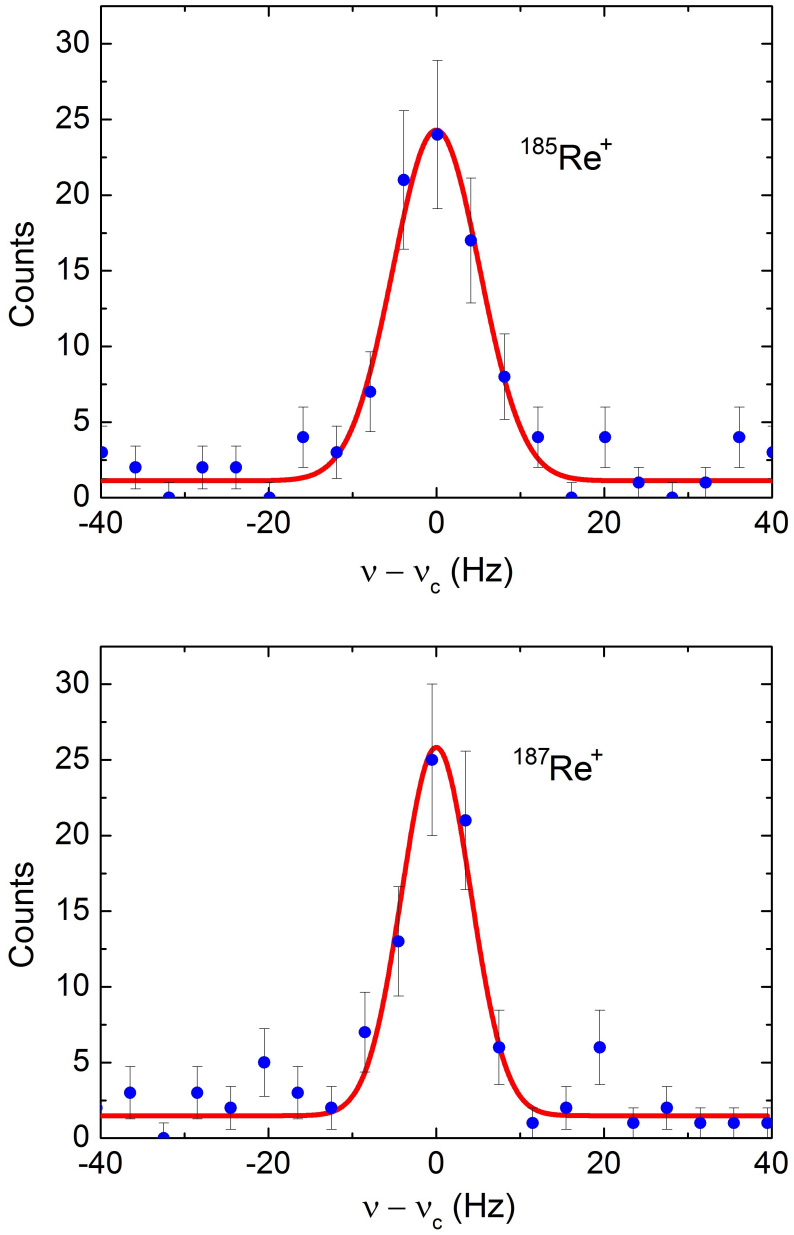

Figure 6.6: Cooling resonances for $^{185}Re^{+}$ (top) and $^{187}Re^{+}$ (bottom). Counts as a function of the quadrupole excitation applied to the central ring of the PPT. The red line is a Gaussian fit to the data. The results from twenty frequency scans were recorded for each measurement.

time remains constant. Figure 6.5.b shows the number of counts as a function of the amplitude of the quadrupole field for a frequency $\nu = 2689067.5$ Hz. Although, the amplitude to increase the number of extracted ions from the measurements is around 300 mV_{pp}, an amplitude for the quadrupole excitation of about 200 mV_{pp} allows better resolving power.

Cooling resonances for $^{185}Re^{+}$ and $^{187}Re^{+}$ ions are shown in Fig. 6.6 (top and bottom panel, respectively). The amplitude of the quadrupole excitation was 250 mV_{pp} and the excitation time was 250 ms. The Gaussian fits yields $\nu_c = 574794.5(5)$ Hz with $FWHM = 10(1)$ Hz for $^{187}Re^{+}$, and $\nu_c = 581017.9(7)$ Hz with $FWHM = 12(1)$ Hz for $^{185}Re^{+}$. The resolving power $m/\Delta m$ is 5.7×10^4 and $m/\Delta m = 4.8 \times 10^4$ for $^{187}Re^{+}$ and $^{185}Re^{+}$, respectively.

Taking into account a difference of 4σ between two adjacent cooling resonances, the sensitivity of the PPT is of about ≈ 20 Hz. Different isotopes or charge states can be easily distinguishable (see Fig. 6.6). Isobaric mass separation will depend on the nuclei under investigation. For example, a frequency difference of 214 Hz is expected for the $^{48}Ca^{+}$-$^{48}Ti^{+}$ ion-pair, which is being studied by several collaborations [106, 107], since ^{48}Ca is a candidate for neutrinoless double-β-decay. The mass-selective buffer-gas technique can be applied in the PPT to this ion-pair. ^{48}Ca is a very long-lived nuclei and can be measured off-line, although, the target need to be enriched due to the low isotopic abundance of ^{48}Ca (0.19%).

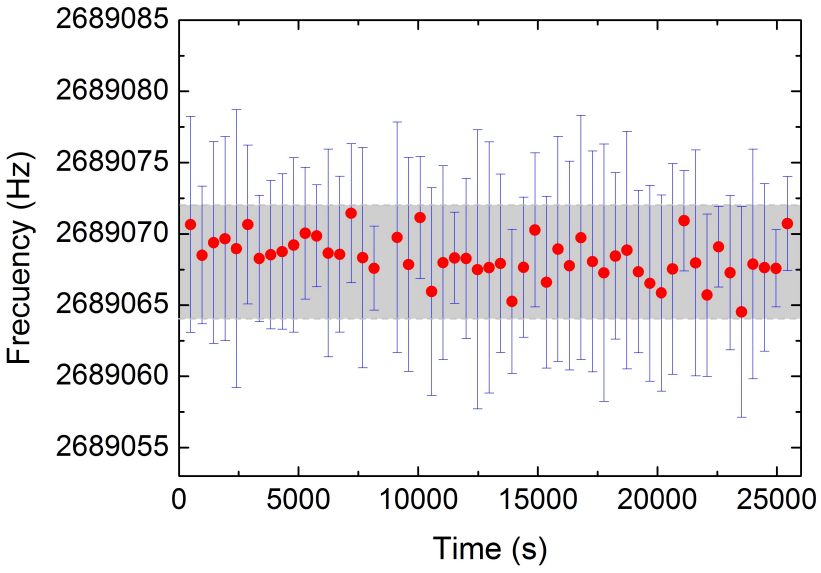

Figure 6.7: Cyclotron frequency values obtained from cooling resonances of $^{40}Ca^{+}$ ions over several hours, to monitor the magnetic field stability. The grey band is the result of adding and subtracting the uncertainty of 1σ to the weighted mean of the measured values.

Table 6.2: Cyclotron frequencies for $^{40}Ca^{+}$, $^{185}Re^{+}$ and $^{187}Re^{+}$ versus their atomic masses [108]. The magnetic field is calculated using Eq. (2.12).

Element	Mass (u)	ν_c (Hz)	$FWHM$ (Hz)	B (T)
$^{40}Ca^{+}$	39.962590864(22)	2689067.5(3)	10.1(5)	6.99800(3)
$^{185}Re^{+}$	184.9529545(13)	581017.9(7)	12(1)	6.99793(14)
$^{187}Re^{+}$	186.9557501(16)	574794.5(5)	10(1)	6.99794(12)

$^{48}Ti^{+}$ is a stable nuclei with a isotopic abundance of 73.72%.

Table 6.2 shows the cyclotron frequencies for $^{187}Re^{+}$, $^{185}Re^{+}$ and $^{40}Ca^{+}$ ions obtained after applying the mass selective buffer-gas cooling technique versus their atomic masses [108]. A magnetic field of 6.99796(14) T is calculated from the cyclotron frequencies and their atomic mass.

The stability of the magnetic field was also monitored during several hours by measuring the cyclotron frequency of $^{40}Ca^{+}$ ions from the cooling resonances. Figure 6.7 shows the cyclotron frequency for $^{40}Ca^{+}$ ions measured every 8 minutes approximately. Thus, each data point is the result from 20 cycles. The total time is above seven hours and no trends above 3 ppm are observed.

6.4 Ion energy distribution

The trapped ions exchange their energy with the helium atoms due to the collisions. The helium atoms will be at the temperature of the vacuum vessel, which will define the minimum achievable temperature for the trapped ions [109]. Since the trapped ions are not in thermal equilibrium with the helium atoms for short cooling times, the energy distribution of ions in the Penning trap can not be expressed by a classical Boltzmann distribution [110]. However, the interaction between the trapped ions with the helium atoms can be described using a viscous-drag model (see Sec. 2.3). The axial energy of the ions is given by

$$E_z(t) = \frac{1}{2} m \left[\omega_z \rho^z(t)\right]^2 . \tag{6.3}$$

Using Eq. (2.28) and Eq. (2.11), this equation can be rewritten as

$$E_z(t) = \frac{qU}{2d_0^2} \left[\rho^z(0) e^{-\alpha_z t}\right]^2 = E_z(0) e^{-2\alpha_z t}. \tag{6.4}$$

An estimation of the ions' energy in the PPT was deduced after applying a different kind of extraction (see Fig. 6.8). A digital delay generator (Stanford Research System model DG645) was used to deliver the voltages stepwise with a delay of a few tens of μs between the different values.

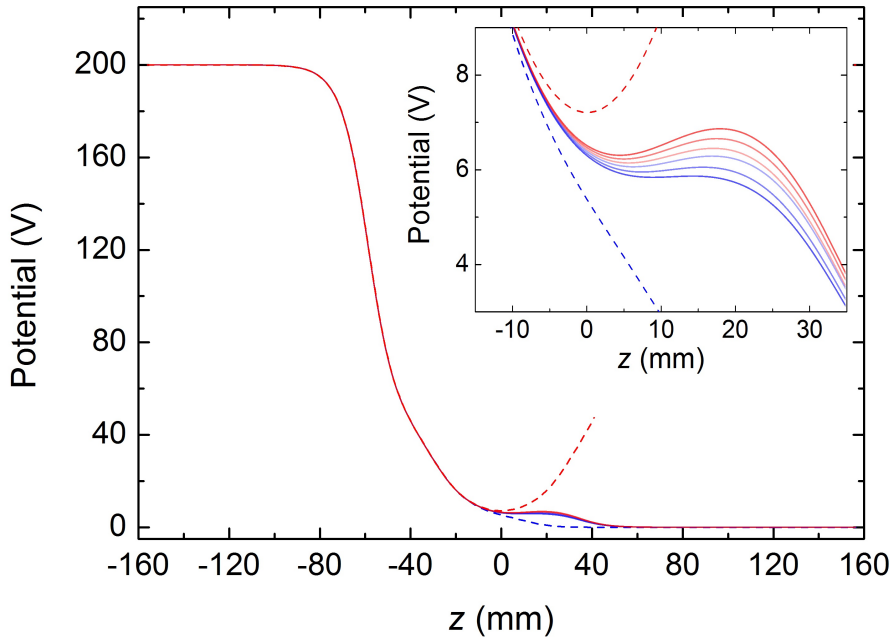

Figure 6.8: Potential shapes along the z axis utilized to extract the ions stepwise from the PPT. They have been obtained using SIMION® version 8.0. The red and blue solid lines represent the potentials along the z axis when applying 8, 7.7, 7.4, 7.1, 6.8 and 6.4 V to the correction electrodes 1B and 2B (shown in Fig. 6.1). The red and blue-dotted lines depict the potential shapes used for trapping and for the fast extraction of the ions, respectively. The bottom of the potential well is zoomed in the upper right side.

Figure 6.9 shows the TOF spectrum of $^{40}Ca^{+}$ ions using the extraction scheme represented in Fig. 6.8. The ions were cooled using mass-selective buffer-gas cooling with a total cycle time of 240 ms. The ions were then ejected out of the trap to the detector by applying sequentially different extraction voltages. Only the ions with axial energy larger than the potential barrier in each case are released from the trap.

The TOF spectrum for the calcium ions shown in Fig. 6.9 was obtained by applying 8.0, 7.7, 7.4, 7.1, 6.8 and 6.5 V to the corrections electrodes in a sequential way every 50 μs, which corresponds to axial energies for the extracted ions of 0.53, 0.40, 0.28, 0.18, 0.08 and 0.02 V, respectively. The measurement is the accumulation of 121 extractions. Table 6.3 shows the percentage of counts for each energy interval. The maximum number of counts is obtained for the energy interval 0.18 - 0.28 eV.

Rhenium ions were ejected in similar way as $^{40}Ca^{+}$, but applying 12, 11, 10, 9, 8 and 7 V to the corrections electrodes in a sequential way every 75 μs, imple-

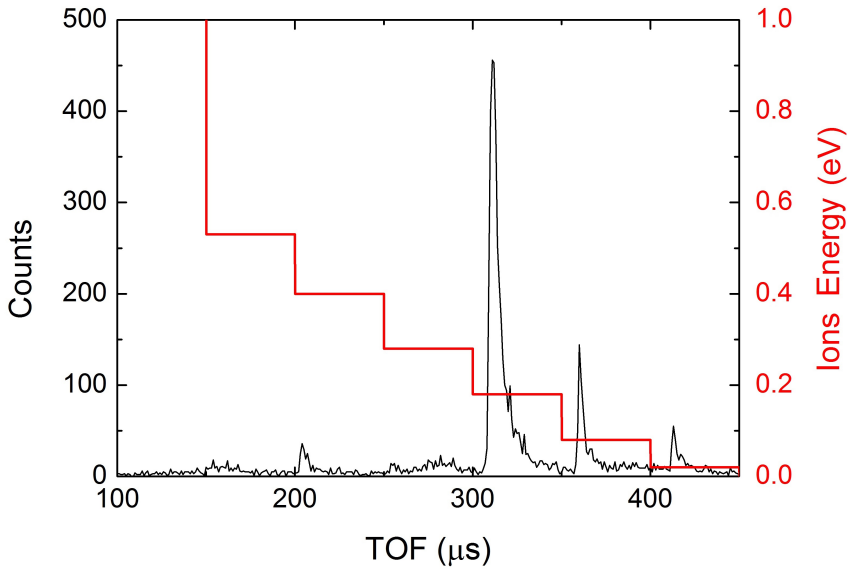

Figure 6.9: Time-of-flight spectrum for $^{40}Ca^{+}$ resulting from a stepwise extraction in the PPT. The voltages for this kind of extraction were varied (decreased) sequentially. The red line represents the difference between the local minimum and maximum of the potential, which is given in the right axis. Further details are given in the text.

menting a potential barrier starting at 2.6 eV, and ending with 0.14 eV. Table 6.3 shows the percentage of counts for each energy interval with a maximum number of counts in the energy interval 0.5 - 1 eV.

Figure 6.10 shows the distribution of $^{40}Ca^{+}$ and $^{187}Re^{+}$ ions as a function of the potential barrier (axial energy). Counts and energy intervals are taken from Tab. 6.3. The total energy of the ions is the sum of the radial and axial energy. Since $\omega_{+} \gg \omega_{-}$, the energy reads (Eq. (2.23))

Table 6.3: $^{40}Ca^{+}$ and $^{187}Re^{+}$ ions per energy interval.

Rhenium ions		Calcium ions	
Energy Interval (eV)	Counts (%)	Energy Interval (eV)	Counts (%)
> 2.5	17.7	> 0.53	2.1
2.5 - 2.0	9.4	0.53 - 0.4	4.5
2.0 - 1.5	16.4	0.4 - 0.28	2.1
1.5 - 1.0	17.6	0.28 - 0.18	71.7
1.0 - 0.5	36.2	0.18 - 0.08	13.2
< 0.5	2.7	0.08 - 0.02	6.4

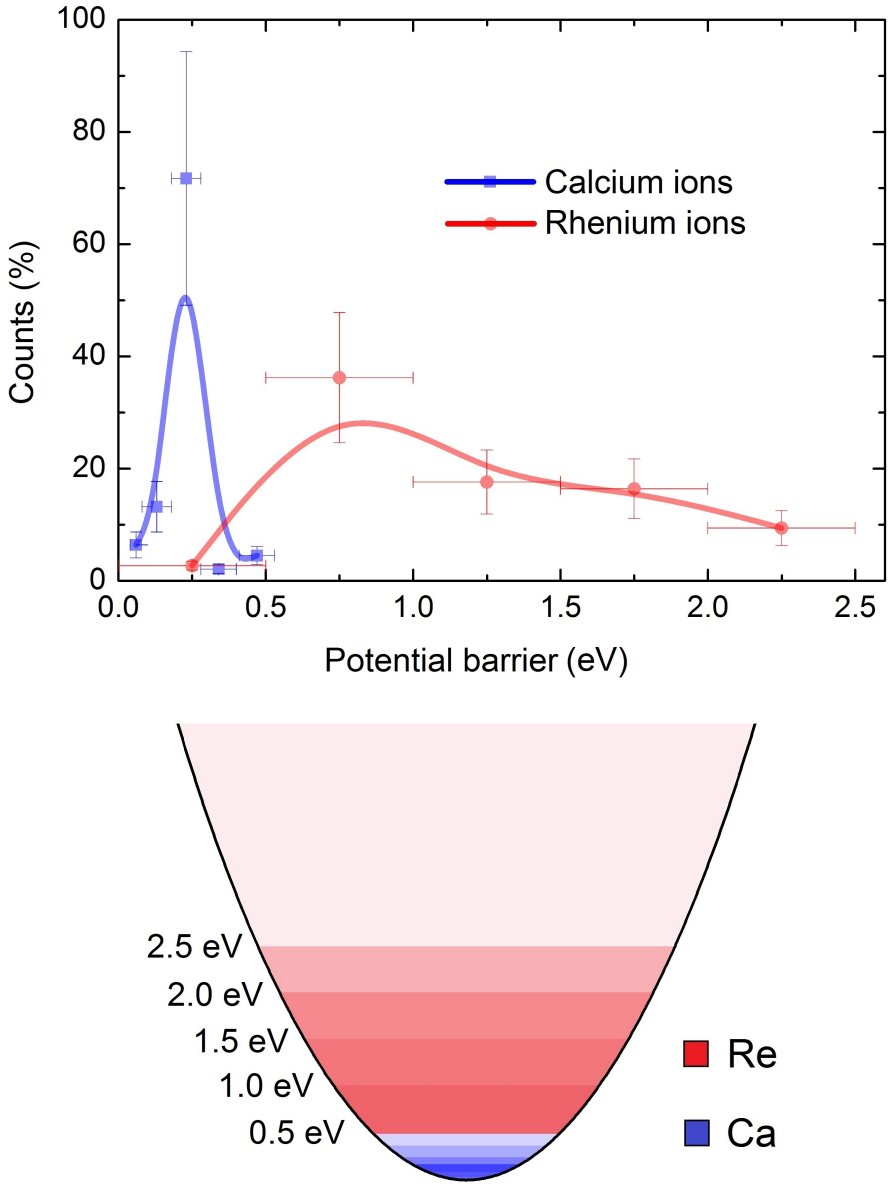

Figure 6.10: Top: Percentage of $^{40}Ca^{+}$ (blue line) and $^{187}Re^{+}$ ions (red line) extracted from the PPT as a function of the potential barrier (axial energy). The data points are taken from Tab. 6.3. Bottom: Sketch showing the distribution of $^{40}Ca^{+}$ (blue) and $^{187}Re^{+}$ ions (red) in the potential well of the trap.

$$E = \frac{1}{2}m\left[\left(\omega_{+}\rho^{+}\right)^{2} + (\omega_{z}\rho^{z})^{2}\right], \tag{6.5}$$

where the axial energy obtained is about 0.2 eV for $^{40}Ca^{+}$ and 0.8 eV for $^{187}Re^{+}$. Thus, the ions are not in thermal equilibrium with the buffer gas. Figure 6.11 shows the axial energy as a function of the time. Using Eqs. (6.4) and (6.5), a cooling cycle of above 340 ms for $^{40}Ca^{+}$ ions and $\approx$ 410 ms for $^{187}Re^{+}$ ones, are

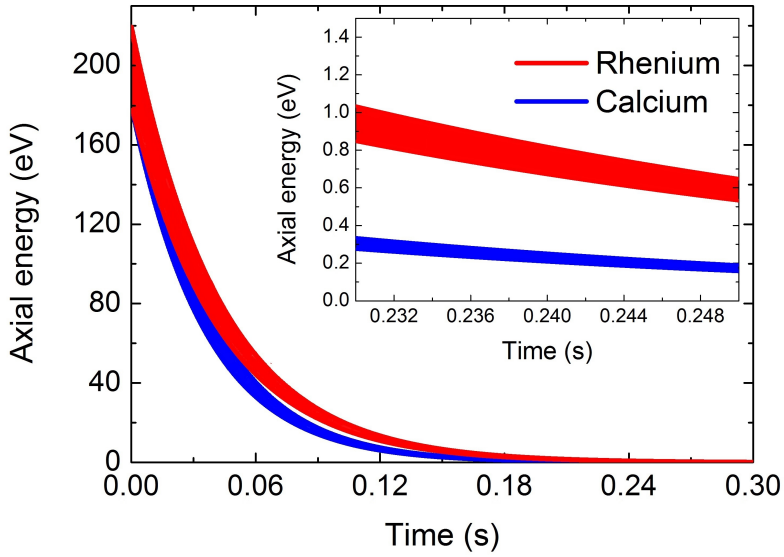

Figure 6.11: Axial energy of rhenium and calcium ions in the PPT as a function of the storage time. The initial energy is in the range of 180-220 eV. The exponential decay has been fitted using Eq. (6.4), to obtain after 240 ms storage time, an axial energy of about 0.23 eV for calcium and 0.75 eV for rhenium. A helium pressure of 10^{-6} mbar providing a decay time of $\alpha_z^{-1} = 35$ ms for calcium ions and $\alpha_z^{-1} = 43$ ms for rhenium ions has been used.

required to obtain trapped ions in thermal equilibrium with the helium atoms ($T \approx 300$ K).

In thermal equilibrium, the energy distribution of ions in a Penning trap follows a classical Boltzmann distribution [110]. The ratio between the Debye length [39]

$$\lambda_{\mathrm{D}} = \left(\frac{\epsilon_0 k_{\mathrm{B}} T}{n_0 q^2} \right)^{1/2}, \tag{6.6}$$

where n_0 is the ion density, and the radius of the ion cloud $r_{\mathrm{b}} = (3N/4\pi n_0)^{1/3}$, with N the total number of ions, gives the high temperature/low density condition ($\lambda_{\mathrm{D}}/r_{\mathrm{b}} \geq 1$) [111]. In this case, this ratio is in the interval from about 5 to 50. Figure 6.12 shows the ion density in the axial direction (left panel), given by [111]

$$n(z) = N \left(\frac{k_{\mathrm{z}}}{\pi k_{\mathrm{B}} T} \right)^{1/2} e^{\left(-\frac{k_{\mathrm{z}} z^2}{k_{\mathrm{B}} T} \right)}, \tag{6.7}$$

where $k_{\mathrm{z}} = qU_{\mathrm{DC}}/\rho_0^2$. The trapped ions are confined within less than a millimeter around the center of the trap. The energy distribution of the trapped ions for

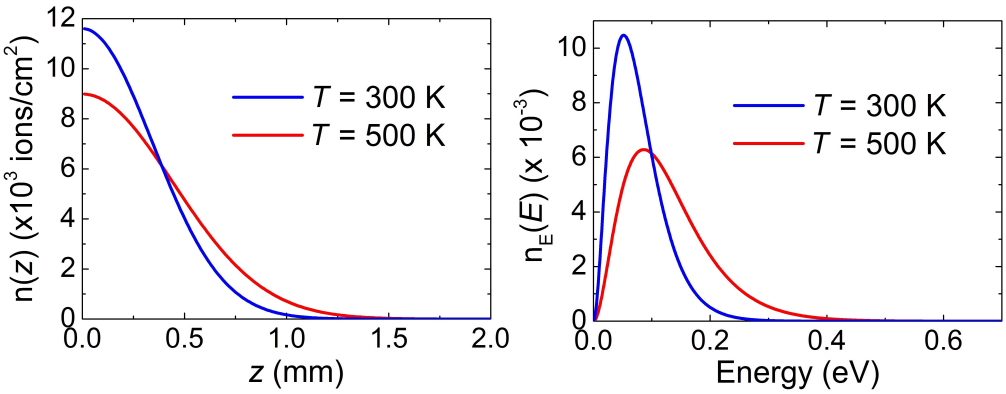

Figure 6.12: Ion density distributions (left) and energy distributions (right) of ions in the PPT for two ions' temperature. The number of total ions is $N = 1000$.

two temperatures is represented in Fig. 6.12 (right panel). This distribution is given by [110]

$$n_{\mathrm{E}}(E) = \frac{E^2}{(8k_{\mathrm{B}}T)^3} e^{\left(-\frac{E}{k_{\mathrm{B}}T}\right)}. \tag{6.8}$$

6.5 Injection into the measurement trap

The ions from the PPT will be injected and stored in the open-ring trap used as Penning trap. This trap is located in the second high-homogeneous region of the superconducting magnet (see Sec. 4.1.3), and will be replaced by the double Penning-(micro)-trap system (see Sec. 3.3.2). The injection of the ions in both systems is described below.

6.5.1 The open-ring Penning trap

Figure 6.13 shows the potential shape along the z-axis in the Penning-traps system. The center of both traps are separated 200 mm. The voltages applied to the electrodes of the open-ring trap are listed in Tab. 6.4. The ions are trapped between $z = -4$ and $z = 4$ mm. The trapping voltages have been chosen to obtain a quadrupole potential to allow axial confinement with V_{EC} = -0.75 V_{RE}. The trap is biased 15.5 V. A detailed study of the quadrupole potential of this trap is shown in Ref. [76].

The potential in the center of the PPT for ion extraction is about 5.4 V, thus the potential in the center of the open-ring trap for ion injection has been biased 5.4 V, which allows the injection without increasing its axial energy. For ion injection from the PPT to the open-ring trap, the ring and coupling electrodes on the left side (1 in Fig. 6.13) are switched from ground to 15.5 and 27.1 V, respectively. For ion extraction, the ring and coupling electrodes on the right

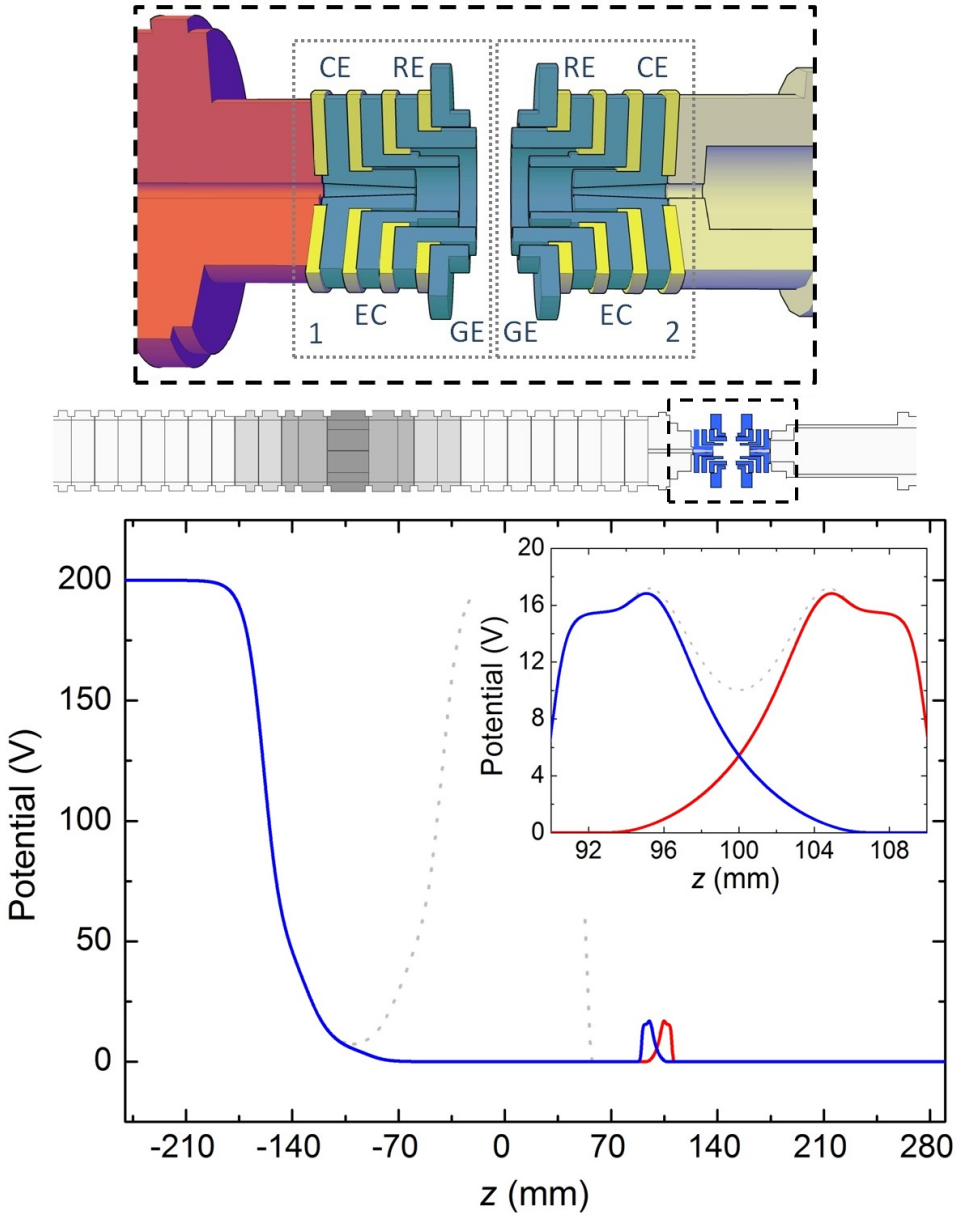

Figure 6.13: Top: Cut from a three-dimensional CAD drawing of the open-ring trap used as Penning trap. The electrodes are drawn in blue. CE, EC, RE and GE represent the coupling, endcap, ring and ground electrode, respectively. The electrodes on the left and right side of the trap are numbered 1 and 2, respectively. Middle: Longitudinal view of the PPT and the open-ring trap. Bottom: Potential shape along the z-axis for ion injection from the PPT into the open-ring trap (solid-red line), trapping (dotted-grey line) and extraction (solid-blue line).

side (2 in Fig. 6.13) are switched from 15.5 and 27.1 V to ground, respectively. Two HV switches (Stahl electronics HS200) are used for injection and extraction

Table 6.4: Voltages applied to the electrodes of the open-ring trap used as Penning trap for injection, trapping, and extraction of ions. Electrodes are named as in Fig. 6.13.

	Voltage		
Electrode	Injection	Trapping	Extraction
Ground electrode 1	15.5 V	15.5 V	15.5 V
Ring electrodes 1	0 V	0 V	0 V
Endcap electrode 1	0 V	27.1 V	27.1 V
Coupling electrode 1	0 V	15.5 V	15.5 V
Coupling electrode 2	15.5 V	15.5 V	0 V
Endcap electrode 2	27.1 V	27.1 V	0 V
Ring electrodes 2	0 V	0 V	0 V
Ground electrode 2	15.5 V	15.5 V	15.5 V

of the ions.

Figure 6.14 shows the trapping efficiency in the open-ring trap as a function of the time simulated using SIMION® version 8.0. This time is the difference of the extraction time of the ions and the time when the electrodes R1 and CE1 are switched on.

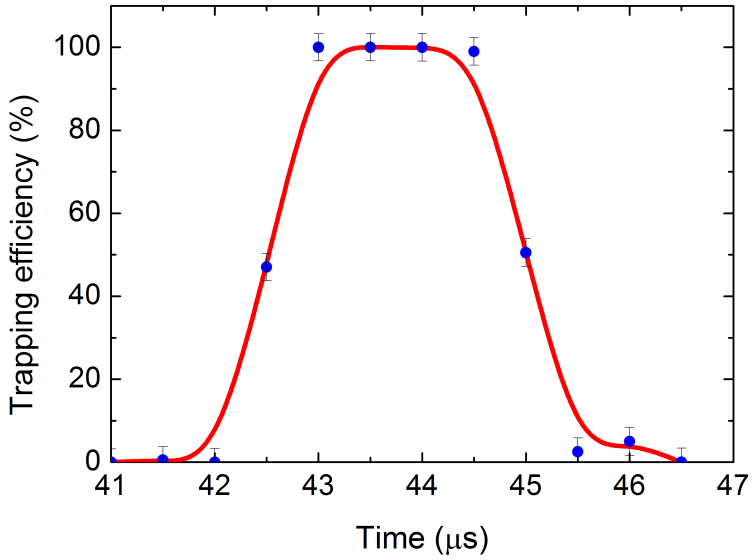

Figure 6.14: Simulation of the trapping efficiency in the open-ring trap as a function of the trapping time. $^{40}Ca^{+}$ ions were extracted from the PPT in thermal equilibrium at 300 K.

6.5.2 The double Penning-(micro)-trap system

Figure 6.15 shows the potential shape for trapping and injection of the ions from the preparation trap to the QS system. This system will be located in the second

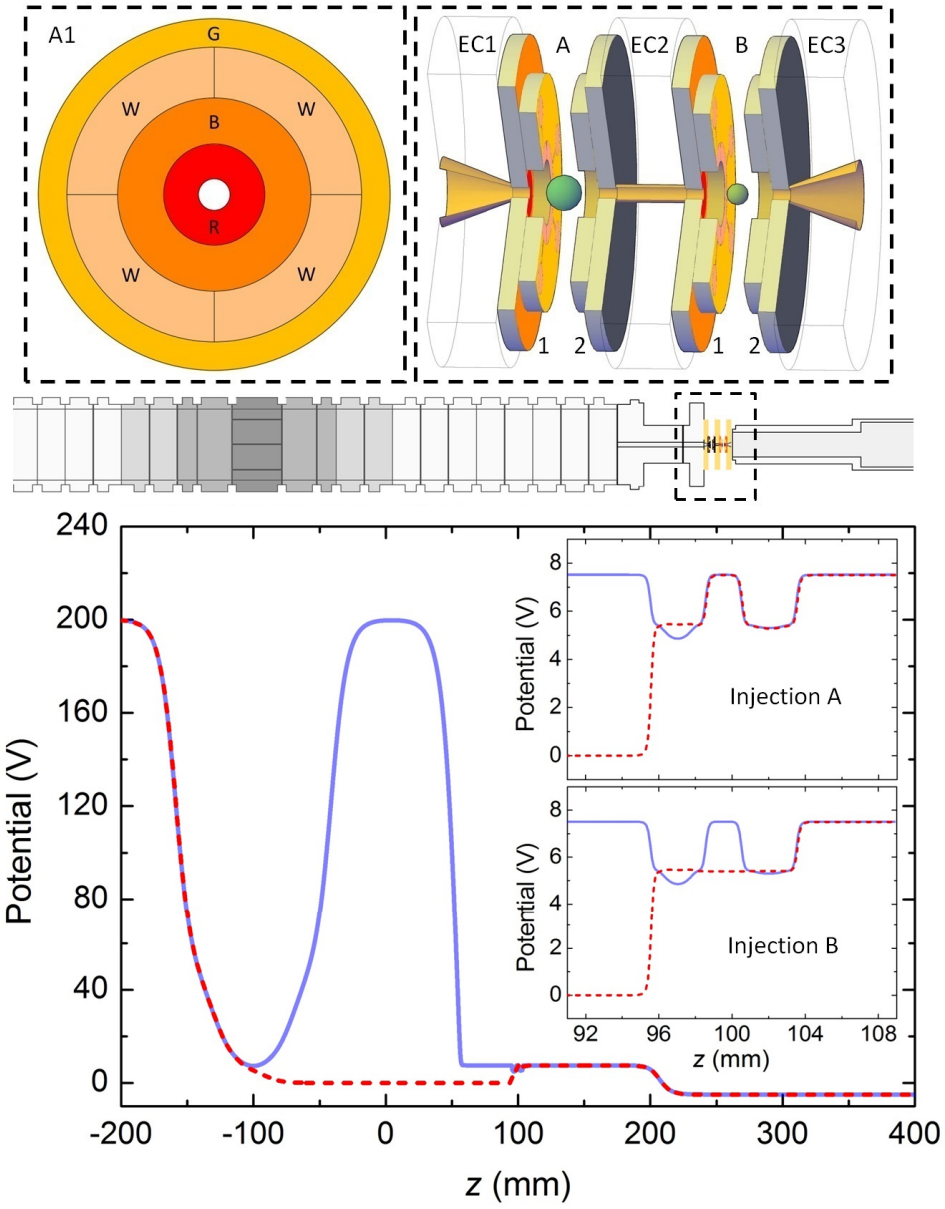

Figure 6.15: Potential shape along the z-axis to trap the ions in the QS system. A 2D drawing of the PPT and the QS system is shown on the middle. The PPT, diaphragm and first lens in the TOF section are colored in grey scale. $z = 0$ is taken as the center of the distance between the two homogeneous regions of the magnetic field. The dotted-red line is the potential shape for ion injection in the first (A) and second trap (B). The solid-blue line is the potential shape to trap ions in the QS system. The top shows a 3D-CAD drawing of the QS and a front view of the A1 trap disks. EC represent the endcap electrodes. The electrode W is segmented to perform excitation techniques.

Table 6.5: Voltages applied to the electrodes of the double Penning-(micro)-trap system for injection from the PPT and trapping. The electrodes and traps are named in Fig. 6.15. $^{40}Ca^{+}$ and $^{187}Re^{+}$ ions, will be confined in trap A and B, respectively.

	Voltages trap A (V)		Voltages trap B (V)	
Electrode	Injection	Trapping	Injection	Trapping
G1	5.4	5.4	5.4	5.4
W1	5.4	4.4365	5.4	5.1932
B1	5.9171	5.9171	5.5137	5.5137
R1	5.4	5.4	5.4	5.4
EC1	0	7.5	0	0
EC2	7.5	7.5	5.4	7.5
EC3	7.5	7.5	7.5	7.5
R1	5.4	5.4	5.4	5.4
B1	5.9171	5.9171	5.5127	5.5127
W1	5.4	4.4365	5.4	5.1932
G1	5.4	5.4	5.4	5.4

high-homogeneous region of the superconducting magnet. Each trap of the QS system is a smaller version (a factor of 5) of the open-ring trap used as Penning trap. The single calcium ion will be stored and laser-cooled in the second trap (B in Fig. 6.15) where the ion will remain all the time. In another cycle, the ion

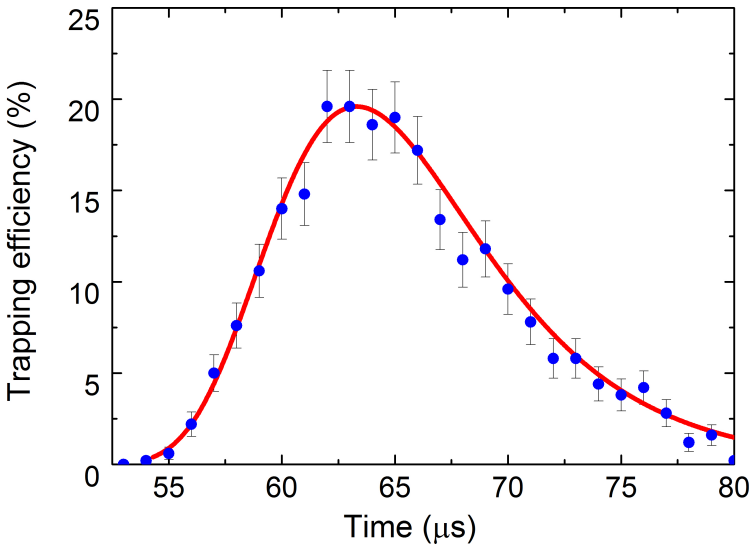

Figure 6.16: Simulation of the trapping efficiency in the micro-trap (labeled B in Fig. 6.15) as a function of the trapping time. $^{40}Ca^{+}$ ions were extracted of the PPT in thermal equilibrium at 300 K.

of interest will be brought from the PPT to the first trap (A in Fig. 6.15) of the QS system for the experiments.

Table 6.5 shows the voltages for trapping and injection in the traps for the ion pair $^{187}Re^{+}$-$^{40}Ca^{+}$. Since the ions are ejected out from the PPT at ≈ 5.4 eV, the double Penning-(micro)-trap system is floating at 5.4 V. Due to the trap electronics, the voltages on electrodes R and B have to be constant, and the EC electrodes are used for trapping. In addition, electrode W is also switched to reduce the axial energy of the ion during the trapping process.

Due to the small size of the QS, only 20% trapping eficiency is obtained (see Fig. 6.16). The voltages to close the trap have to be raised within a time of about 10 μs. The trapping voltages will be applied to the endcap electrodes using a low noise switch (Stahl electronics LS-30) with 15 V maximum input voltage and an output rise time of 22 ns. The voltages to create the harmonic potential will be delivered to the ring electrodes by an ultra-high precision voltage source (Stahl electronics UM 1-5-LN) with an absolute accuracy of 1 ppm.

Chapter 7

Developments for high-performance detection

The method motivating the project TRAPSENSOR, where the strength of the signal arising from the ion of interest will be quantified from the detection of the 397-nm fluorescence photons from a single laser-cooled $^{40}Ca^{+}$ ion, has yielded in the course of this work the trap and the electronic circuit, the former in collaboration with a US company (TRANSLUME) and the latest in collaboration with a German one (Stahl Electronics). In addition, the well-known and successfully applied technique for single-ion detection in the low and medium mass range, based on the amplification and filtering of the image current induced by the ion, has been treated in detail, and a new circuit has been developed at the University in collaboration with a local company (SEVEN SOLUTIOS S.L.). These technical developments are presented in this chapter.

7.1 Mass spectrometry based on optical detection

The coupling of two ions in a 7 T magnetic field has needed a Penning trap, built using a different approach, compared to those used in mass spectrometry. The size of the trap must be small and this has also requested small printed boards for the circuits housing the electronics needed for ion-ion coupling. The design of the double Penning-(micro)-trap system is based on the open-ring trap presented in Sec. 4.3.1, after discarding several surface traps and the cylindrical geometry. This was the outcome of a Bachelor´s thesis, the results of which have not been published yet [76, 77]. A summary of these studies was presented in Sec. 4.3.3 and the way to implement it in the Penning-traps beamline was described in Sec. 6.5. In the following, a brief description showing the most important aspects for the construction will be given. The main part of this section will be devoted to describe the electronics and to present the tests carried out.

7.1.1 Micro-trap construction

Figure 7.1 shows a technical drawing of the double Penning-(micro)-trap system and a picture of some electrodes. Each micro-trap is a factor of 10 smaller com-

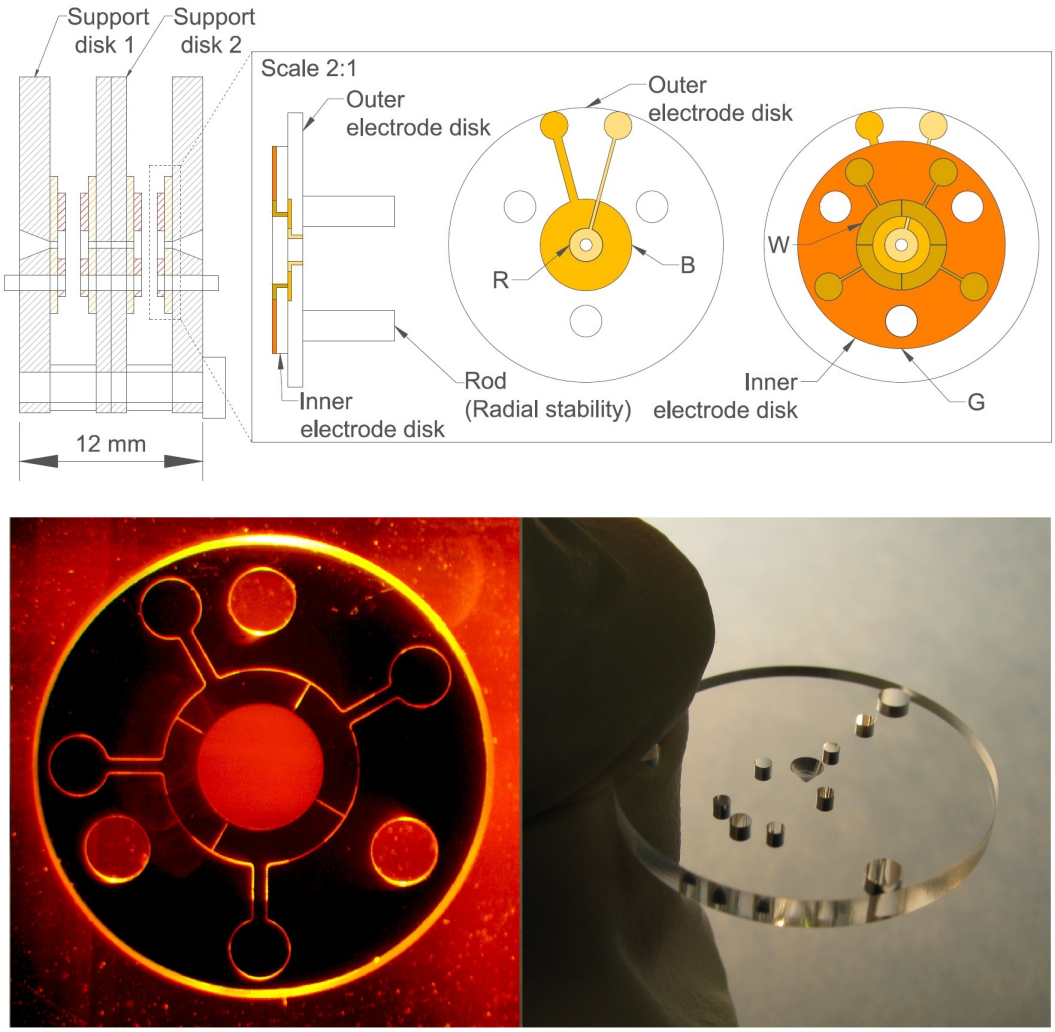

Figure 7.1: Top: Technical drawing of the double Penning-(micro)-trap system. Electrodes R, B, W and G are colored in clear yellow, dark yellow, brown and orange, respectively. Bottom: Photo of some disks of the double Penning-(micro)-trap system. Left: Microphotograph of the disk where the contour of the segmented electrode has been machined using a femtosecond laser. Right: Photograph of the support disk 1. Both pictures were taken at the company TRANSLUME.

pared to the open-ring trap utilized to carried out Doppler cooling on the sensor ion. The ring electrodes had to be replaced by plates made of fused silica. The electrodes are marked with a femtosecond laser. The support disk 1 and 2 have an outer diameter of only 22 mm, and a thickness of 2 and 1 mm, respectively. These disks are fixed to the rest of the Penning-traps beamline by three M1 screws. The support disk 1 has a funnel with an outer diameter of 2 mm and an inner one of 400 μm. This allows injecting the ions from the PPT into the first micro-trap. The supports disk 2 have inner diameters of 400 μm. Another two disks with a standard thickness of 500 μm, and with outer diameters of 6.8 and

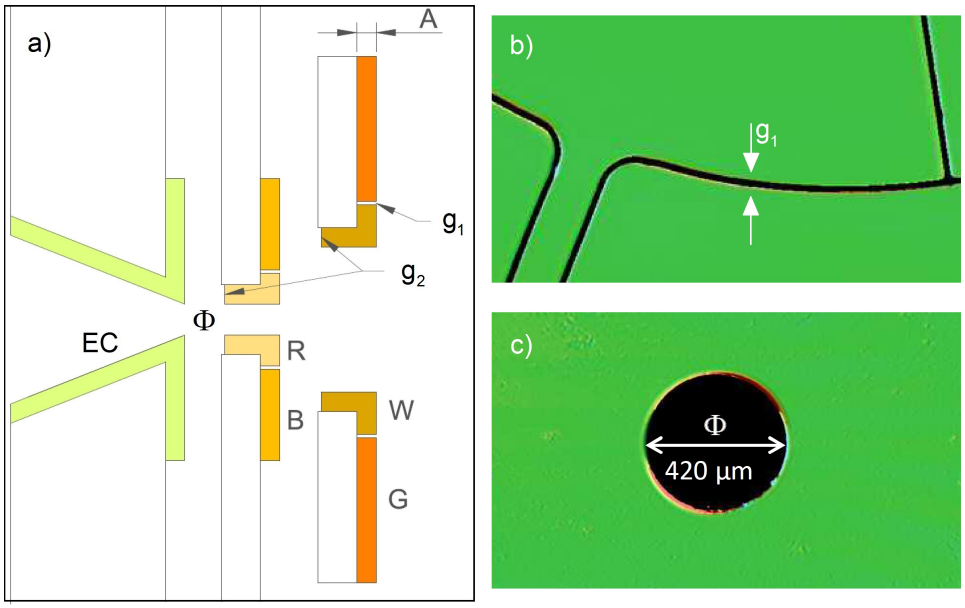

Figure 7.2: a) Technical drawing showing the electrodes to be created by metallic deposition Endcap (EC) electrode is represented by clear green in the support disk 1. Electrodes R and B are colored in clear and dark yellow on the outer disk, respectively. Electrodes W and G are marked in brown and orange on the inner disk, respectively. The gap between two adjacent disks is represented by g_2. b) Picture of the gap between the electrode W and G in the inner disk obtained with an optical profilometer. c) Picture showing the aperture in the outer disk obtained using the same instrument.

9 mm, are fixed to the support disks. Three rods made of fused silica with 1 mm diameter and a length of 6 mm are used to assemble the system and to provide radial stability. Cryogenic-high-vacuum grease (Apiezon® N) will be used to fix together the support, outer and inner disks. All the disks have been machined by TRASLUME[1]. A photograph of the inner electrode and the support disk 1 is shown in the lower part of Fig. 7.1. The electrodes are made by sputtering, creating a titanium layer of 50 nm, and another one of gold of 150 nm on top of it. In the final configuration, the traps will be operated at cryogenic temperature ($\approx$ 4 K), and this material (SiO_2) presents a good stability with an expansion coefficient of about 5.1-5.9 $\times$ 10^{-7} K^{-1} [112].

Figure 7.2.a shows the gaps between electrodes, machined with a femtosecond ablation laser. Figure 7.2.b shows a picture taken with an optical profilometer at the Instituto Nacional de Microelectrónica in Barcelona (Spain). A gap of $g_1 = 15$ μm was measured. Figure 7.2.c shows the inner diameter Φ of the electrode R. The hole in this electrode is required to inject the ions from the PPT, the diameter of which must be as small as possible to allow a strong coupling

[1]Translume 655 Phoenix Drive Ann Arbor 48108 Michigan (United States).

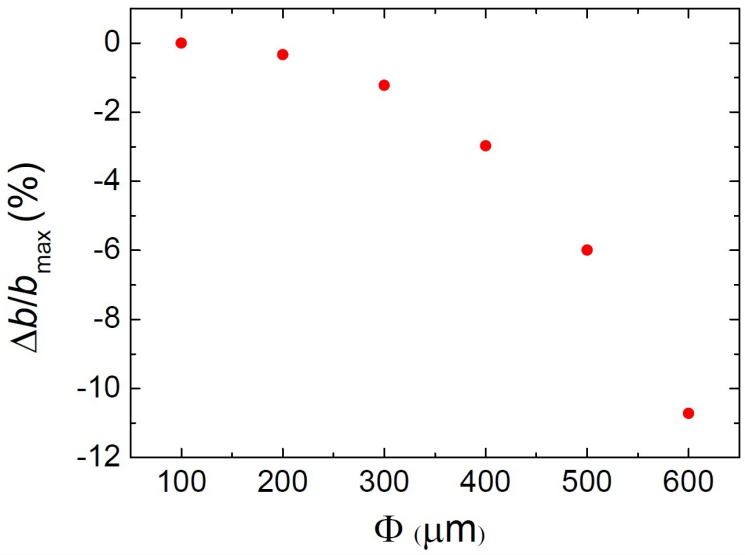

Figure 7.3: Variation of the parameter b as a function of the inner diameter of the trap electrode. The ions are injected through this hole.

between the ion of interest and the sensor ion. Figure 7.3 shows the parameter b, defined in Eq. (3.26), versus the inner diameter of the electrode R. This parameter represents the increase with the time of the oscillation amplitude of the sensor ion in the axial direction of the trap. A final diameter of 400 μm was chosen as a good compromise between a large coupling strength and a high injection efficiency. Although, $^{40}Ca^{+}$ ions can be created inside the trap by photoionization or electron bombardment as described in Sec. 4.3.1, this trap has to be used with ions produced in nuclear reactions like for example it happens at SHIPTRAP at GSI.

7.1.2 Electronics for ion-ion coupling

The main function of the electronics for the double Penning-(micro)-trap system developed by Stahl-Electronics[2] is to switch the coupling between the two ions housed in different traps to allow for energy transfer as shown in Sec. 3.3.2, while maintaining the voltages applied to the electrodes. It is built to work at cryogenic temperature ($\approx$ 4 K), in ultra-high vacuum ($\approx 10^{-10}$ mbar or better) and in a strong magnetic field ($B = 7$ T).

A first requisite for ion-ion coupling is to maintain a good stability in the axial frequency of the ions in the trap during their energy exchange process. For a certain ion-pair, the frequencies of the two ions should be stable to a level below the inverse of the exchange time t_{ex} (Sec. 3.3.2). Table 7.1 shows the voltages for a good harmonic potential in the traps for the ion pair $^{187}Re^{+}$-$^{40}Ca^{+}$ [76].

[2]Stahl-Electronics Hauptstrasse 15, 67582 Mettenheim, (Germany).

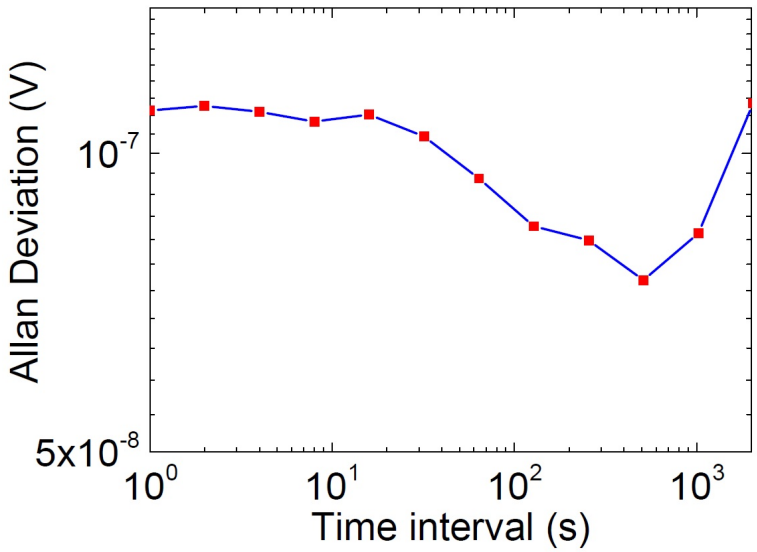

Figure 7.4: Allan deviation of the voltage to be applied to the micro-trap electrodes for ion-ion coupling. A DC voltage of 0.800000 V was settled. The total time for the measurement was about two hours with a measurement cycle of about one second.

EC, R and G electrodes are grounded. The voltages applied originate a minute deviation of the axial frequency of -0.0042 and 0.026 Hz, for $^{40}Ca^{+}$ and $^{187}Re^{+}$, respectively, with respect to the nominal value of 100 kHz. The frequency shift given by Eq. (3.27) results in 0.005 Hz for $^{40}Ca^{+}$ and 0.0011 Hz for $^{187}Re^{+}$ for the ion temperatures given in Tab. 7.1. It is important to note that the oscillation frequency can be easily tuned by varying the voltage V_W maintaining the ratio V_W/V_B constant. In this case $V_W = -A \cdot \nu_z^2$.

For the ion-pair $^{187}Re^{+}$-$^{40}Ca^{+}$, the axial frequency must be stable at a level better than 5.8×10^{-7}. This stability depends only on the voltage applied to the trap electrodes (See Eq. (2.11)). A DC voltage of about 7.5 V is applied to the other electrodes for ion injection and trapping. Although the other electrodes have been grounded for the calculations, simulations using SIMION® version 8.0 has shown that voltages applied to the endcap electrodes do not affect the har-

Table 7.1: Voltages applied to the electrodes of the double Penning-(micro)-trap system to perform a harmonic potential. Optimized values for $\nu_z = 100$ kHz for $^{40}Ca^{+}$ and $^{187}Re^{+}$ ions at 1 mK and 5 K, respectively. V_W and V_B are the voltages applied to the electrodes W and B (see Fig. 7.1), respectively.

Ion	V_W (V)	V_B (V)	C_2 (V/mm^2)	C_4 (V/mm^4)
$^{40}Ca^{+}$	-0.103393	0.190450	0.082	5.18×10^{-5}
$^{187}Re^{+}$	-0.482328	0.786209	0.382	4.93×10^{-5}

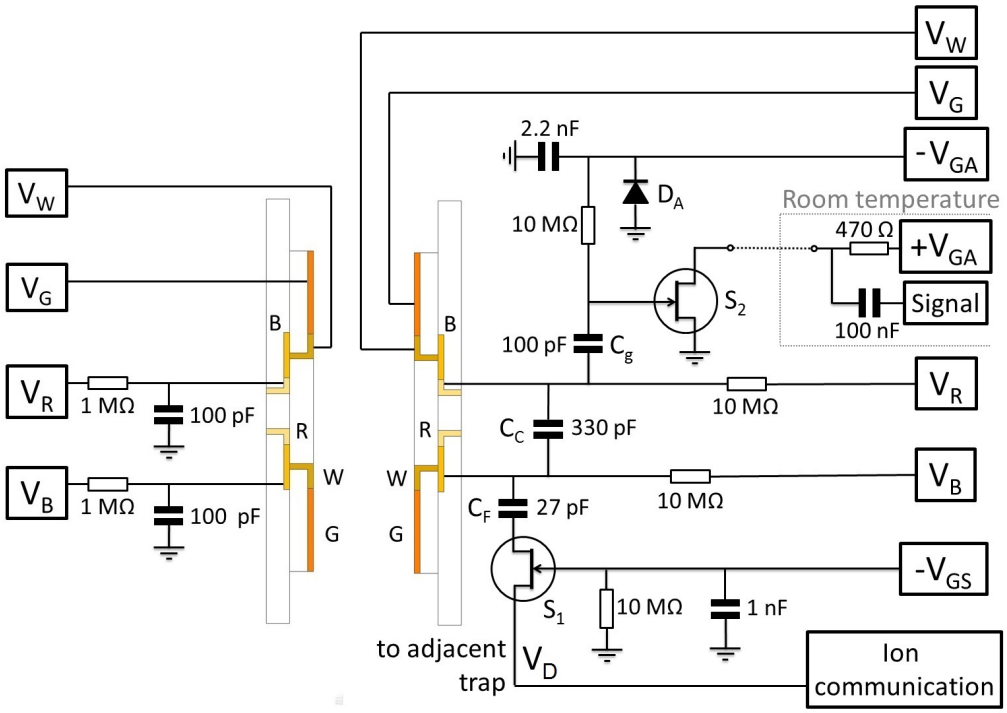

Figure 7.5: Sketch showing the electronic circuit wired to electrodes of one trap of the double Penning-(micro)-trap system. Each trap, needs two printed circuit boards, on the left and on the right. Voltages V_{R}, V_{B}, V_{W} and V_{G} are applied to the electrodes R, B, W and G, respectively. C0G (EIA RS-198 standard codes ceramic class 1) capacitors made of non ferro-electric materials with a change in capacitance (without DC voltage) of 0 ± 30 ppm/K are used. Surface-Mount Device (SMD) non-magnetic thin-film resistors are also used. More details are given in the text.

monic quadrupole potential of the traps.

The voltages to the trap electrodes to define the axial oscillation frequency will be delivered by an ultra-high precision voltage supply (Stahl electronics UM 1-5-LN) providing an accuracy of 1 ppm. The stability of the voltage source was obtained from the difference between the voltage measured using a high-precision multimeter and a reference value of 0.800000 V for several hours. Fig. 7.4 shows the Allan deviation, which is given by [113]

$$\sigma(t_{\mathrm{p}}) = \sqrt{\frac{1}{2(n-1)} \sum_{i=1}^{n-1} (x_{i+1} - x_i)^2}, \tag{7.1}$$

where x_i is the ith sample, n is the number of x_i in the interval and t_{p} the time interval. A negative drift in the order of $10^{-11}\mu$V/s was measured.

Figure 7.5 shows a sketch of the electronics for one of the traps of the double Penning-(micro)-trap system. The electronics is divided in two circuit boards

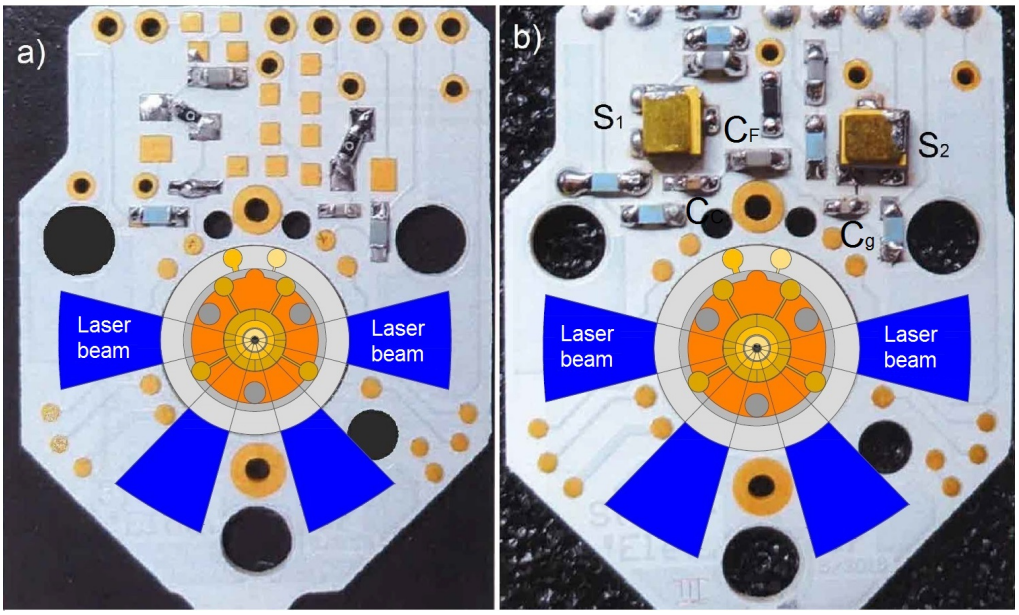

Figure 7.6: Photograph of the electronic boards. The trap electrodes, laser beam and fluorescence collection areas are shown. a) Photograph of one of the PCB to apply voltages to half of the electrodes in the micro-trap. b) Photograph of the PCB to perform ion-ion coupling and amplification.

made of Roger substrate and is identical for each trap. The most important element is the ultra-low noise (ULN) GaAs HEMT used as electrically-controlled switch (S1 in Fig. 7.5). This transistor, developed by Stahl Electronics has a voltage noise of 0.5 nV/$\sqrt{\text{Hz}}$ at 100 kHz (and T = 4 K). Electrodes R and B serve to pick up the AC-charges induced by the ion, and this signal is wired to the adjacent trap for the coupling with the other ion. The capacitances C_{C} and C_{F} allow applying different voltages in electrodes R and B to maintain the good harmonic quadrupole potencial, decoupling the DC voltages from the induced ion signal. The voltage V_{GS} is used to control the ON (V_{GS} = 0) and OFF (V_{GS} = -0.6 V at 4 K) states of the ULN-HEMT S1 transistor. In the ON state, a resistance of about 180 Ω is measured between source and drain. Photographs of the two PCBs are shown in Fig. 7.6. The PCB shown in (a) and (b) are fixed to the support disk 1 and 2 of Fig. 7.1, respectively, using two screws M1.

Figure 7.7 shows the amplitude of an RF signal (100 kHz) in the drain V_{D} as a function of V_{GS} for different voltages applied in the source V_{S} at room temperature. This serves to simulate the ion signal going to the other trap. Although this signal is larger compared to the ion signal, which would be below the noise level, the ion signal will be in resonance with the oscillation of the other ion and will be detectable by observing the fluorescence photons. The OFF state is obtained when applying $V_{\text{GS}} = -4$ V (at room temperature).

Although not exploited in the course of this work, in the PCB shown in Fig. 7.6.b, another ULN GaAs HEMT transistor (S2 in Fig. 7.5) is used to amplify the cur-

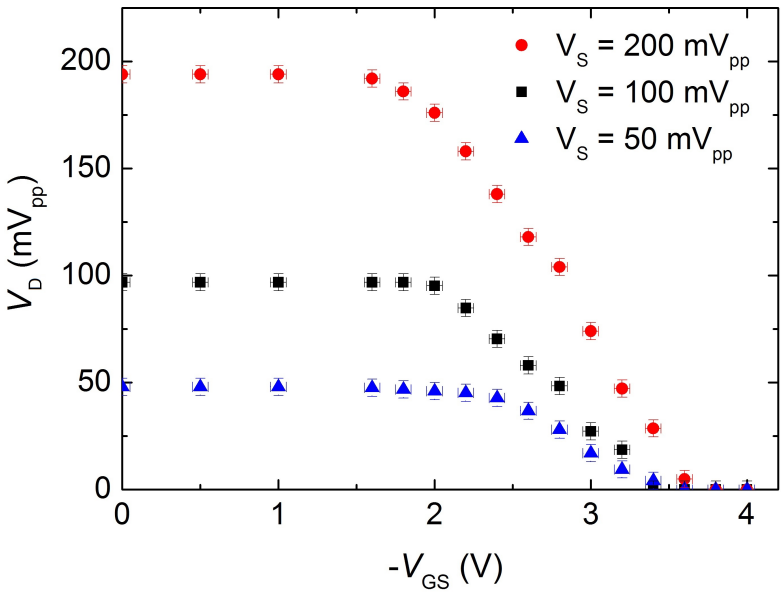

Figure 7.7: Output signal V_{D} of the ULN-HEMT S1 used as switch (ON state) versus the V_{GS} for different input voltages V_{S}.

rent induced by the stored ion in electrodes R and B. A diode (D_{A} in Fig. 7.5) is in the circuit to protect the ULN-HEMT S2 against high-voltages. The capacitance C_{g} is used to decoupled the DC-voltage applied to electrodes R and B, and the voltage applied to the ULN-HEMT S2. A voltage of $V_{\mathrm{GA}} = 0.5$ V is used to feed the transistor. Electronic detection is described in detailed in the following section.

7.2 Mass spectrometry based on electronic detection

The principle of mass determination from the frequencies of the ion eigenmotions measured electronically from the image charge a stored ion induces in the trap electrodes was described in Sec. 3.3.1. The scheme for IIC detection was shown in Fig. 3.5. This section will present the circuit developed at the University in collaboration with a local company[3] and its full characterization in terms of amplification and equivalent noise for broad and narrow band detection, when operating the systems at room and cryogenic temperatures. A 2-stage pulsed tube cryocooler test bench has been built at the University of Granada and utilized for this characterization at vacuum pressures in the order of 10^{-8} mbar.

[3]SEVEN SOLUTIONS Edf. CETIC, Calle Periodista Rafael Gómez Montero, 2, oficina 13, 18014 Granada (Spain).

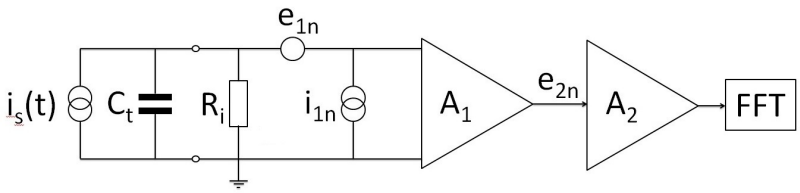

Figure 7.8: Sketch of an electronic circuit used for induced image-current detection in broad-band indicating the main parameters. C_t and R_i are the parasitic capacitance of the trap and the input resistance of the amplifier, respectively. $e_{1\mathrm{n}}$ and $i_{1\mathrm{n}}$ are the voltage and current noise of the amplifier, respectively. $e_{2\mathrm{n}}$ is the voltage noise after amplification. $i_{2\mathrm{n}}$ is neglected and not shown in the figure.

7.2.1 Circuit description

The description will start with the general sketch shown in Fig. 7.8 in order to amplify the current $i_\mathrm{s}(t)$ picked from an electrode in the trap when the ions move towards the opposite one (see Fig. 3.5). The trap electrodes are connected to one pre-amplifier (A_1 in Fig. 7.8) in vacuum, which will be operated at cryogenic temperature. This current through the impedance $Z(\omega)$ of the circuit, generates an output voltage $V_\mathrm{out}(t)$, which can be measured, and amplified in a wide range of frequencies. The gain factor G_1 of the amplifier A_1 is defined as the ratio between the output and input voltages. Another amplification stage (A_2 in Fig. 7.8) is located at room temperature outside vacuum. Fast Fourier Transformation (FFT) is applied later to obtain a specific eigenfrequency of the ion motion.

The impedance of the circuit shown in Fig. 7.8 is given by

$$Z(\omega) = \left(\frac{1}{R_\mathrm{i}} + j\omega C_\mathrm{t}\right)^{-1}, \tag{7.2}$$

and the signal to noise ratio of the circuit by [114]

$$\frac{S}{N} = \frac{i_\mathrm{s}\,|Z(\omega)|\,G_1}{\sqrt{\left(\left[i_{1\mathrm{n}}^2\,|Z(\omega)|^2 + e_{1\mathrm{n}}^2\right] G_1^2 + e_{2\mathrm{n}}^2\right)\Delta\nu}}, \tag{7.3}$$

where the thermal noise (see Sec. 3.3.1) has been included in the current noise of the amplifier $i_{1\mathrm{n}}$. Since the overall noise factor F_0 of the amplifiers built in a multistage configuration is given by [115]

$$F_0 = F_\mathrm{F} + \frac{(F_\mathrm{R} - 1)}{G_\mathrm{F}}, \tag{7.4}$$

where the noise factor is defined as the ratio of the output to input signal-to-noise ratios, F_F is the noise factor arising from the first stage, F_R is the noise factor arising from the subsequent stages, and G_F is the gain factor of the first stage. Only the first stage of amplification is important for the overall noise.

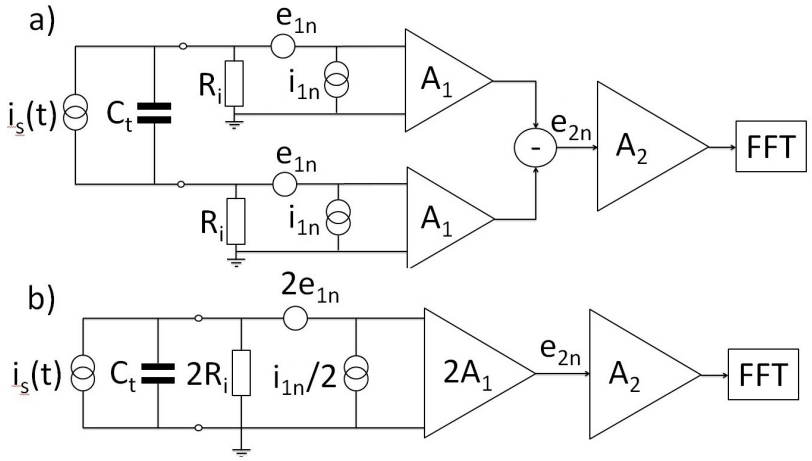

Figure 7.9: a) Sketch of an electronic circuit used for induced image-current detection in broad-band when each trap electrode is connected to an amplifier indicating the main parameters. b) Equivalent model of the circuit.

For high input resistance $R_{\rm i}$, the impedance $|Z(\omega)| \approx R_{\rm i}$ and the relationship $R_{\rm i} \cdot i_{1\rm n} \gg e_{1\rm n}$ is fulfilled. Thus, Eq. (7.3) can be simplified to

$$\frac{S}{N} \approx \frac{i_{\rm s}}{i_{1\rm n}\sqrt{\Delta\nu}}. \tag{7.5}$$

The circuit in Fig. 7.8 can be modified, if each trap electrode is connected to a different amplifier (see Fig. 7.9.a). Figure 7.9.b shows the equivalent model of the circuit represented in Fig. 7.9.a. This architecture allows decreasing the current noise of the amplifier a factor of two and multiplying by the same factor the input resistance of the amplifier [116]. Thus, the gain factor is also doubled, and the signal-to-noise ratio reads

$$\frac{S}{N} \approx \frac{2i_{\rm s}}{i_{1\rm n}\sqrt{\Delta\nu}}. \tag{7.6}$$

This scheme increases a factor of two the signal-to-noise ratio, since the current $i_{\rm s}$ remains the same but the current noise of the amplifier is reduced. The difference between the two amplifier signals is performed at room temperature and is fed into an FFT analyzer. This scheme allows also removing sudden fluctuations of voltages picked up in only one electrode.

Figure 7.10 shows the circuit of one pre-amplifier conceived for a broad-band electronic detector to be operated at cryogenic temperature. Silicon Schottky Diodes with high-speed switching (D_1 in Fig. 7.10) are used to protect the circuit against a possible damage from the applications of high voltages. Two low-noise GaAs Hetero-Juntion Field-Effect-Transistor (HJ-FET), model NE3510M04 provided by the company CEL (T_1 and T_2 in Fig. 7.10) are used in a first stage as common-source amplifier. These HJ-FETs are built in parallel, in order to decrease the frequency corner of the noise spectrum at low frequency (< 1 MHz) [116, 117]. Only two FETs are used to avoid an excessive capacitance. In a second

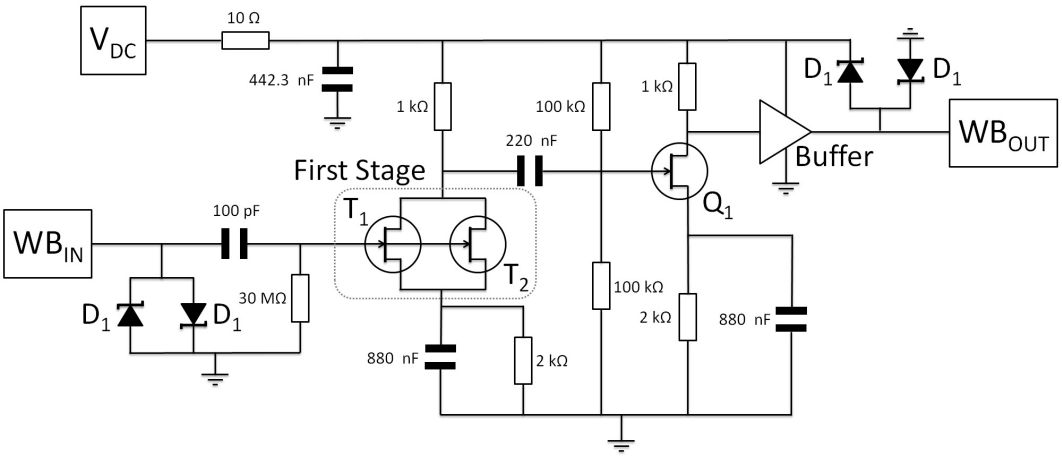

Figure 7.10: Circuit diagram of a preamplifier for one trap electrode, developed in collaboration with the local company SEVEN SOLUTIONS S.L. Input and output signals are represented by $\mathrm{WB_{IN}}$ and $\mathrm{WB_{OUT}}$, respectively. C0G capacitors and SMD thin-film resistors are used. The details are given in the text.

stage, a low noise Enhancement mode Pseudomorphic-High-Electron-Mobility-Transistor (E-PHEMT) is used as common-source amplifier ($\mathrm{Q_1}$ in Fig. 7.10). Finally, a buffer output stage with voltage gain close to unity is used. The buffer amplifier allows using other stage with low input impedance, since this amplifier prevents the load transfer due to the high-impedance of the first stage.

Narrow-band IIC detection

The tiny current originated from the motion of a single ion in the trap can be detected, if the mass-to-charge ratio is small, by attaching an inductance L to the circuit. Figure 7.11 shows a simplified diagram of the circuit for narrow-band ion detection where an inductance L is attached between the trap electrodes and the signal is connected to two amplifiers. The difference between the two signals is fed into an FFT analyzer. The impedance of this circuit was discussed in Sec. 3.3.1. A large voltage drop from the current induced is obtained when the motional frequency equals the resonance frequency of the circuit $\nu = 1/(2\pi\sqrt{LC_\mathrm{t}})$:

$$v_\mathrm{s} = i_\mathrm{s} R_\mathrm{i} = i_\mathrm{s}\omega_\mathrm{LC} L Q = i_\mathrm{s}\frac{Q}{\omega_\mathrm{LC} C_\mathrm{t}}, \tag{7.7}$$

which shows that the capacitance C_t must be as small as possible. For a realistic case, this capacitance is the parasitic one of the trap electrodes and cables. The inductance L will be decided in order to match the resonance frequency of the ion.

The signal-to-noise ratio for narrow-band detection, taking into account the current and voltage noise originated at different amplifier stages, is given by Eq. (7.3). The signal-to-noise ratio improves by using low temperature T, by having a first amplifier with ultra-low voltage noise e_{n1} and by implementing

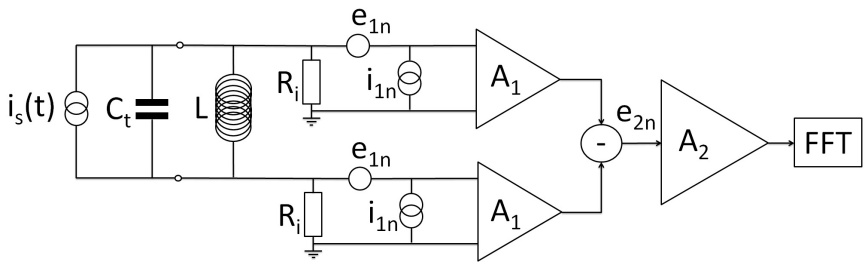

Figure 7.11: Sketch of an electronic circuit used for induced image-current detection in narrow-band when each trap electrode is connected to an amplifier, indicating the main parameters. An inductance L is attached between the trap electrodes.

a high quality factor Q. In this work, the temperature T is reduced by means of a 2-stage pulsed tube cryocooler. Two low-noise GaAs HJ-FET are used as amplifiers in the circuit. The so-called Q-value, defined as the ratio of the energy stored per cycle versus the energy dissipated in a cycle, serves to define the relationship between the resonant frequency and the half-power bandwidth (see Eq (3.19)). This circuit is used as a very narrow band-pass filter around the resonance frequency, and to obtain a gain in the current through L

$$i_{\mathrm{L}} = \frac{1}{j\omega_{\mathrm{LC}} L} i_{\mathrm{s}} R_{\mathrm{i}} = -j i_{\mathrm{s}} Q. \tag{7.8}$$

An ideal LC circuit would have an infinite Q-value, but real circuits have loss mechanisms arising from many factor as temperature, material impurities or bonding stress. The work presented here concentrates in the use of a quartz crystal resonator. This crystal provides the inductance of the LC circuit. This approach is used for the first time since many groups use superconducting coils [47, 118].

7.2.2 Quartz crystal resonator

The quartz crystal is a piezoelectric one, used in electronics circuits to provide stable oscillation frequencies. It changes its shape by applying an external electric field, and generates a voltage signal when returns to its previous one. Figure 7.12 shows an electrical equivalent circuit for a quartz crystal, the so-called Butterworth Van-Dyke model, where it is depicted as a parasitic capacitance C_0 due to the connectors and cables, in parallel to a capacitance C_1 due to the mechanical elasticity, an inductance L, originated from the mechanical inertia, and a resistance R_1, due to the mechanical losses of the system. The equivalent circuit has an impedance given by

$$Z(\omega) = \frac{\left[(j\omega C_1)^{-1} + j\omega L_1 + R_1\right](j\omega C_0)^{-1}}{(j\omega C_1)^{-1} + j\omega L_1 + R_1 + (j\omega C_0)^{-1}}. \tag{7.9}$$

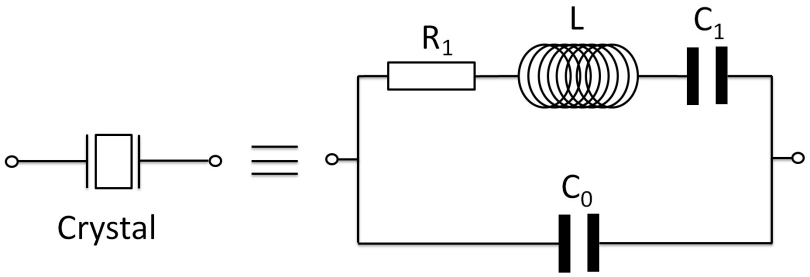

Figure 7.12: Butterworth Van-Dyke equivalent model for a quartz crystal

This impedance is responsible for two resonance frequencies, the series one $\nu_s = 1/(2\pi\sqrt{LC_1})$ with low-impedance, and the parallel one with high-impedance, following the relationship

$$\nu_p = \nu_s \sqrt{\left(1 + \frac{C_1}{C_0}\right)}. \tag{7.10}$$

Only the parallel resonance is important for this work, since a high impedance is obtained for this frequency.

Furthermore, the properties of the quartz crystal, i.e. overtones and frequency ranges, depend on the way the crystal is cut. Cuts are defined by two rotation angles $\hat{\phi}$ and $\hat{\theta}$ around the crystallographic axes. The AT cut, where $\hat{\phi} = 0^o$ and $\hat{\theta} = 34^o$, is the most commonly-used one, with a frequency range for the fundamental tone ranging from 500 kHz to 40 MHz [119]. Figure 7.13 shows the

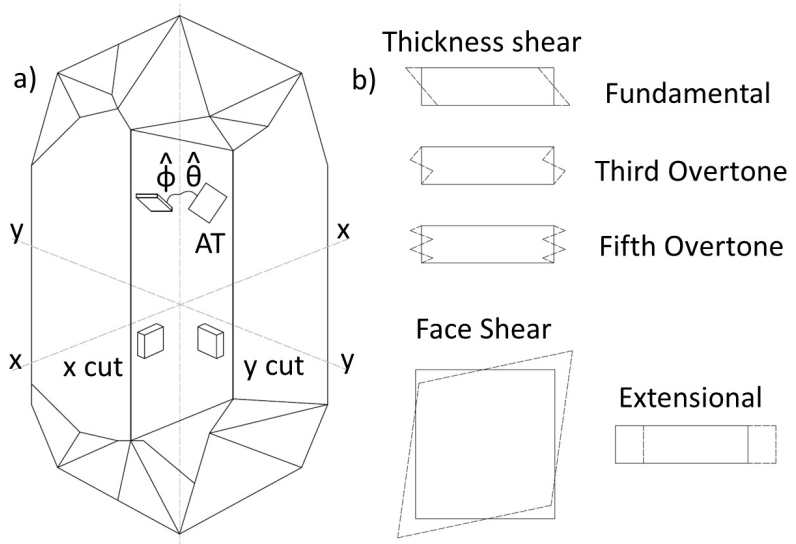

Figure 7.13: a) Crystallographic axes in a natural quartz crystal with an AT cut. b) Overtones and vibration modes for a quartz crystal. Figures adapted from Ref. [120].

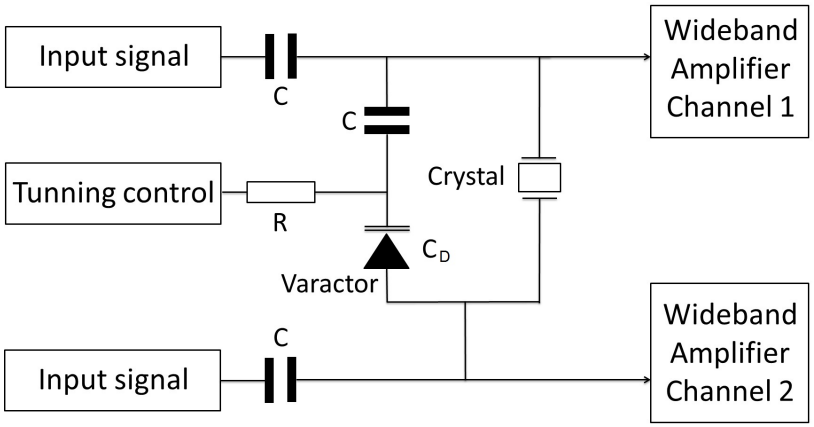

Figure 7.14: Simplified diagram of the circuit for narrow-band detection. A quartz crystal is used for amplification to carry out single-ion detection. A varactor is attached to slightly modify the resonance frequency by means of a control voltage. $C = 10$ pF and $R = 40$ MΩ. The circuit is built at the entrance of the two broad-band amplifiers.

crystallographic axes and the overtones for a natural quartz crystal.

Figure 7.14 shows the simplified diagram of the circuit used for narrow-band detection. The resonance frequency of the circuit can be slightly modified in a range of 300 Hz by means of a GaAs tuning varactor, which acts as a voltage-controlled capacitor. The tunability of the circuit is given by [121]

$$\Delta\nu_{\mathrm{p}} = \nu_{\mathrm{p1}} - \nu_{\mathrm{p2}} = \nu_{\mathrm{s}}\,(\eta_1 - \eta_2)\,, \tag{7.11}$$

where the parameter η reads

$$\eta = \sqrt{\frac{C_0 + C_1 + C_{\mathrm{A}}}{C_0 + C_{\mathrm{A}}}} \tag{7.12}$$

where

$$C_{\mathrm{A}} = \frac{C_{\mathrm{d}} C}{C + C_{\mathrm{d}}}, \tag{7.13}$$

Table 7.2: Values of the parameters of the equivalent circuit for a quartz crystal (see Fig. 7.12), to provide a resonant frequency of 2.69 MHz ± 20%. This is the crystal built in the circuit and tested within this work.

Equivalent component	Value
L	290 mH
R	20 Ω
C_0	3.7 pF
C_1	12 fF

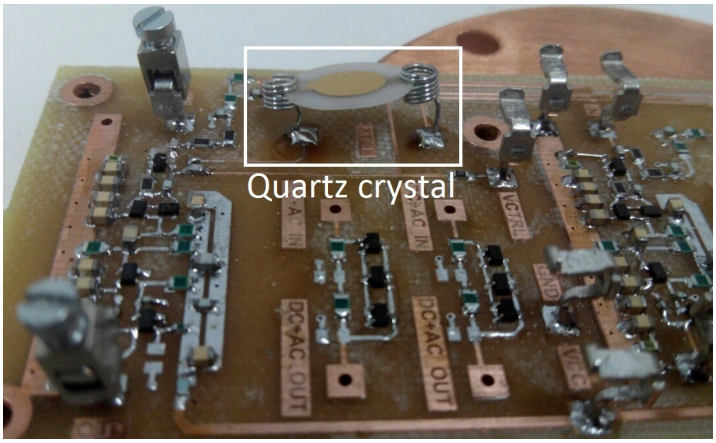

Figure 7.15: Photograph of the quartz crystal integrated in the Printed Circuit Board.

and C is the DC-blocking capacitance of the tunable circuit and C_d the diode capacitance. η_1 and η_2 are the parameters obtained considering the maximum and minimum values of the diode capacitance, respectively. The series resonance frequency is the factor constraining the tunable range of the circuit.

For the work presented in this thesis, a customized quartz crystal produced by Anderson Electronics INC with a resonant frequency of 2.69 MHz ± 20% has been utilized as inductance. This crystal is conceived to detect $^{40}Ca^{+}$ ions with a cyclotron frequency of $\nu_\mathrm{c} = 2689067.5(3)$ Hz. Table 7.2 shows the values of the elements of the circuit for the quartz crystal sketch in Fig. 7.12. The use of this kind of piezoelectric quartz at temperatures down to 1.5 K, in a magnetic field with a strength up to 8 T under UHV conditions, has been shown in Ref. [122]. Figure 7.15 shows a photograph of the PCB for the circuit diagrams of 7.10 and Fig. 7.14 including the quartz crystal and the pre-amplifier. Although the quartz crystals are usually mounted on a holder, due to the use of the crystal under UHV conditions, a bare crystal was built in this case. Two springs serve to fix the crystal to the board and to supply the voltage. Conductive silver paint was used to provide a full contact between the crystal and the springs.

Many groups use coils as resonators in LC circuits or DC SQUIDs (Superconducting QUantum Interference Device). The use of superconducting coils has been reported in several master and PhD these [47, 51, 68, 123]. Also the use of a copper resonator has been reported [124]. Since the Q-value of the coil made of pure copper is limited by the resistance of the wire, superconducting coils are most commonly utilized. The superconducting coils are made of pure niobium (Nb) wire, or niobium-titanium (NbTi) wire, with polytetrafluoroethylene (PTFE) insulator and an external shield made of copper. NbTi wire is most suitable to be used in a high magnetic field since its upper critical field strength is larger compared to a pure Nb wire [125], although pure Nb wire has a surface resistance at cryogenic temperature a factor of 5 smaller than the NbTi one

Table 7.3: Resonator, resonance frequency and Q-value in LC circuits used in different experiments. (1) A DC SQUID is coupled to the superconducting coil.

Experiment	Resonator	Frequency (MHz)	Q-value
TRIGATRAP [47]	Superconducting coil with NbTi wire	0.817	14700
Mainz (g-factor) [125]	Superconducting coil with NbTi wire	2.0	25800
	Coil with OFHC copper	68.2	4700
PENTATRAP [126]	Superconducting coil with NbTi wire	0.6	33000
FSU-TRAP [19]	Superconducting coil with Nb wire(1)	0.213	33000
MPIK/UW-PTMS [2, 127]	Coil with OFHC copper	3.5	1000

[128]. Table 7.3 lists the resonators used in different experiments.

The superconducting coil has high Q-value and has been widely used (see Tab. 7.3), however the use of a quartz crystal resonator provides several advantages:

- The high magnetic field of the Penning trap has no effect in the crystal.
- High Q-values are reached operating the crystal at cryogenic and room temperatures.
- The mechanical support of the crystal is easier to implement and is smaller in size.

7.2.3 Performance

The electronics is divided in two circuit boards made of FR-4 fiberglass with a copper core for heat transfer. Figure 7.16 sketches the layout of the pre-amplifiers and filters in the boards and the connections to the electrodes of the PPT. Two opposite segments from the ring electrode will be used for broad-band detection. Each electrode is connected to one pre-amplifier. Another two segments from the ring electrode, opposite to each other, are used for narrow-band detection. Each electrode is connected to a pre-amplifier, which is coupled to the quartz crystal resonator and the varactor diode. Two segments from correction electrodes are wired to another two pre-amplifiers for axial detection. Second-order low-pass RC filters are built in order to deliver the DC voltages (up to 200 V) to the trap electrodes and perform a good harmonic potential along the trap axis. The cutoff frequency is 2.5 kHz. Second-order low-pass RC filters with low noise E-PHEMT transistors are used as DC and AC filters to provide radial and axial excitation of the ions in the trap by means of external radiofrequency fields. The

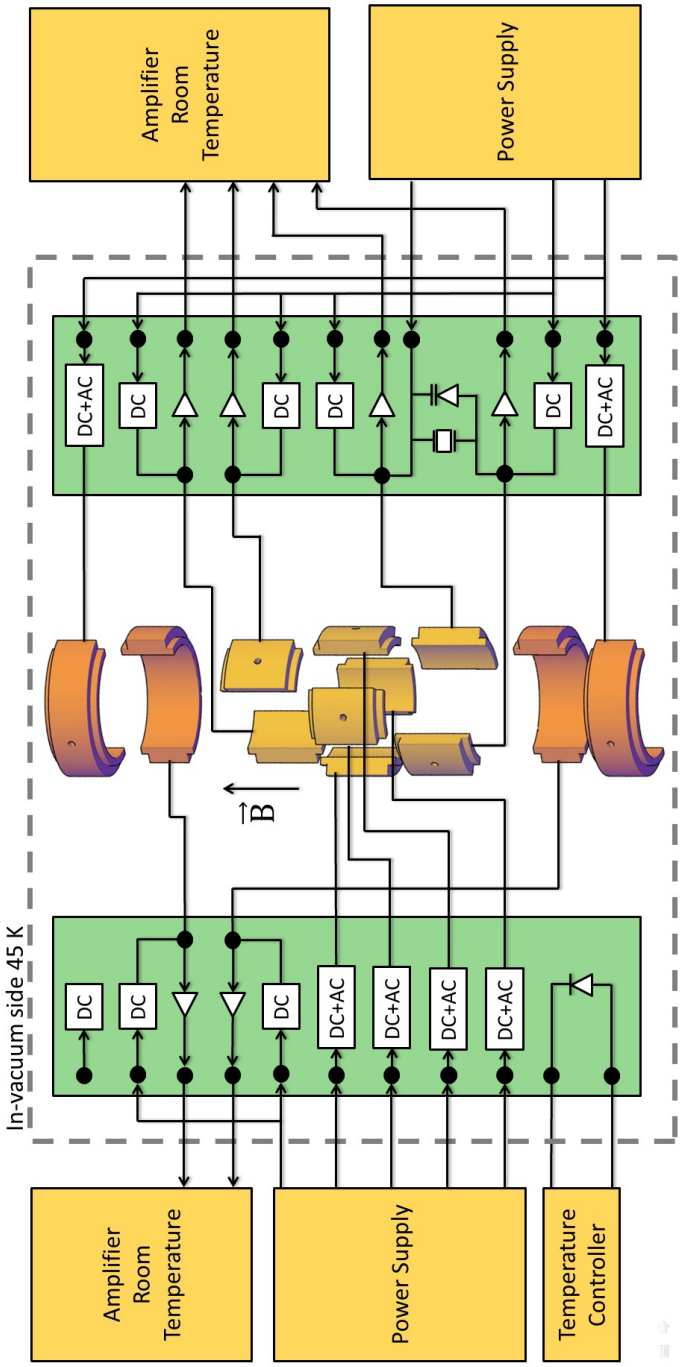

Figure 7.16: Connections diagram between the Printed-circuit-board cards (PCB) and the PPT central electrodes. Ring and correction electrodes are depicted in yellow and orange, respectively. Each card (green rectangles) hose two broad-band and one narrow-band amplifier and six filters. The PCB cards are designed to be used inside vacuum and connected to the second stage of the cryocooler providing 45 K. Amplifiers outside vacuum at room temperature will be also used. Further details are given in the text.

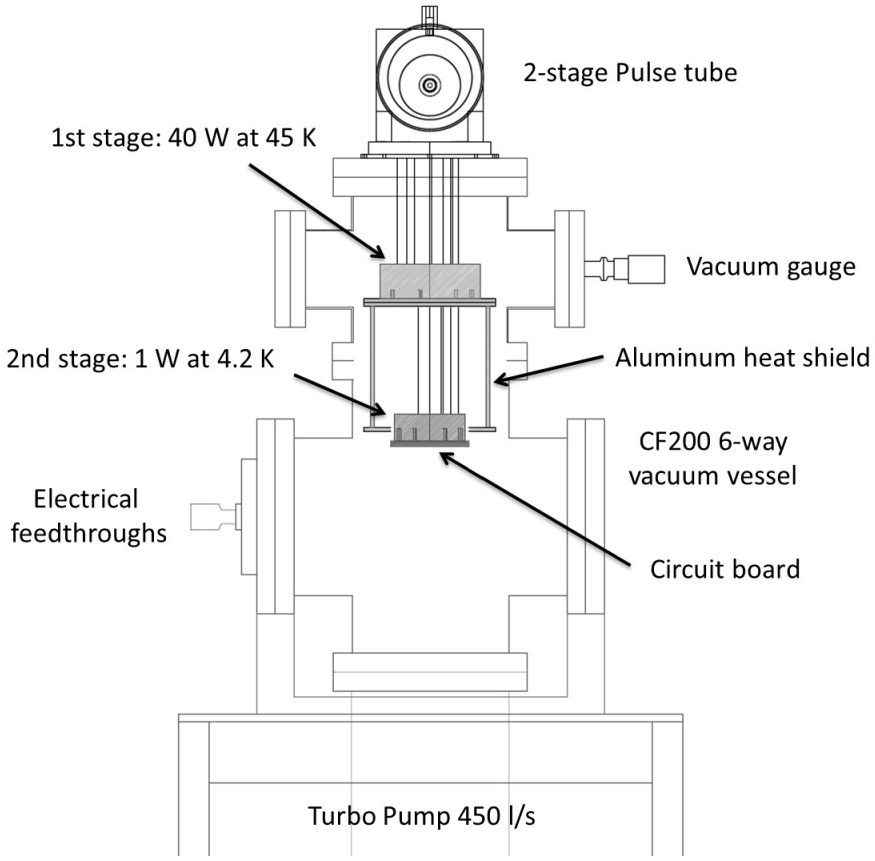

Figure 7.17: Technical drawing of the experimental setup built to the test electronics at cryogenic temperature. The cryocooler is fixed to a customized 6-way DN200CF to DN100CF reducer vacuum cross, which is coupled to a standard 6-way DN200CF one. The vacuum is accomplished by means of a turbomolecular pump (Edwards STP-451C DN160CF) running with a pumping speed of 450 l/s (for N_2) backed by an oil-free dry scroll pump (Edwards nXDS-15i). A pressure in the order of 10^{-7}-10^{-8} mbar is achieved. This is measured with a Full-Range Gauge Active Pirani Cold Cathode (Pfeiffer vacuum PKR 251) connected to a controller unit (Pfeiffer vacuum RVC 300).

temperature of the circuit board is measured using a Schottky diode.

Figure 7.17 shows a two-dimensional technical drawing of the experimental setup to test the electronic circuits at cryogenic temperature. A 2-stage pulsed tube cryocooler; model RP-082B2 from Sumitomo heavy Industries is used. This apparatus produces a continuous close-cycle refrigeration at temperatures in the range of 30 to 45 K in the first-stage and in the range of 3.0 to 4.2 K in the second-stage. The refrigeration capacity is 40 W at 45 K, and 1.0 W at 4.2 K. A cylinder made of OFHC copper with 110 mm diameter and 30 mm length is used for the first-stage and another one, also made of OFHC copper, with 92 mm diameter and 27 mm length allows connecting the circuit board to the second-stage through a customized OFHC plate. Cryogenic high vacuum grease

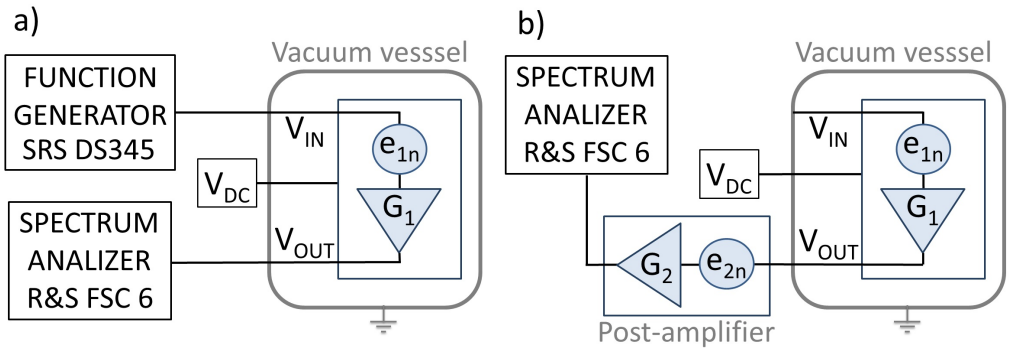

Figure 7.18: a) Diagram of the setup built to measure the gain factor of the amplifier. The RF input signals are delivered by a function generator (SRS DS345) with an RF amplitude of 5 mV_{pp}. A power supply was used to apply a DC-Voltage (V_{DC}) to the amplifier. The output signal was measured by a spectrum analyzer (R&S® FSC 6) with a working frequency range from 9 kHz to 6 GHz, and high sensitivity (-161 dBm at 1 Hz of resolution bandwidth). b) Sketch of the setup to measure the voltage noise density of the amplifier. The input from the preamplifier was grounded, and the output signal was amplified with a low-noise post-amplifier running at room temperature outside vacuum (Stahl Electronics model A7) with 1.7 $nV/\sqrt{Hz}$ voltage noise density from 400 kHz to 10 MHz.

(Apiezon® N) is used between the circuit board and the copper pieces to increase the thermal conduction.

The temperature is measured using a diode (OMEGA engineering model CY7) screwed to the copper piece. A monitor (OMEGA engineering model CYD218) displays the voltage drop and the temperature. Temperatures of about 10 K were measured in the second-stage, two hours after switching on the compressor of the cryocooler.

The pre-amplifier in broad and narrow band configurations were tested after fixing the circuit to the cryocooler. Figure 7.18.a shows a sketch of the setup to measure the gain factor of the amplifier. Figure 7.19 shows the voltage gain of the broad-band amplifier (see Fig. 7.10) in a range from 1 kHz to 10 MHz. A voltage gain of about 57 is obtained in the range of 10 kHz to 4 MHz (broad-band operation) for a voltage supply of 2.5 V when running the circuit at a temperature of 11 K. The voltage gain at room temperature with the same voltage supply is about 10 in the same range of frequencies.

Figure 7.18.b shows a sketch of the setup to measure the voltage noise density of the amplifier. Since the sensitivity of the spectrum analyzer is -161 dBm at 1 Hz of resolution bandwidth, equivalent to 1.993 nV_{RMS} for 50-Ohm systems, a post-amplifier was used to measure the noise density. The output voltage noise density is divided by the voltage gain of the amplifiers to obtain the input one, where only the first stage of amplification is important for the overall noise (see

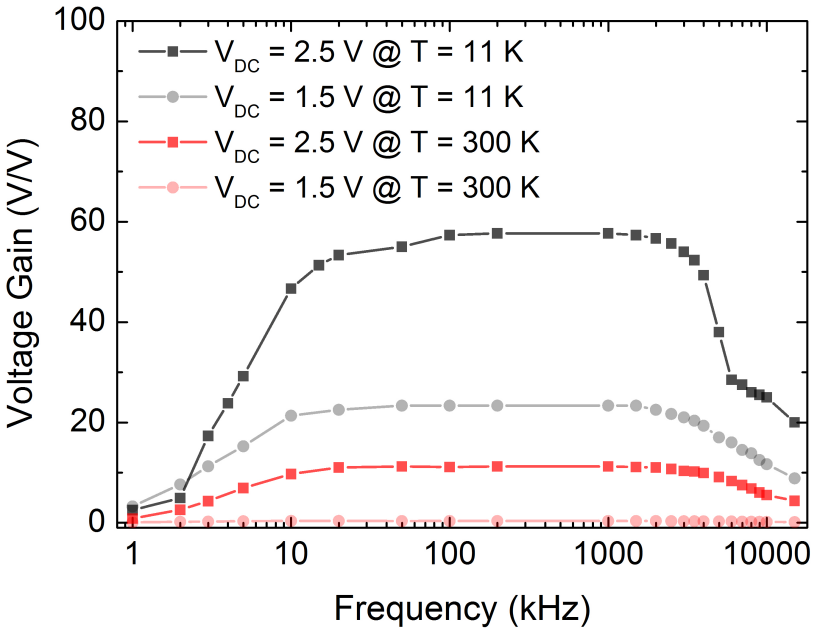

Figure 7.19: BODE plot for the circuit amplifier used for broad-band detection measured at two temperatures and two voltage supply values (V_{DC}). Red and black symbols depict the voltage gain at 300 K and 11 K, respectively. Clear and dark colors represent the voltage gain for voltage supplies of 1.5 and 2.5 V, respectively.

Eq. (7.4)). Figure 7.20 (top) shows the input voltage noise density from the pre-amplifier. The voltage noise density at lower frequency follows the characteristic behavior of a GaAs FET, with a frequency corner at about 1 MHz. The voltage noise density measured from 1 to 4 MHz at 11 K is below 1 nV/$\sqrt{\text{Hz}}$. At room temperature, the voltage noise density increases by a factor of 10. If the circuit is taken as a resistor, the voltage noise decreases a factor of 5 (see Eq. (3.22)). There is a factor of two due to the high voltage gain of the amplifier at low

Table 7.4: Characteristic parameters for several amplifiers. e_n and i_n is the voltage and current noise density at 1 MHz.

Cryo. Amp.	Frequency Range (MHz)	Voltage Gain (V/V)	e_n (nV/$\sqrt{\text{Hz}}$)	i_n (fA/$\sqrt{\text{Hz}}$)
TRAPSENSOR [this work]	0.1 - 10	57	0.9	18
KATRIN [117]	1 - 10	5.5	0.9	100
SE KC05 [129]	0.08 - 3	25	1.2	11
SE HFC50 [129]	0.16 - 50	29.1	0.3	17

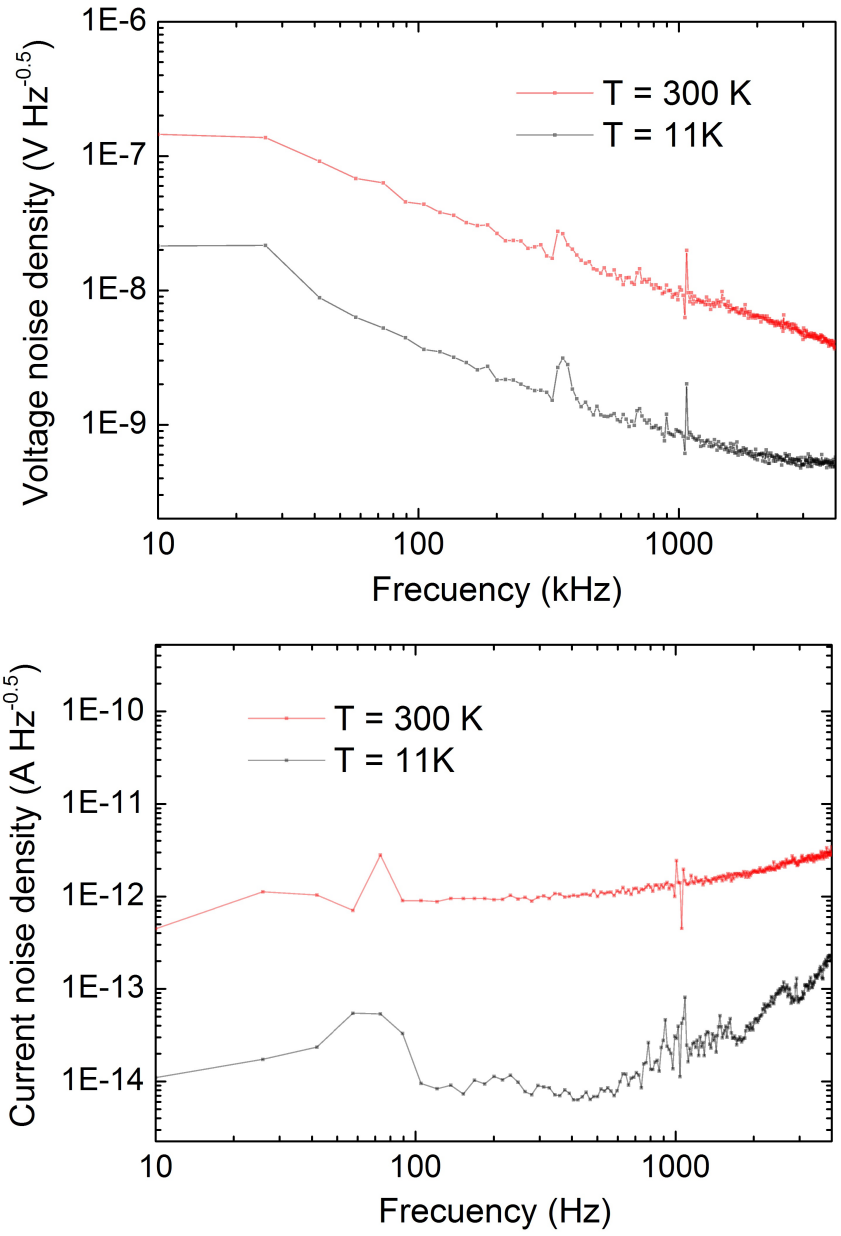

Figure 7.20: Voltage (top) and current (bottom) noise density versus frequency with the circuit inside the vacuum chamber at 11 and 300 K (measured temperatures). A voltage supply of 2.5 V was used. The frequency range is from 10 kHz to 4 MHz. Further details are given in the text.

temperature.

The output current noise density was measured in a similar way as the voltage one (see Fig. 7.18.b), but the input of the preamplifier was not connected. For this case, the impedance of the amplifier was simulated. The current noise density is shown in Fig 7.20 (bottom). The current noise density from 0.1 to

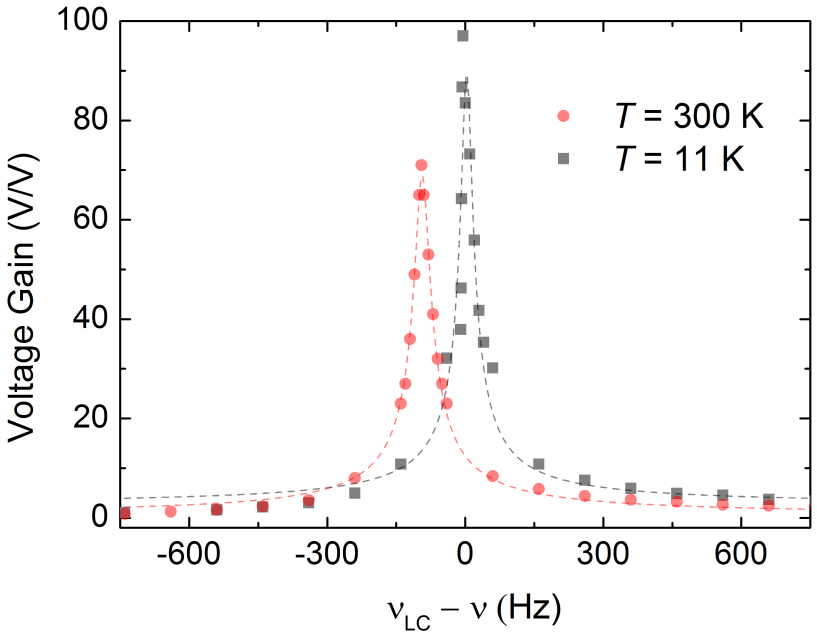

Figure 7.21: BODE plot of the narrow-band amplifier around the resonance frequency for two temperatures. A voltage supply of 2.4 V and a varactor voltage of 11.4 V were used. The dashed lines are Pearson VII fits to the data.

1 MHz at 11 K is of above 10 fA/$\sqrt{\text{Hz}}$. This value is increased a factor of 100 at room temperature. The main outcomes from these measurements are listed for comparison in Tab. 7.4 with other cryogenic amplifiers.

Figure 7.21 shows the voltage gain of the narrow-band amplifier. In this circuit, the quartz crystal (see Fig. 7.15) was used as resonator in the LC circuit. A voltage gain of about 97 is obtained at the resonance frequency 2693243(2) Hz at $T = 11$ K. At room temperature, the resonant frequency is shifted about 100 Hz and a voltage gain of 71 is obtained. This shift in the resonance frequency depends on the crystal cut [120]. These measurements were taken using one pre-amplifier. Since latter there will be two (see Fig. 7.9), this will increase the voltage gain by a factor of ≈ 2. Table 7.5 shows the values of the bandwidth and Q-value for narrow-band circuit at 11 and 300 K. These values are higher than the Q-values of other experiments, obtained by means of superconduct-

Table 7.5: Bandwidth and Q-value provided by the narrow-band circuit for two temperatures.

Temperature	Frequency	Bandwidth	Q-value
11 K	2693243(2) Hz	31(7) Hz	8.7(2.0) $\times 10^4$
300 K	2693146.7(4) Hz	41(1) Hz	6.57(0.16) $\times 10^4$

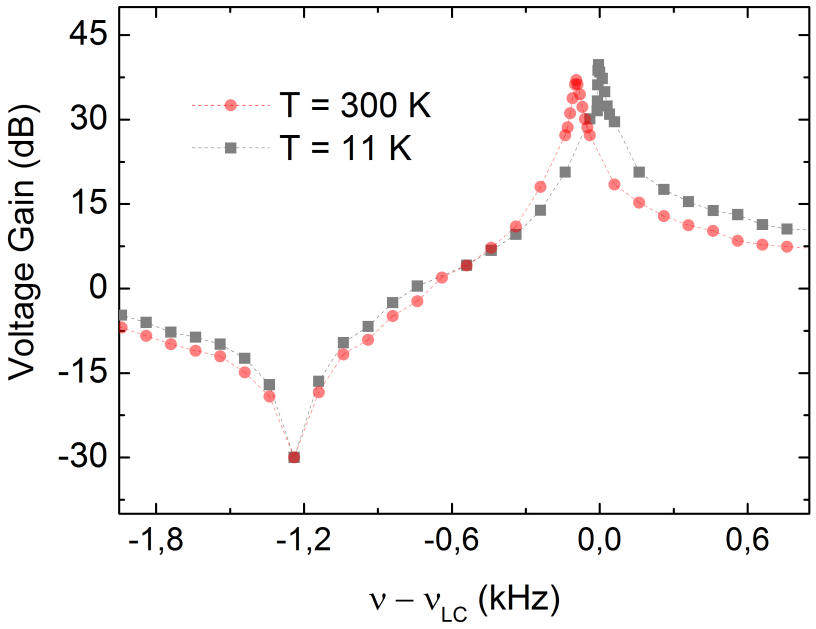

Figure 7.22: BODE plot of the narrow-band amplifier in dB. One can observe the series and parallel resonance frequencies.

ing coils (see Tab. 7.3). A fine tuning of the resonance frequency to match the reduced-cyclotron frequency of the $^{40}Ca^{+}$ ion in the PPT (see Fig. 6.5), depends on the cut of the quartz crystal and will require systematic investigations. Figure 7.22 shows the voltage gain of the narrow-band amplifier in dB, where the series resonance frequency is ν_s =2693.0(0.2) kHz. This resonance is below 5 kHz of the theoretical one (see Eq. (7.10) and Tab. 7.2).

The circuit will be firstly tested with the PPT. The PCBs will be fixed close to the PPT to avoid high capacitance due to the length of the cables. The parallel frequency of the crystal resonator is shifted $\approx$ 1 kHz for a parasitic capacitance due to the trap electrodes and cables of $\approx$ 10 pF. The system will work at 45 K in order to reduce the thermal noise and increase the Q-value of the crystal resonator and the voltage gain of the pre-amplifier. Post-amplification will be carried out at room temperature by the two-channel low noise FT-ICR amplifier A7 produced by Stahl electronics. This post-amplifier has a frequency range from 450 Hz to 25 MHz with a voltage gain at 100 kHz of 100$\pm$ 4% and 25 $\pm$ 4% for narrow-band (high-impedance) and broad-band detection (low-impedance), respectively.

Chapter 8

Summary and outlook

The TRAPSENSOR facility

The work carried out since the beginning of the project TRAPSENSOR presented in this manuscript, has developed in a Penning-traps beamline at the University of Granada. The beamline comprises a laser-desorption ion source coupled to a time-of-flight section for identification of the ion species, a transfer section built with the same specifications as the one existing at the SHIPTRAP facility at GSI-Darmstadt (Germany), a preparation Penning trap and a second Penning trap with a novel geometry to perform precision measurements. All the elements in the Penning-traps beamline have been designed in this work and companies in Spain have built them. The collaboration with GSI-Darmstadt has allowed overcoming several technicalities.

The project is in an international context: it is the only facility of this nature in Spain, and the techniques and instrumentation developed are important for facilities like SHIPTRAP, which gathers researchers from several institutes and for the future Penning-traps facility MATS (precise Measurements on very short-lived nuclei using an Advanced Trapping System) to be built at FAIR (Facility for Antiprotons and Ion Research) [13]. Furthermore, the final aim of improving sensitivity and accuracy, might allow applying such novel technique [34] to determine end-point energies from β-decay processes of interest in neutrino physics [36].

In parallel to the construction and commissioning of the Penning-traps beamline, part of the work presented here was devoted to build another setup comprising eight tunable diode lasers, a stabilized HeNe laser and a wavemeter to study laser cooling in a special Paul trap, which can be referred to as open-ring trap [88]. It was very important to reach the Doppler limit for $^{40}Ca^{+}$ in this device as this serves to develop the geometry of the open-ring Penning trap and the final double Penning-(micro)-trap system, envisaged in the project [75].

The laser-desorption ion source was the first key element of this facility. It is a MALDI-TOF apparatus adapted for the experiments in Granada. It was

commissioned to produce ions in a wide mass-to-charge range from $^{40}Ca^{+}$ to $^{187}Re^{+}$, with kinetic energies ranging from the recommended value for chemistry applications of 20 keV, down to a few hundred eV, providing in this case ion distributions with a temporal width of about a few microseconds [73]. The transfer section similar to the one at SHIPTRAP [81], was built stepwise introducing a pulsed cavity to decrease the ion beam energy from 500 eV in the source to 200 eV for an optimal capture of the ions in the preparation Penning trap. About forty DC-voltages have to be delivered, using several power supplies, for the operation of the system. All these voltages are controlled automatically by a control system similar to the one used at SHIPTRAP or ISOLTRAP facilities [102]. A transmission efficiency in this section of about 70% was achieved. Behind the Penning-traps system, another time-of-flight section was built with a micro-channel plate detector for identification.

The Penning-traps system has been built with ultra-high-vacuum specifications and considering its future use at cryogenic temperature. This system is installed in the bore of a superconducting magnet providing two homogeneous regions with a field strength of 7 T. It is an identical magnet as the one existing at SHIPTRAP [81], JYFLTRAP [130], MLLTRAP [15], TRIGATRAP [47] or as foreseen for MATS at FAIR [13]. The alignment of the Penning-traps system with the magnet bore requested the construction of several components like an electron gun, a segmented diaphragm and several Faraday cups to align the trap tower with the magnetic field lines with an accuracy of 0.35 mm and 0.04°. The center of the preparation Penning trap is located in the first region and the center of the measurement trap in the second one.

The preparation Penning trap

The commissioning and further optimization of the preparation Penning trap was the main objective of this thesis and it was demonstrated that the system meets the requirements for the project TRAPSENSOR and also that can be coupled to existing systems at Radioactive Ion Beam facilities [73]. Mass-selective buffer-gas cooling was applied delivering cleaned and cooled samples in a wide mass-to-charge ratio. This trap has been built following the specifications of the preparation trap for the MATS experiment [13]. The trap tower is made of a stack of three transfer electrodes and twenty-five rings, where the central one and those for correction, are segmented to apply external fields in order to manipulate the ions' motions. A helium gas feeding line was built with a purification system for the mass-selective buffer-gas cooling technique. The pumping barrier between the two traps has a diaphragm with 2 mm inner diameter and a length of 23 mm.

All the sequence for a mass-selective measurement, i.e., production, transport, capture, manipulation and identification needs of eight TTL signals which are delivered by the control system, triggered in turn by the laser-desorption pulse. A mass resolving power of $\frac{m}{\Delta m} = 2.7 \times 10^5$ has been obtained with a total measurement time of 400 ms for $^{40}Ca^{+}$ ions. In the case of rhenium ions, isobaric

separation can clearly be observed when using measurement cycles with a total time of 450 ms. The mass resolving power measured for the two naturally abundant rhenium isotopes is $\frac{m}{\Delta m} = 4.4 \times 10^4$ ($^{187}Re^+$) and $\frac{m}{\Delta m} = 5.8 \times 10^4$ ($^{185}Re^+$). About eight counts per cycle are obtained in resonance for $^{40}Ca^+$ ions, while for $^{187}Re^+$ this rate was five. The magnetic field strength in the first homogeneous region was measured from the cyclotron frequency of $^{40}Ca^+$, considering the mass value given in Ref. [108] yielding 6.99796(14) T. This measurement gives also the stability and the drift of the field during several hours.

The degree of cooling of the ions in the preparation trap was observed by applying a stepwise extraction. Calcium ions, with energies in the interval of 20-280 meV, achieved after a cooling time of 250 ms, were ejected out of the trap. $^{187}Re^+$ ions were also ejected out from the preparation trap with energies of about a few electronvolts, after they were cooled for the same time as the calcium ions. The distribution is different since this ion species is heavier, showing that the maximum number of ions are extracted with energies between 0.5 and 1.0 eV.

Developments for high-performance ion detection

The project TRAPSENSOR is aiming at overcoming present limitations in single ion detection. There is a well-known method of detecting the image current that a stored ions induces in the trap electrodes using high sensitive electronics operated at 4 K. This technique has permitted extraordinary results in mass spectrometry [2, 19, 20]. However, the measurements carried out up to date are limited to ion species with medium or low mass-to-charge ratios. This was the main motivation to impel the project TRAPSENSOR, i.e., to develop a complete different approach of using fluorescence photons instead of electronic detection. Since this approach has not been demonstrated so far, further developments on induce image current detection were carried out in parallel and in collaboration with a local company spin-off of the University of Granada. This was part of the project FPA2012-32076 on *Developments on high-accuracy experiments using ion traps for fundamental physics and applications* funded by the Spanish Ministry of Economy and Competitiveness.

The implementation of the optical method, referred to as *Quantum Sensor* as described in Ref. [34], has requested to design a different kind of Penning trap compared to those existing for mass spectrometry, but also different than those existing for laser spectroscopy in small areas (surface traps). A double Penning-(micro)-trap system has been designed in an academic work and has been built by an U.S. company but also in collaboration with a German one, which has provided the electronics in Roger substrate to stand cryogenic temperatures. Test of the associated electronics has shown the suitability to perform a good harmonic potential and ion communication in the double Penning-(micro)-trap system.

The improvement on electronic detection requests circuitry. The tests have been carried out in broad-band and in narrow-band. A circuit based on two low-noise GaAs HJ-FET as first stage is used in order to amplify the ion signal picked from the trap electrodes. This kind of transistor can be used at cryogenic temperatures. Each trap electrodes will be attached to a different amplifier in order to increase the signal-to-noise ratio, since this configuration decreases the current noise of the amplifier, and multiply by a factor of two its input resistance [116]. A second stage is used as common-source amplifier, and finally, a buffer output stage is utilized. At room temperature, post-amplification will be carried out by a low noise amplifier.

Within this work, an experimental setup to test the electronics at cryogenic temperature was built up. A two-stage pulsed-tube cryocooler was setup in a vacuum chamber. The printed circuit board for broad-band detection was tested in vacuum at room temperature and at 11 K for different values of the supply voltages. A gain of 57 V/V at 11 K in the frequency range from 10 kHz to 3 MHz was measured when the voltage supply was 2.5 V. The gain at room temperature is 10 V/V in the same frequency range. The voltage and current noise densities have been measured yielding 0.9 nV/$\sqrt{\text{Hz}}$ and 18 fA/$\sqrt{\text{Hz}}$, respectively. These are better values than those quoted for previous circuits [117] commissioned for similar experiments.

A quartz crystal was also added to the circuit to create a large impedance and thus deliver a large voltage drop from the induced image current of the oscillating ion. The cut of the crystal was chosen to match the reduced-cyclotron frequency for $^{40}Ca^{+}$. The Q-value obtained was $8.7(2.0) \times 10^4$ at 11 K. This is larger than previous quoted values from other experiments like TRIGATRAP [47], Mainz [125] or FSU-TRAP [19]. The drawback is to match accurately with the cut on the crystal the oscillation frequency of the ion, since the full width at half maximum of the resonant peak is a few tens of Hz, from these outcomes, this is something that needs to be investigated in detail.

Overall, the work presented in this manuscript has put the TRAPSENSOR facility into a shape, which makes this project competitive in the present stage. The developments carried out on detection need to be tested with ions and some technicalities, can be still implemented to allow for a better performance and for the coupling of the two ions in the 7 T magnetic field.

Appendix A

Beyond the project TRAPSENSOR: MATS at FAIR

The PPT built within this work follows the geometrical specifications given in the Technical Design Report for the MATS experiment at FAIR [13]. Figure *A*.1 shows the FAIR facility with a zoom of the current layout of the MATS experiment, which will be located at the end of the Low Energy Branch (LEB) of the Superconducting FRagmentSeparator (Super-FRS). Rare Isotopes Beams (RIB) are produced via fragmentation of a primary heavy-ion beam or via fission of an ^{238}U beam at energies up to 1.5 GeV/u [131]. Subsequently, in-flight separation of the isotopes in the Super-FRS is performed, where the fragments are fully ionized to avoid cross contamination from different ionic charge states by multiple separation stages. The future FAIR facility will provide clean and very intense samples, with a comparatively enhancement of the beam intensity of several orders of magnitude. The MATS experiment will allow applying several techniques to very short-lived radionuclides to perform high-accuracy mass measurements, in-trap conversion electron and alpha spectroscopy, and trap-assisted spectroscopy.

The PPT of the project TRAPSENSOR can be used as a test bench for the preparation trap of the MATS experiment. The sensitivity of the preparation trap has been shown of about 20 Hz (4σ separation between two adjacent peaks) in a wide mass range. A precision of about 10 keV for light-nuclei with mass above $A = 10$, and about 10 MeV for SHEs with masses above $A = 250$, will be reached in the PPT for singly-charged ions. A very important isotope for nuclear physicists is the doubly magic nucleus over the proton dripline ^{100}Sn with a half-life of about 1 s [132], the mass of which could be measured with MATS, provided contaminant ions can be removed with the PPT. At FAIR, ^{100}Sn will be produced in fragmentation reactions. An isotope than might be delivered within a fragmentation reaction is ^{99}In, which has almost the same magnetic rigidity [133]. Since there is a cyclotron frequency difference of 10.9 kHz, separation in

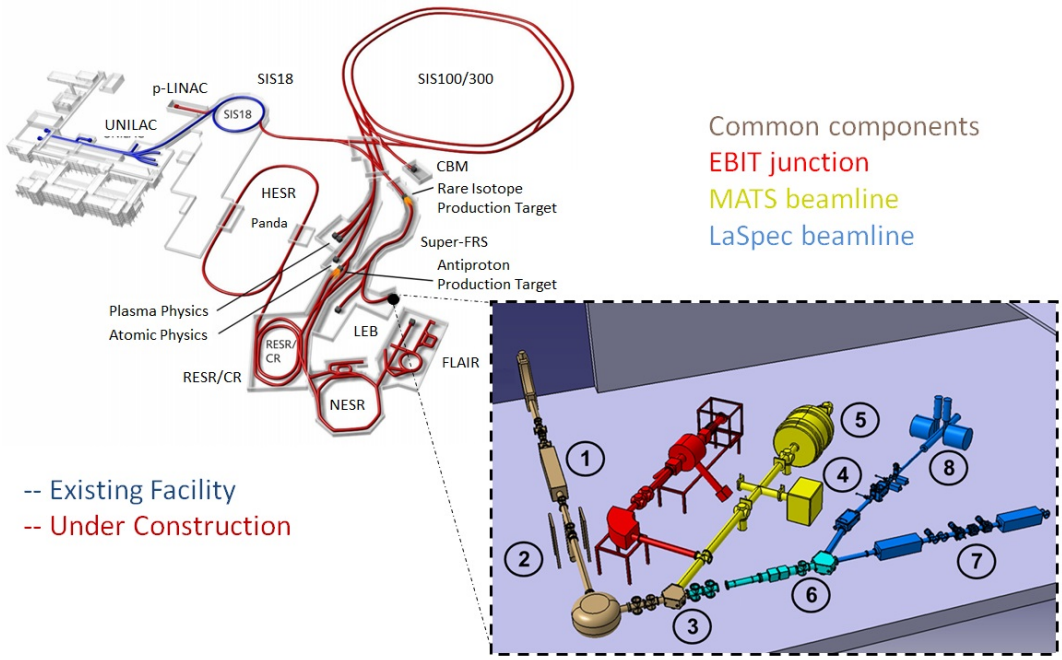

Figure A.1: Sketch of the future FAIR facility [134] under construction in Darmstadt (Germany). The MATS and LaSpec experiments at the end of the LEB of the Super-FRS are shown in the right side: the Buncher section (1), the multi-reflection time-of-flight mass spectrometer (2), and the switchyard (3) are shown in brown; the EBIT (Electron Beam Ion Trap) junction is represented by the red components; The MATS beamline comprising the off-line ion source (4) and the Penning Trap system (5) is shown in yellow. The components of the LaSpec beamline (in blue) are a common line (6), the ion beam line (7) and the atom beam line (8).

the PPT will be possible.

Different cooling mechanisms can be tested for ions species with several charge states and a wide range of masses. Buffer-gas cooling has been demonstrated in this work and electron cooling might be applied. The cooling time for these mechanisms is about several hundred milliseconds [135]. Short cooling times are important for the studies of short-lived nuclei with MATS, thus other mechanism must be studied. Simulations on sympathetic cooling by collisions with laser-cooled $^{24}Mg^{+}$ ions have reported cooling times below 10 μs [136]. With this mechanism, the "hot" ions are cooled due to Coulomb interaction with the "cooled" ones. Sympathetic cooling by laser-cooled $^{40}Ca^{+}$ ions could be used in the PPT of the TRAPSENSOR project. Although the laser beams can be injected along the z axis and $^{40}Ca^{+}$ ions can be used as coolant, the system would need modifications for the detection of the fluorescence. Electrons or laser-cooled ions have the advantage of preventing gas flow from the PPT into the measurement trap.

Electronic detection of the current induced by the ions in the trap electrodes will allow monitoring the charge states during the cooling process in the MATS PPT. This detection technique has been developed within this work. Broadband detection will allow monitoring of the cooling process of ions in a wide range of mass-to-charge ratios. The detection limit as a function of the trapped ion species can be studied from calcium to gold. The sensitivity depends of the trapping time, and the mass and energy of the ions. It will be improved by means of a cryogenic setup.

Appendix B

Resumen en Castellano

El trabajo que aquí se presenta se ha realizado en el marco del proyecto TRAP-SENSOR *High-Performance Mass Spectrometry using a Quamtum Sensor* [34], financiado por el Consejo Europeo de Investigación y que se encuentra en la última fase de desarrollo en la Universidad de Granada. La instalación que se ha construido comenzando en marzo de 2012, es única en España, y, a nivel mundial es la primera instalación donde, el enfriamiento utilizando láseres sobre iones confinados en trampas magnéticas (*Penning traps*) se utiliza para llevar a cabo medidas de masas de ultra alta precisión [1].

B.1 Motivación y objetivos

Medidas de masa con alta precisión son importantes en física fundamental, ya que en el caso de una partícula elemental, la masa es una propiedad fundamental, y en el caso de un átomo, revela información sobre las interacciones entre sus constituyentes. Hoy en día, las trampas de iones magnéticas son los dispositivos más adecuados para llevar a cabo medidas de las masas de partículas elementales y átomos tanto exóticos como estables.

El uso de estos dispositivos en instalaciones de haces radioactivos, por ejemplo la instalación SHIPTRAP en el GSI (Helmholtzzentrum für Schwerionenforschung) en Darmstadt (Alemania), ha permitido por primera vez medir masas de elementos más pesados que el uranio [8, 9], lo que ha dado como resultado estudios relevantes de estructura nuclear en la capa $N = 152$ y esto ha conllevado a obtener mayor información sobre la llamada Isla de Estabilidad, predicha en torno $N = 182$ y $Z = 114$, cuya localización exacta aún se desconoce [10]. Las medidas realizadas con la instalación SHIPTRAP han establecido el límite actual de la técnica utilizada en lo que respecta a sensibilidad. La técnica utilizada en estos experimentos, denominada *Time-of-Flight Ion-Cyclotron-Resonance* (TOF-ICR) [16] necesita de varias decenas de iones para poder obtener un resultado de la medida de un isótopo. Si bien, el desarrollo de una nueva técnica conocida como *Phase-Imaging Ion-Cyclotron-Resonance* (PI-ICR) [17], permite medir la masa de iones con un factor 5 de ganancia en precisión registrando sólo una decena de éstos, aún resultaría insuficiente en el

caso de elementos superpesados (SHEs) donde las tasas de producción a partir de las reacciones de fusión-evaporación son extremadamente bajas, en algunos casos llegando a un átomo por semana [10]. Por tanto, es necesario un método que permita utilizar un único ion del isótopo cuya masa se desea medir.

Además de elementos radioactivos, el uso de trampas magnéticas ha permitido medir masas de elementos estables o con vidas medias muy altas, con precisiones relativas en torno a 10^{-11} o incluso mejor [2, 19, 20]. Este tipo de medidas, las masas de los núcleos padre e hijo en desintegraciones β, o captura electrónica, con una incertidumbre relativa inferior a 10^{-11}, han sido utilizadas junto a resultados obtenidos en experimentos que utilizan microcalorímetros para medir el calor de reacción de la desintegración con una resolución del orden de 1 eV, con el objetivo de proporcionar un límite superior más cercano a la masa del neutrino electrónico (ver por ejemplo [32]).

La instalación TRAPSENSOR se ha construido con el objetivo final de poner en funcionamiento un nuevo dispositivo, denominado sensor cuántico (QS de su acrónimo en inglés *Quantum-Sensor*), que permita superar las limitaciones de las técnicas actuales en lo que respecta a sensibilidad y precisión, que se emplean trampas de iones magnéticas [34]. Este dispositivo consiste en un sistema de dos micro trampas magnéticas. Un ion de $^{40}Ca^{+}$ se enfría hasta el límite Doppler con láser, en una de las dos trampas. El ion objeto de estudio, se almacena en la otra trampa. Es posible trasferir energía de un ion al otro a partir de la carga que inducen en un electrodo común. De esta forma, las frecuencias características del ion de interés en la trampa magnética se pueden medir a partir de la señal de fluorescencia del ion $^{40}Ca^{+}$. Esta técnica se podría utilizar inicialmente con núcleos estables o de vida media muy alta.

El trabajo llevado a cabo en esta tesis tiene varios objetivos. En primer lugar, construir una línea de haz para albergar un sistema de trampas magnéticas, el cual se ha diseñado y construido en este trabajo a partir de sistemas ya existentes y de los estudios realizados. La línea de haz está compuesta por una fuente de producción de iones por ablación láser, una sección de transferencia y el sistema de trampas magnéticas fijadas en el tubo interior de un imán superconductor de 7 T de campo máximo, idéntico al que existen en varios experimentos: SHIPTRAP [81], JYFLTRAP [130] MLLTRAP [15] y TRIGATRAP [47]. Dicho imán tiene dos regiones de campo magnético altamente homogéneas en un volumen de 1 cm^3 cada una y separadas una distancia de 20 cm. En la región de mayor homogeneidad (0.1 ppm), se colocará el sistema de dos micro trampas magnéticas, que actualmente se encuentra en la fase final de construcción. En la actualidad, en esta región se ha colocado una trampa de anillos para realizar por primera vez experimentos de enfriamiento láser de un ion de $^{40}Ca^{+}$ en un campo magnético de 7 T. En la primera región de alta homogeneidad (1 ppm) se sitúa la trampa de preparación. Esta trampa ha sido diseñada y construida siguiendo las especificaciones de la trampa que para el mismo fin se propuso en el fututo experimento MATS (*precise Measurements on very short-lived nuclei using an Advanced Trapping System*) [13] que se construirá en la línea de baja

energía (*Low Energy Branch*) de la instalación FAIR (*Facility for Antiprotons and Ion Research*) [134]. El segundo objetivo de esta tesis, en torno al cual ha girado la mayor parte del trabajo que aquí se presenta, ha sido el diseño, construcción, puesta en funcionamiento y caracterización de la trampa magnética de preparación. La mayor parte de los elementos se han construido en un taller local. Por último, un tercer objetivo ha sido desarrollar técnicas de detección de un solo ion mediante la corriente de carga inducida por éste en los electrodos de la trampa donde está confinado o a partir de la señal de fluorescencia. Para el primer método se han llevado a cabo diferentes pruebas a temperaturas ambiente y criogénica, en ultra alto vacío, utilizando varias configuraciones de circuitos amplificadores basados en FETs de GaAs, en colaboración con una empresa local. En lo que respecta al segundo método, se ha construido la micro trampa y la electrónica en colaboración con una empresa de EE.UU. y otra de Alemania. Se ha probado el circuito para acoplamiento de los iones.

B.2 Estructura y contenido

Esta tesis, además de la introducción y las conclusiones, consta de seis capítulos que se describen brevemente a continuación.

B.2.1 Principios y técnicas utilizadas en trampas de iones

Las trampas de iones permiten almacenar partículas cargadas en un volumen de espacio fásico muy reducido. Existen básicamente dos grupos de trampas de iones: uno donde las partículas se confinan mediante un campo eléctrico variable, y se conocen como trampas de radiofrecuencia o *Paul traps*, y otro donde se confinan por la superposición de un campo eléctrico estático y un campo magnético, que se conocen como trampas magnéticas o *Penning traps*. En este tipo de trampas, el movimiento del ion se puede describir como la superposición de un movimiento axial, paralelo al campo magnético y dos movimientos en el plano radial, uno lento llamado movimiento magnetrón y otro rápido denominado ciclotrón reducido. Las frecuencias características cumplen lo que se conoce como *Invariance Theorem*, donde la suma cuadrática de las frecuencias de los tres movimientos es la frecuencia ciclotrón (ω_c) (véase Sec. 2.2), la cual depende solamente de la intensidad del campo magnético y de la relación carga-masa del ion.

Las técnicas de detección deben de proporcionar las frecuencias características del ion en la trampa, que permitan obtener un valor de su masa. Los métodos se pueden dividir en dos grupos: destructivos y no destructivos. Las técnicas de medida destructivas son aquellas en las que se pierde el ion después de cada ciclo de medida, siendo necesarios varios ciclos para obtener un resultado final. Este es el caso de la técnica TOF-ICR [16], donde la frecuencia ciclotrón se obtiene a partir de la diferencia en tiempo de vuelo del ion extraído. La reducción del tiempo de vuelo viene originada por la modificación de la energía radial de ion en la trampa, que se genera al aplicar un campo eléctrico cuadripolar en la dirección radial, variando en amplitud con una radiofrecuencia entorno a ω_c del ion en cuestión. Esta técnica se utiliza en muchas instalaciones de haces radioactivos y

necesita de varias decenas de iones para obtener un resultado. La técnica PI-ICR [17] hace uso de campos dipolares para medir las frecuencias radiales del ion en la trampa, observando las distintas fases del movimiento a partir del impacto del ion en un detector sensible en posición. La técnica no destructiva que se ha desarrollado hasta la fecha, utiliza la corriente debida a la carga inducida por el ion o los iones confinados en la trampa y, a partir de esta señal en tiempo, se obtiene una señal en el espacio de frecuencias que proporciona las frecuencias características. Una variante de esta técnica ampliamente utilizada en química se conoce como *Fourier-Transform Ion-Cyclotron-Resonance* (FT-ICR) [63]. La técnica se aplica a miles de iones atrapados en un amplio rango de relación carga-masa, o bien, puede ser aplicada, para medidas de precisión, a la detección de un solo ion mediante el uso de un circuito resonante LC. Otra técnica no destructiva es la que se ha propuesto en el marco del proyecto TRAPSENSOR y para la que se ha construido la instalación que aquí se presenta. Además de la sensibilidad, el uso de una técnica u otra, permite reducir efectos sistemáticos y mejorar la precisión. Un rango de incertidumbre relativa en la medida de masa varía desde el orden de 10^{-6} para identificación de isotopos o moléculas, hasta menos de 10^{-11} en el caso de física de neutrinos. En el caso de núcleos radioactivos, la precisión en la medida vendrá determinada por su vida media. Para núcleos de vida media larga o estables, la precisión estará limitada principalmente por la estabilidad del campo magnético [32, 70].

B.2.2 La instalación TRAPSENSOR

La instalación TRAPSENSOR tiene dos partes: una de ellas comprende la línea donde se encuentran instaladas las trampas magnéticas y la otra, que ha servido para las pruebas de los láseres necesarios para estudiar el enfriamiento de un ion de $^{40}Ca^{+}$.

El primer elemento en la línea de haz de las trampas magnéticas, es una fuente de producción de iones por ablación láser [73]. Esta fuente es la adaptación de un aparato comercial llamado MALDI-TOF (*Matrix-Assisted-Laser-Desorption-and-Ionization Time-Of-Flight*), cedido por la Universidad de Mainz. Un láser pulsado con $\lambda = 532$ nm y energía en torno a 200 mJ y anchura temporal de 4 ns, se utiliza para crear los iones. Esta fuente de iones se acopla a varias cámaras de vacío en el interior de las cuales se ha instalado una sección de transferencia formada por quince lentes electrostáticas, dos deflectores y un cuadrupolo, que permite dejar pasar el haz o desviarlo un ángulo de 90º. Después de la producción al interaccionar el láser pulsado con la muestra metálica, los iones se extraen con una energía cinética de 500 eV, y utilizando los electrodos a diferentes potenciales electrostáticos, es posible focalizar el haz y transportarlo hasta las trampas magnéticas. La energía del haz se debe reducir hasta 200 eV pulsando una lente de la sección. El sistema de trampas ha sido alineado con respecto al campo magnético del imán superconductor usando varias tazas de Faraday y un cañón de electrones, diseñados y construidos en este trabajo. Para la detección, los iones son extraídos del sistema de trampas por medio de un sistema de lentes electrostáticas y el número de éstos es registrado por medio de un detector de

micro-canales (MCP). El sistema de vacío está formado por dos bombas turbo-moleculares en la fuente de iones de 800 l/s, cada una colocada a un lado del tubo de vacío que contiene el sistema de trampas magnéticas. Recientemente se ha añadido dos bombas iónicas de 600 l/s y 300 l/s. El conjunto permite obtener presiones de vacío en el rango de 10^{-9} mbar. Varias fuentes de tensión son controladas mediante un PC para aplicar más de 40 señales a lo largo de toda la línea.

En paralelo a la línea de trampas magnéticas, se ha construido una trampa de radiofrecuencia, con su fuente de iones y sistema de vacío y un sistema de láseres [88] desarrollado para los estudios de enfriamiento Doppler del ion $^{40}Ca^{+}$[75], que se deben llevar a cabo con posterioridad en la trampa magnética. La trampa de radiofrecuencia está formada por dos conjuntos de tres anillos concéntricos que permite el acceso con los haces de los láseres en la dirección radial a lo largo de los 360 grados y en la dirección axial. Dicha trampa es idéntica al dispositivo utilizado en el experimento LPCTRAP en GANIL (Francia) [48]. Los iones de $^{40}Ca^{+}$ son creados en el centro de la trampa al ionizar un haz de átomos de calcio por colisión con fotones. En este caso la ionización es resonante y se lleva a cabo utilizando un láser de Ti:Sa y un doblador de frecuencias para obtener una longitud de onda $\lambda = 423$ nm ($4^1S_0 \rightarrow 4^1P_1$), que se superpone con un haz de un láser de diodo que emite con $\lambda = 375$ nm. El sistema láser necesario para enfriar el ion de $^{40}Ca^{+}$ está compuesto por ocho láseres de diodo de cavidad externa sintonizables de longitudes de onda 397 nm ($4^2S_{1/2} \rightarrow 4^2P_{1/2}$), 854 nm ($3^2D_{5/2} \rightarrow 4^2P_{3/2}$) y 866 nm ($4^2D_{3/2} \rightarrow 4^2P_{1/2}$). Un medidor de longitudes de onda de ultra alta precisión (10 MHz, 3 σ) se calibra utilizando la transición de 632 nm de un láser de Helio-Neón y junto a una tarjeta electrónica, permite el bloqueo en frecuencia de los mismos. La trampa de radiofrecuencia está situada dentro de una cámara de vacío DN100CF con varios puertos DN16CF, donde un vacío del orden de 10^{-10} mbar se consigue con una bomba turbo-molecular y una bomba iónica de 300 l/s. La geometría de la trampa de anillos ha servido de partida para el sistema final de enfriamiento en una trampa magnética. Una primera versión ha consistido en reducirla en un factor dos y se ha añadido un electrodo para el acoplamiento [76, 77]. Esta primera versión se ha podido construir utilizando las mismas técnicas de mecanizado que para el resto de trampas. La versión final es un factor 10 más pequeña y las técnicas de construcción han sido diferentes.

B.2.3 La trampa magnética de preparación

La parte principal de esta tesis ha sido el diseño, construcción y puesta en funcionamiento de la trampa de preparación del proyecto TRAPSENSOR, siguiendo las especificaciones de la trampa de preparación propuesta en el documento de construcción técnica (*Technical Design Report*) TDR de las instalaciones MATS y LaSpec de FAIR. La torre que contiene la trampa de preparación está formada por tres electrodos de transferencia, veinte electrodos que conforman las secciones llamadas segmentadas, cuatro electrodos de corrección y un anillo central

segmentado en ocho partes para llevar a cabo excitación en el plano radial del ion en la trampa y detección de corrientes inducidas. Para el diseño de esta trampa se han utilizado materiales con baja permeabilidad magnética, compatibles con su uso en ultra alto vacío, y, con altos coeficientes de transferencia de calor para su uso a temperaturas criogénicas. Por esta razón, los electrodos de la trampa están fabricados en cobre con un baño de plata y oro, y se ha utilizado como aislante eléctrico zafiro. En el centro de la trampa se consigue un potencial harmónico. Para la inyección y extracción de los iones en la trampa se utilizan varios interruptores. Las señales TTL de control para éstos son suministradas por una tarjeta FPGA (*Field Programmable Gate Array*) utilizada como generador de pulsos y conectada al sistema de control (*CS* de su acrónimo en inglés *Control System*). Este sistema, similar al utilizado en instalaciones como SHIPTRAP y ISOLTRAP, permite el control de los instrumentos y el registro y análisis de los datos a partir de las medidas realizadas con el sistema de trampas magnéticas [102].

La trampa de preparación tiene como objetivo fundamental la separación de la especie iónica que se desea medir del resto. Además, los iones de interés se enfrían por colisiones con átomos de un gas, utilizando la técnica conocida como *buffer-gas cooling technique*, que consiste en aplicar un campo cuadripolar a la frecuencia ciclotrónica del ion [50]. Los iones, inicialmente almacenados con una energía cinética de 200 eV en la trampa de preparación, se enfrían hasta 0.025 eV después de aproximadamente 400 ms. Un diafragma situado a la salida de la trampa con un diámetro interior de 2 mm permite que sólo los iones con una determinada frecuencia ciclotrónica, que coincide con la del campo de excitación, y por tanto con una determinada relación carga-masa, sean extraídos. Previamente a la aplicación del campo cuadripolar, se aplica otro, de naturaleza dipolar, variando con la frecuencia del movimiento magnetrón de los iones, que en primera aproximación no depende de la masa. Con esta técnica es posible obtener un poder en resolución en masas del orden de 10^5 [78].

B.2.4 Recientes desarrollos en detección no destructiva

Dos sistemas se están desarrollando en la Universidad de Granada para la detección de un solo ion confinado en una trampa magnética. El primero de ellos está basado en la detección electrónica de las corrientes inducidas por los iones en los electrodos de la trampa. El segundo está basado en la detección de fotones de fluorescencia de un ion enfriado por láser.

Para la medida de las frecuencias características de los iones atrapados a partir de las corrientes que éstos inducen en los electrodos de la trampa, se han desarrollado circuitos pre-amplificadores que pueden funcionar en ultra alto vacío a la temperatura de 4 K en presencia de un campo magnético alto. Los preamplificadores basados en transistores FET de GaAs pueden funcionar en un amplio rango de frecuencias (1 kHz hasta 10 MHz), o bien, mediante el acoplamiento de una inductancia L al circuito y, teniendo en cuenta la capacidad parásita

producida por los electrodos de la trampa y el cableado, crear un circuito resonante LC con un elevado valor Q y funcionar en banda estrecha. Este tipo de circuito permite obtener una alta impedancia para la frecuencia de resonancia ($\omega_{LC} = 1/\sqrt{LC}$), y por lo tanto, una gran diferencia de potencial a partir de la pequeña corriente producida por un solo ion almacenado. En este caso, como elemento resonante se ha elegido un cristal de cuarzo debido a que presenta un elevado valor Q, tanto a temperatura ambiente como a temperatura criogénica. Estos circuitos que se acoplarán a una trampa magnética, se han probado y caracterizado en una cámara de vacío donde se ha instalado un sistema de cabezas frías de tubo pulsado de dos etapas que es capaz de mantener una superficie de cobre, a la que se conecta el circuito, a una temperaturas de 4 K. La señal después del circuito amplificada de estos circuitos se vuelve a amplificar a temperatura ambiente y a la señal resultante se le aplica la transformada de Fourier, lo que permite obtener las frecuencias características de los iones en la trampa.

El método de detección propuesto en el proyecto TRAPSENSOR también se ha desarrollado. Ha sido necesario construir una trampa Penning utilizando técnicas diferentes a las convencionales en espectrometría de masas, debido al reducido tamaño de las mismas. También ha sido posible integrar la electrónica en un circuito de tamaño reducido.

B.3 Resultados y conclusiones

El trabajo llevado a cabo en esta tesis ha consistido en el diseño, construcción, puesta a punto y caracterización de la línea de haz de las trampas magnéticas del proyecto TRAPSENSOR, con especial énfasis en la trampa de preparación. Junto a este trabajo se ha participado activamente en la construcción, puesta en marcha y caracterización del sistema formado por una trampa de radiofrecuencia y un sistemas de láseres para el estudio del enfriamiento láser de un ion de $^{40}Ca^{+}$.

En lo que respecta a la línea de haz de las trampas magnéticas, la fuente láser se ha utilizado para producir iones en un amplio rango en cuanto a relación carga-masa, desde calcio hasta renio. Haces de iones con energía desde 500 hasta 4000 eV se obtienen en distribuciones con una anchura temporal de unos pocos microsegundos. La sección de transferencia ha permitido disminuir la energía del haz, trasportarlo e introducirlo en el sistema de trampas magnéticas con una eficiencia de en torno a 70%. El sistema de trampas magnéticas se ha alineado con respecto al campo magnético del imán con una precisión de 0.35 mm y 0.04º.

En lo que respecta a caracterización, la técnica de selección de masas aplicada en la trampa de preparación resulta un poder de resolución en masa de $\frac{m}{\Delta m} = 2.7 \times 10^5$ para $^{40}Ca^{+}$ con ciclos de enfriamiento de 400 ms. En el caso de iones de renio, los ciclos de enfriamiento utilizados son de 450 ms y el poder de resolución en masa obtenido de $\frac{m}{\Delta m} = 4.4 \times 10^4$ y $\frac{m}{\Delta m} = 5.8 \times 10^4$ para los isotopos $^{185}Re^{+}$ y $^{187}Re^{+}$, respectivamente. El valor óptimo de la presión del gas helio está en torno a 10^{-7} mbar. Utilizando los valores obtenidos a partir

de la técnica de selección para $^{40}Ca^{+}$ y el valor de masa tabulado en la última evaluación [108] se ha determinado el campo magnético en el centro de la trampa de preparación siendo éste 6.99796(14) T. La estabilidad y desplazamiento del campo fue monitorizado durante varias horas.

La reducción de energía de los iones en la trampa de preparación se ha observado aplicando varios potenciales de extracción de forma secuencial. En el caso de iones de $^{40}Ca^{+}$, con ciclos de enfriamiento de 250 ms, un 75% de los iones son extraídos con una energía comprendida entre 180 y 280 meV, un 14% con energía en el intervalo 80-180 meV y un 6% con 20-80 meV. El mismo tipo de experimento realizado con iones de renio ha permitido obtener una distribución de los iones en la trampa después del enfriamiento. Dado que los iones de calcio se transportan a una segunda trampa para realizar enfriamiento mediante láser, se llevaron a cabo simulaciones del transporte de los mismos utilizando las distribuciones medidas y resultando en un máximo de 20%. Tasas de iones de calcio de 8 cuentas por ciclo, y para renio de 5 cuentas por ciclo, fueron obtenidas.

Otra parte importante en este trabajo ha sido el desarrollo de métodos de detección de un sólo ion. Se ha construido y validado el circuito para la detección de corrientes inducidas en una trampa magnética en banda ancha y banda estrecha, midiendo a temperatura ambiente y criogénica. En banda ancha se ha medido una ganancia de voltaje de 55 V/V a una temperatura de 11 K en un rango de frecuencias desde 10 kHz hasta 3 MHz, frente a una ganancia en voltaje de 10 V/V a temperatura ambiente. Las densidades de ruido de voltaje e intensidad medidas fueron 0.9 $\mathrm{nV}/\sqrt{\mathrm{Hz}}$ and 18 $\mathrm{fA}/\sqrt{\mathrm{Hz}}$, respectivamente, a 11 K. Estos valores de ruido son inferiores a los de otros circuitos utilizados en experimentos similares [117]. En banda estrecha, un elevado valor Q de $8.7(2.0) \times 10^4$ a 11 K fue medido. Este valor es superior al presentado en varios experimentos mediantes bobinas de hilo superconductor [47, 125, 19]. Por otro lado, la construcción de los electrodos en el sistema de dos microtrampas magnéticas ha sido descrito, y la electrónica asociado para conectar los iones atrapados se ha construido y probado.

Para finalizar, el trabajo que se ha presentado en este documento ha conllevado a poner la instalación TRAPSENSOR en un estado, que hace que el proyecto sea competitivo. Los desarrollos llevados cabo en cuanto a detección de forma no destructiva de iones en trampas magnéticas han resultado en una mejora de las prestaciones que ahora es necesario probar con iones. Además de la financiación del Consejo Europeo de Investigación, parte del trabajo presentado ha sido financiado por el Ministerio de Economía y Competitividad del Gobierno de España a través de los proyectos FPA2010-14803, FPA2012-32076 y UNGR10-1E-501.

Bibliography

[1] K. Blaum, J. Dilling and W. Nörtershäuser, *Precision atomic physics techniques for nuclear physics with radioactive beams*, Phys. Scr. T152, 014017 (2013).

[2] R.S. Van Dyck Jr., D.B. Pinegar, S. van Liew and S.L. Zafonte, *The UW-PTMS: Systematic studies, measurement progress, and future improvements*, Int. J. Mass Spectrom. 251, 231 (2006).

[3] D. Beck, F. Ames, M. Beck, G. Bollen, B. Delauré, J. Deutsch, J. Dilling, O. Forstner, T. Phalet, R. Prieels, W. Quint, P. Schmidt, P. Schuurmans, N. Severijns, B. Vereecke, S. Versyck and the EUROTRAPS collaboration, *Search for new physics in beta-neutrino correlations with the WITCH spectrometer*, Nucl. Phys. A 701, 369 (2002).

[4] Z. Andjelkovic, R. Cazan, W. Nörtershäuser, S. Bharadia, D.M. Segal, R.C. Thompson, R. Jöhren, J. Vollbrecht, V. Hannen and M. Vogel, *Laser cooling of externally produced Mg ions in a Penning trap for sympathetic cooling of highly charged ions*, Phys. Rev. A 87, 033423 (2013).

[5] G. Gabrielse, N.S. Bowden, P. Oxley, A. Speck, C.H. Storry, J.N. Tan, M. Wessels, D. Grzonka, W. Oelert, G. Schepers, T. Sefzick, J. Walz, H. Pittner, T.W. Hänsch and E.A. Hessels (ATRAP collaboration) *Background-free observation of cold antihydrogen with field-ionization analysis of its states*, Phys. Rev. Lett. 89, 213401 (2002).

[6] S. Ulmer, C. Smorra, A. Mooser, K. Franke, H. Nagahama, G. Schneider, T. Higuchi, S. Van Gorp, K. Blaum, Y. Matsuda, W. Quint, J. Walz and Y. Yamazaki, *High-precision comparison of the antiproton-to-proton charge-to-mass ratio*, Nature 524, 196 (2015).

[7] C. Smorra, K. Blaum, L. Bojtar, M. Borchert, K.A. Franke, T. Higuchi, N. Leefer, H. Nagahama, Y. Matsuda, A. Mooser, M. Niemann, C. Ospelkaus, W. Quint, G. Schneider, S. Sellner, T. Tanaka, S. Van Gorp, J. Walz, Y. Yamazaki and S. Ulmer, *BASE - The baryon antibaryon symmetry experiment*, Eur. Phys. J. Spec. Top. 224, 3055 (2015).

[8] M. Block, D. Ackermann, K. Blaum, C. Droese, M. Dworschak, S. Eliseev, T. Fleckenstein, E. Haettner, F. Herfurth, F.P. Heßberger, S. Hofmann, J. Ketelaer, J. Ketter, H.-J. Kluge, G. Marx, M. Mazzocco, Yu.N. Novikov, W.R. Plaß, A. Popeko, S. Rahaman, D Rodríguez, C. Scheidenberger, L.

Schweikhard, P.G. Thirolf, G.K. Vorobyev and C. Weber, *Direct mass measurements above uranium bridge the gap to the island of stability*, Nature 463, 785 (2010).

[9] E. Minaya Ramirez, D. Ackermann, K. Blaum, M. Block, C. Droese, Ch.E. Düllmann, M. Dworschak, M. Eibach, S. Eliseev, E. Haettner, F. Herfurth, F.P. Heßberger, S. Hofmann, J. Ketelaer, G. Marx, M. Mazzocco, D. Nesterenko, Yu.N. Novikov, W. R. Plaß, D. Rodríguez, C. Scheidenberger, L. Schweikhard, P.G. Thirolf and C. Weber, *Direct mapping of nuclear shell effects in the heaviest elements*, Science 337, 1207 (2012).

[10] E. Minaya Ramirez, D. Ackermann, K. Blaum, M. Block, C. Droese, Ch.E. Düllmann, M. Eibach, S. Eliseev, E. Haettner, F. Herfurth, F.P. Heßberger, S. Hofmann, G. Marx, D. Nesterenko, Yu.N. Novikov, W.R. Plaß, D. Rodríguez, C. Scheidenberger, L. Schweikhard, P.G. Thirolf and C. Weber, *Recent developments for high-precision mass measurements of the heaviest elements at SHIPTRAP*, Nucl. Instrum. Methods B 317, 501 (2013).

[11] S. Schwarz, G. Bollen, D. Lawton, P. Lofy, D.J. Morrissey, J. Ottarson, R. Ringle, P. Schury, T. Sun, V. Varentsov and L. Weissman, *The low-energy-beam and ion-trap facility at NSCL/MSU*, Nucl. Instrum. Methods B 204, 507 (2003).

[12] F. Herfurth, W. Barth, G. Clemente, L.A. Dahl, P. Gerhard, M. Kaiser, O.K. Kester, H.-J. Kluge, C. Krantz, N. Kotovskiy, C. Kozhuharov, M. Maier, J. Pfister, W. Quint, U. Ratzinger, A. Schempp, A. Sokolov, Th. Stöhlker, H. Vormann, G. Vorobjev, A. Wolf and S. Yaramishev for the HITRAP collaboration, *HITRAP-heavy, highly charged ions at rest: Status and experimental opportunities*, J. Phys.: Conf. Ser. 388, 142009 (2012).

[13] D. Rodríguez, K. Blaum, W. Nörtershäuser, M. Ahammed, A. Algora, G. Audi, J. Äystö et al., *MATS and LaSpec: High-precision experiments using ion traps and lasers at FAIR*, Eur. Phys. J. Spec. Top. 183, 1 (2010).

[14] V.S. Kolhinen, M. Bussmann, E. Gartzke, D. Habs, J.B. Neumayr, C. Schürmann, J. Szerypo and P.G. Thirolf, *Commissioning of the double Penning trap system MLLTRAP*, Nucl. Instrum. Methods A 600, 391 (2009).

[15] B. Blank, S. Grévy, P.G. Thirolf and C. Weber, *Perspectives for mass spectrometry at the DESIR facility of SPIRAL2*, Int. J. Mass Spectrom. 349, 264 (2013).

[16] M. König, G. Bollen, H.-J. Kluge, T. Otto and J. Szerypo, *Quadrupole excitation of stored ion motion at the true cyclotron frequency*, Int. J. Mass Spectrom. Ion Proc. 142, 95 (1995).

[17] S. Eliseev, K. Blaum, M. Block, C. Droese, M. Goncharov, E. Minaya Ramirez, D.A. Nesterenko, Yu.N. Novikov and L. Schweikhard, *Phase-imaging ion-cyclotron-resonance measurements for short-lived nuclides*, Phys. Rev. Lett. 110, 082501 (2013).

[18] M. Block, *Mass measurements of Lr and Rf isotopes with SHIPTRAP*, Scientific proposal for experiments presented to the GPAC at GSI, November 2015.

[19] M. Redshaw, J. McDaniel and E.G. Myers, *Dipole moment of PH^+ and the atomic masses of ^{28}Si, ^{31}P by comparing cyclotron frequencies of two ions simultaneously trapped in a Penning trap*, Phys. Rev. Lett. 100, 093002 (2008).

[20] S. Sturm, F. Köhler, J. Zatorski, A. Wagner, Z. Harman, G. Werth, W. Quint, C.H. Keitel and K. Blaum, *High-precision measurement of the atomic mass of the electron*, Nature 506, 467 (2014).

[21] C.L. Cowan Jr., F. Reines, F.B. Harrison, H.W. Kruse and A.D. McGuire, *Detection of the free neutrino: A confirmation*, Science, 124, 103 (1956).

[22] Q.R. Ahmad, R.C. Allen, T.C. Andersen et al. (SNO Collaboration), *Direct evidence for neutrino flavor transformation from neutral-current interactions in the Sudbury Neutrino Observatory*, Phys. Rev. Lett. 89, 011301 (2002).

[23] N. Steinbrink, V. Hannen, E.L. Martin, R.G.H. Robertson, M. Zacher and C. Weinheimer, *Neutrino mass sensitivity by MAC-E-Filter based time-of-flight spectroscopy with the example of KATRIN*, New J. Phys. 15, 113020 (2013).

[24] A. Monfardini, C. Arnaboldi, C. Brofferio, S. Capelli, F. Capozzi, O. Cremonesi, C. Enss, E. Fiorini, A. Fleischmann, L. Foggetta, G. Gallinaro, L. Gastaldo, F. Gatti, A. Giuliani, P. Gorla, R. Kelley, C.A. Kilbourne, B. Margesin, D. McCammon, C. Nones, A. Nucciotti, M. Pavan, M. Pedretti, D. Pergolesi, G. Pessina, F.S. Porter, M. Prest, E. Previtali, P. Repetto, M. Ribeiro-Gomez, S. Sangiorgio and M. Sisti, *The microcalorimeter arrays for a rhenium experiment (MARE): A next-generation calorimetric neutrino mass experiment*, Nucl. Instrum. Methods A 559, 346 (2006).

[25] M. Sisti, C. Arnaboldi, C. Brofferio, G. Ceruti, O. Cremonesi, E. Fiorini, A. Giuliani, B. Margesin, L. Martensson, A. Nucciotti, M. Pavan, G. Pessina, S. Pirro, E. Previtali, L. Soma and M. Zen, *New limits from the Milano neutrino mass experiment with thermal microcalorimeters*, Nucl. Instrum. Methods A 520, 125 (2004).

[26] D.A. Nesterenko, S. Eliseev, K. Blaum, M. Block, S. Chenmarev, A. Dörr, C. Droese, P.E. Filianin, M. Goncharov, E. Minaya Ramirez, Yu.N. Novikov, L. Schweikhard and V.V. Simon, *Direct determination of the atomic mass difference of ^{187}Re and ^{187}Os for neutrino physics and cosmochronology*, Phys. Rev. C 90, 042501(R) (2014).

[27] E.W. Otten and C. Weinheimer, *Neutrino mass limit from tritium β-decay*, Rep. Prog. Phys. 71, 086201 (2008).

[28] L. Gastaldo, K. Blaum, A. Doerr, Ch.E. Düllmann, K. Eberhardt, S. Eliseev, C. Enss, A. Faessler, A. Fleischmann, S. Kempf, M. Krivoruchenko, S. Lahiri, M. Maiti, Yu.N. Novikov, P.C.-O. Ranitzsch, F. Simkovic, Z. Szusc and M. Wegner , *The electron capture ^{163}Ho experiment ECHo*, J. Low Temp. Phys. 176, 876 (2014).

[29] F. Gatti, M.R. Gomes, R. Vaccarone, G. Gallinaro, L. Ferrari and D. Bagliani, *Study of sensitivity improvement for MARE-1 in Genoa*, J. Low Temp. Phys. 151, 603 (2008).

[30] B. Alpert, M. Balata, D. Bennett, M. Biasotti, C. Boragno, C. Brofferio, V. Ceriale, D. Corsini, P.K. Day, M. De Gerone, R. Dressler, M. Faverzani, E. Ferri, J. Fowler, F. Gatti, A. Giachero, J. Hays-Wehle, S. Heinitz, G. Hilton, U. Köster, M. Lusignoli, M. Maino, J. Mates, S. Nisi, R. Nizzolo, A. Nucciotti , G. Pessina, G. Pizzigoni, A. Puiu, S. Ragazzi, C. Reintsema, M. Ribeiro Gomes, D. Schmidt, D. Schumann, M. Sisti, D. Swetz, F. Terranova and J. Ullom, *HOLMES - The electron capture decay of ^{163}Ho to measure the electron neutrino mass with sub-eV sensitivity*, Eur. Phys. J. C 75, 112 (2015).

[31] NuMECS website, http://p25ext.lanl.gov/ kunde/NuMECS/.

[32] K. Blaum, Yu.N. Novikov and G. Werth, *Penning traps as a versatile tool for precise experiments in fundamental physics*, Contemp. Phys. 51, 149 (2010).

[33] S. Eliseev, K. Blaum, M. Block, S. Chenmarev, H. Dorrer, Ch.E. Düllmann, C. Enss, P.E. Filianin, L. Gastaldo, M. Goncharov, U. Köster, F. Lautenschläger, Yu.N. Novikov, A. Rischka, R.X. Schüssler, L. Schweikhard and A. Türler, *Direct measurement of the mass difference of ^{163}Ho and ^{163}Dy solves the Q-value puzzle for the neutrino mass determination*, Phys. Rev. Lett. 115, 062501 (2015).

[34] D. Rodríguez, *A quamtum sensor for high-performance mass spectrometry*, Appl. Phys. B: Lasers O. 107, 1031 (2012).

[35] D.J. Heinzen and D.J. Wineland, *Quantum-limited cooling and detection of radio-frequency oscillations by laser-cooled ions*, Phys. Rev. A 42, 2977 (1990).

[36] J.M. Cornejo and D. Rodríguez, *A quantum sensor for neutrino mass measurements*, Adv. High Energy Phys. 849497, 1 (2012).

[37] Trapped-ion quantum information and simulation group website at the University of Hannover, http://www.iqo.uni-hannover.de/qeti.html.

[38] K.R. Brown, C. Ospelkaus, Y. Colombe, A.C. Wilson, D. Leibfried and D.J. Wineland, *Coupled quantized mechanical oscillators*, Nature 471, 196 (2011).

[39] P.K. Ghosh, *Ion traps*, Clarendon Press, Oxford (1995).

[40] F.G. Major, V. Gheorghe and G. Werth, *Charged particle traps*, Springer, Heidelberg (2002).

[41] H. Dehmelt, *Experiments with an isolated subatomic particle at rest*, Rev. Mod. Phys. 62, 525 (1990).

[42] W. Paul, *Electromagnetic traps for charged and neutral particles*, Rev. Mod. Phys. 62, 531 (1990).

[43] L.S. Brown and G. Gabrielse, *Geonium theory: Physics of a single electron or ion in a Penning trap*, Rev. Mod. Phys. 58, 233 (1986).

[44] F.M. Penning, *Glow discharge between coaxial cylinders at low pressures in a axial magnetic field*, Physica III 9, 873 (1936).

[45] H.G. Dehmelt, *Radiofrequency spectroscopy of stored ions I: Storage*, Adv. At. Mol. Phys. 3, 53 (1967).

[46] L. Brown and G. Gabrielse, *Precision spectroscopy of a charged particle in an imperfect Penning trap*, Phys. Rev. A 25, 2423 (1982).

[47] J. Ketelaer, J. Krämer, D. Beck, K. Blaum, M. Block, K. Eberhardt, G. Eitel, R. Ferrer, C. Geppert, S. George, F. Herfurth, J. Ketter, Sz. Nagy, D. Neidherr, R. Neugart, W. Nörtershäuser, J. Repp, C. Smorra, N. Trautmann and C. Weber, *TRIGA-SPEC: A setup for mass spectrometry and laser spectroscopy at the research reactor TRIGA Mainz*, Nucl. Instrum. Methods A 594, 162 (2008).

[48] D. Rodríguez, A. Méry, G. Ban, J. Brégeault, G. Darius, D. Durand, X. Fléchard, M. Herbane, M. Labalme, E. Liénard, F. Mauger, Y. Merrer, O. Naviliat-Cuncic, J.C. Thomas and C. Vandamme, *The LPCTrap facility: A novel transparent Paul trap for high-precision experiments*, Nucl. Instrum. Methods A 565, 876 (2006).

[49] K. Blaum, G. Bollen, F. Herfurth, A. Kellerbauer, H.-J. Kluge, M. Kuckein, S. Heinz, P. Schmidt and L. Schweikhard, *Recent developments at ISOLTRAP: Towards a relative mass accuracy of exotic nuclei below 10^{-8}*, J. Phys. B At. Mol. Opt. Phys. 36, 921 (2003).

[50] G. Savard, St. Becker, G. Bollen, H.-J. Kluge, R.B. Moore, Th. Otto, L. Schweikhard, H. Stolzenberg and U. Wiess, *A new cooling technique for heavy ions in a Penning trap.* Phys. Lett. A, 158, 247 (1991).

[51] G. Gabrielse, X. Fei, L.A. Orozco, R.L. Tjoelker, J. Haas, H. Kalinowsky, T.A. Trainor and W. Kells, *Cooling and sowing of trapped antiprotons below 100 meV*, Phys. Rev. Lett. 63, 1360 (1989).

[52] D.J. Larson, J.C. Bergquist, J.J. Bollinger, W.M. Itano and D.J. Wineland, *Sympathetic cooling of trapped ions: A laser-cooled two-species nonneutral ion plasma*, Phys. Rev. Lett. 57, 70 (1986).

[53] E.A. Cornell, R.M. Weisskoff, K.R. Boyce and D.E. Pritchard, *Mode coupling in a Penning trap: π pulses and a classical avoided crossing*, Phys. Rev. A 41, 312 (1990).

[54] G. Bollen, S. Becker, H.-J. Kluge, M. König, R.B. Moore, T. Otto, H. Raimbault-Hartmann, G. Savard, L. Schweikhard, H. Stolzenberg and the ISOLDE collaboration, *ISOLTRAP: A tandem Penning trap system for accurate on-line mass determination of short-lived isotopes*, Nucl. Instrum. Methods A 368, 675 (1996).

[55] S. Rainville, J.K. Thompson and D.E. Pritchard, *An ion balance for ultra-high-precision atomic mass measurements*, Science 303, 334 (2004).

[56] G. Gräff, H. Kalinowsky and J. Traut, *A direct determination of the proton electron mass ratio*, Z. Phys. A, 297, 35 (1980).

[57] G. Bollen, H.-J. Kluge, T. Otto, G. Savard and H. Stolzenberg, *Ramsey technique applied in a Penning trap mass spectrometer*, Nucl. Instrum. Methods B 70, 490 (1992).

[58] M. Kretzschmar, *The Ramsey method in high-precision mass spectrometry with Penning traps: Theoretical foundations*, Int. J. Mass Spectr. 264, 122 (2007).

[59] S. George, S. Baruah, B. Blank, K. Blaum, M. Breitenfeldt, U. Hager, F. Herfurth, A. Herlert, A. Kellerbauer, H.-J. Kluge, M. Kretzschmar, D. Lunney, R. Savreux, S. Schwarz, L. Schweikhard and C. Yazidjian, *Ramsey method of separated oscillatory fields for high-precision Penning trap mass spectrometry*, Phys. Rev. Lett. 98, 162501 (2007).

[60] G. Eitel, M. Block, A. Czasch, M. Dworschak, S. George, O. Jagutzki, J. Ketelaer, J. Ketter, Sz. Nagy, D. Rodríguez, C. Smorra and K. Blaum, *Position-sensitive ion detection in precision Penning trap mass spectrometry*, Nucl. Instrum. Methods A 606, 475 (2009).

[61] L. Schweikhard, *Theory of quadrupole detection Fourier Transform-Ion Cyclotron Resonance*, Int. J. Mass Spectrom. Ion Proc. 107, 281 (1991).

[62] W. Shockley, *Currents to conductors induced by a moving point charge*, J. Appl. Phys. 9, 635 (1938).

[63] M.B. Comisarow and A.G. Marshall, *Fourier transform ion cyclotron resonance*, Chem. Phy. Lett 25, 282 (1974).

[64] R.B. Cody, R.E. Hein, S.D. Goodman and A.G. Marshall, *Stored waveform inverse Fourier transform excitation for obtaining increased parent ion selectivity in collisionally activated dissociation: Preliminary results*, Rapid Commun. Mass Spectrom. 1 (6), 99 (1987).

[65] D.J. Wineland and H.G. Dehmelt, *Principles of the stored ion calorimeter*, J. Appl. Phys. 46, 919 (1975).

[66] M. Ubieto-Díaz, D. Rodríguez, S. Lukic, Sz. Nagy, S. Stahl and K. Blaum, *A broad-band FT-ICR Penning trap system for KATRIN*, Int. J. Mass Spectrom. 288, 1 (2009).

[67] P. Horowitz and W. Hill, *The art of electronics*, Cambridge University Press, New York (1989).

[68] R.M. Weisskoff, G.P. Lafyatis, K.R. Boyce, E.A. Cornell, R.W. Flanagan and D.E. Pritchard, *Rf Squid Detector for Single-Ion trapping Experiments* J. Appl. Phys. 63, 4599 (1988).

[69] J. Verdú, *Theory of the coplanar-waveguide Penning trap*, New J. Phys. 13, 113029 (2011).

[70] K. Blaum, *High-accuracy mass spectrometry with stored ions*, Phys. Rep. 425, 1 (2006).

[71] K. Tanaka, H. Waki, Y. Ido, S. Akita, Y. Yoshida and T. Yoshida, *Protein and polymer analysis up to m/z 100000 by laser ionization time-of-fight mass spectrometry*, Rapid Commun. Mass Spectrom. 2, 151 (1988).

[72] B.T. Chait, and S.B. Kent, *Weighing naked proteins: practical, high-accuracy mass measurement of peptides and proteins*, Science 257, 1885 (1992).

[73] J.M. Cornejo, A. Lorenzo, D. Renisch, M. Block, Ch.E. Düllmann and D. Rodríguez, *Status of the project TRAPSENSOR: Performance of the laser-desorption ion source*, Nucl. Instrum. Methods. B 317, 522 (2013).

[74] D. Rodríguez, V. Sonnenschein, K. Blaum, M. Block, H.-J. Kluge, A.M. Lallena, S. Raeder and K. Wendt, *Production of negative osmium ions by laser desorption and ionization*, Rev. Sci. Instrum. 81, 013301 (2010).

[75] J.M. Cornejo, M. Colombano, J. Doménech, M. Block, P. Delahaye and D. Rodríguez, *Extending the applicability of an open-ring trap to perform experiments with a single laser-cooled ion*, Rev. Sci. Instrum. 86, 103104 (2015).

[76] E. Ruiz, *Desarrollo de una microtrampa para experimentos de precisión con iones de* ^{40}Ca, Degree Thesis, University of Granada, Spain (2014).

[77] J.M. Cornejo, M.J. Gutiérrez, E. Ruiz, S. Stahl and D. Rodríguez, *Design of a double Penning-(micro)-trap mass spectrometer based on connecting ions*, In preparation.

[78] J.M. Cornejo and D. Rodríguez, *A preparation Penning trap for the TRAPSENSOR project with prospects for MATS at FAIR*, Nucl. Instrum. Methods. B, DOI:10.1016/j.nimb.2015.11.033.

[79] J.E. Mindwinter, *The theory of Q-switching applied to slow switching and pulse shaping for solid state lasers*, Br. J. Appl. Phys. 16, 1125 (1965).

[80] R.S. Brown and J.J. Lennon, *Mass resolution improvement by incorporation of pulsed ion extraction in a matrix-assisted laser desorption/ionization linear time-of-flight mass spectrometer* Anal. Chem. 67, 1998 (1995).

[81] M. Block, D. Ackermann, D. Beck, K. Blaum, M. Breitenfeldt, A. Chauduri, A. Doemer, S. Eliseev, D. Habs, S. Heinz, F. Herfurth, F.P. Heßberger, S. Hofmann, H. Geissel, H.-J. Kluge, V. Kolhinen, G. Marx, J.B. Neumayr, M. Mukherjee, M. Petrick, W. Plass, W. Quint, S. Rahaman, C. Rauth, D. Rodríguez, C. Scheidenberger, L. Schweikhard, M. Suhonen, P.G. Thirolf, Z. Wang, C. Weber and the SHIPTRAP collaboration, *Ion trap facility SHIPTRAP status and perspective*, Eur. Phys. J. A 25, 49 (2005).

[82] S. Rahaman, M. Block, D. Ackermann, D. Beck, A. Chaudhuri, S. Eliseev, H. Geissel, D. Habs, F. Herfurth, F.P. Heßberger, S. Hofmann, G. Marx, M. Mukherjee, J.B. Neumayr, M. Petrick, W.R. Plaß, W. Quint, C. Rauth, D. Rodríguez, C. Scheidenberger, L. Schweikhard, P.G. Thirolf and C. Weber, *On-line commissioning of SHIPTRAP*, Int. J. Mass Spectrom. 251, 146 (2006).

[83] D. Neidherr, *Entwicklung einer pumpsperre für das Penning-fallemassenspektrometer SHIPTRAP*, Diploma Thesis, University of Mainz, Germany (2006).

[84] W.D. Phillips, *Laser Cooling and Trapping of Atoms*, Nobel Lecture, 199 (1997).

[85] C.J. Foot, *Atomic Physics*, Oxford University Press, New York (2005).

[86] D.R. Crick, S. Donnellan, D.M. Segal and R.C. Thompson, *Magnetically induced electron shelving in a trapped Ca^+ ion*, Phys. Rev. A 81, 052503 (2010).

[87] M. Colombano, *Implementación y puesta a punto de un modulador electroóptico y mejora de las prestaciones de tubos fotomultiplicadores en el proyecto TRAPSENSOR*, Master Thesis, University of Granada, Spain (2015).

[88] J.M. Cornejo, P. Escobedo and D. Rodríguez, *Status of the project TRAPSENSOR*, Hyperfine Interact. 227, 223 (2014).

[89] P. Escobedo, *Desarrollo de un sistema de control para láseres de diodo utilizando moduladores acústico-ópticos*, Master Thesis, University of Granada, Spain (2014).

[90] NIST Atomic Spectra Database website. http://www.nist.gov/pml/data/asd.cfm.

[91] H. Rohde, S.T. Gulde, C.F. Roos, P.A. Barton, D. Leibfried, J. Eschner, F. Schmidt-Kaler and R. Blatt, *Sympathetic ground-state cooling and coherent manipulation with two-ion crystals*, J. Opt. B Quantum Semiclassical Opt. 3, 34 (2001).

[92] C. Vivo, *Estudio de una fuente de iones de superficie en el marco del proyecto TRAPSENSOR y primeros resultados de enfriamiento por láser (laser cooling) de iones de* $^{40}Ca^{+}$, Master Thesis, University of Granada, Spain (2014).

[93] W. Lotz, *Electron-impact ionization cross-section and ionization rate coefficients for atoms and ions from hydrogen to calcium*, Z. Phys. 216, 241 (1968).

[94] J. Doménech, *Producción fe iones de* $^{40}Ca^{+}$ *por el método de fotoionización y estudio de su utilización en el proyecto TRAPSENSOR*, Master Thesis, University of Granada, Spain (2015).

[95] P.H. Dawson, *Quadrupole mass spectrometry and its applications*, Elsevier Scientic Publishing Company, New York, (1995).

[96] NIST cryogenic technologies group website, http://cryogenics.nist.gov/

[97] S. Ulmer, *First observation of spin flips with a single proton stored in a cryogenic Penning trap*, Ph.D. Thesis, University of Heidelberg, Germany (2011).

[98] E.R. Dobrovinskaya, L.A. Lytvynov and V. Pinshchik , *Sapphire: material, manufacturing, applications*, Springer (2009).

[99] Saint-Gobain Crystals website, http://www.crystals.saint-gobain.com

[100] G. Bollen, R.B. Moore, G. Savard and H. Stolzenberg, *The accuracy of heavy-ion mass measurements using time of flight-ion cyclotron resonance in a Penning trap*, J. Appl. Phys. 68, 4355 (1990).

[101] R. Ferrer, *Mass measurements on neutron-deficient nuclides at SHIPTRAP and commissioning of a cryogenic narrow-band FT-ICR mass spectrometer*, Ph.D. Thesis, University of Mainz, Germany (2007).

[102] D. Beck, K. Blaum, H. Brand, F. Herfurth and S. Schwarz, *A new control system for ISOLTRAP*, Nucl. Instrum. Methods A 527, 567 (2004).

[103] S. Rahaman, *First on-line mass measurements at SHIPTRAP and mass determinations of neutron-rich Fr and Ra isotopes at ISOLTRAP*, Ph.D. Thesis, University of Heidelberg, Germany (2005).

[104] G. Gabrielse, *Relaxation calculation of the electrostatic properties of compensated Penning traps with hyperbolic electrodes*, Phys. Rev. A 27, 2277 (1983).

[105] H. Raimbault-Hartmann, D. Beck, G. Bollen, M. König, H.-J. Kluge, E. Schark, J. Stein, S. Schwarz and J. Szerypo, *A cylindrical Penning trap for capture, mass selective cooling, and bunching of radioactive ion beams*, Nucl. Instrum. Methods B 126, 378 (1997).

[106] R. Arnold et al. (NEMO Collaboration), *First results of the search for neutrinoless double-beta decay with the NEMO 3 detector*, Phys. Rev. Lett. 95, 182302 (2005).

[107] S. Umehara, T. Kishimoto, I. Ogawa, R. Hazama, S. Yoshida, K. Matsuoka, D. Yokoyama, K. Mukaida, K. Ichihara, Y. Hirano and A. Yanagisawa, *CANDLES for double beta decay of* ^{48}Ca, J. Phys.: Conf. Ser. 39, 356 (2006).

[108] M. Wang, G. Audi, A.H. Wapstra, F.G. Kondev, M. MacCormick, X. Xu and B. Pfeiffer, *The AME2012 atomic mass evaluation (II). Tables, graphs and references*, Chin. Phys. C 36(12), 1603 (2012).

[109] G.Zs.K. Horvath, R.C. Thompson and P.L. Knight, *Fundamental physics with trapped ions*, Contemp. Phys. 38 (1), 25 (1997).

[110] G.-Z. Li and G. Werth, *Energy distribution of ions in a Penning trap*, Int. J. Mass Spectrom. Ion Proc. 121, 65 (1992).

[111] G.-Z. Li, S. Guan and A.G. Marshall, *Comparison of equilibrium ion density distribution and drapping force in Penning, Paul, and Combined ion traps*, J. Am. Soc. Mass Spectrom. 9, 473 (1998).

[112] Heraeus Quarzglas GmbH website, http://heraeus-quarzglas.com/

[113] IEEE Standards Coordinating Committee 27 on Time and Frequency, *IEEE standard definitions of physical quantities for fundamental frequency and time metrology - Random instabilities*. IEEE Std 1139-1999 (1999).

[114] H. Spieler, *Semiconductor detector systems*, Oxford University Press (2005).

[115] W.M. Leach Jr., *On the Calculation of Noise in Multistage Amplifiers*, IEEE Trans. Circuits Syst. I 42 (3), 173 (1995).

[116] J.G. Ramírez, private communication.

[117] M. Heck, P. Ascher, R.B. Cakirli, H. Golzke, D. Rodríguez, S. Stahl, M. Ubieto-Díaz and K. Blaum, *An online FT-ICR Penning-trap mass spectrometer for the DPS2-F section of the KATRIN experiment*, Nucl. Instrum. Methods A 757, 54 (2014).

[118] D. Phillips, *A precision comparison of the $\bar{p}$-p charge-to-mass ratios*. Ph.D. thesis, Harvard University, United States (1996).

[119] J.A. Lichter, *Crystals and oscillator*, JL9113 Rev. C (1991).

[120] Hewlett Packard Test and Measurement product, *Fundamentals of quartz oscillators*, Application Note 200-2, EE.UU (1997).

[121] T. Kaltenbacher, *Development of ultra low-temperature electronics for the AEgIS experiment*, Ph.D. thesis, Graz University, Austria (2013).

[122] J. Rychen, T. Ihn, P. Studerus, A. Herrmann, K. Ensslin, H.J. Hug, P.J.A. van Schendel and H.J. Güntherodt, *Operation characteristics of piezoelectric quartz tuning forks in high magnetic fields at liquid helium temperatures*, Rev. Sci. Instrum. 71, 1695 (2000).

[123] S.R. Jefferts, T. Heavner, P. Hayes and G.H. Dunn, *Superconducting resonator and a cryogenic GaAs field effect transistor amplifier as a single ion detection system*, Rev. Sci. Instrum. 64, 737 (1993).

[124] R.S. Van Dyck Jr., D.L. Farnham and P.B. Schwinberg, *Precision mass measurements in the UW-PTMS and the electron's "atomic mass"*, Phys. Scr. T59, 134 (1995).

[125] S. Ulmer, H. Kracke, K. Blaum, S. Kreim, A. Mooser, W. Quint, C.C. Rodegheri and J. Walz, *The quality factor of a superconducting RF resonator in a magnetic field*, Rev. Sci. Instrum. 80, 123302 (2009).

[126] A. Dörr, *PENTATRAP: A novel Penning-trap system for high-precision mass measurements*, Ph.D. Thesis, University of Heidelberg, Germany (2015).

[127] C. Diehl, *First mass measurements with the MPIK/UW-PTMS*, Ph.D. Thesis, University of Heidelberg, Germany (2011).

[128] P. Fabbricatore, G. Gemme, R. Musenich, R. Parodi, M. Viviani, B. Zhang and R.J. Sinko, *First measurement of a NbTi RF cavity*, IEEE Trans. Appl. Supercond. 3, 197 (1993).

[129] Stahl-Electronics website, http://www.stahl-electronics.com/.

[130] V.S. Kolhinen, S. Kopecky, T. Eronen, U. Hager, J. Hakala, J. Huikari, A. Jokinen, A. Nieminen, S. Rinta-Antila, J. Szerypo and J. Äystö, *JYFLTRAP: A cylindrical Penning trap for isobaric beam purification at IGISOL*, Nucl. Instrum. Methods A 528, 776 (2004).

[131] H. Gutbrod, I. Augustin, H. Eickhoff, K.-D. Groß, W.F. Henning, D. Krämer and G. Walter, *FAIR Baseline Technical Report*, Gesellschaft für Schwerionenforschung mbH (GSI), Darmstadt (2006).

[132] D. Rodríguez for the MATS collaboration, *The advanced trapping facility MATS at FAIR*, Int. J. Mass Spectrom. 349-350, 255 (2013).

[133] L.L. Bandura, *Next-generation fragment separators for exotic beams*, Northern Illinois University, United States (2009).

[134] FAIR website, http://www.fair-center.eu/

[135] G. Maero, *Cooling of highly charged ions in a Penning trap for HITRAP*, Ph.D. Thesis, University of Heidelberg, Germany (2008).

[136] M. Bussmann, U. Schramm, D. Habs, V.S. Kolhinen and J. Szerypo, *Stopping highly charged ions in a laser-cooled one component plasma of $^{24}Mg^{+}$ ions*, Int. J. Mass Spectrom. 251, 179 (2006).

Agradecimientos

En primer lugar me gustaría destacar que la realización de este trabajo de investigación no hubiera sido posible sin la dirección y ayuda de mi director Daniel Rodríguez Rubiales, cuyo esfuerzo e intenso trabajo ha hecho posible la consecución del mismo.

I also thank Michael Block for providing the gold-plating of the PPT electrodes and the blue-prints of the SHIPTRAP devices and Dennis Neidherr for installing the control system. We also thank Klaus Wendt and Norbert Trautmann for arranging for the loan of the MALDI-TOF system from Mainz University.

Aunque este trabajo ha sido realizado en el Departamento de Física Atómica, Molecular y Nuclear, otras instituciones y empresas han realizado un gran esfuerzo para llevarlo a cabo.

Me gustaría agradecer a la gente de INMACO por el trabajo realizado para mecanizar la gran mayoría de piezas mostradas en esta tesis doctoral. A Manolo jefe, y en especial a los Manolos torneros, que siempre han estado dispuestos a ayudarme con algún diseño, y a realizar cualquier pieza por complicada que fuera, de verdad, muchas gracias.

También quiero agradecer a Santi y Gabriel, de la empresa SEVEN, que en esta última etapa con los circuitos electrónicos realizaron un gran trabajo, en especial, me gustaría agradecer a Gabriel por sus explicaciones sobre la electrónica que se muestra en la última parte de este trabajo.

Además, me gustaría agradecer a todos los que han contribuido en este proyecto a lo largo de estos últimos cuatro años (Antonio, Wilfredo, Rodolfo, Miguel, Juanpi, Berta, Pablo, Carlos, Sadig, Albert, Ernesto, Manu, Martin y Jaime), estudiantes de grado y master, y también doctores, que han ayudado a completar esta instalación, y me han hecho más fácil el trabajo de todos los días. Muchas gracias.

Y por supuesto, a mi familia, a la cual he dedicado este trabajo. A mis hermanas, Pachi, Vane y Alba, que siempre me han apoyado, a mis padres, Juan y Luisa, por su confianza en todo lo que he realizado y a los cuales les debo todo, y a mi esposa, Sandra, por ser el principal pilar de mi vida, por su amor y fiel entrega.